Universidad Autónoma de Madrid

Structure-Property Relationships in Photoresponsive Molecular Materials

Tesis doctoral presentada por

Junqing Shi

Para optar al título de Doctor en Ciencias Físicas

Instituto IMDEA Nanociencia

Departamento de Física de la Materia Condensada

Facultad de Ciencias

Madrid, November 2017

Universidad Autónoma de Madrid

Structure-Property Relationships in Photoresponsive Molecular Materials

Doctoral thesis presented by

Junqing Shi

For the degree of Doctor of Philosophy in Physics by Universidad Autónoma de Madrid

Instituto IMDEA Nanociencia

Departamento de Física de la Materia Condensada

Facultad de Ciencias

Madrid, November 2017

Ph.D supervision:

Supervisor: Dr. Johannes Gierschner (IMDEA Nanociencia, Spain)

Co-supervisor: Dr. Begoña Milián Medina **(**University of Valencia, Spain)

Tutor: Prof. Dr. Rodolfo Miranda Soriano (IMDEA Nanociencia, UAM, Spain)

Structure-Property Relationships in Photoresponsive Molecular Materials

Thesis for the Degree of Doctor of Philosophy

Instituto IMDEA Nanociencia

Departamento de Física de la Materia Condensada

Facultad de Ciencias

Universidad Autónoma de Madrid

Madrid, Spain, 2017

Thesis Defense Committee:

Dr. Emilio M. Pérez (IMDEA Nanociencia, Madrid Spain)

Dr. Dai Zhang (University of Tübingen, Germany)

Dr. M. Carmen Ruiz Delgado (University of Málaga, Spain)

Larry Lüer (IMDEA Nanociencia, Madrid, Spain)

Juan Carlos Sancho-Garcia (Universidad de Alicante, Spain)

Preface

The work presented in this thesis was conducted over a four-and-half year period (2013.09-2018.01), at the Department of Condensed Matter Physics, Faculty of Science, the Autonomous University of Madrid (Universidad Autónoma de Madrid), and the Madrid Institute for Advanced Studies - IMDEA Nanoscience, Madrid, Spain.

List of papers included in the thesis

Paper 1

Solid State Luminescence Enhancement in π-Conjugated Materials: Unraveling the Mechanism beyond the Framework of AIE/AIEE,

Junqing Shi, Luis E. Aguilar Suarez, Seong-Jun Yoon, Shinto Varghese, Carlos Serpa, Soo Young Park, Larry Lüer, Daniel Roca Sanjuán, Begoña Milián-Medina, and Johannes Gierschner,

J. Phys. Chem. C., 2017, **121**, 23166-23183.

Paper 2

Twist Elasticity Controlled Crystal Emission in Highly Luminescent Polymorphs of Cyano-Substituted Distyrylbenzene (βDCS),

Junqing Shi, Seong-Jun Yoon, Lucas Viani, Soo Young Park, Begoña Milián-Medina, and Johannes Gierschner,

Adv. Opt. Mater., 2017, **5**, 1700340.

Paper 3

Designing high performance all-small molecule solar cells with non-fullerene acceptors: comprehensive studies on photoexcitation dynamics and charge separation kinetics,

Junqing Shi, Anna Isakova, Abasi Abudulimu, Marius van den Berg, Oh Kyu Kwon, Alfred J. Meixner, Soo Young Park, Dai Zhang, Johannes Gierschner, and Larry Lüer,

submitted to Energy Envrion. Sci.

List of other papers resulting from this time (not included in the thesis)

Paper 4

Excited State Absorption Spectra of Dissolved and Aggregated Distyrylbenzene - a TD-DFT State and Vibronic Analysis,

Eliezer Fernando Oliveira, **Junqing Shi**, Francisco Carlos Lavarda, Larry Lüer, Begoña Milián-Medina, and Johannes Gierschner,

J. Chem. Phys., 2017, **147**, 034903.

Paper 5

Backbone Twisting in Fluorinated MEH–PPV Polymers: Impact on Exciton Localization and Deactivation,

Rim Milad, **Junqing Shi**, Aranzazu Aguirre, Antonio Cardone, Begoña Milián-Medina, Gianluca M. Farinola, Manef Abderrabba, and Johannes Gierschner,

J. Mater. Chem. C, 2016, **4**, 6900-6906.

Acknowledgements

I am very grateful to the doctoral journey at IMDEA Nanociencia, for giving me knowledge, positive attitude and insistent work spirit to eventually complete this thesis.

I would like to thank all the people who have worked together with me during the last four years, for their long-standing support and great contributions to make this thesis a possibility.

Foremost, my respectful gratitude goes to my main supervisor, Prof. Dr. Johannes Gierschner (IMDEA Nanociencia), for the intellectual guidance through numerous lectures and discussions and for the untiring effort to help me improve my work and revise my thesis. I really appreciate him for providing me so many great opportunities to attend conferences and do inter-lab visits in order to broaden my view and sharpen my learning and presentation skills. He is such a nice person with warm attitude and good sense of humor, as well as a good researcher with invaluable scientific honesty and responsibilities, which keeps inspiring me to become a better version of myself throughout my doctoral study and the follow-up career.

My sincerest thanks extend to my thesis co-supervisor, Dr. Begoña Milián-Medina (University of Valencia), for the thorough introduction into quantum-chemical calculations with unimaginable patience and expertise, and especially for the ability to always see the possible solutions to my problems and difficulties even in cases outside of research.

I would like to express my gratitude to Dr. Larry Lüer (IMDEA Nanociencia) for his careful guidance on the ultra-fast transient absorption (TA) spectroscopy investigation, and the detailed and profound TA data analysis he has performed on the data sets. All the TA experiments presented here were performed with his PhD students Anna Isakova and Abasi Abudulimu and special thanks to them.

I am also very grateful to the following groups of people for the fruitful collaborations that provide many valuable results. I wish to thank Prof. Soo Young Park (Seoul National University) for his advice and proofreading for our drafts, as well as his students Seong-Jun Yoon and Oh Kyu Kwon who synthesized the pristine compounds investigated in this thesis. I would like to thank Prof. Alfred J. Meixner, Dr. Dai Zhang and their student Marius van den Berg (University of Tübingen) for the nice contribution on the Raman and fluorescence

mapping results, where the measurements were performed with Marius van den Berg and all phases of this study were under the guidance of Dr. Dai Zhang. Sincere thanks to Dr. Carlos Serpa (University of Coimbra) for access to the photoacoustic calorimetry (PAC) setup, and for the guidance of experiments and results evaluation. A great deal of thanks to Dr. Daniel Roca Sanjuán and his student Luis E. Aguilar Suarez (University of Valencia) for carrying out the CASSCF computations. Many thanks to Dr. Lucas Viani (Universidad Carlos III de Madrid) for providing the calculated polymorphs of **β-DCS**. Warm thanks also to Dr. Henk Bolink (University of Valencia) for access to the integrating sphere.

I thank all the current and former members of our research group, in particular Dr. Shinto Varghese, Dr. Santanu Bhattacharyya and Dr. Nandajan Paramjyothi Chandramohan, for their cooperation, favors and the stimulating discussions. Also to my fellow labmates and officemates in the institute, for their help and for creating a pleasant atmosphere, in particular Patricia Bondia Raga who helped me a lot with the communication problems in Spanish. Special thanks to the Chinese fellow doctoral students, especially to Longfei Wu who has been my roommate and officemate in the last four years, the countless talks about various topics, the precious memories we shared and the unique friendship between us are very much appreciated. In addition, to the administrative staff and the other researchers of the institute, thanks for creating good working conditions and attractive working environment. IMDEA Nanociencia is a cracking place to work and I am grateful to have the opportunity to do the majority of my research here.

Thanks to all the foundations for supporting my life and my work during this four-year period. The PhD grant (2013-2017) from the China Scholarship Council (CSC) is acknowledged which guaranteed my daily living. Financial support at IMDEA provided by the Spanish Ministerio de Economía y Competitividad (MINECO-FEDER project CTQ2014-58801), as well by the Comunidad de Madrid (Project Mad2D, Grant No. S2013/MIT-3007, and PhotoCarbon, S2013/MIT-284), by the 'Severo Ochoa' Programme for Centres of Excellence in R&D (MINECO project SEV-2016-0686) and by the Campus of International Excellence (CEI) UAM+CSIC. The Laserlab-Europe (grant agreement n°284464, EC's Seventh Framework Program) is acknowledged for providing funding for time-resolved photoacoustic

calorimetry (PAC) measurements at the CQC, Chemistry Department, University of Coimbra, Spain. The European COST Action "Nanospectroscopy", MP1302 is acknowledged for supporting a short-term scientific mission at the Institute for Physical and Theoretical Chemistry, University of Tübingen, for the Raman and fluorescence mapping studies, as well as their support to visit various workshops of the COST action.

And finally, I wish to express the most gratefulness and thanks to my family members and my friends who always stand beside me, for their indirect contributions to this thesis. To my dear parents and my brother, thanks for being so caring, supportive and understanding during this long-term study. Especially my mother, to whom this thesis is lovingly dedicated, her encouragement, tremendous love and emotional support manage to sustain me throughout my thesis writing and always remind me to be positive through my frustrations and difficult times. Warm thanks also to my friends, for the alive long-distance friendship.

Contents

Summary

Small π-conjugated organic materials are of great significance in materials science due to the versatility and superiority in practical applications, especially in opto-electronics. Among the numerous types of small organic materials, those essentially based on the structural motif of the cyano-vinyl synthon have obtained intensive and long-term attention, motivated by the striking behaviors such as the strong luminescent enhancement in the solid state, the prominent twist elasticity of the floppy structure, as well as the good photovoltaic performance. Although many CN-substituted distyrylbenzenes (**DCS**)-type materials have been successfully developed and applied, an in-depth understanding of the structural factors responsible for these particularities is rather limited by now, which has enormous implications for the desired approach of targeted design, to avoid expensive and tedious trial and error synthetic approaches. In this thesis, the pronounced solid state luminescence enhancement (SLE) and the twist elasticity (TE), as well as the high power conversion efficiency (PCE) of organic solar cells (OSCs) based on the cyano-stilbene motif platform, are investigated integrating experimental steady-state & transient absorption and fluorescence measurements and quantum-chemical calculations.

As SLE-active materials with emerging applications in organic (opto)electronics, the issue of SLE, popularized under the (however somewhat misleading) term aggregation-induced emission (AIE), has evolved as a hot field in current materials research. The first part of the thesis will be dedicated to understand the SLE phenomenon derived from one-component systems based on a library of multiple CN-substituted distyrylbenzenes (**DCS** family) with systematically, subtly varying substitution pattern in terms of type and position. Depending on positional isomerism, these compounds exhibit dramatically changed photoresponse upon changes of the environment, going from fluid solution to solid solution and to the single crystalline phase. Moreover, pronounced solid state color shifts are observed even in one and the same compound due to polymorphism. To achieve a full understanding of all these observations, the current work first provides a detailed conceptual analysis of all contributing factors for structural polymorphism, for solid state shifts and SLE, which includes geometrical vs. electronic factors, *intra*- vs. *inter*molecular contributions, radiative vs. nonradiative decay channels. Then, by combining quantitative (ultra)fast optical spectroscopic techniques, appropriate quantum-chemical methods, and structural (X-ray) data, these contributions are systematically isolated, analyzed and quantified. In all, this allows for a full

understanding of the twist-elasticity concept, of the solid state color shifts, but in particular provides a first holistic picture of SLE, where all details involved in the SLE process are fully elucidated and rationalized.

The second part of this thesis will go one step further in materials, addressing specific device applications (i.e. OSCs), to investigate a two-component system made of small molecules and used in a bulk heterojunction (BHJ) OSC. This study is driven by the rapid development of solution-processed fullerene-free all-small-molecule OSCs (ASM-OSC), being a novel, highly promising alternative route to the classical polymer-based OSCs. Although improved stability and high PCE of this new type of cells was demonstrated, the reasons for the good performance of ASM-OSCs are however not clear yet; however, they must be known in order to fully exploit the design capacities of these materials. Here we use a combined computational-experimental approach to study the photoexcitation dynamics of a prototypical all-small-molecule photovoltaic blend, namely p-DTS(FBTTh$_2$)$_2$ as donor and NIDCS-MO as acceptor. Despite high PCE and high open circuit voltages, only very weak excitonic coupling and localized charge transfer (CT) states, and slow exciton dissociation rates are observed, due to even slower parasitic exciton quenching, enabled by the relatively high purity level. The analysis in the current work clearly proves that the morphological and chemical purity of the small molecules, which distinguishes them from classic polymers, slows down parasitic quenching and plays the key role for the good performance of ASM-OSCs. The device behaves like a quasi-ideal cell with negligible activation for charge generation but high activation for charge recombination, which permits to separate the localized CT states.

Keywords: conjugation, organic materials, optoelectronics, fluorescence, transient absorption, quantum chemistry, aggregation induced emission, aggregation caused quenching, excited state deactivation, conical intersection, single crystals, organic solar cell

Resumen

Los materiales orgánicos π-conjugados de pequeño tamaño desempeñan un papel muy relevante en el área de ciencia de materiales debido a su versatilidad y superioridad en aplicaciones prácticas, especialmente, en optoelectrónica. Entre la gran variedad de materiales orgánicos pequeños, aquellos que esencialmente se basan en el sintón ciano-vinilo, han recibido una atención especialmente intensiva y duradera en el tiempo, motivada por el sorprendente comportamiento que presentan en cuanto al gran aumento de luminiscencia en estado sólido, la prominente "twist-elasticity"(TE)[1*] de la estructura flexible, así como el buen rendimiento fotovoltaico. Aunque son numerosos los materiales de tipo distirilbenceno CN-sustituido (**DCS**) que se han desarrollado y aplicado con éxito, el conocimiento detallado de los factores estructurales responsables de estas particularidades es todavía muy limitado, algo que presenta numerosas implicaciones sobre la ansiada estrategia del diseño dirigido, que persigue evitar procedimientos sintéticos tediosos y caros basados en experiencias prueba-error. En esta tesis, se ha investigado el pronunciado incremento de la luminiscencia en estado sólido (SLE), la "twist-elasticity", así como la elevada eficiencia de conversión energética (PCE) de células solares orgánicas (OSCs) basadas en plataformas con el motivo ciano-estilbeno, integrando medidas experimentales de absorción y fluorescencia en estado estacionario y resueltas en el tiempo, y cálculos químico-cuánticos.

En paralelo a los materiales SLE-activos con incipientes aplicaciones en (opto)electrónica orgánica, la SLE, popularizada bajo el (algo confuso) término de emisión inducida por la agregación (AIE), ha evolucionado como un tema candente en el campo actual de investigación de materiales. La primera parte de la tesis se dedicará a la comprensión de los fenómenos SLE derivados de sistemas de un componente basados en una librería de distirilbencenos sustituidos con múltiples grupos CN (familia **DCS**) en los que se ha variado de manera sistemática y sutil el patrón de sustitución según el tipo y la posición. Dependiendo de la isomería posicional, estos compuestos muestran dramáticas diferencias en la fotorrespuesta a cambios en el entorno, al pasar de disolución fluida a disolución sólida y a la fase monocristalina. Es más, se han podido observar pronunciados cambios de color en estado sólido incluso en un mismo compuesto, debido a polimorfismo. Con el fin de lograr una completa racionalización de dichas observaciones, el presente trabajo proporciona, en primer lugar, un análisis conceptual de todos los factores que influyen en el polimorfismo estructural,

[1*] N.T.: El término "twist-elasticity" ha sido recientemente introducido [ref. [An12]-paper of the twist-elasticity] y podría traducirse como elasticidad de giro o para el giro.

en los cambios de color y la SLE, incluyendo factores geométricos frente a electrónicos, contribuciones *intra*- frente a *inter*moleculares, así como canales de desactivación radiativos frente a no-radiativos. A continuación, mediante la combinación de técnicas espectroscópicas ópticas (ultra)rápidas cuantitativas, métodos químico-cuánticos apropiados, y datos estructurales (rayos X), se han aislado, analizado y cuantificado los factores anteriormente mencionados. Todo ello ha permitido lograr una total comprensión del concepto de "twist-elasticity" y de los cambios de color en estado sólido pero, en especial, ha permitido obtener una primera descripción holística de la SLE, donde todos los detalles implicados en el proceso SLE se han elucidado y racionalizado por completo.

La segunda parte de este trabajo de tesis doctoral va un paso más allá de los materiales, abordando aplicaciones de dispositivos específicos (a saber, OSCs), con el fin de investigar un sistema de dos componentes fabricado a partir de moléculas pequeñas en una OSC de tipo "bulk heterojunction" (BHJ). Este estudio está motivado por el rápido desarrollo de las OSCs de moléculas pequeñas (ASM-OSC), sin fullerenos y procesadas en disolución, que constituyen una ruta alternativa muy prometedora a las clásicas OSCs basadas en polímeros. Aunque la mejora en estabilidad y elevada PCE de este nuevo tipo de células solares ha quedado demostrada, las razones de tan buen comportamiento son, todavía, desconocidas; sin embargo, es necesario conocerlas para llevar a cabo la total explotación de las capacidades de diseño de estos materiales. En este caso, se ha hecho uso de una estrategia computacional-experimental combinada para estudiar la dinámica de fotoexcitación de un prototipo de mezcla fotovoltaica de moléculas pequeñas, concretamente p-DTS(FBTTh$_2$)$_2$ como dador y NIDCS-MO como aceptor. A pesar de las elevadas PCE y elevados potenciales de circuito abierto, únicamente se observan acoplamientos excitónicos y estados localizados de transferencia de carga muy débiles, así como bajas velocidades de disociación de excitones, debido a procesos todavía más lentos de "quenching" parásito de excitones, posibilitados por el elevado nivel de pureza. El análisis realizado en el presente trabajo, prueba claramente que la pureza química y morfológica de las moléculas pequeñas, característica que las distingue de los polímeros clásicos, reduce el "quenching" parásito y juega un papel clave en el buen comportamiento de las ASM-OSCs. El dispositivo se comporta como una célula quasi-ideal, con energía de activación despreciable para la generación de cargas, pero elevada para la recombinación de cargas, cosa que permite separar los estados CT localizados.

Palabras clave: conjugación, materiales orgánicos, optoelectrónica, fluorescencia, absorción de estados transitorios, química cuántica, emisión inducida por agregación, “quenchin”

causado por agregación, desactivación de estados excitados, intersección cónica, monocristales, célula solar orgánica.

Chapter 1

Introduction

The spirit of the present thesis is to understand the structure-property relationships of luminescent conjugated organic materials that are available through facile synthesis and manifest their potentials in certain optoelectronic applications. Therefore, in the first part of this chapter (Section 1.1), a general introduction into material science will be given, as well as into structure-property relationship (SPR) - the essential tool to material development; then, in Section 1.2, the characteristics of the specific class of materials, i.e. π-conjugated organic materials, will be comprehensively described in aspects of structure, property and SPRs; in Section 1.3, the solid-state luminescence enhancement (SLE**)** in π-conjugated organic materials will be discussed in the aspects of phenomenology, terminology as well as mechanism; in Section 1.4, the present and future of organic solar cells (OSCs), especially the new trend of solution-processes all-small-molecule organic solar cells (ASM-OSCs) will be outlined.

1.1 Materials Science

1.1.1 Materials and Science

In a broad sense, the term of "material" defines a chemical substance or mixture of substances with practical applications, with an emphasis on solids. As reflected by the history of human civilization, materials have played a key role in the technological evolution, becoming increasingly important in the modern era due to incessant human needs and market requirements.[Nat75] Thus, the availability of materials with desirable properties and novel applications is being a subject of great interest and significance for the scientific community.[Nat95]

Materials science, also commonly termed "materials science and engineering", is a multi-inter-disciplinary field devoting to discover and design new materials, via making use of incorporated elements from a variety of individual fields (such as chemistry and physics of condensed matter, engineering applications, and industrial manufacture).[Roy79] Research topics of general interest in this field can involve all phases of a material, ranging from initial synthesis via industrial processing, to device engineering and performing, with a main focus on materials' creation and improvement.[Cal97] However, for making appropriate decisions about materials in the design process, for the selection and use (especially for realizing the goal of designing a material in need with target instead of experiencing traditional trial-synthesis procedure) the understanding about how the intrinsic structure of a material influences it’s properties and performances, is intriguing and appealing.

1.1.2 Materials Paradigm and Structure-Property Relationship

The material paradigm (MP), conceptually pivotal in materials science study, is the understanding of the inter-relationship between processing, structure, property and performance (4 items) of a material, which can be schematically illustrated either in a linear way of "processing → structure → property → performance", or in the form of a tetrahedron.[Cal97] In plain words, MP reflects that the structure of a substance dictates its properties, which in turn determine performances in certain applications, where the structure is the determining component, and itself again dependent on the way of extraction, processing or manufacture.[Cal97] Considering the core position of structural understanding in MP, structure-property relationship (SPR) can be extracted as essential and fundamental. Through understanding SPR we can know how the chemical structure of a material relates to its properties' behavior and further correlates to relative engineering performance.[Cal97] Therefore, targeted design of structures with desirable properties and tailored performance while consuming drastically less time and money is of high importance. Thus, the full control of the structure parameters as well as resulting structure-sensitive properties are in the center of interest. Here "structure" simply means the arrangement of the components in a material but variable from the atomic (angstroms) up to nano (1-100 nm), micro (100 nm to centimeters) and macro (millimeters to meters) scale; at all scales, matter properties include (however not limited to) mechanical, electrical, optical, chemical, magnetic and thermal properties.[Ral76] Among the structural factors, the atomic or *intra*molecular structure may be responsible for many fundamental chemical, optical and electronic properties,[Ral76] while the *inter*molecular structure may dramatically affect these properties by synergy,[Wür16,Gie13b] which eventually makes SPR a complex matter.

In this thesis, SPR will be investigated on a specific kind of material, aiming to obtain in-depth understanding of the interplay of (*intra*- and *inter*-molecular) structural contributions on photo-induced properties, being of great benefit for offering strategic guidance and inspiration to target materials design.

1.2 Conjugated Organic Materials

Through intensive efforts in the field of material science, enormous numbers of materials have been discovered, characterized in their structure, property and use. Among the large diversity of materials, this thesis has a focus on conjugated organic materials (comprising only small molecules) to derive structure-property relationship as discussed above.

1.2.1 Features of Conjugated Organic Molecules

Electronic Structure: π-conjugation.[Rob77] "Conjugated organic materials" are distinguished from other categories by their specific composition giving rise to their inherent properties. The essential feature are chains of sp^2-hybridized carbon (C) atoms with overlapping adjacent p-type orbitals, bridging the C-C single bonds, to give chains of alternating single and double bonds of the form C=C-C=C. This π-conjugation allows for partial delocalization of π electrons, generally leading to a stabilization of the resulting lowest occupied molecular orbital (LUMO) and, at the same time, destabilization of the highest occupied MO (HOMO) in comparison to the constituting units, leading to smaller HOMO-LUMO energies. Extending the conjugated system, continuous bands with narrowed bandgaps will be obtained, which typically fall into the ultraviolet-visible (UV-Vis) spectral region; this is the apparent origin of the peculiarities in the properties and applications of π-conjugated materials as discussed below.

Peculiarities in Property and Application. Conjugated organic materials exhibit distinctively different optical and electronic properties from their non-conjugated counterparts owing to their ability to absorb light in the UV-Vis range.[Rob77] As conjugated compounds are bio-synthesized in nature, their color, spreading all over the visible spectrum, is the major source for the colored appearance of the plant kingdom.[Tan08] Synthetic chromophores with infinite structure variation (extension of the molecular backbone and specific functionalization) play an important role as industrial colorants etc.,[Zol03] but in particular for light-emission and electron-conduction. Relying on these features and courses, conjugated organic materials have been investigated as promising candidates for a large variety of opto-electronic applications involving organic sensors, photodetectors, electrochromic devices, biochemical probes, organic light-emitting diodes (OLEDs), organic field-effect transistors (OFETs) and organic solar cells (OSCs).[Ost16] Furthermore, organic based opto-electronic devices have advantages in synthesis, processing, cost, performance and tunability in comparison to inorganic counterparts;[Ste07] this drew great attention in laboratories and engineering industries worldwide over the last few decades.

1.2.2 Structure-Property Relationship Study of Conjugated Materials for Optoelectronics

Chemical synthesis offer a versatile route to conjugated organic materials, where the constituting molecules vary in (i) the nature and length of their conjugated backbone, (ii) nature, position and number of chemical (neutral or charged) substituents.[Lan99, Dot97, Oel96] Chromophores with non-repetitive structure are usually called dyes; systems with repetitive structure, but exact composition are called oligomers, while structures but undefined, but long chainlengths are called polymers.[Glo96] With respect to their applications in optoelectronics, a multitude of properties have to be understood, including electronic structures, absorption and emission energies, optical bandshapes, as well as excited state deactivation, i.e. non-/radiative pathways. On one hand, this will sensitively depend on the *intra*molecular factors, electronic and steric effects as imposed by the molecular backbone as well as the substituents. On the other hand, in the condensed phase, *inter*molecular factors will modulate the molecular properties due to *inter*molecular interactions, as imposed by the electronic and geometrical demands of the molecules.[Cor01, Var11, Gie05, Gie13a, Ant12, Gie16] This complex interplay constitutes a big challenge in the field, and requires an in-depth understanding of SPRs to make full use of the materials' versatility by unbiased, targeted design.[Mag12, Shi10, Chi12, Zhu13] A full SPR analysis of conjugated organic materials requires some important steps:

(1) Structural control is essential to establish valid SPRs; at the molecular level this requires the investigation of structurally well-defined small oligomeric materials instead of polymers; at the materials level, the preparation of single crystals is crucial to identify the *inter*molecular arrangement by X-ray analysis.

(2) Identification of *intra*- and *inter*molecular parameters which determine the resulting properties; here, *inter*-dependencies have to be clearly analyzed.

(3) Appropriate spectroscopic methodologies and analytics to identify, quantify and disentangle properties and processes.

(4) Appropriate theoretical (in particular quantum-chemical) approaches, to understand and/or predict properties and to disentangle parameters which are not accessible by experiment.

Such methodology will be applied in the current work to two important classes of organic conjugated materials for optoelectronics, i.e. (A) solid state emitters, being of high importance for OLED, OFET, sensors, photoswitches, memory and bio-imaging applications, and (B) all-small-molecule organic photovoltaics.

These two classes of organic conjugated materials are small (oligomeric) compounds based on the structural motif of the cyano-vinyl synthon. The first class is one-component system named as **DCS** compounds, comprising eight cyano-substituted derivatives of distyrylbenzene (**DSB**) with varying substitution in pattern and/or position. The second class is a binary system composed of solution-processable small-molecule donor and acceptor materials which are used in bulk heterojunction all-small molecule organic solar cell (BHJ ASM-OSC).

1.3 Solid State Luminescence Enhancement (SLE) in π-Conjugated Organic Materials

1.3.1 History and Phenomenology

For some conjugated organic materials, their emission behavior sensitively depends on the environment of the constituting molecules, i.e. whether molecularly dissolved solutions or densely gathered solids, i.e. solid/frozen/highly viscous solutions or condensed phases (single crystals, SC; films; nanoparticles, NP), are considered. The switching of environment can induce strong changes in their emission efficiency, for example, dense packing can turn non-emissive dissolved molecules into intense solid state emitters or promote quenching in the other way around.[Wür11, Wal91,Gie13b] Highly emissive organic crystals which exhibit solid state emission enhancement (SLE) nowadays has evolved to a hot research area in the field of conjugated organic materials due to their potential applications in organic (opto)electronics, involving OLEDs, lasers, sensors, OFETs, OSCs, luminescent bioprobes and light emitters.[Ant06, Var11, An12, Shi10, Hot95, Zha16, Ng15, Li14, Chi12, Gie13a, Gie13b, Zhu13, Gie16, Wür16, Tan13, Wür11] In any case, emission enhancement from nearly non-luminescent solutions to luminescent solid state samples is a long known phenomenon and several mechanism have been proposed over the decades to explain it. In the 1930s, Jelley and Scheibe independently described the luminescence enhancement phenomenon on isocyanines,[Wür11] emphasizing the *inter*molecular (i.e. inter-chromophore) contributions (so-called "J-aggregation"). Since the beginning of the 1960s, the emission enhancement of stilbenoid-type compounds involving stilbene and tetraphenylethene (TPE) were investigated;[ElB68, Sal68, Fis75, Bar81, San90, Kle95] there, the intramolecular contributions were thoroughly examined by conducting experiments under low temperature and/or high viscosity conditions, as well as by the synthesis of sterically hindered or rigidified oligomers. In the 1990s, Oelkrug and Hanack investigated all combinations of non/-emissive solution/solid state phases enabled by systematically changing

the substitution pattern of distyrylbenzene (**DSB**); especially by introducing the cyano functionality in the vinylene unit (i.e. di-cyano-styrylbenzene, **DCS** derivatives).[Oel96, Oel98, Döt98, Hoh98, Lan99, Lan01, Hn02, Sch01, Leu02] In this case, probably for the first time, the significance of *intra*- vs. *inter*molecular contributions was stressed by the authors through concurrently investigating solid solutions and (poly)crystalline phases[Oel98] which comprise dissolved and aggregated molecules, respectively; as recently reviewed.[Gie13a, Gie13b, Gie16] Several years later (at the beginning of 20th), Tang's group popularized this phenomenon as "aggregation-induced emission" (AIE),[Luo01,Tan13] and accordingly, the opposite of AIE was called "aggregation-induced quenching" (ACQ). Realizing that aggregation was often not the reason for the luminescence enhancement, they made "restricted intramolecular rotation" (RIR) responsible as the main cause in systems such as silole derivatives and TPE through further low temperature and highly viscose experiments (while the experiments from the 1960s on TPE and other stilbenoid systems along with their far-reaching mechanistic understanding of luminescence enhancement were hardly recognized). In any case, the community deriving from Tang's work has made significant contributions which give a modern driven to this old field, especially in the aspects of materials' discovery and application exploration.

1.3.2 Terminology and Mechanism

The now broadly disseminated AIE and ACQ terminology might be misleading due to the fact that they imply a mechanistic understanding (i.e. "caused", "induced"), which confuses the (in principle long known) complex interplay of possible *intra*- and *inter*molecular contributions. As the followers' community also realized this complexity by following the forefathers in doing experiments in solid or frozen solutions, and stressing *intra*molecular mechanisms (RIR), the "aggregation" terminology in the end seems rather to confuse readers than helping for an understanding, making the AIE a somewhat infelicitous label. In fact, in the IUPAC definition,[Ale07] aggregation is for describing a "process whereby dispersed molecules or particles form aggregates", which thus is not applicable to highly viscous or solid solutions where molecules are still well dispersed. For reflecting this ambiguity, the term "aggregation-induced enhanced emission" (AIEE)[An02] was introduced and stressed the synergy of *intra*- and *inter*molecular contributions in the earlier study of **DCS** derivatives.[An12]

In order to provide a physical sound terminology, we propose a new general term for the observed phenomenon - solid state luminescence enhancement (SLE), being purely phenomenological and thus "innocent". It should be mentioned in this context that also the ACQ term is equally problematic, since also here a mechanistic understanding is evoked. However, it was shown earlier for **DSB**,[Gie13a] that condensed phase samples can behave differently with respect to their photophysics, but depending on their morphology. In fact, while (spin-coated or vapor-deposited) thin films or nanoparticles of **DSB** are low emissive, **DSB** single crystals are highly emissive despite identical *inter*molecular arrangement. It was shown in the mentioned paper that the apparent difference between the system lies in the morphology: different to the single crystals, thin films or nanoparticles are polycrystalline in nature with domains of typically 20 nms size compared to sub-mm sized single crystals. For this reason, quenching by trap states, which are in particular formed surfaces and interfaces, are the decisive factor for the observed different photophysics. In single crystals trap concentrations are low due to high structural purity and small surface-to-volume ratio; moreover, average distances to the surfaces are large, which rationalizes the observed high luminescence due to suppressed quenching.

1.3.3 The Physical Origin of SLE

As mention above, "solid state luminescence enhancement" - SLE - represents a physical sound, phenomenological term, as "solid state" includes not only molecular aggregated solids like amorphous, or poly/single crystalline materials, but also molecular dissolved solids, i.e. frozen or solid solutions, for instance poly-methyl methacrylate (PMMA), and other highly viscous matrices.

Despite the fact that many SLE materials have been successfully developed, the mechanistic understanding is still limited due to the above mentioned *intra*- and *inter*molecular contributions of excited state deactivation which might widely vary for different systems. For clarifying this question, photophysical insights are needed but are still largely missing. Thus, based on a full consideration of all controlling parameters of SLE, extensive investigations are required, which include fluid solution, solid solution (in PMMA matrix) as well as solid single crystals; concurrently via properly combining experiment and quantum-chemical calculations to disentangle the *intra*- and *inter*molecular origins of SLE from each other in a reasonable way, and to achieve a holistic photophysical picture of the SLE mechanism.

Breaking down the complexity of the SLE mechanism, some key points need to be clarified. Firstly, it should be kept in mind that the photoluminescence (PL) quantum yield Φ_F is a quantity decided by two variables, i.e. the radiative (k_r) and nonradiative (k_{nr}) rates. Thus, the change of one single variable does not necessarily determine the value of Φ_F in the end; for instance, H-aggregation does not necessarily quench the fluorescence (as suggested by ACQ) under trap-free conditions (i.e. single crystals), because in this case the large decrease of k_{nr} is dominant although H-type coupling reduces k_r. Secondly, *intra*- and *inter*molecular factors can both impact both rates (see Scheme 1.1); for instance, *inter*molecular J-type packing

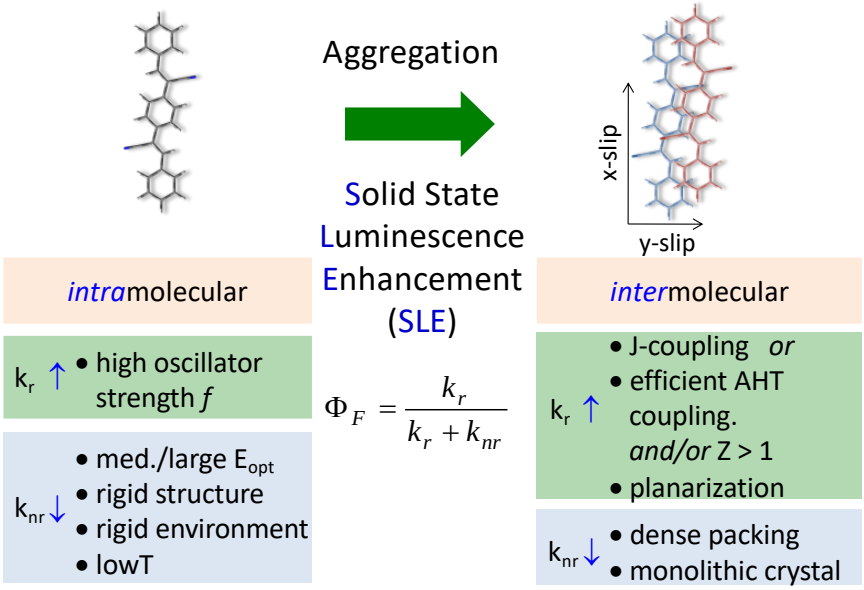

Scheme 1.1: Controlling factors of SLE. *Intra*- vs. *inter*molecular contributions and radiative vs. nonradiative contributions.

increases k_r while e.g. *intra*molecular excited state switching due to changes in polarity or polarizability of the solvent could dramatically lower k_r.[Koh98] It should be reminded here that the excitonic contributions (H-/J-coupling) to k_r should be treated by a adequate quantum chemical method[Gie13b, Gie16] instead of the classical molecular exciton model introduced by Kasha;[Kas65] see Chapter 2; such approach will be undertaken in this work. Thirdly, electronic and geometrical factors can (equally) contribute to the solid state spectral and photophysical properties; again, here quantum-chemical methods are indispensable to disentangle these contributions.

Finally, a multitude of nonradiative deactivation pathways such as ($S_1 \rightarrow S_0$) internal conversion (IC), intersystem crossing (ISC) to the triplet manifold, photochemical processes

like trans-cis isomerization (as in the case of stilbene),[Kle95] and trapping[Gie13a] both contribute to k_{nr}, making it a quite complex issue. Among them, IC (and ISC) depends sensitively on the energetics and shapes of the S_n (n = 0,1,2...) potential energy surfaces PES (and possibly further involved triplet states) and their thermal population, being thus subject to subtle environmental changes such as temperature and viscosity; in fact, "floppy" molecules with shallow torsional potentials are especially vulnerable to changes of the environment. Thus, the most anticipated scenario for the majority of SLE materials is IC. However, due to the difficulties in the experimental and theoretical description of IC, the understanding of systems with ultrafast excited state deactivation via IC, in particular for large systems, is limited despite intense research over the years. Experimentally, pump-probe experiments with ultrafast time-resolution are required.[Won98, DiP07, Cha12, Zha17] Theoretically, a reliable description of all involved PES is required, particularly in the state-crossing regions which give rise to conical intersections (CI) to promote such processes along local coordinates. For this reasons, simplified approaches to tackle these IC are questionable;[Niu10] this is in particular true for harmonic approaches which employ 2-states models based on normal modes, since all three approximation might fail: in fact, the PES of S_0 at the state-crossing region (i.e. with high energy; 1.5-3.5 eV) becomes very anharmonic; furthermore, the path towards the CI is usually not following a normal mode but a local coordinate, and, moreover, might involve more than two states.

In addition, common quantum-chemical methods like time-dependent density functional theory (TD-DFT) generally fail in the description of excited state PES in the region of the CI. Although higher correlated methods using multi-configurational wavefunctions (e.g. the complete-active-space self-consistent field/ complete-active-space second-order perturbation theory (CASSCF/ CASPT2)) can deal with this problem in a reliable manner,[Roc12] they are typically limited to systems with a maximum of about 16 π-electrons. In fact, some progresses have been made in the last several years on characterizing the IC processes of SLE-active materials. For example, the IC processes in tetraphenylsilole and $B_{18}H_{20}$ (NC_5H_5) hybrid composite were recently elucidated,[Pen16, Lon17] providing a qualitative description of the mechanism; however, a quantitative understanding of the IC processes could not be gained due to the largely reduced active space. A dynamic description of IC was recently obtained in TPE,[Prl16] enabled by mixed quantum-classical trajectory surface hopping approaches. There even higher approximations were used in the methodology considering the high cost of the semi-classical dynamics computations. Thus, methods which can properly deal with the PES

description in large π-electron system like **DSB** are a pressing issue in SLE mechanism studies.

Based on the proper definition of the principal parameters which control SLE, and the recognition of the bottle-neck of SLE mechanism studies, this thesis examines the optical and photophysical properties in a series of structurally closely related prototypical SLE-active **DCS**-compounds under systematic structure variation, see Scheme 1.2.

For this, molecular origins of color variation and SLE are analyzed, including *intra*-/*inter*-molecular contributions, radiative and nonradiative pathways (IC, ISC) and electronic vs. geometrical factors. For this, experiments in various environments (i.e. fluid and solid solutions, single crystals including different polymorphs), are conducted, using

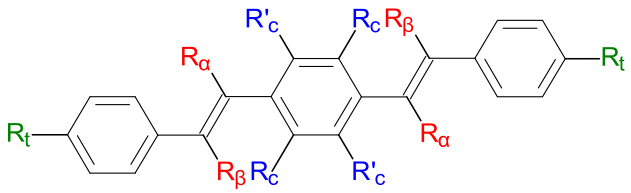

Scheme 1.2: General structure of the **DCS**-compounds used in this work.

different steady-state and (ultrafast) time-resolved spectroscopic techniques (i.e. (transient) UV-Vis absorption, PL, photoacoustic spectroscopy) and appropriate quantum-chemical calculation methods (i.e. TD-DFT and CASSCF).

1.4 The Present and Future of Organic Solar Cells (OSCs)

1.4.1 Classic Concept of OSCs (polymer:fullerene): Strategy and Restrictions

In the past 15 years, organic solar cells (OSCs) have emerged as a new class of photovoltaic devices with novel applications due to a unique combination of features, i.e. low prices due to facile and cheap synthesis and fabrication, as well as the perspective of large-area, shape-adapted, light-weighted, and semi-transparent devices[Dou13] (see the physical processes in OSCs in Scheme 1.3). The most exploited materials' strategy to achieve high power conversion efficiency (PCE) of OSCs is to use conjugated homo- or co-polymers as electron donors (**D**), while fullerene derivatives (in particular [6,6]-phenyl-C_{61}-butyric acid methyl ester; PCBM) were used as acceptors (**A**), which show exceptional acceptor abilities unmatched by other materials.[Ran07, Ben92, He11] This **D**:**A** heterojunction strategy favors exciton

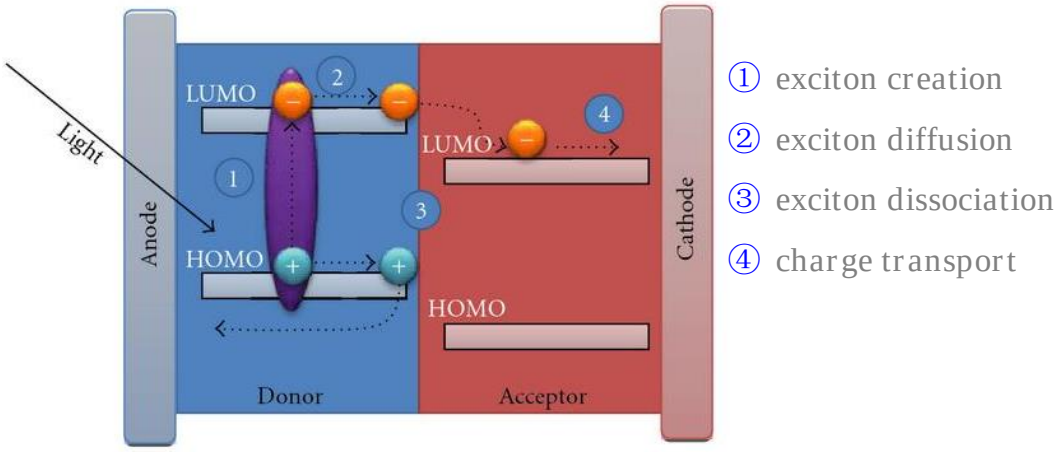

Scheme 1.3: Simple illustration of the physical processes in OSCs, adapted from Ref. [Chi10].

splitting into free charges (exciton dissociation) which can only happen in close proximity of **D**:**A** interfaces. Due to the small exciton diffusion length in the polymers, bulk heterojunction (BHJ) morphologies were used, to guarantee efficient charge separation at the **D**:**A** interface.[Etx15] Indeed, utilizing this strategy, PCEs have grown successfully and eventually surpassed the 10% mark.[NREL]

However, in order to achieve effective exciton diffusion to the interface, the domain size should be within the range of the exciton diffusion length (typically about ten nanometer); meanwhile the domains should be large enough to build a continuous percolating pathway for

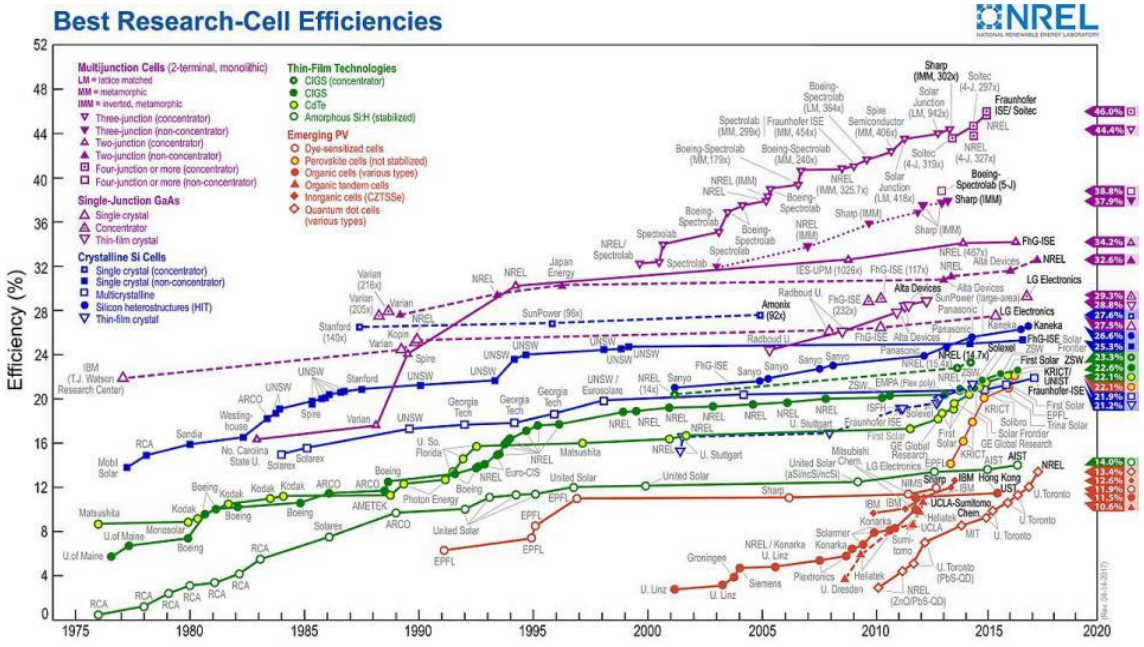

Scheme 1.4: Certified best PCEs for various photovoltaic cells over time, provided by [NREL].

electrons and holes that the separated charge carriers can finally reach the corresponding electrodes, i.e. avoiding halfway recombination in isolated domains. This restriction causes problems for polymeric OSCs.[Etx15] Firstly, the balance between optimal length scale and percolation pathway is difficult to reach, which is usually done through compromising the miscibility of donor and acceptor materials. This compromise requires much operational effort, and no common recipe is feasible for all possible **D**:**A** combinations. Secondly, even if the balance is reached, morphology might be unstable under operational conditions. Furthermore, often poor photochemical stability of both donor and acceptor phases is observed. Finally, many other factors, which limit the photovoltaic performance have to be compromised at the same time. For example, sufficient driving force (**D**-**A** LUMO offset) is needed for exciton dissociation in order to compete exciton deactivation, while it limits the maximum achievable open circuit voltages V_{OC}. Moreover, low optical bandgaps of polymers give rise to increased light absorption, but may lead to an increased yield of charge recombination from the intermediate charge transfer (CT) state; the latter limits the maximum achievable short circuit currents V_{SC}. The compromise between these factors however is subject to the morphological evolution, which makes polymeric cells prone to rapid performance degradation under operational conditions along with poor stability. These shortcomings of polymer:PCBM BHJ OSCs might be the reason why - after an initial strong improvements of the PCE, not much progress has been seen over the last few years (Scheme 1.4). Therefore, novel concepts and alternative routes are increasingly followed to re-stimulate the field.

1.4.2 Novel Trend in OSCs: Progress and Problems

The important new trend beyond the classic polymer:PCBM BHJ OSC concept over last few years is to go beyond the frame of fullerene-acceptors and to replace (co)polymers by small molecules. Much progress in non-fullerene based OSCs has been reported in the last few years,[Lin12, Fac13, Eft14, Lin14, Sau15, Lia17, Che17b] e.g. solely polymer-based OSC.[Fac13] In addition, simple chemistry and new concepts to synthesize solution-processable small molecules start to break the dominance of traditional (co)polymers;[Lin12, Eft14, Mis12, Fer16, Li16, Bin16, Ko17, Che17b, Kwo15, Kwo16, Yan17] in fact, mixed small-molecule/fullerene as well as polymer/small-molecule OSCs have been developed, reaching PCEs of 10-12% and showing long-term stability.[Li16, Bin16, Ko17]

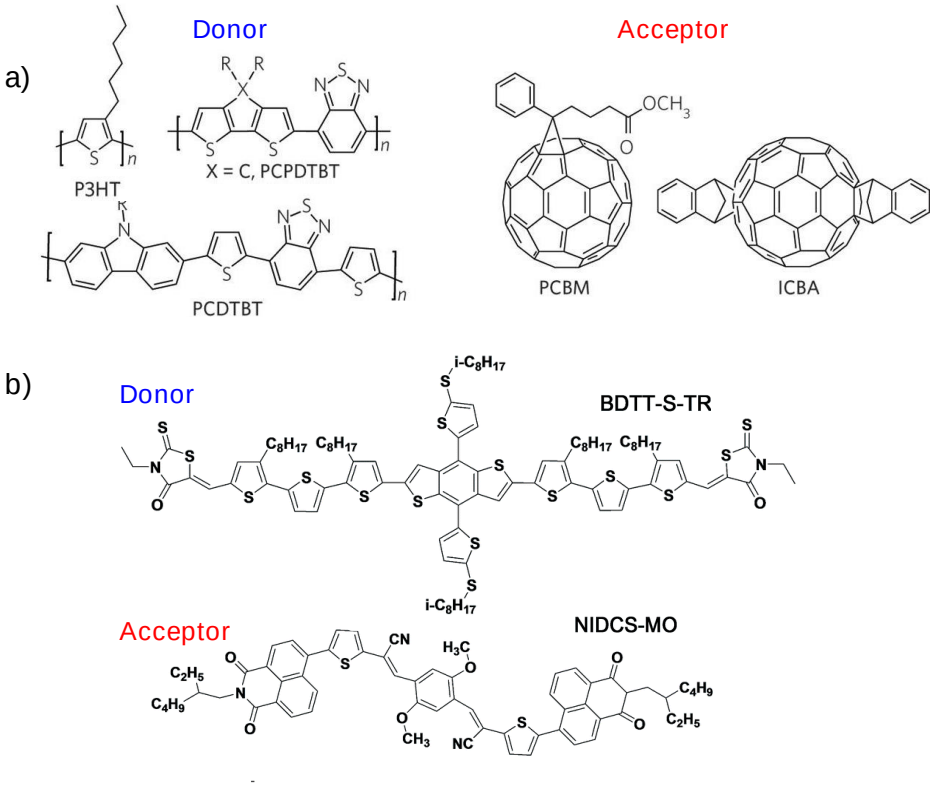

Scheme 1.5: Examples of a) classical (co)polymer:PCBM, and of b) novel small-molecule-based photovoltaic materials.[Kwo16]

The latest trend is to replace both donor and acceptors by simply synthesized solution-processable small molecules, thus offering polymer-free and non-fullerene OSCs. Only in the last two years, several solution-processed all-small-molecule OSCs (ASM-OSCs) have been reported,[Che17b, Kwo15, Kwo16,Yan17] and more heartening news is that their PCEs already reached 9 % by now.[Yan17] In addition, all-small-molecule OSCs are supposed to be beneficial against classic polymer:PCBM type cells in several aspects, including possible improved morphological[Kwo15] and photochemical stability,[Ko17] enhanced light absorbance, as well as electronic issues by optimized charge and exciton transport. However, the advantages of this concept in principle and underlying photophysical reasons for good device performance are by now not fully understood. Thus, to fully explore the advantages of this novel concept, interpretation and evaluation particularly of the photovoltaic elementary dynamics are in demand. Such approach is followed in the current thesis, examining a prototypical example of all-small-molecule photovoltaic blend[Kwo15] to reveal its intrinsic features.

1.4.3 Properties and Processes in All-Small-Molecule OSCs

Considering the intrinsic structural features of solution-processed small molecules in comparison to polymers, several advantages are expected,[Liu13, Kya13, Ron14] including diminished batch-to-batch variation due to high *intra*molecular structure precision, low-cost purification because of high chemical purity, tunable and controlled optical bandgap over a broad range arising from tailored and precise chemical structure, good (photo)chemical stability and long life-time supported by *intra*molecular structural and environmental factors, longer *inter*-chain exciton diffusion lengths due to a better ordered *inter*molecular arrangement and increased excitonic coupling; this may offer the possibility to overcome the limitations of domain size and subsequently realize bilayer structures, meanwhile break the restrictions on absorbance and thickness, as discussed above. In the present work, we aim to reveal and confirm the advantages of this new concept with photophysical proofs. For this purpose, we choose a representative of highly efficient non-fullerene all-small-molecule OSC to carry out a combined photophysical, computational and structural investigation.

A first groundbreaking example of non-fullerene all-small-molecule OSC was reported by the group of S. Y. Park at Seoul National University.[Kwo15] They synthesized an efficient non-fullerene small-molecule acceptor (NIDCS-MO, see Scheme 1.6), which contains two electron withdrawing groups (DCS plus NI) that accept electrons in synergy and self-assemble with complementary tendencies. This electron acceptor was combined with a widely used small-molecule donor, (p-DTS(FBTTh$_2$)$_2$),[Pol12] see Scheme 1.6. The BHJ OSC, showed a maximum PCE of 5.4%, exhibiting a pronounced temeparture (optimized annealing conditions is 110ºC).[Kwo15] In this report, the good photovoltaic performance was ascribed mainly to the favorable optimized nanoscale phase separation which is due to the crystallization in the donor phase upon annealing and leads to efficient charge extraction; the matched energy levels and complementary absorption spectra between **D** and **A** were considered as well.

Our work aims to provide an investigation into the photovoltaic elementary processes to rationalize the effective charge extraction in order to obtain more general design principles with respect to the particular features of all-small-molecule OSCs. For this purpose, we performed a combined spectroscopic, computational, and microscopic study to understand the photoexcitation dynamics on this cell; this reveals the properties and dynamics of both neutral and charged excited states in the relevant time scale from femtoseconds (*fs*) to microseconds

(μs), e.g. the delocalization lengths of singlet excited states and charged states, the rates of charge transfer and parasitic exciton quenching at defects. All these results point to a drastically different dynamics of charge generation in solution-processed all-small-molecule BHJ OSCs from polymer-based OSC.

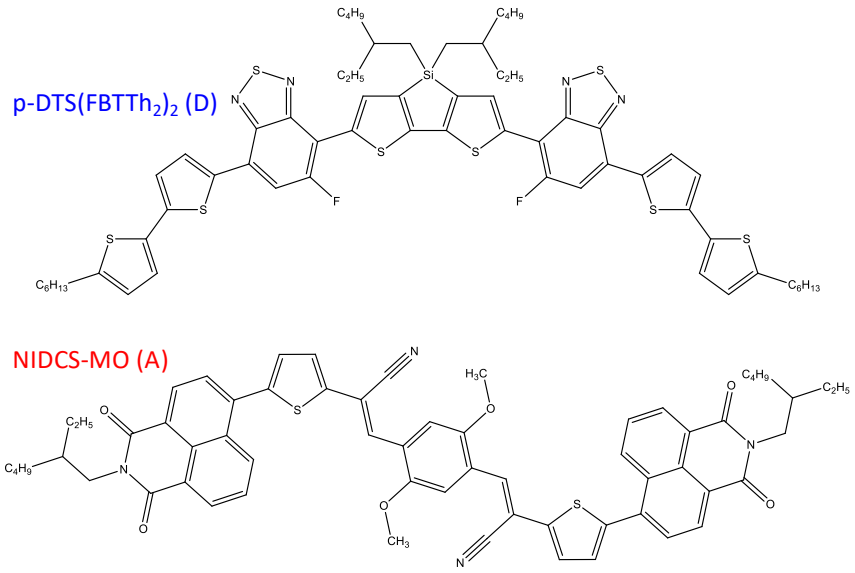

Scheme 1.6: Molecular Structure of solution-processable donor and acceptor molecules for ASM-OSCs used in this work.[Kwo15]

Chapter 2

Theoretical Foundation

In this Chapter, the theoretical foundation of the research presented in this thesis is discussed. This includes in particular the parameters which control the optical and photophysical properties of conjugated organic materials, and how to treat them theoretically and experimentally. In a first step, the simple isolated molecule will be discussed (Section 2.1), including electronic transitions, vibronic coupling and deactivation of the excited states. Section 2.2 will deal with the molecular interactions which occur in densely packed solids, to understand the significant influence of *inter*molecular interactions on the spectra and the photophysical dynamics; this will include geometrical, exitonic, excimeric and polarizability contributions, which may impact spectral positions and bandshapes, as well as radiative and nonradiative rates including trapping. Finally, Section 2.3 will discuss the quantum-chemical methodology used to calculate the properties of the molecules and molecular aggregates.

2.1 Electronic, Optical & Photophysical Properties of Conjugated Organic Molecules

2.1.1 Classical Model of Absorption

Lorentz (classical electron) Oscillator Model. H. Lorentz thought an atom as a small mass (electron) bound to another much larger mass (nucleus) by a spring-like force that behaves according to Hook's law. Thus, an applied field under resonance would simply displace the electron back and forth from the equilibrium by interacting with the charge of the electron, bringing the electron into harmonic oscillation and causing the spring either compressing or stretching. This pure classical description of atom-field interaction is the so-called Lorentz oscillator model, which bears a number of basic insights into the interaction problem, but is limited in its explanation and quantification, requiring a quantum chemical treatment (see below); in spite of it, this model is still considerably used as it manages to visualize the atom-field interaction elegantly. Based on the same concept, the molecular vibration can also be described by this mass spring oscillator model, i.e., two nuclei are connected by a spring-like chemical bond.

Oscillator Strength and Absorbance (Lambert-Beer Law). In a simple view, oscillator strength means the amount of electrons available to oscillate with the external field, thus expressing the ability for light absorption. For a classical oscillating dipole (i.e. a damped harmonic oscillator in a homogeneous electromagnetic field), the oscillator strength can be related to the molar extinction coefficient (ε_m) via the cross section of absorption and the polarizability tensor of the

absorber; within the model of a 'mathematic dipole' (i.e. the molecule is assumed as an infinite thin rod), this results in

$$f = 4.319 \cdot 10^{-9} [cm^2 \cdot mol \cdot l^{-1}] \cdot n \cdot \int \varepsilon_m(\nu) d\nu \qquad (2.1)$$

where n is the refractive index of the solvent. The molar extinction coefficient ε_m can be directly extracted readily from the recorded absorption spectrum measured in $A = \lg(I_0/I)$ by applying Lambert-Beer Law

$$A = \varepsilon_m \cdot c \cdot L \qquad (2.2)$$

where c is the molar concentration and L is the path length (typically 1 cm).

2.1.2 Electronic Transitions in Conjugated Molecules

The classical electromagnetic theory, as shortly introduced above, can well explain the occurrence of resonances originating from damped harmonic oscillators, which interact with the electromagnetic field, to give rise to an absorption spectrum. On the other hand, the theory does not explain the (atomistic) reasons for the occurrence of the resonance, and thus to understand energies, intensities, polarization and spectral shapes of the various absorptions observed in a solution of conjugated molecule, a step forward is needed.

Resonance Condition, Stationary States and the Transition Dipole Moment. Such understanding was achieved with the development of quantum mechanics, which in the application to molecular systems is commonly called quantum chemistry. The basic idea is the quantization of the states of matter with respect to electron, spin and geometry, i.e. vibrational, rotational and translational degrees of freedom. Thus, the resonance condition can be formulated as

$$E_{photon} = h\nu = E_f - E_i \qquad (2.3)$$

so that a photon can only be absorbed if the energy corresponds to the energy difference between two stationary states of the molecule. Furthermore, the photon can only be absorbed if the light can interact with the (induced) transition dipole moment (TDM) μ between the states.

Here μ is a vector which is related to the oscillator strength by

$$f = \frac{8 \cdot \pi^2 \cdot m_e}{3 \cdot e^2 \cdot h} \cdot \nu_A \cdot \left|\vec{\mu}_{if}\right|^2 = 4.226 \cdot 10^{52} \left[\frac{cm}{C^2 m^2}\right] \cdot \nu_A \cdot n_A \cdot \left|\vec{\mu}_{if}\right|^2 \qquad (2.4)$$

Wavefunction and Schrödinger Equation. According to the first postulate of quantum mechanics, the state of a system is fully described by a function of the spatial and spin coordinates of the particles, and time. If the potential energy of the system is independent on time, its stationary states can be obtained by solving the nonrelativistic, time-independent Schrödinger equation,

$\hat{H}\Psi=E\Psi$ (2.5)

where $\hat{H}$ is the Hamiltonian operator associated to the energy of the system formed by the electrons and the nuclei, Ψ is the wavefunction which contains information about all the properties of the system, and E is the total energy of the system in such state; the molecular Hamiltonian contains terms related to the kinetic energy of electrons and nuclei, nucleus-nucleus repulsion energy, electron-nucleus attraction energy, and electronic repulsion energy.

With wavefunctions Ψ from the time-independent Schrodinger equation, the transition dipole moment TDM μ is obtained through

$$\vec{\mu}_{if} = \int \psi_i^* \hat{\mu} \psi_f d\tau \overset{Dirac}{=} \left\langle \psi_i \middle| \hat{\mu} \middle| \psi_f \right\rangle \neq 0 \quad (2.6)$$

which has to be non-zero for an allowed transition.

The wavefunction itself has no direct physical meaning, but its square can be interpreted as the probability of finding the electron at a given region in space. As electrons and nuclei are very different in mass and thus react at very different time scales to an external perturbation (i.e. light absorption), the total wavefunction can be usually (however not always) expressed as a product of the wavefunctions of nuclei and electrons (Born-Oppenheimer approximation)

$$\psi_{j,\upsilon}(q,Q) = \psi_j^Q(q)\chi_\upsilon^j(Q) \quad (2.7)$$

where $\psi_j^Q(q)$ is the wavefunction describing the electrons, which depends parametrically on the coordinates Q of the nuclei, and $\chi_\upsilon^j(Q)$ is the wavefunction describing the nuclei, which depends parametrically on the coordinates q of the electrons.

If applied to electronic transitions between an initial (*i*) and a final (*f*) state, the Franck-Condon (FC) principle is derived, and the TDM takes the form

$$\vec{\mu}_{if} = \left\langle \psi_i \middle| \hat{\mu} \middle| \psi_f \right\rangle = \underbrace{\left\langle \psi_{i,el} \middle| \hat{\mu} \middle| \psi_{f,el} \right\rangle}_{electronic} \underbrace{\left\langle \psi_{i,sp} \psi_{f,sp} \right\rangle}_{spin} \underbrace{\left\langle \psi_{i,vib} \psi_{f,vib} \right\rangle}_{vibrational\ F_{n,m}} \quad (2.8)$$

where

$$F_{n,m}^2 = \left| \left\langle \psi_{i,vib} \psi_{f,vib} \right\rangle \right|^2 \tag{2.9}$$

is called the Franck-Condon factor.

Electronic Transition Description - MOs, CI, States. To obtain the electronic wavefunctions, molecular orbitals (MOs) are constructed from the atomic orbitals (AOs) through linear combination (LCAO method),[Roo51]

$$\underset{\text{MO}}{\psi_j} = \sum_i \underset{\text{AO}}{c_{ji}\varphi_i} \longrightarrow \hat{H} \sum_i c_{ji}\varphi_i = \varepsilon_j \sum_i c_{ji}\varphi_i \tag{2.10}$$

and solutions are found via the variational principle.[Atk11] At a basic quantum-chemical level, electronic transitions in conjugated molecules can be treated by Hückel Molecular Orbital (HMO) Method; here, only (anti) bonding π(π*)-type MOs are considered, which are built from adjacent p-type AOs by LCAO method, while σ-type bonds are neglected. In the following, we'll shortly discuss butadiene as the simplest example of a neutral conjugated system. According to HMO, the eigenvalues of the MO energies are obtained as a function of the coulomb integral α and the resonance integral β as

$$E_k = \alpha + \frac{1 \pm \sqrt{5}}{2}\beta \tag{2.11}$$

and the LCAO coefficients at a C-atom *k* in an MO *l* are obtained as

$$c_{kl} = \sqrt{\frac{2}{5}} \cdot \sin\left\{\frac{\pi \cdot k \cdot l}{5}\right\} \tag{2.12}$$

which allows to draw the MO diagram as shown in Figure 2.1. Electronic transitions are then obtained as one-electron excitations to give the various one-electron configurations. Whether these excitations are allowed can be answered by symmetry considerations, i.e. calculating the product of the symmetries (Γ = 'symmetry of') between the initial (*i*) and final (*f*) configuration as well as that of μ, which has to contain the total symmetrical element in the given point group (A_g for the C_{2h} point group of *trans*-butadiene).

$$\Gamma = \Gamma_i \cdot \Gamma_\mu \cdot \Gamma_f \tag{2.13}$$

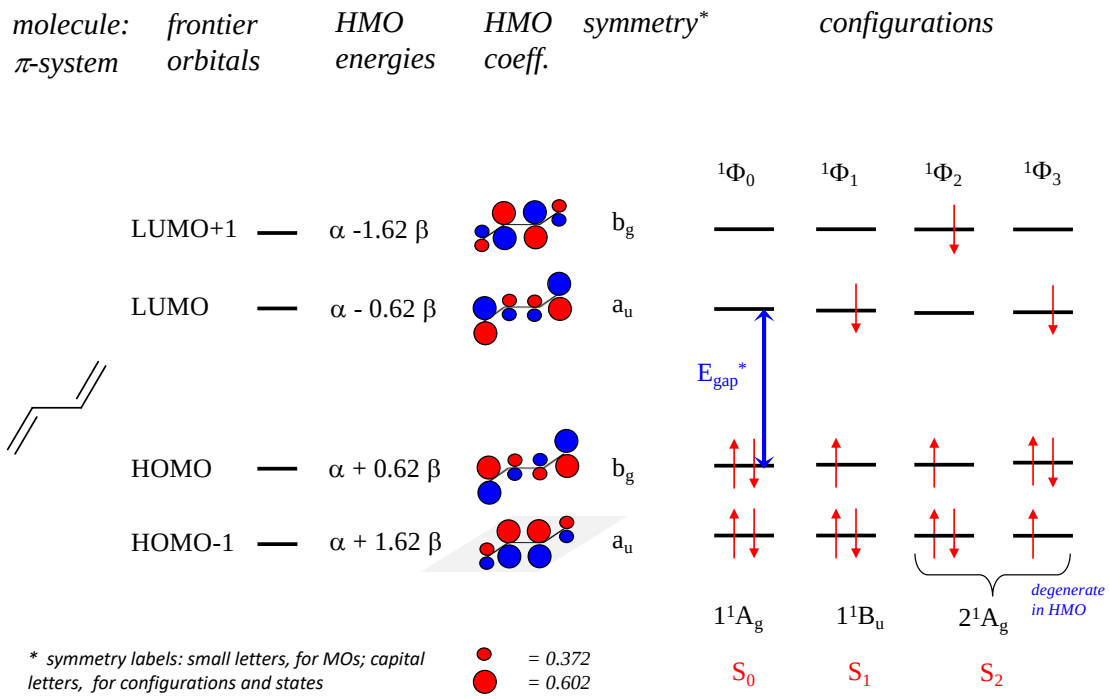

Figure 2.1: An example of the HMO method applied to butadiene: MOs energies, LCAO coefficients and configuration diagram based on one-electron excitations; the two highest (lowest) (un)occupied orbitals are indicated, the symmetry of MOs (small letters), configurations and states (capital letters) are displayed. Courtesy of J. Gierschner.

Real electronic states are obtained by going beyond the one-electron picture, i.e. forming linear combinations of the configurations (configuration interaction; *CI* [Atk11]), thus being not equivalent to the transition between frontier MOs due to the influence of *CI*. For the majority of linear conjugated organic oligomers, including distyrylbenzene (**DSB**), the lowest excited singlet state S_1 is symmetry allowed, and the $S_0 \rightarrow S_1$ transition essentially corresponds to the transition from the highest occupied to the lowest unoccupied MO (HOMO→LUMO), because of the small *CI* resulting from large energetic separations between HOMO, LUMO and the following MOs (see Figure 2.2). This is generally valid for a vast majority of conjugated compounds (although important exceptions exist). At the same time, for most linear conjugated compounds, the $S_0 \rightarrow S_1$ transition carries most of the oscillator strength from the whole absorption spectrum due to the delocalized character of HOMO and LUMO, thus dominating the absorption spectrum. It should be remarked that for excitations originating from higher energies, for example excited state absorption (ESA) of **DSB**, all transitions starting from S_1 show strong *CI* due to the close lying to following MOs, see Figure 2.2.

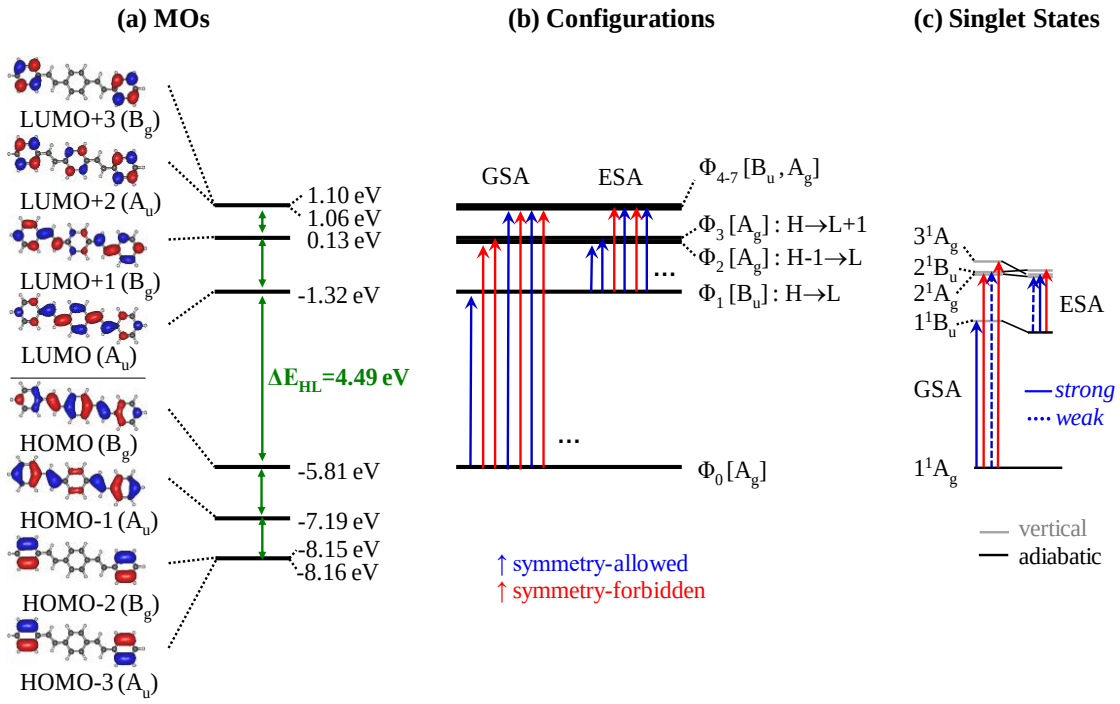

Figure 2.2: DFT (BHLYP) calculated electronic and optical properties of **DSB**.[Eli17] (a) Energies and topologies (isosurface value 0.03 a.u) of MOs; the four highest (lowest) (un)occupied orbitals are indicated. (b) Configuration diagram of the allowed (blue arrows) and forbidden (red arrows) one-electron excitations. (c) Resulting singlet state diagram with vertical (grey) and adiabatic (black) transitions.

Selection Rules. As described above, allowed transitions require a nonzero TDM. Symmetry-allowed transitions were discussed above; however it should be noted that violations are found to the symmetry selection rule, so that symmetrically forbidden transitions can be somewhat allowed through Herzberg-Teller coupling (HTC), which mixes symmetry-allowed transition through vibrations of adequate symmetry to the symmetry-forbidden transition (i.e. to give in total symmetrical product). This leads to intensity borrowing by symmetry-forbidden from symmetry-allowed transitions, which is more effective if the energy separation between these states is small.

Even stricter than the symmetry selection rule is the spin selection rule, which allows only for transitions between states of the same spin (S↔S, T↔T); this can be violated by spin-orbit coupling either by heavy atoms, or by essentially orthogonal wavefunction, i.e. involving n-π* transitions (e.g. carbonyls) or charge-transfer (CT) transitions; furthermore, less strict rules are 'non-zero differential overlap' and 'alternant pairing'.[Kle95]

2.1.3 Chemical Constitution and Environmental Effects on Absorption

Substituent Effects. The electronic transition energy can be significantly influenced by nature, number and position of substituents attached to a certain backbone, e.g. CN, N, X (F, Cl). In fact, in experiment, analogue compounds with different functional groups often show variable absorption and/or emission colors by shifted spectral maxima. On one hand, this impact on the electronic transition energies can be driven by geometrical effects, due to the sterical demands by the substituents, which can lead to substantial molecular twists and breaks the conjugation and results in significant blue-shifts; a particular pronounced example is for instance the phenylene-vinylene based polymer MEHPPV with fluorine-substituents in the vinylene units (F-MEHPPV), revealing a perpendicular situation of adjacent phenyl rings; this induces a hypsochromic (blue) shift of 0.9 eV against the unsubstituted MEHPPV, see Figure 2.3.[Mil16, Mil17]

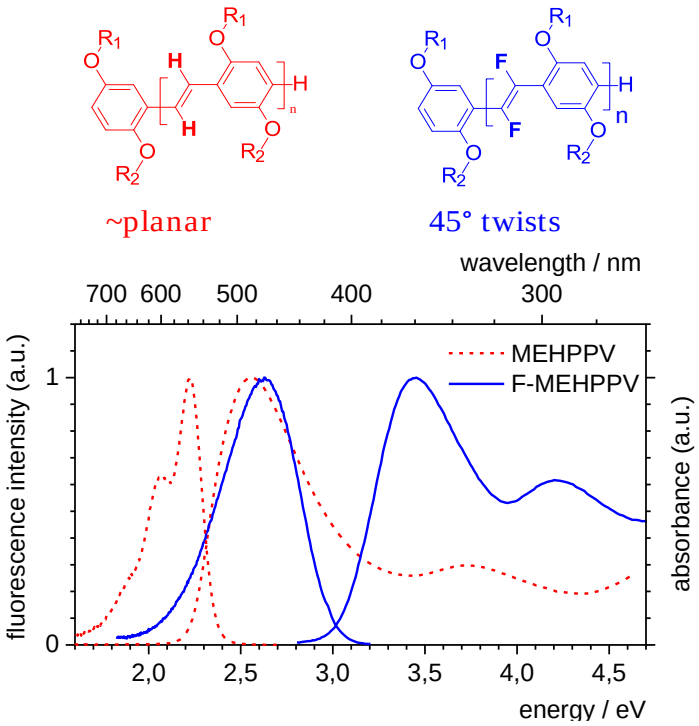

Figure 2.3: Emission (left) and absorption (right) spectra of MEHPPV (almost planar; dashed lines) and F-MEHPPV (strongly twisted; solid lines) in $CHCl_3$.[Mil16]

On the other hand the substituent effects may be triggered by their electronic impact, which can contain two parts. The inductive effect is related with the electronegativity (EN) of the substituent, i.e. to withdraw (-I) or provide (+I) electron density to the π-system and leads to a hypso- or bathochromic shift of the spectrum; the mesomeric effect is related to available p-type electrons of the substituents (±M effect), which generally enlarges the conjugation and

thus induces a bathochromic shift (this -CN, -OR groups). In case, both effects are present, the M-effect usually prevails; a notable exception is fluorine due to the extraordinary high EN.[Mil17] The electronic impact depends sensitively on the substitution position; well known is e.g. the *para*-/*ortho*- vs. *meta*-effect,[Gor87] however, substituent effects can be subtle and non-intuitive.[Mil08]

Solvent Effects. The solvent media has a significant impact on the energy of electronic state, thus giving rise to shifted transition energies. This effect should be in particular taken into account when comparing theoretical and experimental results, since the former are usually carried out in vacuum, whereas the latter are usually performed in solution. Generally, solvent effects can be classified into two types, one is the nonpolar solvent effect due to the polarizability of the environment, and the other is the polar solvent effect due to the polar-polar interaction which rearranges the static dipoles in solution after light absorption. A further possible effect in polar solvents is specific solute-solvent interaction. Nonpolar solvent effects can be well treated by classical reaction-field theory, where the easiest solution, relying on spherical cavities, is the Onsager model. Shape-adapted models are nowadays implemented in quantum-chemical program packages, such as PCM (polarizable continuum model) in Gaussian; non-equilibrium PCM for nonpolar solvents as well as explicit solvent shell (QM/MM approaches) for polar solvents are available. It should be finally mentioned that polarizability effects are also present in the condensed phase, i.e. amorphous and crystalline phases; in particular in crystals, polarizability effects can be highly anisotropic and can thus be large;[Ege02] in polymers they can become the dominant term in the solid state shifts.[Gie07]

The solvent has also a significant impact on spectral broadening processes, due to static and dynamic contributions of the polarizability for the (typically anisotropic) solvent molecules, which leads to Gaussian-shaped distribution, with which the vibronic spectra of the molecules are convoluted.

2.1.4 Vibronic Coupling

Vertical and Adiabatic Electronic Transition. As introduced above, an essential element to describe electronic excitations in conjugated organic molecules is the Born–Oppenheimer approximation, and subsequently the Franck-Condon principle. Accordingly, electronic and nuclear motions can be separately treated due to the huge difference between their masses, so that the total wavefunction can be written as the product of the electronic and nuclear components, see eq. 2.7. Thus, for an electronic excitation, the nuclei do not react

instantaneously, and the excitation is vertical (Franck–Condon (FC) principle). The electronic transition thus ends up in particular vibrational levels proportional to the square of the overlap between the vibrational wavefunctions of the initial and final states (FC factor; see eq. 2.9), being equally valid for absorption and fluorescence processes. These overlap depend in general on the shape of the potential energy curves along all normal coordinates of vibrational motions in the initial and final states and give the spectra their specific shapes.

Vertical transition energy (E_{vert}) and adiabatic energy (E_{00}) determine the specific optical properties of the compound under study. According to the FC principle, E_{vert} can be calculated at a quantum-chemical through a single point calculation (the energy of the final state at the geometry of the initial state, while E_{00} is obtained as the energy difference of initial and final states in their optimized geometries). The equilibration/reorganization energy (ΔE_{eq}) is the energy difference between E_{vert} and E_{00}

$$E_{vert} = E_{00} + \Delta E_{eq} \qquad (2.14)$$

Experimentally, E_{vert} can be identified as the most probable transition and thus obtained through integrating the absorption ($E_{vert}(abs)$) and emission ($E_{vert}(em)$) spectra according to

$$E_{vert}(abs) = \frac{\int A(E)EdE}{\int A(E)dE} \qquad E_{vert}(em) = \frac{\int I_F(E)EdE}{\int I_F(E)dE} \qquad (2.15)$$

where A(E) representing the absorbance and $I_F(E)$ the fluorescence intensity at a given energy, respectively.[Gie07] E_{vert} can be approximated with the maximum of absorption (emission), which is mathematically valid for symmetrically shaped bands. The energy difference between the maxima of absorption and emission is called Stokes-shift as indicated in Figure 2.4.

For rigid molecules with perfect mirror symmetry, E_{00} can be evaluated directly from the spectra as the intersection (IS) between absorption and emission (i.e. the position of the overlapped 0-0 vibronic band), see Figure 2.4. For flexible molecules with asymmetric absorption and emission at room temperature, the situation is more complex and E_{00} can be approximated via several different strategies (Figure 2.4): the position of the lowest vibronic feature of emission (F_1) is a reasonable first approximation for E_{00} if the broadening of the emission spectrum is not too large; another reasonable estimate of E_{00} is the onset of the absorption spectrum, which is however often hard to determine, especially in samples where light scattering is significant (e.g. in spin-coated or vapor-deposited films); finally, the energy at the intersection of the

absorption and emission spectra can also be an approximation of E_{00}; in any case, all these approximations somewhat over- or underestimate E_{00}, see Figure 2.4.

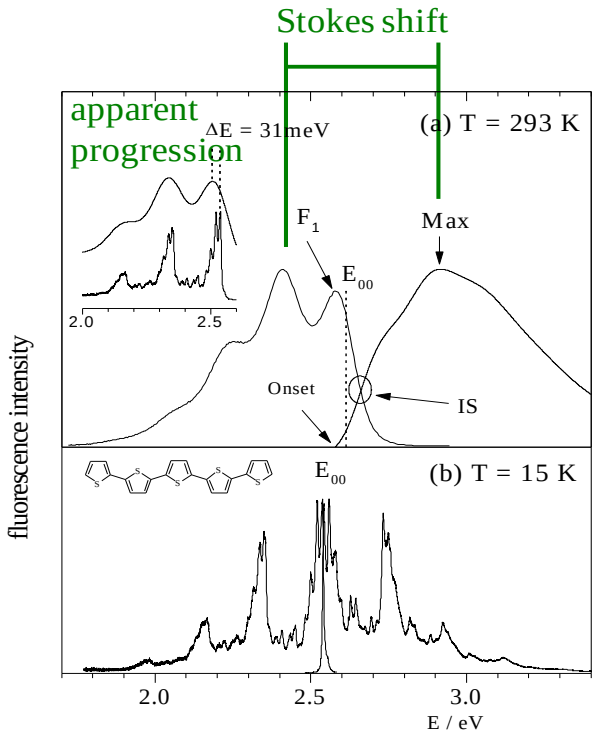

Figure 2.4: Emission (left) and absorption (right) spectra of quinquethiophene (5T) in tetradecane at T = 293 K (upper) and T = 15 K (lower). Inset: low-temperature emission spectrum, convoluted with a Gaussian bandwidth of 1100 cm^{-1}.[Gie03, Gie07]

Vibronic Fine Structure. The change of the molecules' electronic configuration via electronic excitation gives rise to significant changes in the molecule's geometry giving rise to a characteristic vibronic pattern of the spectrum, which arises from the effective vibronic coupling of a few specific vibrational modes. The latter are visible however only under specific conditions at low temperatures as shown in Figure 2.4 (e.g. rigid, homogeneous environments or in the Jet stream) while at room temperature they are significantly broadened (Figure 2.4). This line broadening effects include (thermal) polarizability fluctuations of the environment as discussed above, but also thermal population of low frequency out-of-plane modes (see below). This leads to a collapse of the complex vibronic modes to one 'apparent' mode, which is however not corresponding to one specific vibration.

Vibronic Coupling Calculation. The most simplest model to calculate vibronic coupling are displaced undistorted harmonic oscillator model (see Figure 2.5). Here the displacement arises from the geometry change upon electronic (de)excitation as described above. The

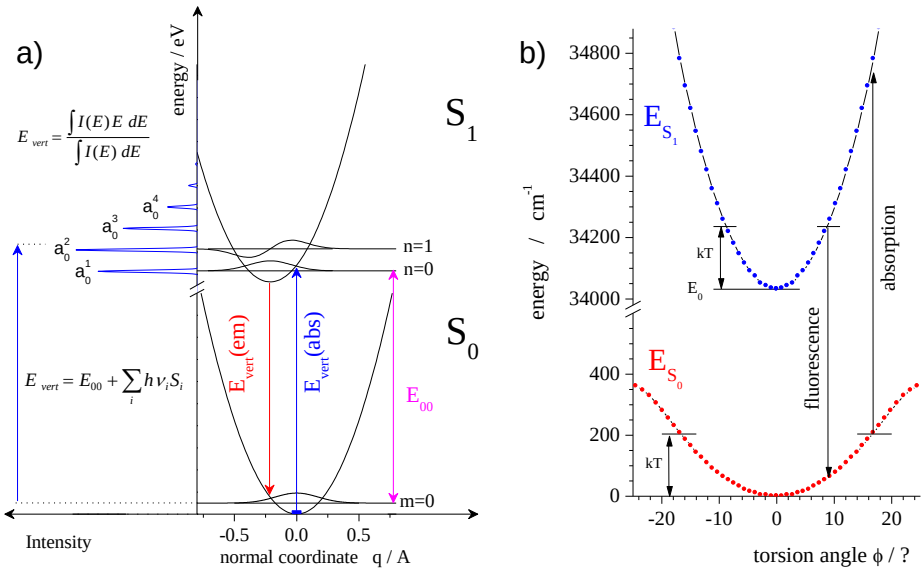

Figure 2.5: Schematic representation of the potential energy surfaces PES for two different harmonic models: a) displaced, undistorted harmonic oscillators in the normal coordinate representation coupled to symmetry-allowed, high-energy, in-plane modes; the vertical (E_{vert}(em), E_{vert}(abs)) and adiabatic (E_{00}) electronic transitions are indicated. b) undisplaced, distorted oscillators coupled to out-of-plane torsional modes; the vertical transitions associated to the absorption and emission processes are indicated.[Gie02, Gie07] Courtesy of J. Gierschner.

simple harmonic approach (i.e. a parabolic shape of the potential curves) with equal spacing between the vibrational levels is justified by the fact that anharmonicities (described for example by more realistic Morse potentials) are typically not important at energies below 10 kT (ca. 0.25 eV). Moreover, undistorted oscillator (i.e. same vibrational frequencies in the initial and final state) are usually justified if the geometries in ground and excited states are not too different from each other. This is in particular true for rigid molecules, which thus exhibits mirror image symmetric absorption and emission spectra with fine vibronic structure at any temperature. In this approximation, the Franck-Condon factors for transitions from the m = 0 vibrational quanta in the initial state to the n quanta in the final state (0 K limit) are calculated via

$$F_{n0}^2(k) = \frac{(S_k)^{n_k}\, e^{-S_k}}{n_k!} \qquad (2.16)$$

with S_K as the Huang-Rhys factor. This progression, generated from one specific vibration, leads to intercombinations (i.e. convolutions of different progressions) in a multi-mode picture.

For flexible molecules with planar equilibrium structure (e.g. **DSB**), mirror symmetry is observed at low temperatures as for rigid molecules.[Gie02] At room temperature, strong thermal populations of the torsional coordinates (i.e. twists around the formal single bonds) are observed; however the torsional potentials are much more shallow in S_0 compared to S_1 (Figure 2.5), due to the stronger single bond character in S_0, which leads to a mirror image symmetry break.[Gie02] Concurrently. the emission spectrum is more structured relative to absorption. For molecules with twisted equilibrium structures, asymmetrical absorption and emission spectra are also observed at low temperatures.[Hei05]

2.1.5 Deactivation in Solution

Jablonski Scheme. As shown in the Jablonski scheme of Figure 2.6, light absorption from the ground singlet state S_0 generates an excited singlet state S_n upon photoexcitation. Then, deactivation of S_n takes place via a sequence of internal conversion ($IC_{n\rightarrow n-1}$) and thermal relaxation (TR) steps until S_1 is reached. A series of competitive processes originate from here to return to S_0. Due to the large energy gap of S_1 to S_0, according to the "energy gap rule", the probability for $IC_{1\rightarrow 0}$ is relatively small compared to IC in the excited state manifold; this enables the competing process of fluorescence, which originates exclusively from S_1 in solution according to Kasha's rule and with a natural lifetime (k_F^{-1}) in the *ps* to *ns* range due to

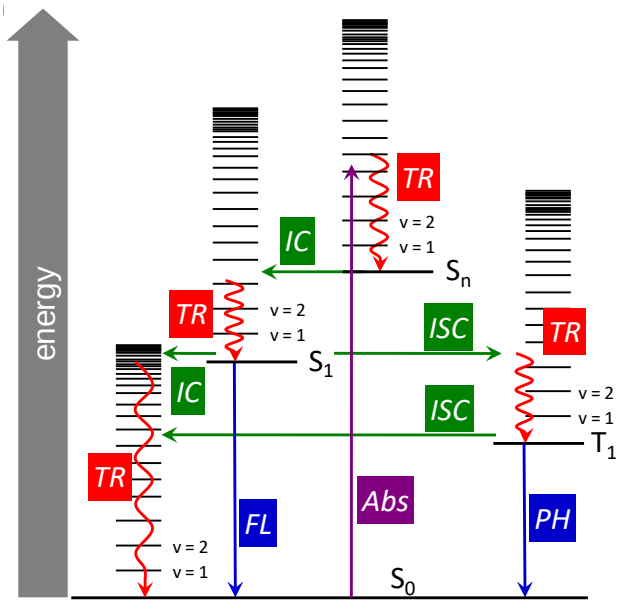

Figure 2.6: Jablonski term scheme including singlet (S_n) and the lowest triplet (T_1) states; Abs = absorption, FL = fluorescence, PH = phosphorescence, TR = thermal relaxation, IC = internal conversion, ISC = intersystem crossing, v = vibrational quanta). Courtesy of J. Gierschner.

the spin-allowed character. Intersystem crossing (ISC) is a further path but directing to the triplet manifold (T_n) possibly enabled by spin-orbital coupling (SOC) and followed by nonradiative deactivation of T_1, or phosphorescence from there with significantly longer lifetimes in range of μs to *ms* due to its spin-forbidden nature. Furthermore, photochemical processes like *trans-cis* isomerization as in the case of stilbene may also take place. The PL lifetime τ_F of S_1 is determined by all these processes originating from there is given by

$$\tau_F^{-1} = k_F + k_{nr}\,(k_{IC} + k_{ISC} + ...) \qquad (2.17)$$

and the PL quantum yield is given by

$$\Phi_F = k_r \tau_F = k_r /(k_r + k_{nr}) \qquad (2.18a)$$

Thus radiative

$$k_F = \Phi_F / \tau_F \qquad (2.18b)$$

and nonradiative $k_{nr} = (1-\Phi_F)/\tau_F$ (2.18c)

rates can be readily extracted from experimental measurements of τ_F and Φ_F.

Determination of k_r. As described above, the radiative rate k_r can be extracted from the PL quantum yield and lifetime via eq 2.18b; on the other hand, it can also be determined from the absorption spectrum via the Stickler-Berg (SB) relationship.[Str62, Vik74]

$$k_{r,SB} = 0.667\left[cm^2 s^{-1}\right]\left\langle \tilde{\nu}_F^{-3}\right\rangle^{-1} n^2 \cdot \tilde{\nu}_A^{\,-1} f \qquad (2.19a)$$

where $\left\langle \tilde{\nu}_F^{-3}\right\rangle^{-1} = \int I(\tilde{\nu})d\tilde{\nu} \Big/ \int \tilde{\nu}^{-3} I(\tilde{\nu})d\tilde{\nu}$ and $\tilde{\nu}_A, \tilde{\nu}_F$ are the energies of absorption and emission (in cm^{-1}), *f* is the oscillator strength of the absorption, responsible for the emission spectrum in a given medium of refractive index n.

For the determination of k_r via the Strickler-Berg relationship from quantum-chemistry, an approximate equation can be used instead of eq. 2.19a, reading

$$k_{r,SB} = 0.667\left[cm^2 s^{-1}\right]\frac{\tilde{\nu}_{F,vert}^3}{\tilde{\nu}_{A,vert}} n^2 f \qquad (2.19b)$$

where $\tilde{\nu}_{A,vert}$, $\tilde{\nu}_{F,vert}$ are the calculated vertical energies in absorption and emission.

Nonradiative Decay Channels. Differently from the radiative channel which mainly depends on the oscillator strength of the responsible transition, the nonradiative channel depends

sensitively on the energetics and shapes of the potential energy surfaces PES along different coordinates, and on their thermal population. The theoretical treatment of IC is difficult, but some general rules can be derived: due to "energy gap rule", the rate k_{IC} is expected to decrease with larger energy gaps, lower temperatures, rigid molecular backbones and rigid environments. Thus, luminescence driven by the suppression of k_{IC} is a probable scenario for solid state luminescence enhancement (SLE).

For that a reliable description of IC involved all PES are required, and usually invloves a conical intersection (CI). At least the S_0 and S_1 states, but often more states along local geometrical coordinates are usually required to properly describe the access of the CI. For this reason, simplified approaches typically fail to describe IC, e.g. involving harmonic models, and/or two-state models and/or normal coordinates.

2.1.6 Solid-State Effects: From Isolated to Interacting Molecules

a) Molecular Exciton Model

Kasha's Model. The molecular photophysics are significantly modulated in molecular assemblies due to the presence of *inter*molecular interactions. The molecular exciton model introduced by Kasha in the 1950s is to quantify the excitonic coupling between mono-molecular electronic transitions. In Kasha's original model, neighboring dimers are characterized with a constant center-to-center distance and treated by simple point dipoles applying point dipole approximation (PDA). Through changing the rotation orientation of two parallel transition dipole moments $\vec{\mu}_{01}$ quantified by their strength and energies, two extreme cases of coupling can be formulated, i.e. H-aggregates formed in side-by-side arrangements with blue-shifted absorption and reduced k_F against the monomer; collinear J-aggregates with red-shifted absorption and enhanced k_F. Thus, H/J-aggregated type can be determined from the blue/red-shift in absorption spectra. In this case, the inversion point between H/J-aggregates is found at the 'magic angle' value of $\theta_i = 54.7^o$. It has to be stressed here that only in perfect H-aggregates the emission is strictly forbidden by giving a zero oscillator strength *f* of the lowest excited state; any slight deviation from parallel arrangement will give non-zero *f* and thus allow partially emission. Furthermore, the treatment is done on a purely electronic basis, thus vibronic effects are not considered in Kasha's original formulation.

Molecules in Solid: beyond Kasha's Model. Kasha's original model cannot apply to densely packed molecular assemblies (eg. crystals), due to four factors, i.e. (i) the presence of non-nearest neighbor interactions, (ii) the involvements of vibronic coupling, (iii) the breakdown of

the PDA, which has to be replaced by a quantum-chemical corrected picture, and (iv) the unrealistic constant center-to-center distance model; instead a more realistic dimer picture with constant inter-plane separation should be chosen.[Gie13b, Gie16] An improved Kasha dimer model replaces the PDA by a quantum-chemical (QC) model, where neighboring molecules are characterized rather by a constant inter-plane separation and shifted against each other along their long molecular axis. For example, in the molecular crystals of **DCS**-type compounds, $\vec{\mu}_{01}$ coincide with their longest molecular axis x, see Figure 2.7. In this model, the inversion point θ_i depends on nature and *inter*molecular separation of the molecules, thus H-/J-aggregation in molecular crystals cannot be decided solely on X-ray data by comparing the pitch angle with the magic angle $\theta_i = 54.7^o$ as frequently done in literature. It should be noted that this model still relies on dimers, and is thus not quantitative; in fact, non-nearest neighbor interactions have to be taken into account for getting quantitative results. Furthermore, vibronic effects are not included; thus, in reality, aggregate-type Herzberg-Teller (AHT) coupling may increase the oscillator strength *f* of the emitting states in H-aggregates.[Wyk15a,Spa10] Finally, as mentioned above, already small deviations of the transition dipole moment from the ideal arrangement (i.e. in crystal arrangements with more than one molecule per unit cell) will equally increase *f*. It should also be stressed in this context that, whatever Kasha's model or QC model, the exciton model tells only something about *f* and thus about the radiative rates k_r, and does not yield Φ_F since latter depends equally on all nonradiative processes (see below).

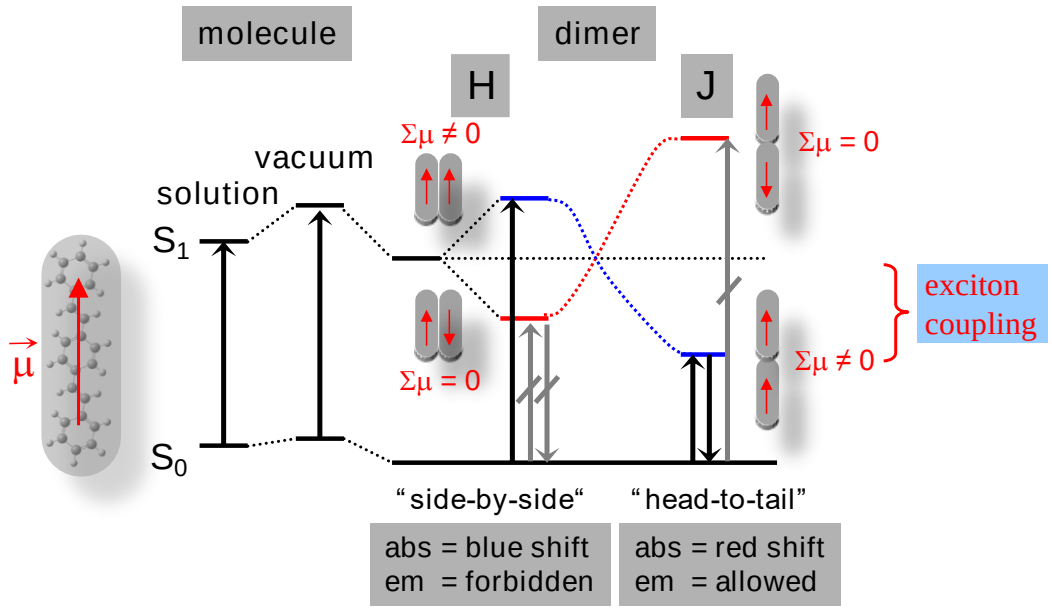

Figure 2.7: Modified Kasha's exciton model,[Gie13b, Gie16] obtained by quantum-chemical calculations for a dimer of cofacial **DSB** separated by 4 Å.

b) Spectral Shifts & Shapes

Interacting molecules in the condensed phase (i.e. amorphous, poly- or single crystalline materials) give rise to distinctively different optical spectra and photophysics compared to the isolated molecules in solution, due to the small *inter*molecular separations and thus complex *inter*molecular interactions. One influence of dense packing is the change of spectral features (spectral shift and shapes) by possible *intra*molecular contributions (geometry changes vs. free molecule, in particular de-/planarization) as well as from *inter*molecular contributions originating from excitonic coupling (see above), excimeric effects, and polarizability effects.

Excimeric effects arise from *inter*molecular contributions to vibronic coupling due to changes of the *inter*molecular arrangement upon electronic de-/excitation, which lead to an effective coupling of low-frequency lattice phonons; such changes arise from strong charge-transfer contributions, and thus typically occur only in arrangements with strong π-π overlap.[Gie04a, Gie05, Wyk15b] These effects can be treated in an atomistic way through QMMM calculations which include FC and HT effects both for correctly describing the vibronic coupling in molecular crystal;[Wyk15b] such calculations are however beyond the goal of the present investigation.

Polarizability effects were discussed in Section 2.1.3 for fluid solutions; they are equally valid for the condensed phase, usually inducing a bathochromic shift against solution due to the higher polarizability of the surrounding conjugated molecules compared with the solvent. While this effect is present already in amorphous solids, which becomes even stronger in (poly)crystalline solids due to its highly anisotropic character.[Ege02]

c) Excited State Deactivation

In addition to the changes of spectral features as discussed above, dense packing in the condensed phase considerably affects radiative and nonradiative deactivation rates and thus the PL quantum yield compared to dilute solution; this is now widely anticipated by the (however misleading) aggregation induced/caused emission enhancement/quenching (AIE/ACQ) terminology. The problems of the terminology was discussed in Section 1.3.2 of the Introduction, where we argued for a phenomenological term, i.e. "Solid State Luminescence Enhancement" (SLE).

The radiative rates k_F in the condensed phase can be enhanced/reduced by both *intra*- and *inter*molecular factors. For the *intra*molecular part, de-/planarization leads to (slight) de-/increase of k_F due to de-/increase of the effective conjugation (see also Section 2.1.3); furthermore, the enhanced polarizability in the condensed phase increases k_F according to the

Strickler-Berg relation (eq. 2.19). For the *inter*molecular part, k_F may in-/decrease due to J-/H-aggregate formation; however, many highly emissive H-type single crystals are still observed in experiment,[Gie13b, Gie16] due to effective aggregated-type HT (AHT) coupling and, at the same times, effective suppression of nonradiative processes under trap-free conditions, see below.

The nonradiative rates k_{nr} in the condensed phase can again be enhanced/reduced by both *intra*- and *inter*molecular factors. The *intra*molecular part in particular concerns k_{IC} (and k_{ISC}) which is typically reduced in the condensed phase due to dense packing, where the rigidity restricts large-amplitude molecular motions. This is in fact considered as the main origin of enhanced emission in solid states, especially for H-aggregated solid.[Gie13a] An important *inter*molecular factor is trapping due to structural (point) traps, excimers, polarons etc.,[Gie13a] which can be effectively reached via fast exciton diffusion (driven by large exciton coupling). Trap concentrations are in particular large at surfaces and interfaces, and are thus in particular important in polycrystalline solids due to high surface:volume ratios, and small average distance to the surface/interface. Therefore, in single crystalline samples, i.e. under essentially trap-free conditions, both J- and H-aggregates are highly emissive, whereas in polycrystalline samples fluorescence quenching is frequently observed.

2.2 Quantum-Chemistry and Computational Methods

In the last sections, a basic introduction to the quantum-chemical theory to understand the electronic, optical and photophysical properties of conjugated organic molecules and their assemblies has been provided. In this section, the goal is to outline the basic theoretical background of the quantum-chemical methods that have been used throughout the thesis work in order to calculate the geometrical and electronic structures as well as the vibrational and spectroscopic properties of all the compounds under study.

In this work, methods based on density functional theory (DFT) have been widely used to characterize the systems under investigation, due to the good balance between accuracy and computational costs. Only in the cases where DFT was insufficient to give a correct description of the problem, i.e. regions near a conical intersection (CI), more sophisticated methods have been applied, i.e. the complete active space self-consistent field (CASSCF). The details/procedures for the computations based on these methods and the results obtained will be presented later in Chapters 3 and 4, respectively.

The description of the basic concepts behind both methods will be briefly tackled starting from the foundations of quantum mechanics, through Hartree-Fock (HF) and post-HF methods and, finally, DFT.

2.2.1 Wavefunction-based Methods

Wave Function Theory. As we have explained in Section 2.1, microscopic particles (in particular, many-electron molecules and their assemblies) are quantum systems which give discrete quantum states and require quantum theory for description. In molecular systems, the behavior of the electrons (electronic properties) is determinant for all other (chemical, optical, photophysical) properties and the former is described by wavefunctions which can be obtained from the Schrödinger equation (eq. 2.5).

However, the Schrödinger equation can only be solved exactly for two-particle systems, and solutions for many-electron systems can only be obtained by introducing approximations.

Born-Oppenheimer approximation, as explained above, assumes that the electronic and nuclear motions are independent, i.e., the electrons move in a field of frozen nuclei. In this way, the Hamiltonian operator can be split into an electronic and a nuclear term, resulting in two independent Schrödinger equations (see eq. 2.7). In this way, the separated electronic Schrödinger equation can be solved at fixed nuclear configurations. In the frame of BO, the electronic Hamiltonian is reduced and generalized into three terms: a kinetic energy term, a nuclear attraction term and an inter-electronic interaction term. However, the electronic Schrödinger equation is still unsolvable for systems with more than one electron due to the inter-electronic interaction term, and needs more approximations.

Hartee-Fock method (HF). The first important approximation appeared in the 1930s through the Hartree-Fock theory.[Har28, Foc30, Mil04] The essence of the HF approximation is to replace the unsolvable many-electron problem by many one-electron problems in which the correlated motion of electrons is treated in an average way. To be specific, it assumes one electron moving in the presence of an average potential due to the presence of the other electrons. Within this framework, the wavefunction is written as a single determinant of one-electron wavefunctions (spinorbitals), called Slater determinant, that is antisymmetric to the exchange of any two electrons, satisfying the Pauli Principle for fermions (e.g. electrons). In doing so, part of the electron correlation is taken into account, since two electrons with parallel spin cannot share the same region in space (Fermi hole). In molecular systems, the single-electron wavefunctions, or molecular orbitals (MO), can be built using the LCAO (linear combination of atomic orbitals)

approximation.[Roo51] To obtain the exact HF ground state energy and exact HF ground-state wavefunction, optimization of the orbitals, i.e. minimization of the energy with respect to all orbitals, is done by an iterative process referred to as a self-consistent-field (SCF) procedure, applying the variational principle.[Atk11]

As mentioned above, within the HF approximation each electron feels the influence of the other electrons only as an average distribution and, although part of the electron correlation is taken into account by satisfying Pauli exclusion principle, no correlation exists between electrons with different spin function, leading to errors in the calculated wavefunctions and energies.

Several strategies have been developed to overcome such a problem, giving rise to the so-called *post-HF methods*. These methods take the HF model as a starting point and add corrections on it. According to the strategy to solve the equations, they can be classified as variational e.g. configuration interaction (*CI*),[Mec53, Mil04] perturbational e.g. Møller Plesset methods (MP*n*),[Mol34, Mil04] or coupled cluster (CC).[Ciz66, Mil04] Depending on the wavefunction taken as a reference, methods can be single- or multi-configurational.

Up to now, all methods mentioned in the text are single-configurational, meaning that the wavefunction of the system is described by only one electronic configuration or Slater determinant. However, such a wavefunction might be poor in some situations where the HF MOs are not adequate to describe the system, e.g. the problem of bond dissociation processes or the description of conical intersection (CI) regions. Multiconfigurational methods appeared to give an answer to such problems. Among them, multiconfigurational self-consisten field (MCSCF) is an extension of HF where the MCSCF wavefunction is built as a linear combination of determinants. The MOs used to build the determinants and the coefficients of the linear expansion are obtained as a result of a simultaneous optimization process. The complete active space SCF (CASSCF) method[Roo80, Mil04] is the most popular one. Herein, orbitals and electrons are classified as inactive, active and secondary, depending on the role they play in the construction of the polyelectronic wavefunction. The CASSCF wavefunction is built as a linear combination of all possible configurations considering only the active orbitals and electrons. The main difficulty lies on the choice of the active space. At this level, the static (long-range) electron correlation, related to the existence of quasi-degenerated electronic configurations, is considered. The rest of the electron correlation (short-range/dynamic) can be introduced through variational methods (multireference *CI*)[Hur73, Bue74, Mil04] or perturbation theory (complete active space perturbation theory to second order, CASPT2)[And90, Mil04]. This

kind of calculations is computationally very demanding and can be only applied to small to middle-size systems.

2.2.2 Density Functional Theory

Density Functional Theory (DFT) is a popular and powerful computational method to investigate the ground state electronic structure of many-body systems (in particular atoms, molecules and solids), which was developed by Hohenberg, Kohn[Hoh64] and Sham[Koh65] and founded by the two Hohenberg-Kohn Theorems. The first Hohenberg-Kohn Theorem states that the ground state energy of the many-electron system is determined uniquely by the electron density, which depends only on three variables. The second one states that the correct ground state density for a system is the one that minimizes the total energy through the energy functional, i.e., the exact ground state energy is obtained by minimizing the energy with respect to the electron density (trial variable in this case) applying the variational principle. This electron-density dependent idea greatly simplifies the many-electron problem since it means that all properties of the true system can be extracted from a non-interacting (fictitious) system which has exactly the same electron density at all points.

DFT, compared to HF, is developed under a different formalism which considers that the ground state energy of a many-electron system can be written as a functional of the electronic density. However, the exact mathematical expression of this functional is not known, and approximations are needed, on the cost of the variational principle.

The Form of the Density Functional and Kohn-Sham DFT. The next step in the evolution of DFT was given by Kohn and Sham when they developed a method to obtain both the density and the energy. According to them, the exact density of charge in the ground state is given by

$$\rho(\mathrm{r}) = \sum_{\mathrm{i}=1}^{\mathrm{n}} |\varphi_{\mathrm{i}}(\mathrm{r})|^2 \qquad (2.20)$$

where φ_i are the Kohn-Sham orbitals.

$$E[\rho] = -\frac{\hbar^2}{2m_e}\sum_{i=1}^{n}\varphi_i^*(r_1)\nabla_1^2\varphi_i(r_1)dr_1 - \sum_{I=1}^{N}\int\frac{Z_I e^2}{4\pi\varepsilon_0 r_{I1}}\rho(r_1)dr_1 + \frac{1}{2}\int\frac{\rho(r_1)\rho(r_2)e^2}{4\pi\varepsilon_0 r_{12}}dr_1dr_2 + E_{XC}[\rho] \qquad (2.21)$$

The form of the density functional, see eq. 2.21, comprises the kinetic energy term of the electrons, the electron-nucleus Coulomb interaction term, the Coulomb interaction between the total charge distribution at two positions r_1 and r_2, as well as the non-classical electron-electron interactions (exchange and correlation energy, E_{XC}, which is also a functional of the density).

The first three terms can be calculated in an exact way, whereas the E_{XC} is difficult to obtain since the exact exchange-correlation energy functional is not known and, once more, approximated expressions need to be introduced before solving the equations in a self-consistent manner.

Approximations to the Exchange-correlation Functional. The first level of approximation, the local density approximation (LDA), assumes that the energy depends locally on the density in the same way as in the uniform electron gas, representing the simplest way to illustrate exchange-correlation energy. Some examples of LDA functionals are VWN and PW92.

Generalized gradient approximations (GGAs) consider that the exchange-correlation energy is a function not only of the density but also of its gradient, e.g. SVWN, PWP and BLYP.

Hybrid functionals include an exchange part as a linear combination of HF, LDA and GGA exchange terms, and combine it with a local and/or gradient corrected correlation part, e.g. B3LYP and B3P86.

More sophisticated functionals add long-range correction and dispersion terms to the previous approximations, e.g. CAM-B3LYP and B3LYP-D, respectively.

Since B3LYP and CAM-B3LYP have been the choice for this work, a more detailed description will be given.

Hybrid Functionals B3LYP and CAM-B3LYP. The main strategy of this class of approximation to the exchange-correlation functional is to incorporate a portion of exact exchange from Hartree-Fock theory with the rest of the exchange-correlation energy from DFT sources, in order to improve the performance. One of the most commonly used hybrid functional is B3LYP, which stands for Becke, 3-parameter, Lee-Yang-Parr.

Global-hybrid functionals[Pev11] are special hybrid functionals which have a constant percentage of HF exchange independently on density, density gradient, inter-electronic distance, or position in space. B3LYP is one of the most commonly used global-hybrid GGA functionals, with 20% HF exchange. Although B3LYP appears to offer the greatest contribution in DFT method (measured by the number of applications in published papers), it is however inappropriate for a number of issues such as polarizabilities of long chains,[Cas95, Bau96, Toz98] description of Rydberg states and charge transfer (CT) excitations.[Toz99, Dre03, Ber03] In these cases, corrected functionals are required for obtaining better accuracy. Range separated functionals where the inter-electronic Coulomb operator (exchange) can be split into a short-range (SR) and long-range (LR) parts are appropriate for study processes at large distances such as electron

excitations to high orbitals. Dispersion corrected functionals where the dispersion correction is done by the modified KS-DFT formalism[Gri04] are of choice if dispersion interaction is significant, for example in interacting molecules with high polarizability.

CAM-B3LYP is an example of hybrid exchange-correlation functional that combines the hybrid qualities of B3LYP with the long-range correction using Coulomb-attenuating method (CAM) method.

2.2.3 Time-Dependent DFT (TD-DFT)

Density functional theory became an efficient tool to describe the ground state electronic structure of large molecules, including properties such us bond energies, potential energy surfaces, geometries, vibrational structure and charge distribution. However, in its original formulation, it is not able to calculate the dynamic response properties of many-electron molecular systems in the presence of time-dependent potentials such as electric or magnetic fields. At a later stage, DFT was generalized to include the effects of time-dependent perturbations, resulting in the formulation of the time-dependent density functional theory.[Cas95, Cas98, Gro90, Mil04]

TD-DFT[Cas09] has become a popular tool for computing the characteristics of electronically excited states, and more specifically, the properties directly related to the optical (absorption and emission) spectra of conjugated organic molecules. It can be considered as an extension of DFT with analogous conceptual and computational foundations. To be specific, Runge-Gross (RG) theorem proves that the time-dependent wavefunction is equivalent to the time-dependent electronic density, which means all properties of the interacting complicated system are contained in the time-dependent evolution of the electron density, as in the basic ideas of ground-state DFT. The application of this idea to the treatment of excited states is based on the response function theory, which states that the development of an observable with time can be determined if there's an external electric/magnetic field applied on the molecular system. In the absence of the time-dependent electric field, the system under study is assumed to stay in its electronically ground state described by the standard time-independent Kohn-Sham equation. The effect of the external electric field can lead the observed properties to be frequency-dependent by oscillating with the resonance frequency. TD-DFT captures the development of observable properties arising from the response to external potentials, offering an efficient method to investigate response properties such as excitation energies and excited state properties, where excitation energies are obtained on the basis of the linear time-dependent

response of the time-independent ground-state electron density to a time-dependent external electric field. As TD-DFT relies on single excitation theories, it is very effective in the treatment of low-lying excited states in π-conjugated molecules.

2.2.4 Frequency Calculation

The geometry optimization of a molecule goes through the calculation of the first derivatives of the energy with respect to the nuclear coordinates. The resulting structure corresponds to a stationary state of the potential energy surface. To disentangle whether such structure describes a stable minimum or a transition state, a vibrational analysis needs to be performed.

A vibrational analysis within the harmonic approximation needs the calculation of the second derivatives of the energy with respect to the nuclear coordinates of the system, to obtain the vibrational frequencies and the normal mode vectors. Mixed derivatives with respect to the nuclear coordinates and the electric field components provide the infra-red (IR) and Raman intensities. Real frequencies for all normal modes confirm that the geometry corresponds to a stable minimum, whereas the presence of imaginary frequencies indicates that such structure is a transition state.

Chapter 3

Materials and Methods

3.1 Materials & Preparation

As described in the Introduction, two cyano-vinyl-based systems are presented in this thesis. We started with a one-component system to investigate the photophysical mechanism of solid-state luminescence enhancement (SLE); then, in a second step, enhance the complexity of the system, we chose a two-component system applied in OSC to elucidate the beneficial photophysics behind the superior device performance. All the compounds involved in this thesis are synthesized by Prof. Soo Young Park's group at Seoul National University, South Korea.

3.1.1 DCS-Compounds (for SLE study)

The **DCS** library (Scheme 3.1) consists of eight compounds in total, obtained via functionalizing distyrylbenzene (**DSB**) with cyano groups (CN) either in the inner (α) or in the outer (β) position of both vinylene units, optionally adding alkoxy groups; the latter are either placed as di-methoxy (MeO) groups in the central aromatic ring (**MO**-compounds), and/or as di-butoxy (BuO) groups in the terminal aromatic rings (**DB**-compounds). For comparison, the unsubstituted compound, i.e. **DSB** was investigated. Synthesis and characterization of these compounds have been reported elsewhere.[Yoo10,Yoo11a,Yoo11b,Yoo13,Var14] Handling of the samples (storing, preparation of the solutions and crystal growth) was done in the dark to avoid photo-isomerization (and possible photo-oxidation). UV/Vis absorption, photoluminescence (PL) and PAC measurements in fluid solution were carried out in chloroform ($CHCl_3$; Sigma-Aldrich, spectroscopic grade) with an absorbance of typically A ≤ 0.1 except for pump-probe spectroscopy (A ≈ 1 in 1,4-Dioxane, Sigma-Aldrich, spectroscopic grade). Experiments in solid solution were performed in a PMMA (poly(methyl methacrylate), Sigma-Aldrich) matrix at low concentration (cM ≈ 10^{-4} M); here, vigorous vibration (done by platform shaker Vibramax 100) was performed during mixing $CHCl_3$ solution with PMMA powder to further prevent aggregation.

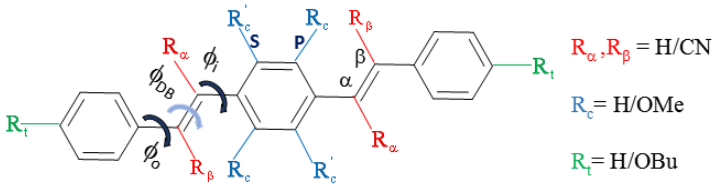

Scheme 3.1: The **DCS** family under study. Substitution pattern (R_α, R_β, R_t, R_c) of the cyano (CN), methoxy (MeO) and butoxy (BuO) substituents; torsional angles around the inner (α) and outer (β) vinyl-phenyl bonds (ϕ_i, ϕ_o) and the vinyl double bond (ϕ_{DB}); MeO orientation at the central ring (P, S).

PMMA films were fabricated in different ways for different experiments: for steady state and time-resolved optical spectroscopy measurements, PMMA films were deposited on glass slides via drop casting; for PAC experiments, the PMMA slides were prepared by doctor blading through a Cube Film Applicator (Elcometer 3505).

Although single-crystal structures for these nine compounds have been reported already,[Yoo10,Yoo11a,Yoo11b,Yoo13,Var14] PL lifetime measurements on two single crystals (**α-DBDCS**, **β-DCS**) were not done by now. Herein, single crystals of these two compounds were grown respectively, from $CHCl_3$/hexane mixture solutions (**α-DBDCS**) and in chloroform solution through hexane vapor diffusion (**β-DCS**) at room temperature. Furthermore, **β-DCS** was characterized by X-ray analysis, identifying a new polymorph (PM3), distinguished from two reported ones (PM1 and PM2);[Xu12, Li12, Cha12] different to PM3, PM1 was obtained earlier through a physical vapor transport (PVT) method,[Xu12] and PM2 was obtained from vapor phase sublimation.[Li12, Cha12] For PM3, also steady state fluorescence measurements were performed. To compare the optical properties of **β-DCS** under variable conditions, the information of nanoparticle suspensions prepared in THF/water mixture (cM = 2×10^{-5} M) and thin films grown by vacuum deposition was taken from early report.[Yoo11b]

3.1.2 Binary Cyano-vinyl-based D:A System (for ASM-OSC study)

The donor (**D**) compound p-DTS(FBTTh$_2$)$_2$ was purchased from 1-Material Inc;[Poll12] the synthesis of the acceptor (**A**) compound NIDCS-MO was described elsewhere;[Kwo15b] see the chemical structures in Scheme 3.2. Dilute solutions (A ≤ 0.05) of these compounds were prepared in chloroform ($CHCl_3$; Sigma-Aldrich, spectroscopic grade) by stirring at 55 ºC during 12 h. Pure and blended films of the donor and acceptor under different thermal conditions (as-cast and annealed) were prepared by spin-coating from solutions of pure compounds (10 mg/mL in chloroform) as well as their 1:1 mixture; spin-coating (1800 rpm, 60 s) of these solutions was done on glass substrates (10 x 10 mm^2) to obtain devices with a thickness of 90-110 nm. Thermal annealing was done at 110 ºC for 20 min, being the optimal procedure for high power conversion efficiency (PCE) of this material mixture.[Kwo15] Basic optical spectroscopy and photophysics measurements (PL lifetime and quantum yields) were performed on dilute solutions as well as spin-coated films; time-resolved transient absorption spectroscopy, as well as Raman and fluorescence microscopy measurements were performed only on spin-coated films at OSC's request.

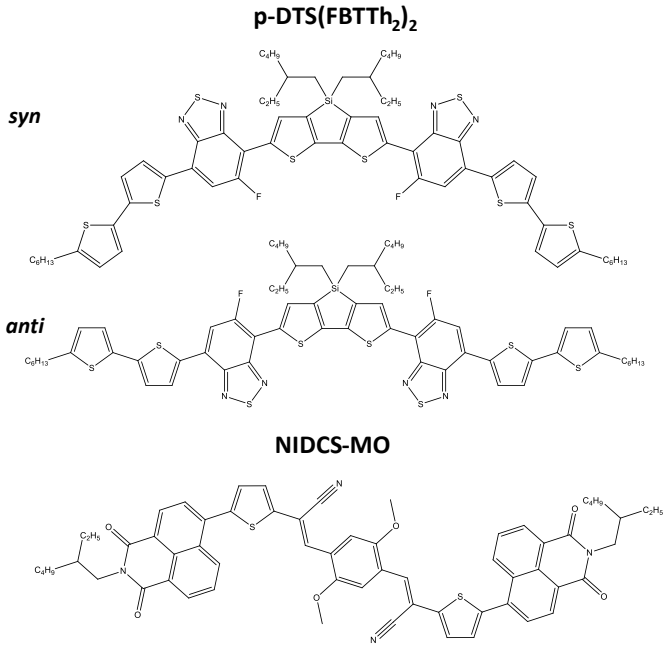

Scheme 3.2: Chemical structures of donor p-DTS(FBTTh$_2$)$_2$ (*syn*- and *anti*-rotamers) and acceptor NIDCS-MO.

3.2 Setups & Methods

As described in the Introduction, optical and photophysical investigations of the different samples were carried out combining steady state with time-resolved techniques at different time scale, supplementing with quantum-chemical calculations. Furthermore, specific experiments were performed selectively on some systems, such as X-ray experiments for crystal structure analysis of **β-DCS** and various microscopy experiments to determine the morphological structure of the **D**:**A** blends.

3.2.1 Experimental Details

a) Experimental Details on **DCS**-Compounds

Spectroscopic Characterization. Optical (UV-Vis absorption, Abs; photoluminescence emission, PL) spectra and basic photophysics (PL quantum yield Φ_F and lifetime τ_F) measurements were performed on fluid $CHCl_3$ solution and solid PMMA film (Abs spectrum is unmeasurable due to the very high extinction; therefore, PL excitation spectrum PLE was measured instead) of all eight **DCS**-compounds and **DSB**. Furthermore, single crystals of **α-DBDCS** and **β-DCS**, which were prepared as described in the Material part (Section 3.1.1), were investigated by PL spectroscopy. UV-Vis absorption spectra were recorded on a UV-Vis spectrophotometer (Varian Cary 50) using 1 cm quartz cuvette (Suprasil). Light exposure,

which induces photoisomerization in some of the compounds (*vide infra*), was minimized by sample handling in the dark, and rapid spectral sampling. Room-temperature PL and PLE spectra were acquired on a spectrofluorimeter (Horiba FluoroLog 3) equipped with a high pressure Xenon lamp and a Hamamatsu R928P photomultiplier tube; the PLE and PL spectra were corrected for the characteristics of the lamp source and of the detection system, respectively.

PL quantum yields (Φ_F) were measured in two different approaches (relative and absolute). Relative Φ_F of $CHCl_3$ solutions were measured using quininesulfate in 0.5 M sulfuric acid as a standard reference (Φ_F = 0.54);[Bro11] absolute Φ_F of PMMA films and (single) crystals were determined in an integrating sphere setup (Hamamatsu C9920; at the group of Dr. Henk Bolink, Valencia) equipped with a xenon high-pressure lamp and a multichannel analyzer at 350 nm excitation wavelength. For the crystal measurements, we utilized the smallest possible sizes (< 1 mm) to reduce re-absorption, and at the same time allow for enough intensity, due to the limited sensitivity of the integrating sphere. Anyway, it should be noted that even under these conditions, reabsorption is unavoidable; for that reason the reported values for Φ_F of the crystals represent the lower limit of the intrinsic PL quantum yields. It should be further noted that the sensitivity of the integrating sphere is not high, giving rise to a high absolute error; this is in particular problematic for PMMA samples with low Φ_F.

PL lifetime (τ_F) experiments were performed by the time-correlated single photon counting (TCSPC) technique with an Acton SP2500 spectrometer (PicoQuant) equipped with a PicoHarp300 TCSPC board (PicoQuant) and a PMA 06 photomultiplier (PicoQuant). A HydraHarp-400 TCSPC event timer with 1 ps time resolution was used to measure the PL decays. The excitation source was a 405 nm picosecond pulsed diode laser (LDH-D-C-405, PicoQuant) driven by a PDL828 driver (PicoQuant) with FWHM < 70ps. The decay time fitting procedure was carried out by deconvolution with the instrument response function (IRF) using the Fluofit software (PicoQuant). All the setup pieces and software are from PicoQuant. To reduce reabsorption in the crystal measurements, we utilized the smallest possible sizes, detected under front-face conditions and irradiation of the crystal edge only; like this, the very non-exponential PL lifetimes observed at strong reabsorption of the crystal become increasingly exponential at low reabsorption.

Femtosecond Transient Absorption (TA) Spectroscopy. TA measurements were carried out on a probe wavelength scale ranging from 470 nm-740 nm, from 100 fs to 400 ps, at different excitation intensities. Optical pulses centered at 775 nm were generated from a Ti:sapphire laser

(Clark-MXR, CPA-2001) driven at 1 kHz by a regenerative amplifier, and split into two parts. A fraction of the fundamental 775 nm pulses passed through an optical delay line, which was controlled via a mechanical translation stage, and directed to a sapphire plate in order to obtain a white light continuum, which we used as the probe beam. One part of the probe beam was focused onto the sample (about 134 μm spot size) with a spherical mirror. After passing through the sample, the probe beam was focused onto the slit of our prism spectrometer (Entwicklungsbüro Stresing GmbH) which consists of a dual channel CCD array (2 X 256 pixels, VIS-enhanced InGaAs, Hamamatsu Photonics Inc). The other part of the probe beam was used as a reference to reduce laser fluctuation induced noise. The second part of the fundamental 775 nm pulses was sent to a second harmonic generator to achieve the pump pulse centered at 387 nm, and chopped at 500 Hz. Then the pump beam was focused onto the sample (about 260 μm spot size) to overlap with the probe beam, and blocked after the sample. Intensities of both pump and probe beams were controlled via neutral density filters. All the measurements were carried out on the magic angle (otherwise stated), by setting the polarization angle of both pump and probe beams with λ/2 plates. Data acquisition and the global analysis of transient absorption spectra was done by custom built Python software, using open source libraries (numpy, scipy, pyserial, matplotlib, pyQt, among others).

Photoacoustic Calorimetry (PAC) Experiment. PAC experiments were performed with Dr. Carlos Serpa at Univ. Coimbra. For this, $CHCl_3$ solutions of all the **DCS**-compounds were prepared, and measured using a homemade front-face PAC cell design described by Arnaut et al.[Arn92] The instrumentation, the procedure employed in the measurement, and the data analysis protocol were reported in detail elsewhere.[Ser00, Sei99, Sch10] In short, the PAC data was acquired on a setup composed of a unfocused Nd:YAG laser (EKSPLA PL2143A, 35 ps pulse duration, 10 Hz, ~8 mm beam diameter) and a 2.25 MHz Panametrics transducer (model A106S) which is pre-amplified with a Panametrics ultrasonic preamplifier (model 5676); the former is for sample excitation and the latter is for detecting the acoustic waves generated by non-radiative processes. All the dilute solution samples were irradiated at 355 nm and 2-hydroxybenzophenone was used as photoacoustic reference. The quantification of multifold nonradiative pathways was based on excitation energy balance; for calculation details see Result & Discussion chapter.

Differential Scanning Calorimetry (DSC). The DSC measurement of **β-DCS** in PM3 was performed on a TA Instruments Discovery DSC. The sample was crimped in a Tzero (TM) aluminum pan and the temperature range was 20-280 ºC at a ramp of 5.00 º/min.

X-ray Analysis of Single Crystals (SC X-ray). X-ray structural analysis of the **β-DCS** single crystal were done at the SIDI, Campus UAM Cantoblanco, Madrid. For this, a suitable crystal with ca. 0.35 mm length, 0.06 mm width was selected and mounted on the tip of a glass fiber, which was also used for the PL measurements above. Diffraction data were collected at 100 K on a Bruker D8 Kappa diffractometer equipped with a SMART APEX II CCD detector with Mo Kα (λ = 0.71073 Å) radiation. Data were integrated with SAINT[Sai00] and empirical methods as implemented in SADABS[Sad02] were used to correct for absorption effects. Structures were solved with direct methods using SHELXS-97.[She01] SHELXL-2004 was used for refinement against all data by full-matrix least-squares methods on F2. All non-hydrogen atoms were refined with anisotropic displacement parameters. Hydrogen atoms were refined isotropically on calculated positions using the riding model implemented in SHELXL-2014. Final R-values and GOOF on F2 for refinement on 1483 reflections collected, using 0 restraints and 118 parameters are: R [I>2sigma(I)]: R1 = 0.0868, wR2 = 0.2028; R (all data): R1 = 0.1453, wR2 = 0.2328; GOOF = 1.095. The crystal structures were visualized and the packing diagrams were generated using Mercury 3.9 visualization program.[She01] Additionally to the data collection carried out at 100K, unit cell parameters were determined at 296 K to rule out a possible phase transition at low temperatures. Cell parameters at 296 K are a = 5.8602(15) Å, b = 3.9118(10) Å, c = 36.866(9) Å, α = 90, β = 94.433(14), γ = 90, V = 842.6(4) Å. The files CCDC 1542079 contain the crystallographic data and can be obtained free of charge via www.ccdc.cam.ac.uk.

b) Experiment Details on Cyano-vinyl-based **D**:**A** System

Spectroscopic Characterization. UV-Vis absorption (Abs) spectra, room-temperature PL spectra, PL quantum yields Φ_F and lifetimes (τ_F) were acquired on the same instruments as described for the **DCS**-compounds above. To be noted, since the emission here extends beyond the wavelength range of the PMT sensitivity, the τ_F of donor film is not measurable by our setup and the others (acceptor and blend films) were measured with very low photon counts signal. The uncertainty of lifetime values due to this reason should be taken into account.

Transient Absorption (TA) Spectroscopy. TA measurements of **D**:**A** OSC were performed on the same setup as described for the **DCS**-compounds above, while under different pump and probe wavelengths. The probe beam used here covered the visible and infrared regions, i.e. 470-740 nm and 840 nm-1400 nm. The pump pulses of about 120 fs duration, modulated at

500 Hz, were tuned from 490-710 nm, which was obtained through a dual stage non-collinear optical parametric amplifier (NOPA, Horiba Jobin Yvon GmbH) operated without compression stage.

Raman and Fluorescence Microscopy. Raman and fluorescence maps have been measured at the group of Dr. Dai Zhang/Prof. Alfred Meixner at Univ. Tübingen. For this, the signals were collected with a home built confocal setup using a parabolic mirror with a numerical aperture (NA) of 0.998.[Dre01] As excitation source a 636.3 nm diode laser (Picoquant PDL 800-D) was used and operated in continuous wave mode. Using λ/2 plates a higher order laser mode was generated to excite the samples with a radially polarized laser beam at ~0.5 μW for both confocal and tip enhanced near-field PL spectra. Gold tips were obtained via electrochemical etching of gold wires (Chempur, 99.99% purity) in concentrated hydrochloric acid solution with a platinum ring as counter electrode.[Rog16] These gold tips were then glued to a tuning fork which was brought in the focus to perform shear-force scanning probe microscopy and near-field spectroscopy.[Wan10, Wan11, Wan14, Hor15] A scanning electron microscope (SEM) image of the gold tip used for this experiment and its corresponding PL spectrum are shown in Figure 3.1. Using an Ametek 7270 DSP lock-in amplifier a constant tip:sample distance was kept during scanning. PL spectra were then recorded using a liquid nitrogen cooled CCD chip in combination with a Spectra pro 300i (Acton Research) spectrometer, by a 150 grooves/mm grating with an integration time of 2 seconds per spectrum except for the PL spectrum of gold tip (10 seconds).

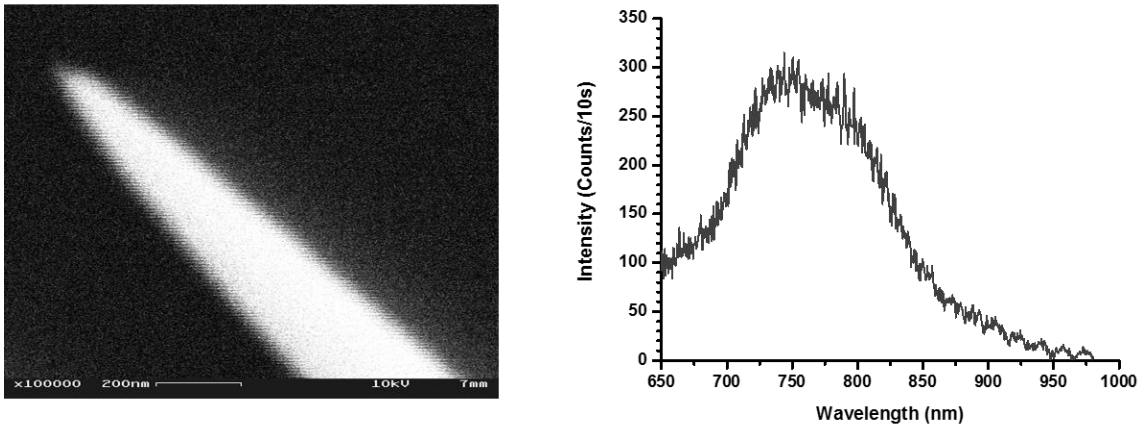

Figure 3.1: SEM image of the gold tip used, and the gold PL spectrum (10s integration time).

3.2.2 Computational Details

a) Computational Details on **DCS**-compounds

The geometries of the **DCS**-type compounds were optimized under C_i symmetry restriction (for **DSB**, C_{2h} symmetry was used) in vacuum at the density functional theory (DFT) level of theory. Thus, only anti-rotamers (as defined earlier) were considered,[Gie13a] in agreement with the available X-ray data. For compounds with MeO groups in the central ring, the calculations were performed for two rotational conformers indicated by (**P**) and (**S**) in Scheme 3.1; for details see Chapter 4. To reduce the computational effort, in the compounds with butoxy groups the latter were replaced by methoxy groups. Vertical singlet and triplet excited states were calculated using time-dependent density functional theory (TD-DFT) in vacuum as well as in $CHCl_3$ using the polarizable continuum model (PCM). Adiabatic singlet and triplet transitions were calculated by relaxing the S_1 and T_1 geometries respectively. According to group theory, the symmetry allowed π-π* type singlet transitions of the **DCS**-type compounds in the C_i point group from the ground state (1^1A_g) take place to the bright n^1A_u (n = 1,2...) states, while the n^1A_g (n = 2,3...) are essentially dark; for **DSB** (C_{2h}) the corresponding states are the n^1B_u and n^1A_g, respectively. The barriers for the torsions around specific single and double bonds indicated in Scheme 3.1 were monitored by DFT calculations via scanning frozen bonds in steps of 15° with full geometry relaxation under this restriction. Torsional angles around phenylene-vinylene single bond (ϕ_i/ϕ_o) ranges from 0 to 90° due to symmetry reason, extends to 180° for vinylene double bond (ϕ_{DB}) to include *cis-trans* isomerization. In all calculations, the B3LYP functional and the 6-311G* basis set were employed as implemented in the Gaussian09 program package.[Gau09] Molecular orbitals (MOs) were visualized with GaussView 5.0. Furthermore, electrostatic potential surfaces (ESP) were calculated at the DFT (B3LYP/6-311G*) level of theory; The Avogadro program (Version 1.2) was used to plot the ESP surfaces.[Avo12, Han12]

For the cluster calculations of the **DCS**-compounds and of the different polymorphs of **β-DCS**, molecular geometries and nearest neighbor arrangements were extracted from the available X-ray analysis. The molecules were then B3LYP-optimized, however imposing the torsional angles found in the X-ray analysis. Replacing the monomers/dimers/tetramers of the X-ray analysis by these B3LYP-optimized molecules, single point TD-DFT calculations were then performed at the CAM-B3LYP level (6-311G* basis set); for comparison, the same procedure was applied to the fully relaxed monomers.

Polymorph computations of **β-DCS** were performed by Dr. Lucas Viani from Universidad Carlos III de Madrid. The calculations were based on a multi-step crystalline domain approach,

making use of classical molecular dynamics (MD) to promote the formation of local crystalline domains within an amorphous system. The computational protocol was first applied to the fully relaxed structure (CLC1); in a second calculation to the forced geometry (CLC2), as found in the polymorph (PM3) grown by us.

CASSCF computations were performed in the group of Dr. Daniel Roca, Valencia, to determine the electronic-structure properties of the ground and lowest-lying singlet excited states at the Franck-Condon and CI regions of the PES. The atomic natural orbital S-type valence double-ζ plus polarization (ANO-S-VDZP) basis set was used.[Pie95] The active space comprises the 12 most relevant π-electrons distributed in 12 natural orbitals [hereafter, CASSCF(12-in-12)]. The MOLCAS 8.1 quantum-chemistry package of software was used for these computations.[Mol16]

b) Computational Details on **D**:**A** System

The geometries of the donor and the acceptor molecules were optimized at the DFT level of theory in vacuum under C_2 symmetry restriction; the symmetry restriction keeps the symmetrical situation of the molecules while allowing for complete conformational freedom. For the donor, the optimization was performed for two rotational conformers (*syn*, *anti*) defined by the orientation of closest fluorine with respect to the central sulphur atom (see Scheme 3.2). Molecular orbitals (MOs) were visualized with GaussView 5.0.

Vertical and adiabatic singlet transitions of the donor and acceptor molecules were calculated using the same approaches as described for the **DCS**-compounds above. In all calculations, the alkyl (e.g. ethyl and butyl) chains in the central and terminal rings were simply replaced by methyl groups to reduce the computational effort; the B3LYP functional and the 6-311G* basis set were employed as implemented in the Gaussian09 program package.[Gau09] For the dimer calculation of the donor, we constructed a dimer by arranging two B3LYP-optimized molecules in the way taken from a published X-ray analysis,[Lov13] and performed a single point TD-DFT calculation at the CAM-B3LYP level (6-311G* basis set).

Chapter 4

Results and Discussion

The 'Results and Discussion Part' will discuss the investigations on the two different cyano-vinylene based systems. Part A is dedicated to the general mechanism study of solid state luminescence enhancement (SLE) in one-component **DCS**-compound systems (Sections 4.1 to 4.5); Part B will the discuss the performance elucidation of a solution-processed bulk-heterojunction all-small molecule organic solar cells (BHJ ASM-OSCs; Sections 4.6 to 4.9).

Part A SLE of DCS-compounds

As described in the Introduction, **DCS**-type compounds obtained by introducing the cyano functionality in the vinylene unit of distyrylbenzene (**DSB**) is an important prototype of SLE materials; in this part a specific library of **DCS**-compounds with similar and systematically varied structure is used to examine the optical properties and photophysics of the SLE process. Due to the complexity of the current research, we will first detail the structure variation (Section 4.1) in the materials under study. We will then give an overview of the results obtained (Section 4.2.), describing optical spectra and photophysics in fluid solution (Section 4.2.1), solid solution (Section 4.2.2), as well as in the single crystalline state (Section 4.2.3). The discussion on these results will be done in Sections 4.3 to 4.5, which will systematically elucidate a series of key problems, i.e. geometries and twist elasticity of molecular structure (Section 4.3), spectral features (i.e. positions, intensities and shapes) in liquid and solid solution and matrix-dependent photophysics (Section 4.4), to finally turn to the crystalline state (Section 4.5).

4.1 The DCS Family under Study

A specific collection of compounds is investigated in this part. As displayed in Scheme 4.1, the member compounds are derived from step-wise functionalization of the unsubstituted distyrylbenzene (**DSB**) backbone via varying substitution' pattern and position: starting with introducing cyano (CN) groups in the vinylene double bonds, then optionally adding co-substituted alkoxy groups in aromatic rings; the CN groups are placed either in the inner (α) or outer (β) position of the two vinylene units; alkoxy substitution can be either placing di-methoxy (MeO) groups in the *ortho*-positions of the central aromatic ring, and/or positioning di-butoxy (BuO) groups in the *para*-positions of the two terminal aromatic rings; in doing so, a family containing eight different **DCS**-compounds is built. The definition and symbolization shown in Scheme 4.1 are specified here: the vinylene carbon adjacent to the central phenylene ring is defined as α-position, and the other one next to the terminal ring is β; two rotamers, differing in the orientation of di-MeO groups in the central ring with respect to the vinylene

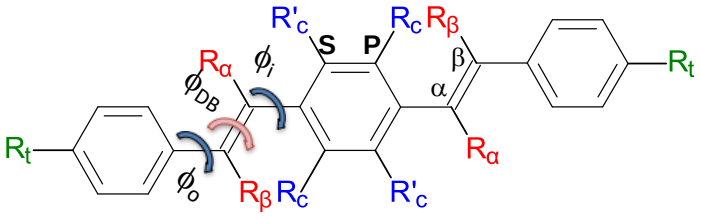

	R_α	R_β	R_t	R_c
α-/β-DCS	CN / H	H / CN	H	H
α-/β-DBDCS	CN / H	H / CN	BuO	H
α-/β-MODCS	CN / H	H / CN	H	MeO
α-/β-MODBDCS	CN / H	H / CN	BuO	MeO

Scheme 4.1: The **DCS** family under study: substitution pattern (R_α, R_β, R_t, R_c) of the cyano (CN), methoxy (MeO) and butoxy (BuO) substituents; torsional angles around the inner and outer vinyl-phenyl bonds (ϕ_i, ϕ_o,) and the vinyl double bond (ϕ_{DB}); MeO orientation at the central ring (P, S).

unit, are symbolized as form **P** (i.e. **p**arallel orientation) and **S** (i.e. '**s**enkrecht', perpendicular orientation). The nomenclature of these compounds is also listed in Scheme 4.1: *para*-distyrylbenzene (**DSB**) is substitution-free and presented as the parent backbone; the other eight di-CN-substituted derivatives based on **DSB** are named as **DCS**-compounds, the latter can be divided into two series which are positional isomers, i.e. (a) **α-CN** series and (b) **β-CN** series; each series comprises four analogues, that is, **DCS** which is solely CN-substituted at **α** or **β** position; **DBDCS** which is additionally BuO-substituted in each terminal ring; **MODCS** which is alternatively *para*-di-MeO-substituted in the central ring; **MODBDCS** which possess both BuO and MeO groups; for the comparative discussion later, **MODCS** and **MODBDCS** can be grouped into **MO**-compounds, while **DBDCS** are **DB**-compounds. Two facts need to be mentioned here in advance: according to the X-ray analysis of the respective single crystals,[Var13, Yoo11a, Yoo10, Yoo13, Shi17, Var14] the **S**-rotamer was found for **α-/β-MODCS** and **β-MODBDCS**, while the **P**-rotamer was present in **α-MODBDCS**;[Yoo13] in addition, the optical and photophysical properties in fluid solution and single crystals of some compounds in this library were characterized and published already.[Yoo10, Yoo11a, Yoo11b, Yoo13, Var14] Nevertheless, these data sets were either incomplete due to some missing measurements, and/or a systematic comparative analysis in different environments was not done due to the case of solid solution was neglected by now. Herein, it will be described in the following Sections that the systematic variation of the **α/β** position as well as of MeO/BuO substitution significantly influence the optical and photophysical properties in the fluid solution as well as in the solid state (referring

to the solid (highly diluted) PMMA films and single crystals). Diverse phenomenological signatures, resulting from a series of subtle structural changes, enable this library to offer all the probable property-controlling parameters, which allows for a unique insight into structure-property relationships in this and related classes of compounds.

4.2 Description of Absorption and Emission Properties

Spectral shapes and position, peak intensity, PL quantum yields (Φ_F) and lifetimes (τ_F) are the important parameters for absorption and emission properties evaluation. Focusing on these parameters, the result description of different compounds in variable environment will be logically done in a systematically comparative way: for a given environment, i.e. fluid and solid solution (highly diluted PMMA film, monolithic crystals), these parameters are compared for the different compounds under study. Then, based on this description, the (inter alia dramatic) changes of properties for the different compounds as well as in different environments will be discussed.

4.2.1 Fluid Solution

Two aspects of the properties in dilute solution ($CHCl_3$) will be compared between all the compounds, one is the change of the spectral aspect and the other is the evolution of PL quantum yields and lifetimes. The UV-Vis Abs and PL spectra of all the compounds are plotted in Figure 4.1, see the corresponding maxima in Table 4.1; PL quantum yields (Φ_F) and lifetimes (τ_F) are shown in Figure 4.2 and Table 4.11.

Staring from the parent compound **DSB**, the PL spectrum is vibronically structured with two subbands positioned at 3.18 eV (390 nm) and 3.01 eV (412 nm), which were assigned as apparent 0-0 and 0-1 bands.[1] Compared to the PL spectrum, the absorption spectrum is less structured; a maximum at 3.48 eV (356 nm) as well as a small recognizable shoulder at ~4.1 eV (302 nm) are observed. With respect to the photophysical parameters, **DSB** is showing strong emission with a quantum yield of Φ_F = 0.87 and a corresponding lifetime of τ_F = 1.16 ns, which agrees well with the numbers reported earlier.[Gie02, Gie05,Gie13a]

[1] As we have explained in Section 2.1.4, here the term 'apparent' indicates that the visible vibronic structure is not due to one single vibration, but arising from progressions and *inter*combinations of several modes, which however are not resolved at ambient conditions, but collapse into one 'apparent' progression.[Gie02, Wu05] Concomitantly, a single 'apparent' Huang-Rhys factor S can be extracted by fitting the spectra with one Poisson distribution with S as the argument.[Gie02]

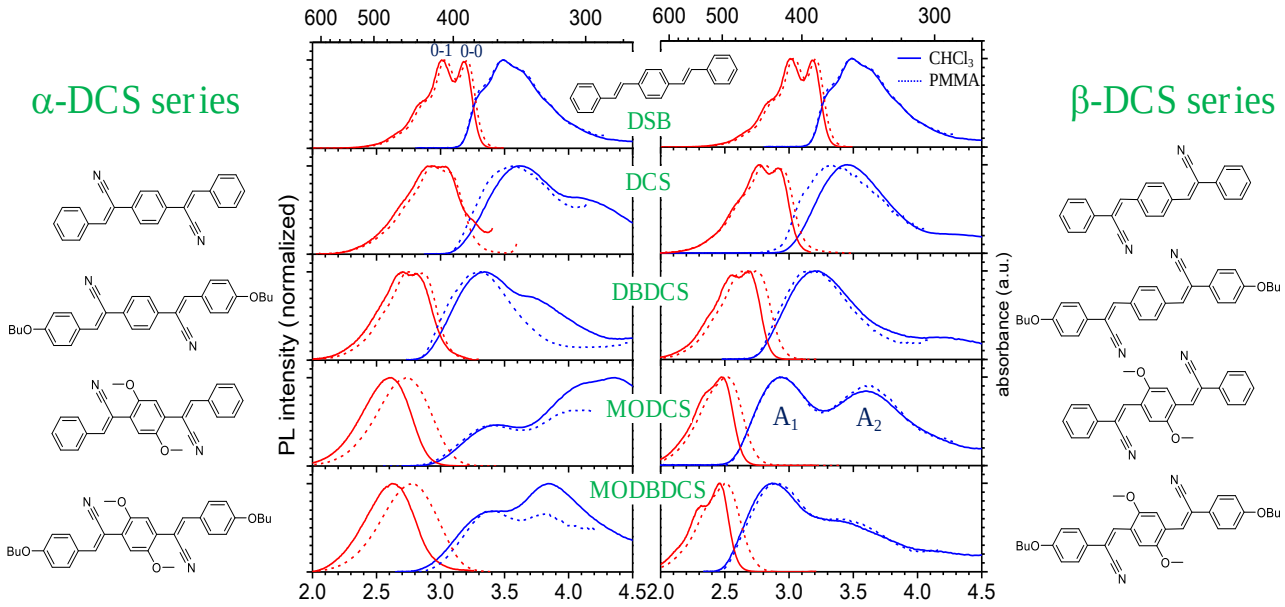

Figure 4.1: Absorption and PL spectra of **DSB** (top) the **DCS** series (α-series, left; β-series, right) in solution ($CHCl_3$, solid lines) and PMMA (dashed lines).

Within the **DCS** family, red-shifted PL and Abs spectra are generally observed where the vibronic feature are mostly lost if compared to that of **DSB**; the **α-DCS** absorption appears as an exception within this series, and the degree of spectral shifts varies largely for the different compounds. For example, the red-shift in the β-series is significantly more pronounced relative to the α-series, where the shifting amount depends on the presence of subsequent substitution besides CN; in fact, the shift increases within the sequence **DCS** → **DBDCS** → **MODCS** ≈ **MODBDCS**, i.e., the largest red-shift of the PL spectrum against **DSB** is happening in **β-MODBDCS,** with an amount of 0.7 eV and finally locating the peak maximum at 2.46 eV (505 nm). The loss of vibronic structure behaves differently in the PL spectra and in the Abs spectra. For the PL spectra, the loss of vibronic structure in the α-series is more pronounced than in the β-series; in the α-series, the vibronic structure can be washed out completely, in particular when MeO substitution is located in the central ring (**α-MODCS**, **α-MODBDCS**). In the β-series, the PL spectra are only slightly broadened against that of **DSB**, the vibronic structure is anyway sustained independently upon the subsequent substitute groups (BuO, MeO). The 0-1/0-0 band ratio (i.e. of the 'apparent' Huang-Rhys factor)[1] decreases dramatically along with the introduction of alkoxy groups, see Table 4.1. For the absorption spectra, the vibronic structure is washed out once the CN has been introduced; i.e., the Abs spectra of all the **DCS**-compounds are completely unstructured, different from **DSB**. To be noted, the substitution with MeO

Table 4.1: Optical data of **DSB** and the **DCS** series in $CHCl_3$ and PMMA: peak position of absorption (E_{abs}) and PL (E_{em}), Stokes Shift $E_{Stokes} = E_{abs}(A_1) - E_{em}$, adiabatic energy E_{00}, relative intensity ratio f_1/f_2 of the absorption subbands A_1 and A_2 (see Figure 4.1).

		E_{abs} (A_1, A_2) / eV [a]	f_1/f_2	E_{em} / eV [b]	E_{Stokes} / eV	E_{00} / eV [c]
DSB	$CHCl_3$	3.48		3.01 (3.18)	0.47	3.26
	PMMA	3.48		3.04 (3.20)		3.27
α-DCS	$CHCl_3$	3.61		2.93 (3.02)	0.68	3.24
	PMMA	3.53		2.95 (3.05)		3.21
α-DBDCS	$CHCl_3$	3.34		2.70 (2.81)	0.68	2.99
	PMMA	3.32		2.76 (2.86)		2.99
α-MODCS	$CHCl_3$	3.45, 4.37	0.65	2.60	0.85	2.96
	PMMA	3.41 ,4.05	0.63	2.74		3.07
α-MODBDCS	$CHCl_3$	3.43, 3.84	0.58	2.62	0.81	2.97
	PMMA	3.38 ,3.83	1.02	2.78		3.08
β-DCS	$CHCl_3$	3.46		2.77 (2.92)	0.79	3.05
	PMMA	3.33		2.80 (2.95)		3.05
β-DBDCS	$CHCl_3$	3.19		(2.54) 2.68	0.51	2.84
	PMMA	3.13		(2.62) 2.74		2.88
β-MODCS	$CHCl_3$	2.95, 3.60	1.11	(2.37) 2.47	0.48	2.62
	PMMA	2.92, 3.61	1.03	2.51		2.67
β-MODBDCS	$CHCl_3$	2.87, 3.40	1.19	(2.32) 2.46	0.41	2.57
	PMMA	2.92, 3.42	1.37	2.50		2.64

[a] absorption maxima. [b] = PL maxima with apparent (sub)bands in parenthesis. [c]= from the intersection of absorption and PL spectrum; for PMMA film, the PLE spectrum was used.

groups in the central ring splits the main absorption band into two subbands, revealing 'camel hump' shape, being a signature of **MO**-compounds' absorption.[Oel98]

In respect of the photophysical parameters as shown in Figure 4.2, the PL quantum yields and lifetimes of different substituted-**DCS**-compounds have been changed sharply from **DSB**, being a result of CN substitution; herein the changes of lifetime are generally correlated with that of the quantum yields. Specifically speaking, the trend of this change in two structural-isomer series are distinctively different, being sensitive to the variation of the substitution pattern and position. In the α-series, all the compounds show drastically decreased Φ_F (**<**0.01) compared

to **DSB**, equally non-emissive in practice, i.e. independent upon the substituent pattern. In the **β**-eries, the decrease of Φ_F is also observed but varies largely between alkoxy-substituted and non-substituted compounds; that is, the presence of the alkoxy substitution (MeO, BuO) in addition to CN shows an enhancement effect on fluorescence, the value of Φ_F increases from **β-DCS** ($\Phi_F = 0.01$) → **β-MODCS** ($\Phi_F = 0.20$) → **β-MODBDCS** ($\Phi_F = 0.31$) → **β-DBDCS** ($\Phi_F = 0.54$). Except for **β-DCS** which behaves non-fluorescent like the **α-DCS** series**,** the **β-DCS** series are much brighter than their isomers in **α-DCS** series and moderately (or high) luminescent in fluid solution. The lifetime range is sharply different for luminescent compounds (**β-DCS** series except for **β-DCS**) and for the practically non-luminescent compounds (**α-DCS** series plus **β-DCS**); for the former, all the lifetime values are around 1 ns, while for the latter the lifetime values are below ps; see the specific numbers in Table 4.11.

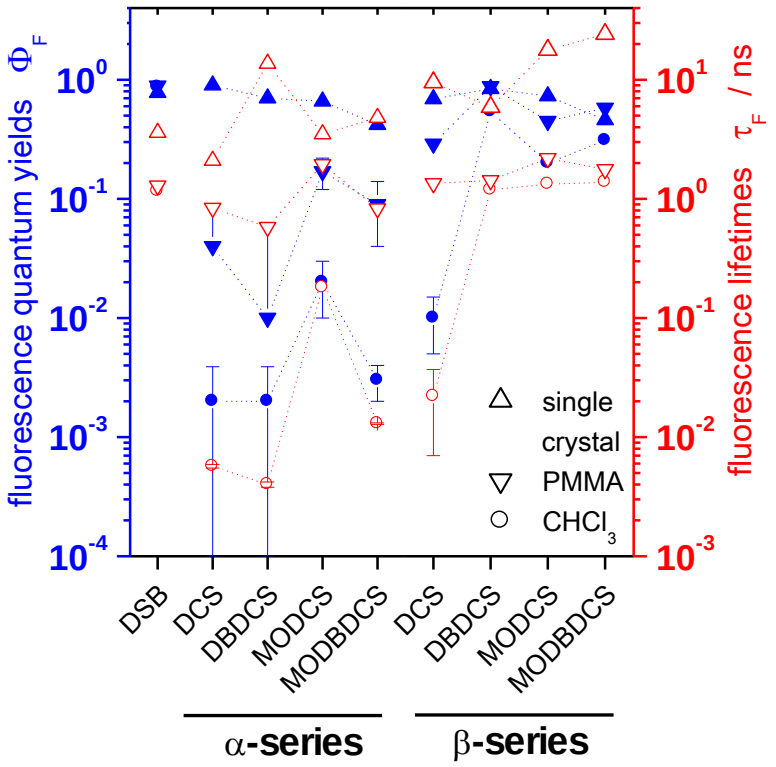

Figure 4.2: PL quantum yields (solid symbols, in blue) and lifetimes (open symbols, in red) of **DSB** and the **DCS** series in $CHCl_3$ (●), PMMA (▼), and single crystal (▲).

4.2.2 Solid Solution (PMMA Film)

As mentioned in the Introduction, the emission properties are subject to the environment rigidity ascribed to the restriction exerted on the structures, for example, **DCS**-type compounds show the attribute of emission enhancement from flowing molecule-dispersed solution to the

condensed, aggregated state. Considering a more general scope for solid state luminescence enhancement (SLE), PMMA is introduced as a transition medium to create a status between the characteristics of a 'real' solution (fluid solution) and a 'real' solid (e.g. single crystal), i.e. solid solution, to study the structural and photophysical reason for SLE in this type of solid state. Two things need to be kept in mind for the PMMA-caused emission change study: on one hand, PMMA matrix is used to disperse the substance molecules where aggregates should be excluded to make sure that only one variable parameter differs from dilute solution to PMMA; i.e., the *intra*molecular structure. For this purpose, low concentrations of the molecules ($c_M \approx 10^{-4}$ M) are prepared via adding PMMA. On the other hand, PMMA matrix is used to provide a rigid environment for the molecules, and largely restricted intramolecular motions will consequently result into important changes in the spectral aspects (position and bandshape) but particularly in the aspect of photophysics (PL quantum yields and lifetimes) compared to that in dilute solution, which are displayed in Figure 4.1 and Figure 4.2. To be noted, in this comparison, PL excitation (PLE) spectra were used instead of Abs spectra because the latter cannot be recorded for PMMA samples.

For **DSB**, the PL and PLE in PMMA basically reproduce that in $CHCl_3$ solution, both for the spectral positions and shapes. Differently, for the **DCS**-compounds, PMMA influences the spectral aspects significantly and variably between different compounds. For **α/β-DCS** and **α-DBDCS**, the spectra are still similar to fluid solution, however less than for **DSB**; for all the MeO-substituted compounds as well as **β-DBDCS**, a significant blue-shift of the PL spectra in PMMA against $CHCl_3$ is observed, while the onset of the Abs spectra are only slightly changed. Moreover, the bandshapes of the Abs spectra change largely in particular for the MeO-substituted compounds in the α-series; the vibronic features of the PL spectra for all the compounds in the β-series are prone to get blurred when going from $CHCl_3$ to PMMA.

As seen in Figure 4.2, PMMA activates the SLE attribute for **DCS**-type compounds successfully, that is, the **DCS**-compounds show (substantially) enhanced PL quantum yields when going from dilute solution to the PMMA matrix, whereas **DSB** shows similar (high) quantum yield and lifetime as in the fluid solution. However the extent of the enhancement again depends strongly on the substitution pattern and position: for the **β-DCS** compound and the α-series which are similarly low luminescent in $CHCl_3$ solution, the Φ_F increase caused by PMMA is more pronounced in the former compound than in the latter; thus, the former turns out to be moderately emissive in PMMA, i.e. Φ_F climbs up steeply from 1% to 29%. Conversely, the α-series is still quite low emissive even in PMMA; for the alkoxy-substituted compounds

in β-series which are already emissive in $CHCl_3$ solution, they become even more luminescent in PMMA, with Φ_F of an value 88% in **β-DBDCS,** which is close to that in **DSB**.

4.2.3 Single Crystals and Different Polymorphs

Besides the non-aggregated solid state (i.e. PMMA), the 'classical' solid state was investigated, where intermolecular interactions can also significantly influence the emission property and provoke the SLE phenomenon in **DCS**-type compounds; i.e. being now correlated not only with the constrained *intra*molecular structure but further complex with the resulted *inter*molecular arrangement. Although monolithic and polycrystalline samples (such as vapor-deposited or spin-coated films, or nanoparticle suspensions) can both provide the aggregated solid environment, only monolithic (single) crystals are suitable for the above investigation purpose due to two considerations: one is that the *inter*molecular structure is well defined and easy to characterize (by X-ray) or predict (by computation) in single crystals; the other is that high material purity, small surface:volume ratio and long distances towards the surface in monolithic crystals can reduce the probability of free exciton being trapped.[Gie13a] Such trapping can indeed induce the opposite phenomenon to SLE and thus completely mask the SLE effect as mentioned in introduction. Although single crystals for all the compounds have been obtained and reported earlier,[Var13, Yoo11a, Yoo10, Yoo13, Var14] the photophysical data for two compounds (**α-DBDCS, β-DCS**) are still not known yet; for this reason, we especially grew single crystals for these two compounds and recorded quantum yields and lifetimes on them. For **α-DBDCS**, the single crystal is obtained from a mixture solution of $CHCl_3$ and hexane; for **β-DCS**, the single crystal is obtained in $CHCl_3$ solution with hexane vapor diffusion. It should be noted that the **β-DCS** reported here is different from the two published polymorphs of **β-DCS** (which were obtained from the gas phase);[Xu12, Li12, Cha12] the resulting crystal structure of the current **β-DCS** polymorph will be reported in the next section. Combining with the other photophysical data directly taken from literatures, a full data set for all the different compounds is displayed in Figure 4.2. Importantly, independently on the molecule itself (substitution pattern and position) and its specific *inter*molecular arrangement (ranging from J- to H-aggregates;[Yoo13, Gie13b] which will be shown in the next section), the single crystals of all the compounds are highly luminescent, with Φ_F values varying widely in a range from 42 to 90%. Comparing the single crystal Φ_F of a certain compound with that in liquid solution, an increase of Φ_F is observed in all cases; that is, each **DCS**-compound in this collection is exceptionally SLE active, hardly dependent on *intra*molecular nor *inter*molecular factors, which will be discussed later. On the

contrary, such factors are reflected in largely different PL lifetimes, ranging from ca. 2 ns to about 20 ns, see Figure 4.2.

As mentioned before, the single crystals of **β-DCS** grown by us show different structure to the two ones reported by others in literatures. Thus, now three polymorphs of single crystalline are known for **β-DCS**, being particularly valuable these three polymorphs all offer X-ray measurable quality,[Xu12, Li12, Cha12] which creates a promising chance to study the structural reason for the appearance of polymorphsim in this class of compounds and for explaining the polymorph-sensitive emission (*vide infra*). The three polymorphs are simply denoted as PM1, PM2 for the known ones and PM3 for the current polymorph of this work; the optical spectra and corresponding maxima values are displayed respectively in Figure 4.3 and Table 4.2 (crystal structures will be shown later in next section).

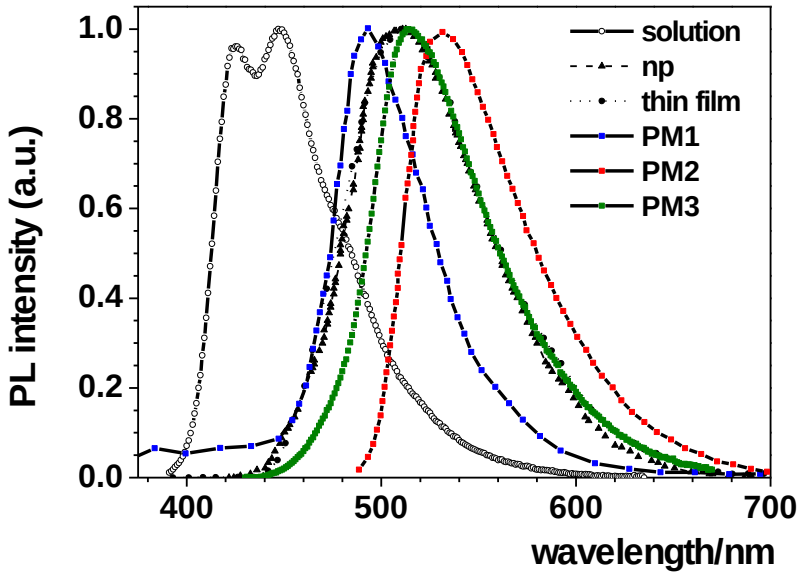

Figure 4.3: PL spectra of **β-DCS** in different environments and polymorphs: solution ($CHCl_3$), nanoparticle (NP) suspension,[Yoo11b] thin film,[Yoo11b] crystals of PM1[Xu12] and PM2[Li12, Cha12] and the present PM3 crystal.

Before looking at the spectral position shift, there's one issue objectively existed in crystal' emission spectrum need to be pointed out, that is, substantial reabsorption due to the high optical density. This significantly influences the crystal spectra; for example, with reabsorption probabilities of φ = 0.5 and more,[Gie13a] this can lead to an apparent (though artificial) bathochromic shift of up to 0.1 eV and give rise to a steep slope of the spectra at the high energy side. Taking this steep slope as a clue, it's assumed that pronounced reabsorption is strong for the reported PM1[Xu12] and PM2[Li12, Cha12] in Figure 4.3. Instead, for PM3, the reabsorption

probability φ has been minimized by reducing the light penetration at the edge of an anyway small needled shaped crystal with ca. 0.35 mm length and 0.06 mm width.

Table 4.2: Optical and photophysical data of **β-DCS** in different environments and polymorphs: solution ($CHCl_3$; polymethylmethacrylate, PMMA), nanoparticle suspension (NP), thin film, and single crystal. Maximum of absorption and emission (λ_{abs}, λ_{em}), PL quantum yield and lifetime (Φ_F, τ_F), amplified spontaneous emission (ASE).

	λ_{abs} / nm	λ_{em} / nm	Φ_F	τ_F / ns	ASE	Ref.
$CHCl_3$	358	(424) 447[a]	0.01	0.03		this thesis
PMMA	372	(421) 443 [a]	0.29	1.35		this thesis
NP (THF/H_2O)	312	518 [b]	0.42	10.9 [d]		[Yoo11b, Cha12]
Film	308	514 [b]	0.52	19.2 [d]		[Yoo11b]
PM1: tube	—	480 [b]	—[c]	—[c]	yes	[Xu12]
PM2: plate	—	531 [b]	0.75	14.7 [d]	no	[Li12, Cha12]
PM3: needle	—	514 [b]	0.69	9.5 [d]	no	this thesis

[a]vibronically structured, [b] unstructured, [c] not determined. [d] intensity-average of a bi-exponential fit.

Comparing the PL spectra of the single crystals with that in fluid solution, spectral shifts are clearly shown in Figure 4.3 and Table 4.2: the three polymorphs exhibit featureless PL spectra which are all red-shifted against solution, however by variable amount, i.e., ~0.20 eV for PM1 while 0.45 eV and 0.37 eV for PM2 and PM3 respectively. Comparing the PL spectra of the three different polymorphs and with nanoparticles or thin films, the spectral shift are not what indicated in Figure 4.3 because the artificial bathochromic shift effect mentioned above needs to be taken into account at this point, thus, the spectral positions of emission for PM2 and PM3 are rather comparable; furthermore, the PM3 emission coincides largely with the reported emissions of **β-DCS** in nanoparticle suspensions and vapor-deposited films.[Yoo11b] On the other hand, PM1 exhibits a distinctively different spectrum, hypsochromically shifted by ca. 0.2 eV against the other polymorphs, which can be correlated with the packing structures as discussed further down.

4.3 Structural Properties

The elucidation of structures is crucial for revealing the origin of the emission in organic solid materials. Although it's broadly known and simply said that structures decide properties, how to identify the decisive structural factors and quantify the corresponding contributions on the

resulting emission (i.e. spectral and photophysical properties) is an issue of difficulty, owing to the complexity of this matter. Normally, structure of single molecule is correlated with liquid solution's emission by default; however it can easily be largely changed in the aggregated state due to changes in the molecular structure as well as by cooperative interactions. Thus, the influence of both, *intra*- and *inter*molecular structures on the apparent solid emission should be equally estimated. In fact, the relation can be complex; the contributions from two sides subtly interplay with each other, for example cooperative *intra*molecular and *inter*molecular contributions may give rise to enhanced emission, or the *inter*molecular contribution may be dominant etc. This will depend sensitively on the specific (class of) material. Instead of paying effort to identify the structural correlations for different types of materials in kind of top-down approach, we choose here a bottom-up approach, identifying relevant *intra*- and *inter*molecular structural factors in the first step; herein, structure investigation is assisted by quantum chemical calculations to learn about energetics and potential energy surfaces (PES) of the molecules in free and restricted environments.

4.3.1 Molecular Structures

The geometry of single molecule's structure is particularly investigated due to its close correlation with the emission parameters such as the oscillator strength and the spectral position. From experiment, the molecular structures in solution cannot be directly determined. In fact, the available experimental geometries from x-ray analyses on single crystals of the **DCS**-compounds [Bar00, Xu16a, Xu16b, Yoo10,Yoo11a,Yoo13,Var14] can vary largely from those in solution due to the constrained environment; this will be discussed further down. Hence, the equilibrium geometries (and potential energy surfaces for selected structural parameters; *vide infra*) of all compounds are elucidated by DFT (in vacuum) via full optimization under specific symmetry restrictions. Relevant bond angles and torsional angles are denoted in Figure 4.4 and the corresponding values are listed in Table 4.3; selected bond lengths are shown in Table 4.4.

The results in Table 4.3 suggest that strong twists in the structure is a general signature for the **DCS**-type compounds, which however vary upon substitution (pattern, position, orientation) and in particular sharply upon the environment change such as from solution to single crystal; in this section only the torsion in vacuum are described, the one in single crystal will be mentioned in the next section. It's known from earlier studies that **DSB** exhibits a planar equilibrium geometry in vacuum and in solution,[Gie02,Gie13a] although the average structure is apparently non-planar due to the active thermal population of the shallow torsional potentials

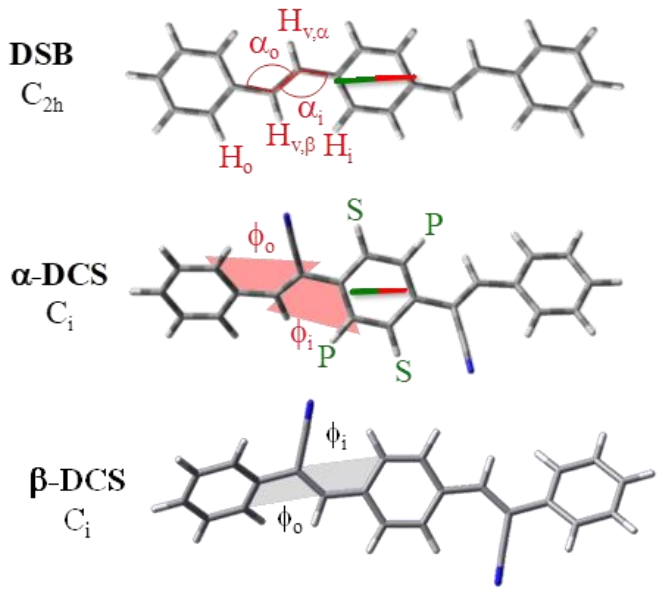

Figure 4.4: DFT-optimized structures of **DSB**, **α-DCS** and **β-DCS** in the electronic ground state (S_0); relevant atoms, angles and torsions are indicated, as well as the substitution positions (**S**, **P**) of the MeO groups at the central ring, and the TD-DFT calculated $S_0 \rightarrow S_1$ transition dipole moment $\vec{\mu}_{01}$ (red-green bi-colored line).

around the vinyl-phenyl single bonds as indicated in Figure 4.4.[Gie02, Sri09] The introduction of CN groups deforms the planar geometry in **DSB** strongly due to the increase of the steric hindrance with the neighboring H-atoms (H_i, H_o; Figure 4.4) compared to **DSB**. For **α-DCS**, upon free optimization within the C_i symmetry point group, substantial twist happens at the inner vinyl-phenyl single bond with a value of $\phi_i = 30^o$ (Table 4.3); meanwhile, an increase of the bond length from 1.461 Å in **DSB** to 1.486 Å is observed (Table 4.4), while only slight twist in the outer part with a value of $\phi_o = 9^o$ (Table 4.3) is found, since here the structure can react in an alternative way, i.e. the bond angle is largely open to $\alpha_o = 132^o$. For **β-DCS**, an analogue situation with similar torsional values but different location of distribution is found, i.e., a substantial twist around the outer vinyl-phenyl bond with $\phi_o = 32^o$, whereas a slight twist around the inner one with $\phi_i = 7^o$, see Table 4.3. For **DB**-compounds (**α-/β-DBDCS**), compared to the only CN-substitution (**α-/β-DCS**), the situation qualitatively doesn't change by additional BuO-substitution in the terminal rings; however, somewhat quantitative changes in torsional angles are observed due to slight changes in the electronic structure (i.e. frontier MO topologies; the latter will be discussed in more detail, see Section 4.4).

Differing from BuO substitution in the terminal rings, MeO substitution in the central ring has a pronounced effect on the resulting geometry; however, thus depends sensitively on the

position of the CN group (i.e. α- vs. β-series) and the orientation of the two MeO groups (whether **P-** or **S**-rotamers, Scheme 4.1 / Figure 4.4); see Table 4.3.

Table 4.3: (TD)DFT calculated torsional angles (in vacuum) for the **DCS** series in the S_0 (1^1A_g) and S_1 (1^1A_u) electronic states; ϕ_i/ϕ_o are torsional angles around the inner/outer vinyl-phenyl bonds (see Scheme 4.1/ Figure 4.4) .

compound	rotamer	α-series		β-series	
		S_0	S_1	S_0	S_1
		i / o (°)	i / o (°)	i / o (°)	i / o (°)
DCS		30 / 9	1 / 1	7 / 32	5 / 15
DBDCS		29 / 5	0 / 0	6 / 30	5 / 16
MODCS	**P**	28 / 13	26 / 7	39 / 32	29 / 23
	S	49 / 6	36 / 7	15 / 30	4 / 17
MODBDCS	**P**	29 / 5	22 / 7	39 / 30	26 / 21
	S	48 / 4	31 / 8	13 / 26	3 / 13

Table 4.4: (TD)DFT calculated bond lengths (in vacuum) of TS, **DSB** and the **DCS** series in the ground (S_0) and the first excited singlet state (S_1); the values for the inner/outer vinyl-phenyl bonds (r_i/r_o) and the vinyl double bond (r_{DB}) are listed.

		α-series				β-series		
		r_i	r_o	r_{DB}		r_i	r_o	r_{DB}
TS	S_0	1.465		1.345				
	S_1	1.413		1.417				
DSB	S_0	1.461	1.464	1.347				
	S_1	1.422	1.433	1.384				
DCS	S_0	1.486	1.459	1.359	S_0	1.457	1.487	1.360
	S_1	1.448	1.430	1.401	S_1	1.418	1.462	1.400
DBDCS	S_0	1.485	1.453	1.362	S_0	1.456	1.484	1.361
	S_1	1.448	1.429	1.401	S_1	1.420	1.464	1.400
MODCS(P)	S_0	1.490	1.461	1.357	S_0	1.452	1.487	1.362
	S_1	1.469	1.438	1.391	S_1	1.426	1.470	1.392

MODBDCS(P)	S_0	1.489	1.456	1.359	S_0	1.451	1.483	1.363
	S_1	1.461	1.433	1.396	S_1	1.420	1.466	1.396

For MO-compounds in the **α**-series, i.e. **α-MO(DB)DCS**, the torsional angles are hardly changed upon MeO substitution for the **P**-rotamers, while for **S**-rotamers the considerable $C_{CN}\cdots O_{MeO}$ interactions between the CN and MeO groups lead to a significantly stronger twist of the inner vinyl-phenyl bonds, i.e. $\phi_i \approx 49^o$;[2] for the MO-compounds in the **β**-series, the **P**-rotamers are subject to considerable $C_{CN}\cdots O_{MeO}$ interactions, widening the twist of the inner angle to $\phi_i = 39^o$, while in the **S**-rotamers, ϕ_i increases only slightly to about 13-15°. According to the X-ray analysis, the **P**-rotamer only exists in the single crystal of **α-MODBDCS**, while **S**-rotamer is found in all other **MO**-compounds. From a point of view, in the **α**-series the **P**-form might be somewhat favored against **S** because the former is subject to less $C_{CN}\cdots O_{MeO}$ interactions and allows for favorable packing in the condensed state, whereas the same argument holds for the **S**-form in the **β**-series. From energetic point of view, based on DFT, the unfavorable $C_{CN}\cdots O_{MeO}$ interactions make **P**-rotamers only somewhat favored against **S** by -0.06 eV in **α-MODBDCS**, while in **β-MODBDCS** the **S**-rotamer is substantially favored against **P** by -0.34 eV.

In all, strong torsions are inherent to the **DCS**-type compounds, and more significantly, they are able to vary in a broad range of angles. It should be mention already at this point that the torsional potentials around the phenyl-vinylene single bonds are very shallow, so that at ambient conditions a broad range of twists are expected in weakly restricting environments, e.g. in fluid solutions; this has a significant impact on the resulting optical and photophysical properties, to be discussed in Section 4.4. Even in restricted environments, as in the condensed state, these shallow potentials are of great importance: slight changes in the growing condition for single crystals can give rise to new polymorphs with distinctive molecular twists, being an intriguing issue of great importance for applications as sensors and security materials. Even more striking, for substituted **DCS**-compounds, structurally similar compounds gave rise to completely different packing motifs; all these issues will be discussed in the following Sections (4.3.2 and 4.3.3).

[2] It should be stressed at this point that methoxy-substitution in the central ring does not provide substantially different geometries than hexyl-substitution as previously suggested.[Oel96]

4.3.2 Solid State Packing Structures

a) Overview on Crystal Packings for the **DCS**-compounds

Crystal structures of **DSB** and of the eight **DCS**-compounds under study have all been determined by x-ray analysis in the past;[Var13, Yoo11a, Yoo10, Yoo13, Xu12, Var14] polymorphism has been observed for **DSB** (PM1,2),[Wu03,Var13] **α-DCS** (PM1[Yoo11a]; PM2[Xu16a, Xu16b]) and **β-DCS** (PM1[Xu12]; PM2[Li12, Cha12]); in the course of the current project, a further polymorph of **β-DCS** (PM3) has been discovered, which will be discussed in Section 4.3.2 (b). Compared to the twists in DFT-calculated equilibrium geometries (Table 4.3), the molecular twists in the single crystals are (partially significantly) changed, however very different for the specific compounds, see Table 4.5 and Figure 4.16. For instance, compounds **α-DBDCS**, **α-MODCS**, **α-MODBDCS**, **β-DCS**, **β-MODBDCS** gain a more planar structure in the respective crystals, while compounds **α-DCS**, **α-MODCS**, **β-DBDCS** get even more twisted in the crystals. Therefore, in general, the observed twists are not directly correlated with the cyano-vinyl synthon; instead, it's a manifestation of inherent torsional flexibility which reacts sensitively to the specific multi-substitution pattern as well as to the conditions of crystal growth.

Table 4.5: Rotamers found in the single crystal (SC) X-ray analysis and their torsional angles; ϕ_i/ϕ_o are around the inner/outer vinyl-phenyl bonds (see Scheme 4.1/ Figure 4.4).

compound	**α-series**		**β-series**	
		X-ray		X-ray
	rotamer	i / o (°)	**rotamer**	i / o (°)
DSB		0 / 0		
DCS		26 / 32		Table 4.6
		4 / 7		
DBDCS		4 / 6		28 / 27
MODCS	**S**	39 / 23	**S**	31 / 13
	P	4 / 20	**S**	0 / 0

Looking at the packing modes for the compounds, a large variety of nearest neighbor arrangements can be seen (Figure 4.16). This concerns on one hand the arrangement of the π-systems,[Gie13b] ranging from so called "π-stacks" with a cofacial arrangement of planar molecular backbones (e.g. **α-MODBDCS**) to "herringbone" arrangements with an edge-to-face

arrangement of the π-systems (e.g. **DSB**), see Scheme 4.2;[Gie13b] whereas intermediate situations with 'micro-herringbone' arrangements of twisted systems (e.g. edge-to-face arrangements of the phenyl rings) are observed e.g. for **α-DCS**. On the other hand, it concerns the shift of neighboring molecules along their long and/or short axes (x- and y-slips, respectively), see Scheme 4.2.[Gie13b] The x-slip mainly determines amount and sign of exciton coupling, which gives rise to all different packing types ranging from H- to J-aggregates with variable extent, see Figure 4.16. The impact of all these factors on the resulting optical properties will be discussed in Section 4.5.

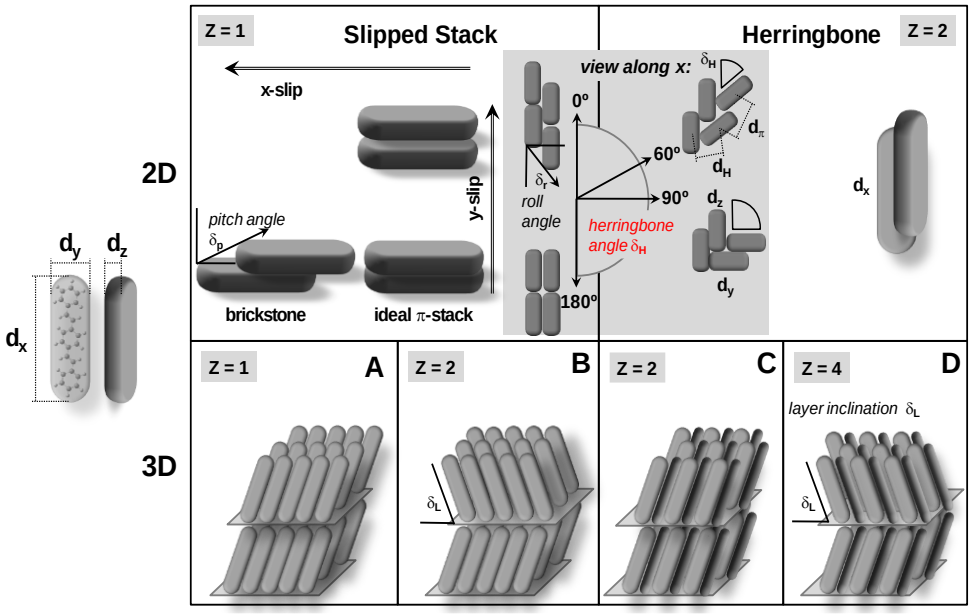

Scheme 4.2: Schematic intermolecular arrangements (in two-(2D) and three-(3D) dimension) in conjugated organic molecular crystals.[Gie13b]

It should be stressed at this point, that the correlation between the isolated intramolecular structure and the resulting twists and intermolecular packing in the solid is by no means easy to understand due to the large number of variables, although predictive calculations become increasingly better (*vide infra*). For the moment, it might be sufficient to remember that a few simple rules for the *inter*molecular arrangements can be formulated:[Gie13b] substitutent-free rod-shaped molecules like **DSB** generally tend to adapt herringbone (HB) instead of π-stack arrangements, which is favored by stronger attractive H-π- against π-π-interactions; the presence of functionals groups with strong local dipoles (eg. CN) can switch HB to π-stack or J- to H-aggregate by the induced H-bonding and strong dipole-dipole interactions with the neighboring π-system; meanwhile, the steric hindrance of the induced functionals groups may twist the *intra*molecular geometry and thus can turn HB to μ-HB structures.

b) Polymorphism in **β-DCS**

As mentioned above, two polymorphs of **β-DCS** have been successfully determined by single crystal (SC) x-ray analysis in the past by other groups.[Xu12, Li12, Cha12] While these polymorphs were grown from the gas phase, we grew a new polymorph (PM3) from $CHCl_3$ solution with hexane vapor diffusion, giving good quality crystals to be analyzed by X-ray (for the complete set see Appendix 1). Nearest neighbor arrangements of the three polymorphs are shown in Figure 4.5, showing distinctively different intra- and intermolecular features. The difference between these crystal structures will be explained in three steps, in a first step the rotating form of the two CN-groups in monomer will be clarified (i.e. *syn* or *anti* rotamers; the mutual arrangement of the two CN-groups indicated in Figure 4.5); in a second step, the changes of *intra*molecular twist will be seen in Table 4.6; in a third step, the changes in crystal structures driven by different *intra*molecular twists will be illustrated (Figure 4.7). The reason for the largely varied twists for the different polymorphs (the so-called "twist elasticity") will be rationalized in Section 4.3.3. The way how these (*intra*- & *inter*molecular) structural changes lead to significant changes in the optical (Figure 4.3) and photophysical response (Table 4.2) of the molecular solids will be elucidated in Section 4.4.

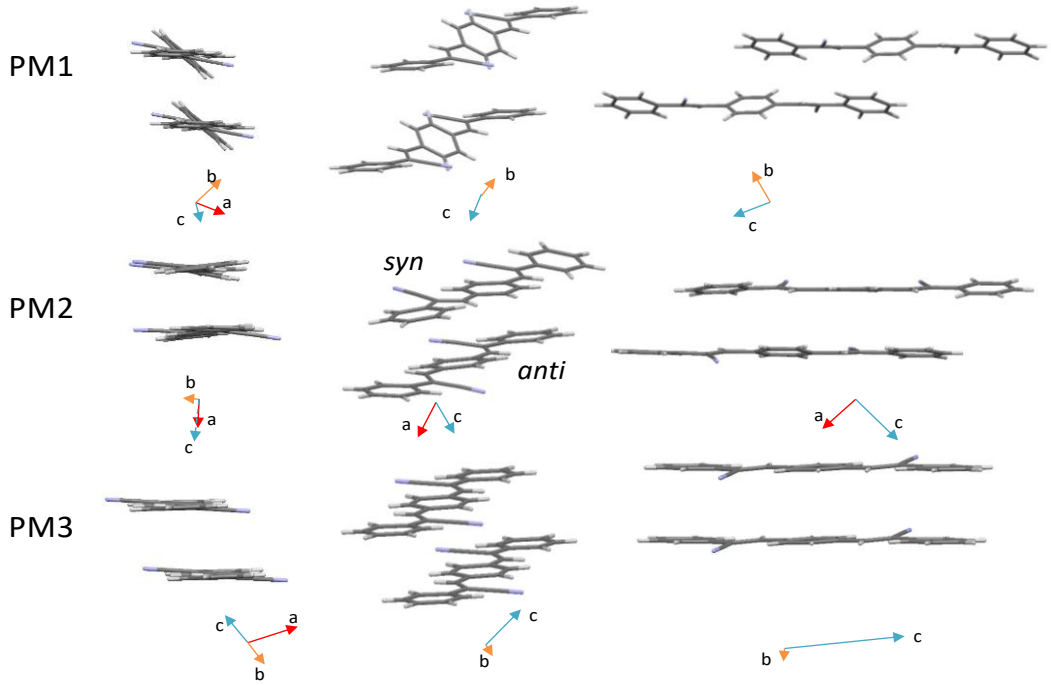

Figure 4.5: Single crystal X-ray structures of **β-DCS** in three different polymorphs: nearest neighbor arrangement for PM1 (CCDC 815708),[Xu12] PM2 (CCDC 860278),[Cha12] and PM3 (CCDC 1542079) along different view directions; crystallographic axes (a, b, c) and rotamers in PM2 (*syn*, *anti*) are indicated.

In PM1 and PM3, only *anti*-rotamers exist (i.e. with respect of the mutual orientation of the cyano-groups), while two different rotamers - *syn* & *anti* in a 1:1 stoichiometry coexist in PM2, which mainly drives the different structure of PM2 compared to PM1. The *intra*molecular twists in PM1 and PM2 are both quite pronounced (Table 4.6) with torsional angles $\phi_{i/o}$ around the inner/outer (i/o) single bonds of ϕ_i = 27º, ϕ_o = 17º in PM1 (*anti*), and $\phi_{i,1,2}$ = 7º, 6 º, $\phi_{o,1,2}$ = 7º, 14 º (PM2, *syn*) and $\phi_{i,1,2}$ = 7º, 16 º, $\phi_{o,1,2}$ = 10º, 10º (PM2, *anti*); in contrast, PM3 reveals a close-to-planar molecular backbone, i.e. ϕ_i = 4º and ϕ_o = 5º. The nearly planar structure of PM3 favors a side-by-side arrangement of neighboring molecules (A, B), showing a substantial π-π overlap with a π-π-distance of 3.5 Å in between, which is mainly driven by dipolar interactions of the CN group as shown in the electrostatic potential surfaces EPS (see Figure 4.6).

Table 4.6: Structural parameters for different conformations of **β-DCS**: symmetries, relative ground state energies (E_0); torsional angles ϕ_i/ϕ_o as defined in Figure 4.3, X-ray density ρ.

molecular conformation	**rotamer**	**symmetry**	**E_0 [a] / eV**	**ϕ_i / º**	**ϕ_o / º**	**ρ / g·mol^{-1}**
PM1 [b]	*anti*	C_i	0.048	27	17	1.25
PM2 [c]	*anti*	C_1	0.052	7 , 16	10 , 10	
	syn	C_1	0.073	7 , 6	7 , 14	1.26
PM3	*anti*	C_i	0.052	4	5	1.31
optimized [d]	*anti*	C_i	0	7	32	—
planar [e]	*anti*	C_{2h}	0.054	0	0	—

[a] calculated Hartree-Fock energies relative to the fully optimized one (for details see Chapter 3, Materials and Methods). [b] Ref. [Xu12]. [c] Ref. [Cha12].[d] fully DFT optimized [e] forced planar optimization.

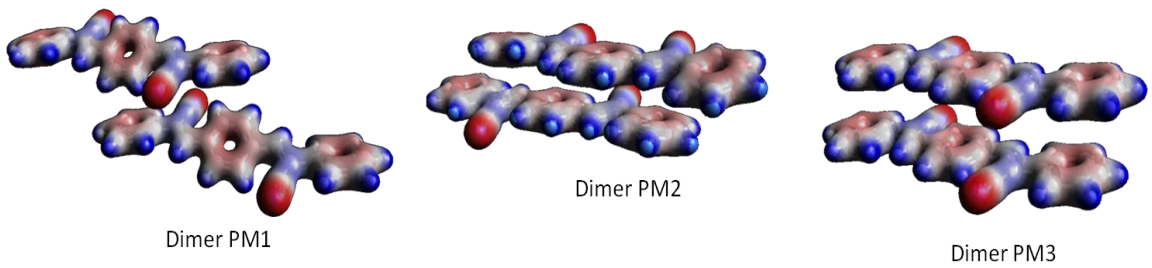

Figure 4.6: Electrostatic potential surfaces (EPS) for **β-DCS**'s polymorphs under study; nearest neighbor arrangements are displayed, calculated at the DFT (B3LYP/6-311G*) level of theory.

Consequently, the mutual shift of molecules A and B along the long axis (x-slip) and the short axis (y-slip) are distinctive, very small (ca. 0.6 Å) for the former while 1.5 Å for the latter, so that nitrogen N_A is placed on top of $C_{CN,B}$. For the twisted structure of PM1, such side-by-side arrangement is not possible, instead a 'micro-herringbone' structure is obtained, where the phenyl rings align in an edge-to-face arrangement with an inclined angle ca. 50º; in doing so unfavorable π-π interactions are reduced, giving rise to an anti-parallel alignment of the CN units, and a considerable x-slip (7.4 Å) that counts 36 % of the single molecule's length (20.3 Å). PM2, exhibiting a moderate twist, i.e. in between PM1 and PM3, realizes a π-stacked arrangement with an average π-π-distance of 3.3 Å and a x-slip of 3.6 Å (18%), which is an intermediate situation with respect to PM1 and PM3 and driven by the co-existence of *syn*- and *anti*-rotamers in PM2; this indicates a complex energetic interplay to balance the dipolar and π-π interactions.

The thermodynamic stability of certain polymorph can be evaluated by the free energy gain during this polymorph formation, the latter can be estimated from the X-ray densities ρ, which is so-called "density rule" defined in earlier works.[Ber02] As Table 4.6 shows, the gas-phase deposited PM1 and PM2 polymorphs exhibit almost identical densities $\rho \approx 1.25$ g/mol, indeed suggesting very similar thermodynamically stable situations. On the other hand, the solution-prepared polymorph PM3 reveals a significantly larger density $\rho = 1.31$ g/mol, suggesting PM3 as the most thermodynamically favorable polymorph.

So far, a clear correlation between molecular twist and crystal arrangement has been revealed, which is particularly pronounced, when the situation in PM1 (strong twist; strong x-slip) is compared with that in PM3 (very small twist; very small x-slip). Theoretical calculations for *inter*molecular arrangement simulation have been performed in the course of the investigations, where this correlation is pertinently reproduced. All the calculations were based on a multi-step crystalline domain approach, where local crystalline domains within an amorphous system are formed utilizing classical molecular dynamics (MD). The computational protocol were subsequently applied to two different molecular geometries, i.e. first the fully relaxed geometry as DFT optimized result (CLC1), which exhibits strong twists in outer part, and second the forced geometry (CLC2) as seen in PM3, which is nearly planar. Upon crystal formation using the method introduced above, two distinctively different arrangements have been obtained (Figure 4.7), which turned out to be quite similar to the X-ray results. The relaxed CLC1 adapts an *inter*molecular arrangement with a substantial x-slip, which is fairly similar to the situation in PM1. On the other hand, the close-to planar CLC2 adapts a very small x-slipped

*inter*molecular arrangement, which is very similar to the case of PM3. The calculated density of CLC2 is significantly higher than that of CLC1, which qualitatively agrees with the experimental results.

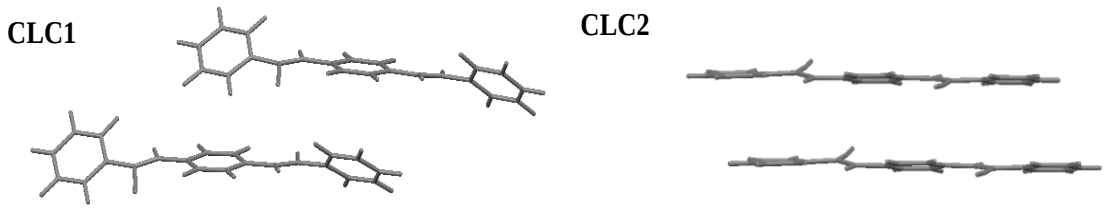

Figure 4.7: Calculated polymorphs of **β-DCS** (nearest neighbor arrangements are displayed): CLC1 was initiated from a fully relaxed structure; CLC2 was initiated from the molecular geometry found in PM3.

4.3.3 Twist Elasticity

As we have seen in the previous Section, both subtle changes in the substitution pattern as well as different preparation condition for the same compound, gave rise to widely varying molecular twists in the solid state, ranging from (partial or complete) planarization of the twisted **DCS** structures or even stronger twists. These phenomenological signs are the outcome of an inherent ability - "twist elasticity", which is particularly active in the class of **DCS**-compounds and provoked due to the cyano-vinyl synthon.[An12] Twist elasticity conceptually refers to the flexibility manifested in the intramolecular torsion when external stimuli such as packing confinement and preparation condition exert.[An12] Thus, the polymorphsim of **β-DCS** with the observed strong differences in molecular twists offers a unique example to reveal this concept. Qauntum-chemical calculations at the DFT level will be used to rationalize the origin of 'twist elasticity', which is seen as an essential point for the understanding of structure-property relationships in the **DCS**-type compounds.

In the parent backbone of **DSB**, as shown in Figure 4.4, a small sterical hindrance is present between the H-atoms in the vinylene unit and the central and terminal aromatic rings ($H_v \cdots H_{i,o}$ = 2.14 Å); the resulted stress on the molecular geometry can be easily compensated via slightly opening the vinylene bond angles from the 'ideal' angle of a sp^2 hybridized carbon (120°) to $\alpha_{i,o}$ = 127° without deforming the planarity.[Gie02] By doing so, a planar equilibrium geometry of **DSB** is realized in vacuum and solution, supported by DFT calculations;[Gie13a] this is a fact also confirmed indirectly through optical spectroscopy (see Section 4.4);[Gie02] though the average structure is non-planar, which is owing to the practical coexistence of differently

twisted conformations, the latter are realized by active thermal population along the torsional potentials which is broad and shallow around the vinyl-phenyl single bonds.[Gie02, Sri09] In single crystals of **DSB**, a planar structure is observed as well.[Wu03,Var13]

CN substitution in the outer vinylene unit forming **β-DCS** significantly enhances the sterical interaction with the neighboring H-atoms as mentioned in Section 4.3.1(Figure 4.4). A fixed CN group was artificially placed in the same position of **DSB** to check the situation of the introduced sterical hindrance, with a distance of 1.43 Å, that is the C-C_{CN} bond length found in the optimized **β-DCS**. In doing so, the non-bonded distance of CN group with the neighboring H_o/H_i atoms are both shorter than the van-der-Waals distance (2.6 Å), so that with the terminal ring is $C_{CN}\cdots H_o$ = 2.31 Å, while that with the central ring is $C_{CN}\cdots H_i$ = 2.02 Å, which confirms the consequence of a strong stress caused by CN substitution. Upon fully free optimization of **β-DCS** in the C_i symmetry point group, the enhanced sterical hindrance by the CN group is released via two distinctive pathways, i.e. open the bond angle of $\alpha_{i/o}$ a/o twist the dihedral angle of $\phi_{i/o}$. For reaching the optimal geometry of **β-DCS**, the inner vinyl-phenyl bond opens considerably with the bond angle α_i = 132º (against 120º of a sp^2 hybridized C atom). At the same time, the molecule twists slightly with a dihedral angle of ϕ_i = 7º, accompanied with the almost unchanged distance of $C_{CN}\cdots H_i$ = 2.42 Å against **DSB**, showing a preference of bond opening vs. twist. For the outer vinyl-phenyl bond, the angle opening is resisted by the remaining $H_{v,\alpha}\cdots H_o$ interaction, thus a preference of twist enhancement is observed. That is, the bond angle slightly opens to α_o = 122º, while the bond twist is sharply increased to ϕ_o = 32º along with a bond length increase from 1.461 Å in **DSB** to 1.487 Å (see Table 4.4), which relaxes the hindrance considerably to give a non-bonded distance close to the van-der-Waals value, so that $C_{CN}\cdots H_o$ = 2.57 Å. On the other hand, forced planarization of **β-DCS** (C_{2h} symmetry) exhibits a geometry with $C_{CN}\cdots H_i$ = 2.40 Å and $C_{CN}\cdots H_o$ = 2.42 Å, while α_i = 133º and α_o = 124º, which favors the two relaxation ways.

Comparing the calculated energies of different geometries (taken from x-ray results, forced planarization, fully optimization), the favorable geometrical relaxation under different torsional angles can be directly reflected. As Table 4.6 shows, the forced planar conformation is destabilized by only 0.054 eV (5.2 kJ/mol) against the fully optimized one; a similar situation occurs when the molecular conformations are calculated by fixing the torsional angles to those found in the X-ray analysis. In PM1, a destabilization of 0.048 eV (4.6 kJ/mol) is obtained, very similar to that in PM3 and *anti*-PM2 (both 0.052 eV; 5.0 kJ/mol); on the other hand, *syn*-PM2

gives a larger destabilization (0.073 eV; 7.0 kJ/mol) due to the specific orientation of the CN groups. These similar and small energy differences between different molecular conformations suggests that the largely different twists are equally favorable as a geometrical relaxation, particularly seen in PM1 and PM3, in all proving the twist elasticity concept in this class of compounds. In addition, the differential scanning calorimetry (DSC) analysis indicates a polymorph transition originated from the current PM3 (see Figure 4.8), supporting the existence of polymorphs with similar energetic stability.

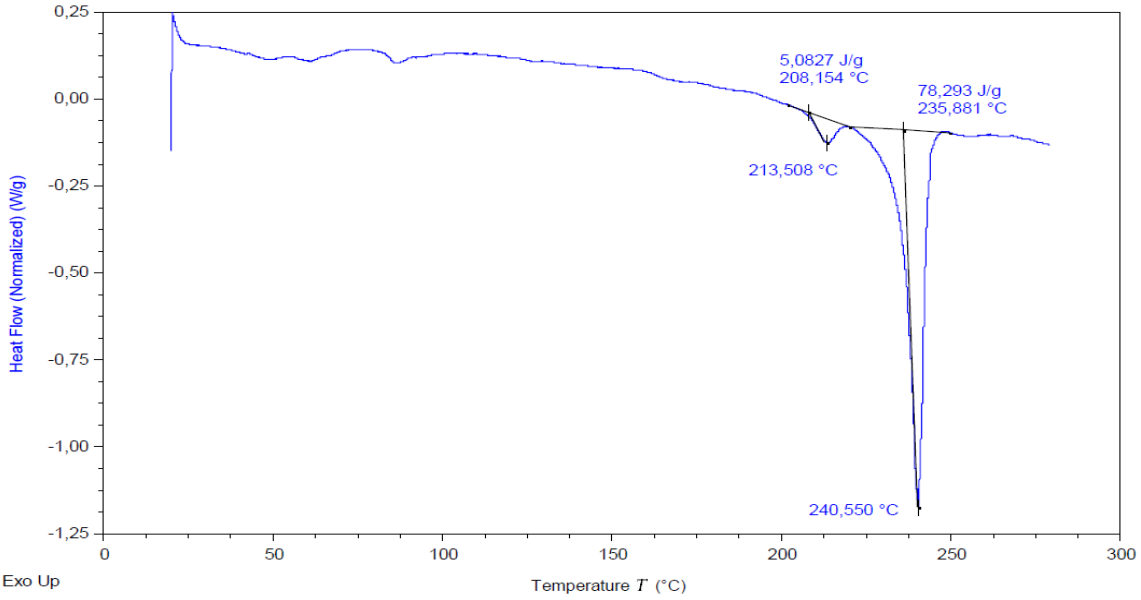

Figure 4.8: Differential Scanning Calorimetry (DSC) measurement of PM3; the endothermic peak at 241 ºC is assigned to the melting point; the peak at 214 ºC is tentatively assigned to a polymorph transition.

4.4 Elucidation of the Optical and Photophysical Properties in Solution

4.4.1 Spectral Properties

a) Positions and Intensities

In this section, the changes in position and intensity of the bands in optical spectra will be elucidated, between different **DCS**-compounds and against **DSB**, where the effect of specific substitution and positional variation (α vs. β) will be revealed. Before discussing the various properties in the **DCS**-compounds, the ones in parent compound **DSB** need to be recalled.

DSB. For the parent compound **DSB**, the spectral and photophysical properties in liquid solution are already clearly illustrated, see more details in a recent review paper.[Gie13a] As reproduced by our own measurements (Figure 4.1), there's one strong band dominating the visible range of

the absorption spectrum,[Oli17] which is describe by the allowed electronic transition of $S_0(1^1A_g) \rightarrow S_1(1^1B_u)$,[Gie02] the latter is mainly described by a one-electron excitation, i.e., the electron promotion principally occurs between the highest occupied to the lowest unoccupied MOs (HOMO→LUMO). In addition, there's a less strong shoulder positioning at the higher energy (4.1 eV) of the absorption spectrum, which arises from the symmetry-allowed transition $S_0(1^1A_g) \rightarrow S_2(2^1B_u)$ and the assignment is determined by spectral decomposition in the earlier reported paper.[Gie05] The experimentally recorded energy and oscillator strength for the vertical $S_0 \rightarrow S_1$ transition are reasonably well reproduced by the TD-DFT calculations, as seen in Table 4.7 and 4.8; according to the calculations, the transition dipole moment $\vec{\mu}_{01}$ is oriented along the long axes of molecule **DSB**, as displayed in Figure 4.4.[Gie05] The vibronically resolved PL spectrum together with the less structured absorption spectrum are revealing the situation about the changes in geometries and torsional potentials in the ground and first excited states. In fact, the equilibrium geometries in S_0 and S_1 are both planar, while the torsional potential in S_0 is much more shallower than that in S_1, which is due to a typical shortening of the (phenyl-vinylenne) single bond length when going from the ground to the excited state, which results from the loss of single bond's character in the excited state.[Gie02, Sri09]

Table 4.7a: TD-DFT calculated vertical transitions in absorption of the **DCS** series in **vacuum**: transition energies $E_{vert,abs}$, main composition (contributions > 5%; H = HOMO, L = LUMO) and oscillator strengths *f* of excited singlet states (S_1, S_2 and/or S_3) and triplet state (T_1). Energy difference ΔE is the higher excited singlet states/first excited triplet state with respect to the first excited singlet state. For MeO-compounds, **S** and **P** rotamers are given. **DSB** is listed for comparison.

Ci		**TD-DFT in vacuum**		
	$E_{vert,abs}$ / eV	**composition**	***f***	**ΔE**
DSB (C_{2h})	$S_1(B_u)$: 3.18	H-L (81)	1.81	
	$S_2(A_g)$: 3.88	H-1-L(55); H-L+1(45)	0.00	0.7
	$T_1(B_u)$: 1.89	H-L (91) H-1-L+1(6)	0.00	-1.29
α-DCS	$S_1(A_u)$: 3.22	H-L (100)	1.33	
	$S_2(A_g)$: 3.65	H-1-L(29); H-L+1(70)	0.00	0.43

	$T_1(A_u)$: 2.05	H-L (83)		-1.17
		H-1-L+1(13)		
α-DBDCS	$S_1(A_u)$:3.06	H-L(100)	1.59	
	$S_2(A_g)$: 3.47	H-1-L(47);	0.00	0.41
		H-L+1(52)		
	$T_1(A_u)$: 1.99	H-L (83)	0.00	-1.07
		H-1-L+1(12)		
α-S-MODCS	$S_1(A_u)$: 2.99	H-L (97)	0.41	
	$S_3(A_u)$: 3.77	H-1-L (96)	0.65	0.78
	$S_2(A_g)$: 3.31	H-L+1 (95)	0.00	0.32
	$T_1(A_u)$: 2.22	H-L (66);	0.00	-0.77
		H-1-L (13);		
		H-2-L+1 (16)		
α-S-MODBDCS	$S_1(A_u)$: 3.03	H-L (96)	0.70	
	$S_3(A_u)$: 3.64	H-2-L (94)	0.58	0.61
	$S_2(A_g)$: 3.37	H-2-L+1 (6.0);	0.00	0.34
		H-1-L (6.3);		
		H-L+1 (87)		
	$T_1(A_u)$: 2.19	H-L (71);		-0.84
		H-1-L+1 (16);		
		H-2-L (6);		
β-DCS	$S_1(A_u)$:3.03	H-L(100)	1.49	
	$S_2(A_g)$: 3.67	H-1-L(86);	0.00	0.37
		H-L+1(13)		
	$T_1(A_u)$: 1.81	H-L(91)	0.00	-1.22
		H-1-L+1(5)		

β-DBDCS	$S_1(A_u)$: 2.77	H-L(99)	1.51	
	$S_2(A_g)$: 3.24	H-1-L(95)		0.47
	$T_1(A_u)$: 1.71	H-L(88)	0.00	-1.06
		H-2-L(5)		
β-S-MODCS	$S_1(A_u)$: 2.65	H-L(96)	0.86	
	$S_2(A_u)$: 3.23	H-1-L(95)	0.55	0.58
	$S_3(A_g)$: 3.53	H-2-L(68);	0.00	0.88
		H-L+1(31)		
	$T_1(A_u)$: 1.61	H-L(92)	0.00	-1.04
β-S-MODBDCS	$S_1(A_u)$: 2.55	H-L(98)	1.28	
	$S_2(A_u)$: 3.09	H-2-L(97)	0.26	0.54
	$S_3(A_g)$: 3.19	H-1-L(91);	0.00	0.64
		H-L+1(7.7)		
	$T_1(A_u)$: 1.54	H-L(93)	0.00	-1.01

Table 4.7b: TD-DFT calculated vertical transitions in absorption of the **DCS** series in **$CHCl_3$**: transition energies $E_{vert,abs}$, main composition (contributions > 5%; H = HOMO, L = LUMO) and oscillator strengths *f* of excited singlet states (S_1, S_2 and/or S_3). Energy difference ΔE is the higher excited singlet states/first excited triplet state with respect to the first excited singlet state. For MeO-compounds, **S** and **P** rotamers are given. **DSB** is listed for comparison.

	TD-DFT in $CHCl_3$			
	$E_{vert,abs}$ / eV	**composition**	***f***	**ΔE**
DSB (C_{2h})	$S_1(B_u)$: 3.04	H-L(100)	2.00	
	$S_2(A_g)$: 3.88	H-1-L(60);	0.00	0.84
		H-L+1(39)		
α-DCS	$S_1(A_u)$: 3.12	H-L	1.50	
	$S_2(A_g)$: 3.62	H-1-L(17);	0.00	0.5
		H-L+1(82)		

α-DBDCS	$S_1(A_u)$: 2.95	H-L(100)	1.77	
	$S_2(A_g)$: 3.44	H-1-L(42);	0.00	0.49
		H-L+1(56)		
α-S-MODCS	$S_1(A_u)$: 2.89	H-L (99)	0.48	
	$S_3(A_u)$: 3.70	H-1-L (98)	0.79	0.81
	$S_2(A_g)$: 3.22	H-L+1 (97)	0.00	0.33
α-S-MODBDCS	$S_1(A_u)$: 2.94	H-L (97)	0.84	
	$S_3(A_u)$: 3.56	H-2-L (96)	0.70	0.62
	$S_2(A_g)$: 3.30	H-2-L+1 (5);	0.00	0.36
		H-L+1 (91)		
β-DCS	$S_1(A_u)$: 2.88	H-L(100)	1.63	
	$S_2(A_g)$: 3.60	H-1-L(92);	0.00	0.72
		H-L+1(6.4)		
β-DBDCS	$S_1(A_u)$: 2.62	H-L(100)	1.62	
	$S_2(A_g)$: 3.13	H-1-L(98)		0.51
β-S-MODCS	$S_1(A_u)$: 2.51	H-L(98)	1.01	
	$S_2(A_u)$: 3.15	H-1-L(98)	0.55	0.64
	$S_3(A_g)$: 3.49	H-2-L(76);	0.00	0.98
		H-L+1(23)		
β-S-MODBDCS	$S_1(A_u)$: 2.40	H-L(99)	1.43	
	$S_2(A_u)$: 3.01	H-2-L(98)	0.24	0.61
	$S_3(A_g)$: 3.09	H-1-L(96)	0.00	0.69

Table 4.7c: TD-DFT calculated vertical transitions in emission of the **DCS** series in **$CHCl_3$**: transition energies in $E_{vert,em}$, main composition (contributions > 5%; H = HOMO, L = LUMO) and oscillator strengths *f* of the first excited singlet (S_1) and triplet states (T_1). DFT-calculated adiabatic energies E_{adiab} are displayed. For MeO-compounds, **S** and **P** rotamers are given. **DSB** is listed for comparison.

C_i (TD-DFT) series	**α– CN**				**β– CN series**			
	$E_{vert,em}$ / eV	**composition**	***f***	**E_{adiab} / eV**	**$E_{vert,em}$ / eV**	**composition**	***f***	**E_{adiab} / eV**
DSB (C_{2h})	$S_1(B_u)$: 2.78	H-L	1.93	2.97		H-L		
	$T_1(B_u)$:1.89	H-L	0.00	1.46		H-L		
DCS	$S_1(A_u)$:2.68	H-L	1.56	2.90	$S_1(A_u)$:2.57	H-L	1.65	2.78
	$T_1(A_u)$:2. 04	H-L	0.00		$T_1(A_u)$:1. 81	H-L	0.00	0.84
DBDCS	$S_1(A_u)$:2.59	H-L	1.83	2.78	$S_1(A_u)$:2.40	H-L	1.73	2.57
	$T_1(A_u)$:1. 99	H-L	0.00	1.25	$T_1(A_u)$:1. 71	H-L	0.00	1.77
P-MODCS	$S_1(A_u)$:2.47	H-L	0.72	2.68	$S_1(A_u)$:2.33	H-L	0.73	2.48
	$T_1(A_u)$:1. 94	H-L	0.00		$T_1(A_u)$:1. 94	H-L	0.00	
S-MODCS	$S_1(A_u)$:2.46	H-L	0.55	2.70	$S_1(A_u)$:2.32	H-L	0.93	2.47
	$T_1(A_u)$:2. 22	H-L	0.00		$T_1(A_u)$:1. 61	H-L	0.00	
P-MODBDCS	$S_1(A_u)$:2.50	H-L	1.21	2.68	$S_1(A_u)$:2.28	H-L	1.20	2.50
	$T_1(A_u)$:1. 92	H-L	0.00		$T_1(A_u)$:1. 88	H-L	0.00	
S-MODBDCS	$S_1(A_u)$:2.48	H-L	1.00	2.72	$S_1(A_u)$:2.25	H-L	1.47	2.39
	$T_1(A_u)$:2. 19	H-L	0.00		$T_1(A_u)$:1. 54	H-L	0.00	

Table 4.8: Comparison of the allowed and forbidden vertical transitions in planar (C_{2h}) and nonplanar (C_i) geometries of the **DCS** series, calculated by TD-DFT in vacuum. For details: transition energy E and oscillator strength *f*; the first allowed excited singlet state in planar (1^1B_u) and nonplanar geometry (1^1A_u); the energy difference between the first dark and bright singlet states ΔE. For MeO-compounds, the second allowed excited singlet state (2^1B_u for planar, 2^1A_u for nonplanar) is given, the values with parentheses is of **P** rotamer. **DSB** is listed for comparison.

			E(1^1A_u) (*f*) / eV	**E(2^1A_g) (*f*) / eV**	**E(2^1A_u) (*f*) / eV**	**ΔE = E(2^1A_g) - E(1^1A_u)**
DSB		pl	3.18 (1.82)	3.88 (0.00)		0.70
α-DCS		pl	3.05 (1.46	3.56 (0.00)		0.51
		npl	3.22 (1.33)	3.65 (0.00)		0.43
α-DBDCS		pl	2.91 (1.72)	3.39 (0.00)		0.48
		npl	3.06 (1.59)	3.47 (0.00)		0.41
α-MODCS	**S**	pl	2.68 (0.95	3.28 (0.00)	3.32 (0.45)	0.60
		npl	2.99 (0.41)	3.31 (0.00)	3.77 (0.65)	0.32
	P	pl	2.86 (0.94)	3.39 (0.00)	3.51 (0.66)	0.53
		npl	2.90 (0.77)	3.37 (0.00)	3.58 (0.62)	0.47
α-MODBDCS	**S**	pl	2.65 (1.35)	3.22 (0.00)	3.29 (0.30)	0.57
		npl	3.03 (0.70)	3.37 (0.00)	3.64 (0.58)	0.34
	P	pl	2.83 (1.40)	3.35 (0.00)	3.48 (0.47)	0.52
		npl	2.88 (1.17)	3.34 (0.00)	3.53 (0.48)	0.46
β-DCS		pl	2.91 (1.60)	3.55 (0.00)		0.64
		npl	3.03 (1.49)	3.67 (0.00)		0.64
β-DBDCS		pl	2.68 (1.66)	3.20 (0.00)		0.52
		npl	2.77 (1.51)	3.24 (0.00)		0.47
β-MODCS	**S**	pl	2.55 (0.99)	3.40 (0.00)	3.14 (0.53)	0.85
		npl	2.65 (0.86)	3.53 (0.00)	3.23 (0.55)	0.88
	P	pl	2.59 (0.92)	3.45 (0.00)	3.26 (0.66)	0.86
		npl	2.81 (0.60)	3.62 (0.00)	3.53 (0.66)	0.81
β-MODBDCS	**S**	pl	2.48 (1.40)	3.13 (0.00)	3.05 (0.27)	0.65
		npl	2.55 (1.28)	3.19 (0.00)	3.09 (0.26)	0.63
	P	pl	2.52 (1.36)	3.18 (0.00)	3.14 (0.35)	0.66
		npl	2.76 (0.94)	3.42 (0.00)	3.35 (0.40)	0.66

The very small spectral shift in PMMA against $CHCl_3$ suggests that these two matrices are providing very similar polarizabilities.[Ege02] Furthermore, very similar spectral shapes in PMMA and $CHCl_3$ are observed for PL spectra, which is particularly the case for absorption. Giving that the rigidity of solid matrix should have a significant effect on narrowing the shape of the torsional potential along with giving more pronounced vibronic structure in the corresponding spectrum, the slight variation of spectral shape in PMMA against $CHCl_3$ above demonstrates that PMMA hardly affects the shape of the torsional potential in S_0, even it's quite shallow. Thus, PMMA matrix is thought to be solid but different from the really rigid and highly ordered environments such as perhydrotriphenylene; the latter can strongly steepen the shallow torsional potential in S_0 and sharpen the vibronic feature in the absorption spectrum of **DSB**.[Sri09] The point is that quite considerable free volume exists in PMMA; this makes it 'soft' relative to more rigid matrices (although certainly more solid compared to liquid solutions).

*Red-shifts in **DCS** and Computational Reproduction.* As seen in Figures 4.1, 4.9 and Table 4.1, generally red-shifted PL spectra against **DSB** are observed for all **DCS**-compounds in the α- and β-series, where the position of the strongest vibronic subband is used for the spectral shift comparison; the amounts of the red-shift vary largely upon the substitution pattern and position, showing a trend valid for both α- and β-series, i.e. the red-shift increases in the sequence **DSB** < **DCS** < **DBDCS** < **MODCS** ≈ **MODBDCS**, while α < β, see Figures 4.1, 4.9.

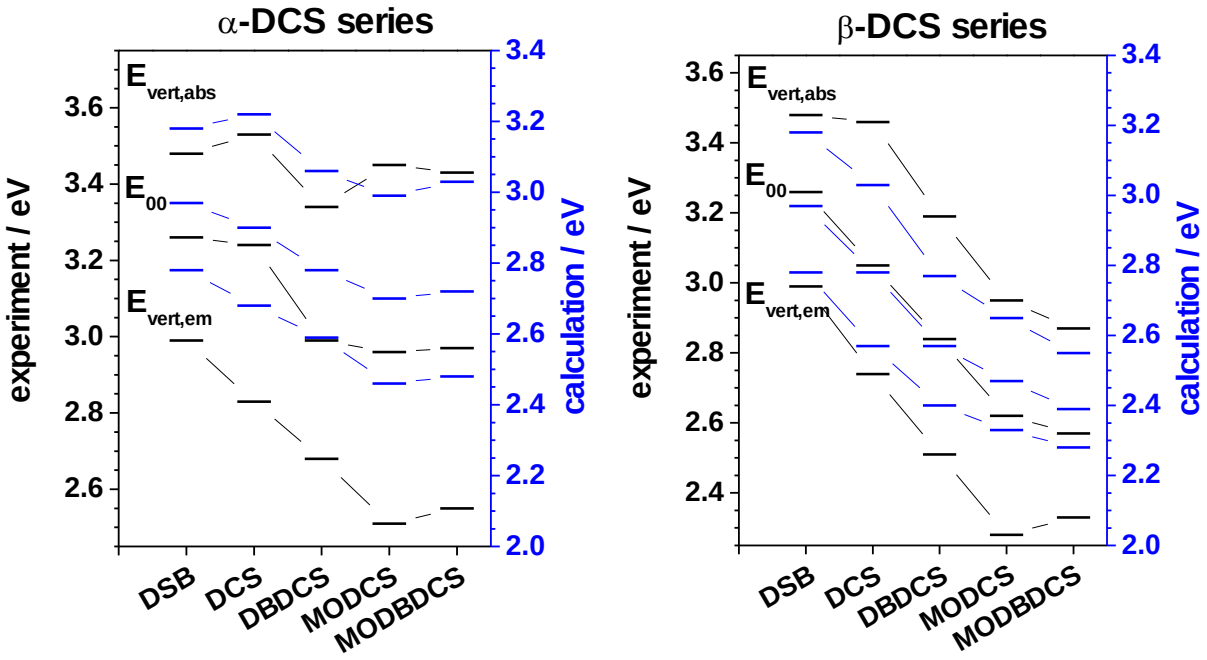

Figure 4.9: Comparison of experimental (black) and calculated (blue) adiabatic and vertical transition energies in absorption and emission (E_{00}, $E_{vert,abs}$, $E_{vert,em}$); for the TD-DFT data set, see Table 4.7 and 8.

This trend is also true for the electronic origin (adiabatic energy E_{00}), where the intersection point of the PL and the absorption spectra is used to determine E_{00}; compared to other methods (like using the onset or the apparent 0-0 band of PL),[Gie07] the intersection approximation best fits the situation here, that is variably shaped PL spectra for different compounds. The agreement between TD-DFT calculations and experiments is qualitatively well for the adiabatic energies; i.e., although the calculated values exhibit variation in the absolute position against the experimental ones, the trend of the red-shift upon substitution for both series is reasonably well reproduced, see Figure 4.9. On the other hand, for the vertical transitions, the agreement between TD-DFT calculations and experiments is rather poor, qualitatively and quantitatively, which is particularly seen in the emission; the reason is mainly found in thermal population effects, which will be discussed in more detail in Section 4.4.1 (b).

Substituent Effect: Sterical vs. Electronic. In some aspects, the **DCS**-compounds show similarities to **DSB**: like in **DSB**, the main absorption band for the entire **DCS** family arises from the symmetry-allowed $S_0(1^1A_g) \rightarrow S_1(1^1A_u)$ transition, the latter is dominated by a HOMO→LUMO excitation with a configuration interaction coefficient of > 95% (see details in Table 4.7); in addition, the transition dipole moment $\vec{\mu}_{01}$ of any **DCS**-compound under our investigation is oriented along the long molecular axes, essentially the same as that in **DSB** (Figure 4.4). Giving the clear and exclusive electronic transition picture, a simple analysis of the MOs (basically HOMO and LUMO) and of the geometries is expected to provide an essential understanding about the substituent effects, concerning both spectral shifts and spectral shapes.

In general, substituent effects are an interplay of two different factors, the sterical /geometrical effect and the electronic effect. While in experiment, the two effects are entangled, theory allows to disentangle the changes in geometry and electronic nature in our mind, to quantify their respective contribution. The sterical effect can be analyzed via the calculation upon forced planarization, the electronic effect involving inductive, mesomeric effects can be profiled by the energy variation of the MOs. Herein, the deformation of the planar system will break the conjugation and will thus blue-shift the spectra. For the electronic effect, the CN group exhibits a negative inductive (-I) and a positive mesomeric (+M) effects, while alkoxy groups exhibit a positive inductive (+I) and a positive mesomeric (+M).

The β-CN > α-CN Effect. With all the controlling parameters conceptually set, firstly the **β > α** red-shift effect of CN substitution is discussed as the most striking substituent effect on the

spectral properties. The **β > α** effect means that the red-shift of the **β**-series against **DSB** is much larger than that for the **α**-series; taking the **α**-/**β**-**DCS**-compounds for example, the red-shift in E_{00} of **β**-**DCS** against **DSB** from experiment is -0.21 eV, while it is just -0.03 eV for **α**-**DCS**. Although the CN group twists the molecular geometry significantly, this sterical change gives only a small influence on the electronic transition, which is revealed via similar S_1 state energies for forced planar and relaxed non-planar geometries by TD-DFT (ΔE = 0.04 eV, see Table 4.8). Thus, the main effect of the CN group is of electronic nature (ΔE = 0.14 eV). For elucidating the reason behind the **β**-CN **> α**-**CN** effect, the influence of the CN group on the electronic nature is revealed through MO analysis (Figure 4.10).

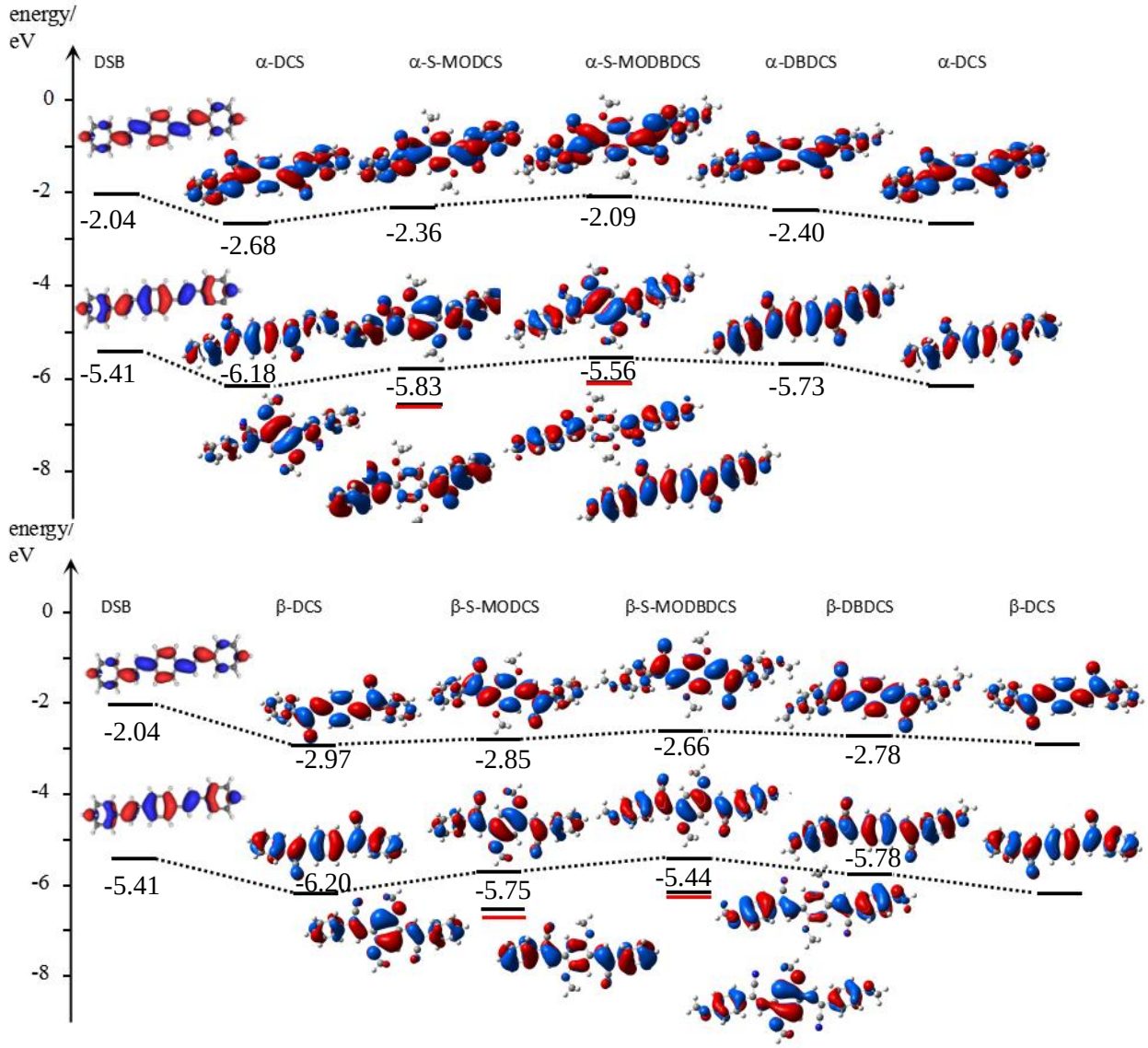

Figure 4.10: Electronic density contours (isosurface value 0.03) for the frontier orbitals of **α**/**β**-**DCS** series in vacuum. For compounds with MeO groups, HOMO-1 and HOMO-2 (in red) are involved. **DSB** is given for comparison.

As seen in Figure 4.10, the introduction of CN group in the vinylene units generally stabilizes both frontier MOs (HOMO and the LUMO) due to the negative inductive (-I) effect of CN, while the LUMO is stronger stabilized than the HOMO due to the positive mesomeric (+M) effect of CN on top. This results in smaller HOMO-LUMO energy gaps for the **DCS**-compounds against **DSB**, agreeing in trend with the red-shifts observed in experiment. This effect (stabilization LUMO > HOMO) is true, independent on the α- or β-position, while the stabilization of the LUMO is stronger when the CN substitution is done in the β-position of **DSB** compared to the α-position; this results in a large red-shift of the electronic transition for the β- vs. the α-series, which is in agreement with experiment. The stronger stabilization of the LUMO in the β- vs. the α-series can be explained through a resonance effect, termed as 'enhanced resonance stabilization' and abbreviated by ERS in the following, which is analogous to the well-known *para*-/*ortho*- vs. *meta*-effect in aromatic compounds.[Gor87] Simply speaking, the formulation of the probable resonance isomers for certain molecule is changed upon the position of the imaginary residential charges; here, more variety in the resonance structure gives rise to a larger stabilization in the total energy. Specifically speaking, when the negative charge resides on the carbon atoms, same number of zwitterionic resonance structures can be formulated in both CN-substitution cases, which stabilize S_1 of the α- and β-compounds equally. Differently, when the negative charge resides on the nitrogen atom, difference arises between **β-DCS** and **α-DCS** as shown in Scheme 4.3; in fact, the double number (i.e. eight) resonance structures can be formulated for **β-DCS**, while in **α-DCS** it's only four, in all stabilizing S_1 in the β-series stronger against that in the α-series.

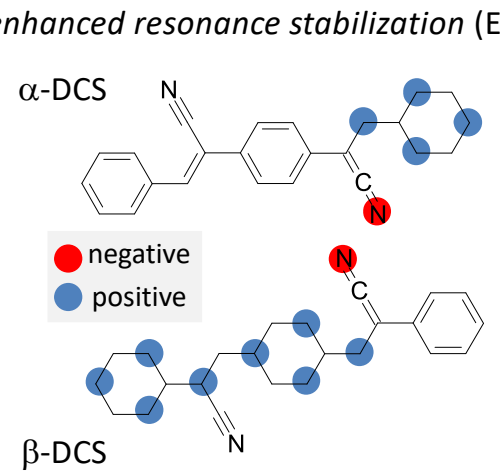

Scheme 4.3: Illustration of enhanced resonance stabilization (**ERS**): given in blue are the possible positions of the positive charge for **α-DCS** and **β-DCS** when the negative charge (red) is located at the nitrogen atom.

By now, the effect of the introduced CN group on spectral position has been described, i.e., red shifts the electronic transition and the shift differs depending on the substitution position (β > α); the reasons behind the effects have been elucidated clearly, i.e., the CN-induced red-shift is mainly due to the electronic effects (-I and +M) of CN itself, the positional dependence of this shift (β > α) relies on the strong resonance effect (ERS) in the configuration of the β-series.

MO vs. non-MO Effect Differing upon BuO's Presence and CN Position. After the effect of the primary CN substitution, the influences of the subsequent alkoxy substitution are discussed now, which includes not only the change in the spectral position but also the variation in the number and intensity of the absorption bands; again, the latter exhibits a positional dependence on α and β. For the same reason as for the CN group, the introduction of alkoxy-groups in the *para*-position of the terminal rings as well as the *ortho*-positions of the central ring additionally red-shifts the spectra, mainly due to the +M effect on top of the +I effect of the alkoxy groups; meanwhile a general destabilization of the frontier MOs is observed, e.g. if **MODCS** is compared with **DCS**. Noteworthy, methoxy-substitution in the central ring additionally splits the HOMO (see Figure 4.10) into HOMO and HOMO-1, which was discussed earlier in the literature.[Oel01] The MO splitting can generate two allowed electronic transitions, which correspond to the 1^1A_u and 2^1A_u states according to the TD-DFT calculation (see Table 4.7), in agreement with the experimental fact that two absorption subbands (denoted by A_1, A_2) are observed for the **MO(DB)**-compounds (see Figure 4.1). The oscillator strength (f_1, f_2) of the two subbands are basically comparable (though varying), which gives the characteristic 'camel hump' shape to the absorption spectra of the **MO**-compounds; see Figure 4.1.[Oel98] The ratio f_1/f_2 of the two oscillator strengths is differing depending on the presence of the extra butoxy substituents in the terminal ring, i.e., a higher f_1/f_2 ratio is observed in the **MODB**-compounds compared to **MO**-compounds, due to the influence of the introduced BuO groups on the electronic structure of the compounds; i.e., giving larger LCAO coefficients of the terminal rings in the frontier MOs. On the other hand, the ratio f_1/f_2 in **MO(DB)**-compounds is varying also depending on the substitution position of CN; i.e., the ratio is higher for β-CN substitution than that for α, see Figure 4.1. Differently from the BuO enhancement effect, which is mainly a electronic effect, the CN-positional enhancement effect is mainly a geometrical effect, i.e., driven by the sterical interaction of CN with the MeO groups; this is clearly demonstrated by comparing this ratio for different TD-DFT calculated geometries (planar v.s. nonplanar) between the α- and the β-series: in planar geometry calculations, the f_1/f_2 hardly exhibits any difference for α vs. β, as well as for **P**- against **S**-rotamers; while in fully optimized geometry

calculations, the f_1/f_2 shows significant differences. In fact, the **α-MO(DB)**-compounds give lower f_1/f_2 values than the **β**-analogues, and the S-rotamers exhibits lower f_1/f_2 values against the **P**-isomers, for details see Table 4.8. To a certain extent, the intensity change of f_1/f_2, as driven by the geometrical distortion, can be a indicator or a clue for the molecular twist and also the MeO orientation; for example, the lower f_1/f_2 ratio for **α-MO(DB)DCS** found in experiment can in turn be considered as a strong indication for the significant twists in **α**- vs. **β**-analogues The latter effect is clearly demonstrated by the calculated geometries; furthermore, it's a new argument for supporting the prevalence of the **S**-rotamer. The latter shows a much more distorted structure than **P**-isomers in the comparison of **α-MO(DB) vs. β**-analogues by the DFT calculations (Table 4.3), agreeing better with the experimental observations.

b) Spectral Shape

In this section, the variation in the spectral shape for all the compounds and in different matrices ($CHCl_3$ and PMMA; as described in Section 4.2) will be explained; the change of spectral shape in this context particularly refers to the resolution loss of the vibronic structure in the emission and absorption spectra. The corresponding illustration will be done mainly relying on the analysis of the calculated torsional potentials, to be specific, based on the torsional potentials' variation upon differing substitution and matrix.

Deviation between Theory and Experiment for $E_{vert.}$ As mentioned above, for the pure electronic transitions $E_{00,}$ the trends of substitution found in experiment are quite well reproduced by TD-DFT; while for the vertical transition energies $E_{vert,}$ an apparent mismatch of the calculations with experiment is observed for several compounds, as well as both for absorption and emission (Figure 4.9). Accordingly, the reorganization energies $E_{re,}$ which are related to E_{vert} by $E_{re} = |E_{vert}-E_{00}|$, are systematically underestimated by TD-DFT, as seen in Figure 4.9. For comparing the calculated and experimental E_{vert}, several points need to be noted. regarding how to extract the E_{vert} properly from the experiment spectra. Firstly, in this context, the PL and absorption maxima cannot be simply identified as the E_{vert} due to the asymmetric spectral shapes.[Gie07] The suitable method instead is to extract the emission E_{vert} from the experimental PL spectrum by eq. (4.1).[Gie02]

$$E_{vert} = \int E \cdot I(E)dE \,/\, I(E)dE \qquad (4.1)$$

Secondly, for the E_{vert} of emission, the integration operation according to eq. (4.1) can be directly done on PL spectrum, because the latter is directly due to the emission from S_1 to S_0; on the other hand, for the E_{vert} of absorption, integrating just the absorption spectrum cannot

avoid the integration over the higher excited states (i.e. S_n with $n > 1$). Therefore, a procedure introduced earlier is exploited to clean out the contribution of the higher vertical transitions in the absorption spectrum.[Gie05] For this, the PL spectra are first mirrored at E_{00} and then convolute with an exponential function, which accounts for the thermal population of low frequency torsional modes.[Gie02] In doing so, a convoluted spectrum is generated, which follows closely the low energy part of the absorption spectrum. Peforming the integration with eq. (4.1) on this spectrum gives then the absorption E_{vert} caused by the $S_0 \rightarrow S_1$ absorption. All E_{vert} values used for comparison in this thesis are extracted via this procedure.

Relation of Torsional Potentials and Spectral Shape. As pointed out in Section 4.2, for compound **DSB**, the loss of vibronic feature in the absorption spectrum is driven by a thermal effect. Similarly, the above discussed deviation between experiment and calculation for E_{vert} is ascribed to the thermal population of low frequency modes; in fact, the latter can (significantly) affect the transition energies, in particular the $E_{ver,}$ while in theory, this influence is not included in the computational scheme applied here, which gives the mismatch of theory with experiment. The absorption spectra of the **DCS**-compounds are entirely featureless, unlike the **DSB** case where the absorption spectrum is still slightly structured. This sharp contrast strongly indicates that the thermal effect become more important in the absorption of the **DCS**-compounds and gives rise to the spectra with no vibronic feature, see Figure 4.1. Furthermore, considering that the most striking difference between the **DCS**-compounds and **DSB** in the aspect of spectral shapes is the strong molecular twist along with shallow torsional potential surfaces, the strong thermal effect present in the **DCS**-compounds against **DSB** is probably driven by the changes in geometry, and thus of the torsional potential upon substitution. This has been confirmed in the cases of substituted oligothiophenes and polyphenylenevinylenes, which have been discussed previously; there, the thermal effect is ascribed to the flattening of the torsional potentials around the vinyl-phenyl bonds upon substitution.[Mac09,Mil16] For the **DCS**-compounds. which have the principal same structural motif as polyphenylenevinylenes, considerable twists in the ground state torsional angles are observed upon CN-substitution (Table 4.3). At the same time, very shallow torsional potential hypersurfaces of S_0 are observed compared to the already shallow potential in **DSB**, see Figure 4.11; due to the flattened torsional potential of S_0 upon CN substitution, thermal population of low frequency modes gives rise to less structured absorption spectrum.[Gie02]

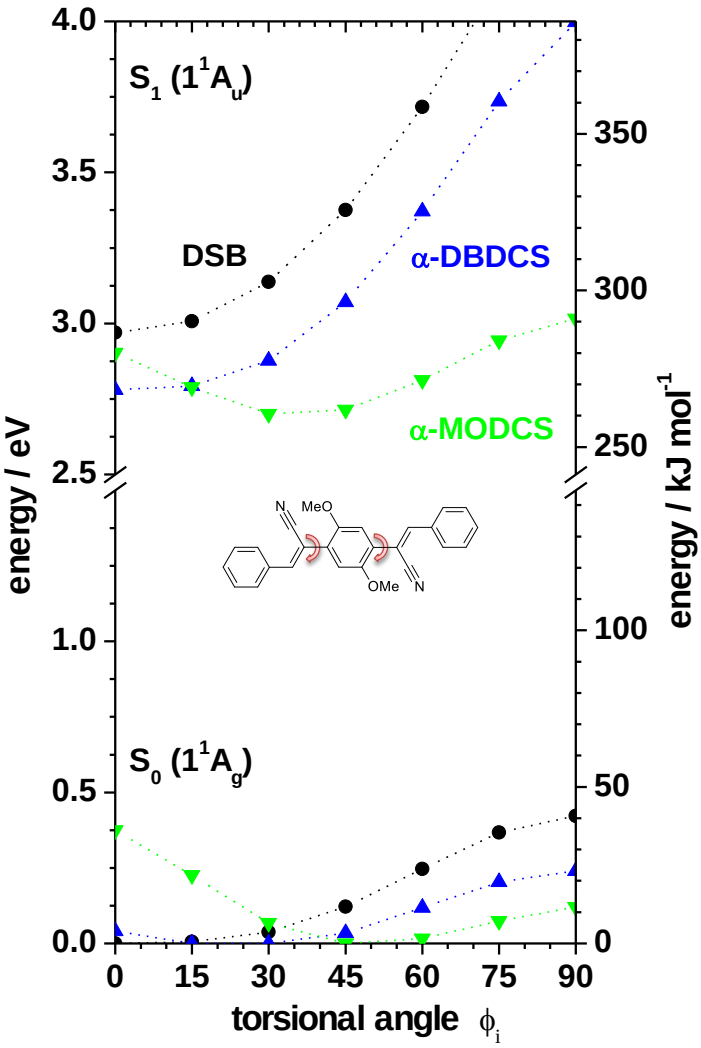

Figure 4.11: Torsional potentials around the inner vinyl-phenyl bonds ϕ_i for **DSB**, **α-DBDCS** and **α-MODCS** in the electronic ground state S_0 (1^1A_g), and the first excited singlet state S_1 (1^1A_u; 1^1B_u for **DSB**), calculated by TD-DFT (in vacuum).

Variation of the Torsional Potentials' Shape by Substitution and Matrix Effects. As just elucidated, for the **DCS**-compounds, the appearance of vibronic structure in optical spectra is closely connected to the shape of the torsional potential; the latter largely varies upon different substitution. This, as well as the electronic situation and the environment (i.e. fluid vs. solid solution), results in varying resolution of the vibronic features in absorption vs. emission.

The majority of the **DCS**-emission spectra are somewhat vibronically structured compared to the almost nonstructured absorption spectra (i.e. similar to **DSB**, which is ascribed to the largely reduced twists in S_1 ($\phi_{i/o}$ = 0-17°, Table 4.3), together with the steepened torsional potentials (Figure 4.11) compared to S_0.[Gie02, Mac09, Sri09] Compared to **DSB**, the **DCS**-compounds exhibit a general blurring of the PL spectra; the much sharper vibronic feature of **DSB**-PL is due to the

fact that the steeper S_1 torsional potential of **DSB** compared to the **DCS**-compounds; the blurring phenomenon of the **DCS**-PL spectra exhibits a distinct dependence on the presence of MeO groups and the position of CN group; in particular strong blurring effects in the PL spectra are observed for **α-MODCS** and **α-MODBDCS**; this can be specifically understood by the calculations for the case of **S**-rotamer in **α-MO(DB)**-compounds, where the twists remain particularly high in S_1 with ϕ_i = 31-36° (Table 4.3). This is due to the strong sterical interaction of the central MeO group with the **α**-CN groups, along with the flat torsional potentials, which are shallower than that for the other **DCS**-compounds for example **β-(DB)DCS** (Figure 4.11 and Figure 4.12). Because of the hypso- and bathochromic shifts induced by the flattened torsional potentials of S_0 and S_1, respectively, the Stokes shift could be considered as a sensitive measure for the overall molecular distortion.

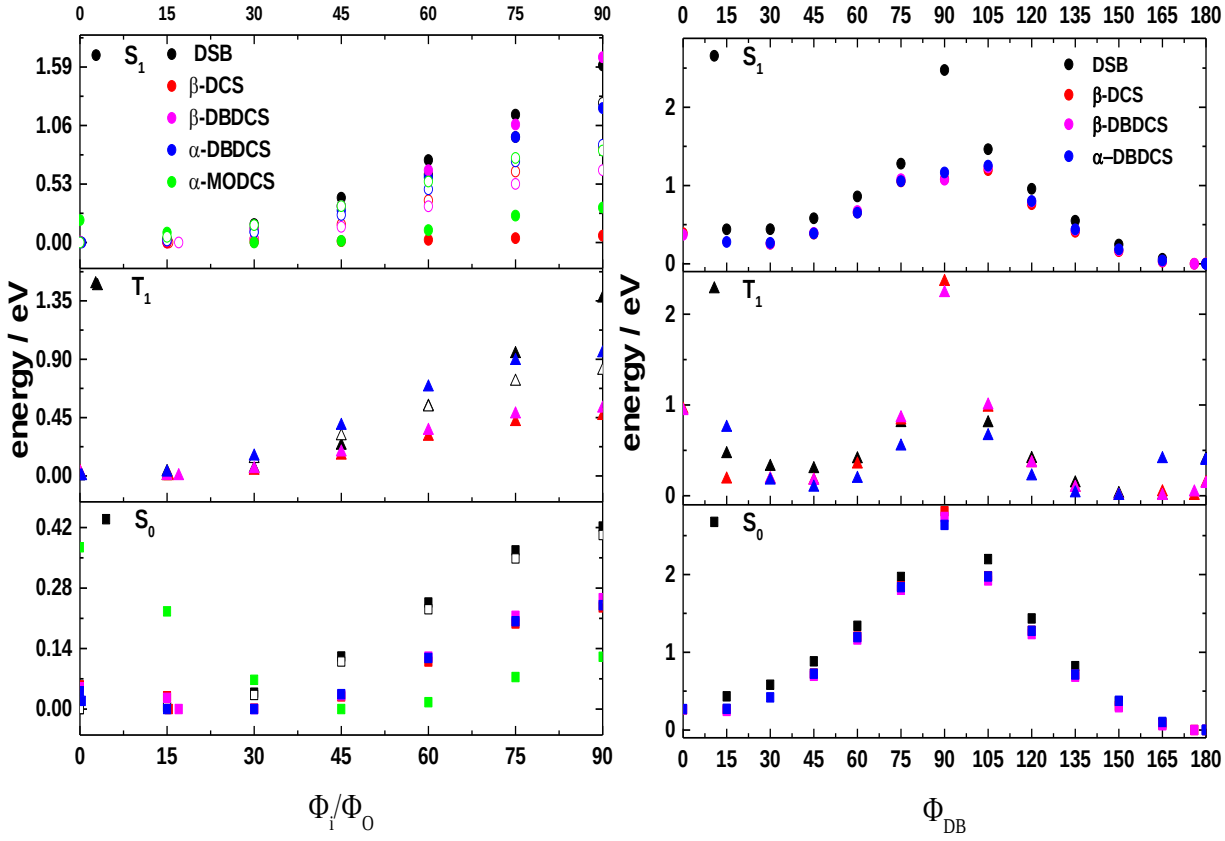

Figure 4.12: Torsional potentials for **DSB**, **β-DCS**, **α/β-DBDCS** and **α-MODCS** around the vinyl-phenyl single bonds (inner ϕ_i, solid symbols; outer ϕ_o, open symbols) and vinyl double bond (ϕ_{DB}) in the electronic ground state S_0 (1^1A_g; ■/□), the first excited triplet state T_1 (1^3A_u, 1^3B_u for **DSB;** ▲/△) and the first excited singlet state S_1 (1^1A_u, 1^1B_u for **DSB;** •/○), calculated by TD-DFT (in vacuum). See the data set in Table 4.9.

Table 4.9a: Torsion potentials around the inner/outer vinyl-phenyl bonds (ϕ_i/ϕ_o) for **DSB**, **β-DCS**, **β-DBDCS**, **α-DBDCS**, **α-MODCS** in the electronic ground state S_0, the first excited singlet S_1 and triplet T_1 states.

										ϕ_{opt}
ϕ_i/ϕ_o (°)			Torsional Potential /eV							(°)
			0	15	30	45	60	75	90	
DSB	I	S_0	0	0.006	0.038	0.12	0.25	0.38	0.42	0
		T_1	0	0.057	0.23	0.53	0.94	1.37	1.54	0
		S_1	0	0.038	0.17	0.41	0.75	1.16	1.60	0
	O	S_0	0	0.005	0.032	0.11	0.23	0.35	0.40	0
		T_1	0	0.032	0.13	0.31	0.53	0.73	0.81	0
		S_1	0	0.029	0.13	0.33	0.62	0.96	1.26	0
β-DCS	O	S_0	0.055	0.030	0	0.029	0.11	0.20	0.24	32
		T_1	0.033	0	0.042	0.16	0.30	0.42	0.46	13
		S_1	0.008	0	0.035	0.16	0.38	0.64	0.86	15
β-DBDCS	O	S_0	0.050	0.026	7.0E-5	0.032	0.12	0.22	0.26	30
		T_1	0.029	0.002	0.054	0.18	0.35	0.48	0.52	12
		S_1	0.008	3.1E-4	0.028	0.14	0.33	0.53	0.65	17
α-DBDCS	I	S_0	0.041	0.019	2.1E-5	0.034	0.12	0.20	0.24	29
		T_1	0	0.028	0.15	0.39	0.68	0.89	0.95	0
		S_1	0	0.013	0.097	0.29	0.59	0.95	1.22	0
α-MODCS	I	S_0	0.37	0.23	0.068	0	0.016	0.074	0.12	45
	I	S_1	0.20	0.089	0	0.014	0.11	0.24	0.32	30
	O	S_1	0	0.051	0.16	0.33	0.55	0.77	0.83	0

Table 4.9b: Torsion potentials around the vinyl double bond (ϕ_{DB}) for **DSB**, **β-DCS**, **β-DBDCS**, **α-DBDCS** in the electronic ground state S_0, the first excited singlet S_1 and triplet T_1 states.

ϕ_{DB} (°)	Torsional Potential / eV

															ϕ_{opt} (°)
		0	15	30	45	60	75	90	105	120	135	150	165	180	
DSB	S_0	-- [a]	0.43	0.58	0.88	1.34	1.97	4.14	2.20	1.43	0.82	0.37	0.093	0	180
	T_1	--	0.46	0.32	0.30	0.40	0.80	--	0.80	0.41	0.14	0.022	0	0.40	165
	S_1	--	0.44	0.44	0.58	0.86	1.28	2.47	1.46	0.96	0.55	0.24	0.062	0	180
β-DCS	S_0	0.27	0.27	--	0.73	1.20	1.85	2.81	1.98	1.28	0.72	0.31	0.069	0	179
	T_1	0.95	0.18	0.18	0.17	0.35	0.83	2.36	0.97	0.36	0.089	0	0.041	0.14	149
	S_1	0.39	--	0.25	0.38	0.65	1.05	1.08	1.20	0.76	0.41	0.16	0.027	0.004	176
β-DBDCS	S_0	0.27	0.25	--	0.70	1.16	1.80	2.74	1.92	1.23	0.69	0.29	0.06	0.002	178
	T_1	0.93	--	0.18	0.17	--	0.86	2.23	1.00	0.36	0.09	0.002	0.039	0.13	150
	S_1	0.37	--	0.26	0.39	0.67	1.08	1.07	1.23	0.79	0.43	0.17	0.03	0.003	176
α-DBDCS	S_0	0.27	0.27	0.42	0.72	1.19	1.84	2.64	1.97	1.27	0.71	0.38	0.10	8.9E-4	179
	T_1	--	0.75	0.17	0.09	0.19	0.54	--	0.66	0.22	0.029	0	0.41	0.39	150
	S_1	--	0.28	0.27	0.39	0.65	1.05	1.17	1.25	0.80	0.44	0.18	0.04	0	180

[a] -- indicates that the calculation could not be done due to the close distance between atoms under the frozen dihedral angles.

Thus, **DSB** shows a Stokes shift between PL and absorption of $\Delta E_{St} \approx 0.5$ eV, while it increases to 0.7 eV in **α-DCS** and 0.8 eV in **α-MO(DB)DCS** (Table 4.1); this is also true for **β-DCS**, while for the other **β**-compounds the Stokes shifts are ≤ 0.5 eV.

Finally, the solid matrix PMMA influences the absorption and emission spectra in a different manner for the various **DCS**-compounds in comparison with **DSB**; this concerns not only the vibronic structure but also the spectral positions of both maxima and onsets. For **DSB**, as pointed out above, PMMA hardly makes any difference for the absorption and emission spectra against fluid solution, particularly the very similar spectral onsets and absorption maxima for PMMA vs. $CHCl_3$ confirms our statement on similar polarizabilities and torsional potentials in both environments; the latter is ascribed to the considerable free volume in PMMA,[Wäs97] which allows for sufficient motion of the single bond torsions. For **DCS**-compounds, the spectral positions of absorption are again very similar in PMMA and $CHCl_3$. However, PMMA remarkably blue-shifts the PL maxima against $CHCl_3$; this effect is particularly strong for **α-**

MO(**DB**)-compounds**,** which also significantly enlarges E_{00} (Figure 4.1); on the other hand, PMMA generally blurs the **DCS**-spectra. These changes give indication of a flattening of the torsional potential. We ascribe this to some specific interactions with the polar environment of PMMA. The **DCS**-compounds with the both present both alkoxy and cyano functionalities might be more prone to such interactions due to the stabilization of polar resonance structures in S_1 state compared to S_0.

Trans-cis Isomerization ($CHCl_3$ vs. PMMA; α- vs. β-series); the Proof of Calculation. For the absorption spectra of the α-series in $CHCl_3$, with the time under illumination, an increase of absorbance for the band in the higher energy region (3.5-4.3 eV) is noticed, which gives strong evidence for a photochemical processes. This photoreaction is specifically assigned as *trans-cis* isomerization in the **DCS** context, with clear experimental evidence. In fact, according to earlier publications, *trans-cis* isomerization was found to be present in compounds with the same principal structural motif as in α-**MODCS**[Lan01] and α-**DBDCS**,[Mar16] in agreement with our observations. Furthermore, (TD)DFT calculations predict a blue shift of the main absorption band for the *cis*-isomer against the *trans* by ca. 0.3 eV (Table 4.10), reasonably agreeing with the energetic positions observed in experiment (Figure 4.1). Finally, it should be pointed out that the bands at higher energy exhibit (much) lower absorbance in PMMA compared to that in $CHCl_3$, while this influence is only strongly indicated in α-series and no any clue for β-series (Figure 4.1). In all, this suggests that cis-trans isomerization is a reaction which depends sensitively on the environment as well as on the CN-substitution position. It should also be stressed in this context that a *cis-trans* equilibrium can be reached only after 15 mins if under the irradiation of the mercury lamp in $CHCl_3$;[Lan01] thus, short-time illumination cannot effectively produce the *cis*-isomer, which we suppose is the same case for both two CN-series.

The environment dependence can be explained by the rigidity of the PMMA matrix, which inhibits such isomerization processes by exerting the restriction on large amplitude motions such as that driving the isomerization process, i.e. a twist around the vinylene doubles. On the other hand, the ineffective *cis-trans* isomerization in the β-compounds compared with the α-series is not mainly due to the short time of irradiation, as pointed out above, but probably due to the extended conjugation in the β-series, i.e. the prevalence of ERS. For better understanding this point, it should be reminded in this context that *trans-cis* photoisomerization was in particular observed in stilbene[Sal03] as well as its different derivatives (1-cyano and 1,1'-dicyano-stilbene),[Gul08, Van02, Yeh04, Dob16, Seo14, Chu13] however not in the longer conjugated

DSB,[San90] which in all indicates that extended conjugation is an important parameter which limits isomerization. Relied on this correlation, the ERS prevalence as discussed above can offer a plausible explanation for the difference in the α-/β-series; the longer conjugation caused by strong ERS stabilization of the β-compounds might effectively inhibit the isomerization. This argument is further supported by the calculation of ground state energies, i.e., the *trans*-isomers of the β-series is energetically much more stabilized against the α-series, which is particularly pronounced for the **MO**-compounds (Table 4.10).

Table 4.10a: (TD)-DFT (B3LYP//B3LYP) calculations of the ***cis*** vs. ***trans*** isomers: energy difference of the ground state energies $\Delta E(S_0)$ for ***trans-trans*** (*tt*) vs. ***cis-trans*** (*ct*) and **cis-cis** (*cc*). Vertical energy E and oscillator strength *f* of the first excited state S_1 for tt, ct and cc; energy difference of the first excited state energies $\Delta E(S_1)_{ct}$ for *tt* vs. *ct* and *cc*.

	$\Delta E(S_0)$ / eV		**$E(S_1)$ / eV (*f*)**						**$\Delta E(S_1)_{ct}$ / eV**	
	tt-ct	***tt-cc***	***tt***		***ct***		***cc***		***tt-ct***	***tt-cc***
DSB	-0.21	-0.41	3.18	(1.81)	3.33	(1.16)	3.48	(0.65)	-0.15	-0.23
α-DCS	-0.12	-0.23	3.22	(1.33)	3.35	(0.82)	3.50	(0.54)	-0.13	-0.28
α-DBDCS	-0.13	-0.25	3.06	(1.59)	3.18	(0.97)	3.33	(0.69)	-0.12	-0.27
α-MODCS	-0.06	-0.11	2.99	(0.41)	3.08	(0.26)	3.18	(0.15)	-0.09	-0.19
α-MODBDCS	-0.06	-0.13	3.03	(0.70)	3.14	(0.44)	3.26	(0.28)	-0.11	-0.23
β-DCS	-0.13	-0.25	3.03	(1.49)	3.13	(1.14)	3.25	(0.87)	-0.10	-0.22
β-DBDCS	-0.13	-0.24	2.77	(1.51)	2.86	(0.97)	2.94	(0.68)	-0.09	-0.17
β-MODCS	-0.15	-0.30	2.65	(0.86)	2.77	(0.72)	2.91	(0.60)	-0.12	-0.26
β-MODBDCS	-0.15	-0.29	2.55	(1.28)	2.68	(1.00)	2.82	(0.82)	-0.13	-0.27

Summing up the results of this section, the variation of spectral shapes among the different **DCS**-compounds, as well as in two environment have been elucidated; in solution, the blurring of absorption spectra is due to active thermal effect ascribed to the flattening of molecular twist along with the TORSIONAL POTENTIAL caused by the sterical effect of the introduced substituents. For PMMA we showed that considerable free volume is found, which allows for effective torsional motion; furthermore, we found indications for specific polar interactions. Both effects together were able to explain the varying spectral bandshapes among the compounds. The PMMA environment however inhibits large amplitude motions; for this reason,

cis-tran isomerization, which was clearly observed for the majority of the α-series in $CHCl_3$, is not seen in PMMA. The effectiveness of this photoreaction is limited in the β-series, which is ascribed to the extended conjugation by the ERS effect.

Table 4.10b: Torsions around the inner/outer vinyl-phenyl bonds (ϕ_i, ϕ_o) and vinyl double bond (ϕ_{DB}) in ***cis-cis*-DCS** series at ground state (S_0), calculated by DFT (in vacuum). For the MeO-substituted compounds, only **S** rotamers are given.

cis-cis	**α-DCS**				**β-DCS**		
	ϕ_i (°)	ϕ_o (°)	ϕ_{DB} (°)		ϕ_i (°)	ϕ_o (°)	ϕ_{DB} (°)
DSB (C_2)	34	36	7				
DCS (C_i)	50	27	7		25	52	7
DBDCS (C_i)	51	22	7		26	49	8
MODCS (C_i)	61	23	7		29	49	9
MODBDCS (C_i)	61	19	7		29	44	10

Table 4.10c: Torsions around the inner/outer vinyl-phenyl bonds (ϕ_i, ϕ_o) and vinyl double bond (ϕ_{DB}) in ***cis-trans*-DCS** series at ground state (S_0), calculated by DFT (in vacuum). For the MeO-substituted compounds, only S rotamers are given.

cis-trans	**α-DCS**				**β-DCS**		
	ϕ_i (°)	ϕ_o (°)	ϕ_{DB} (°)		ϕ_i (°)	ϕ_o (°)	ϕ_{DB} (°)
DSB	33/7	37/6	7/180				
DCS	48/31	29/9	7/179		26/4	51/31	7/179
DBDCS	47/32	24/7	8/179		25/4	49/31	8/178
MODCS	58/50	25/5	7/177		30/13	48/30	9/178
MODBDCS	61/50	17/6	7/177		29/14	43/27	10/177

4.4.2 Photophysics

As described in Section 4.2, the efficiency for PL as expressed by the PL quantum yield Φ_F varies largely among the **DCS**-compounds upon substitution pattern and position (MO vs. *non*-MO; α vs. β), as well as the matrix ($CHCl_3$ vs. PMMA), covering different degrees of emission

from hardly emissive to moderately and even highly emissive; indeed exhibiting SLE when going from fluid solution to PMMA. It should be stressed in this context, that the occurrence of SLE in PMMA is different, which cannot be properly described by the broadly known AIE effect, because this solid phase is free of aggregates; it is concurrently investigated here along with the SLE in single crystals (see next section) to prove the importance of *intra*molecular contribution to the solid state emission enhancement phenomenon. In this section, these significant changes of Φ_F for the different **DCS**-compounds and in different environments are firstly qualitatively rationalized, based on the investigation of the photophysics, i.e. the excited state deactivation processes (i. e. PL, IC, ISC, but also photoreactions); the driving factor of SLE in PMMA is elucidated, based on the quantitative analysis of k_r and k_{nr}. The probable scenario for the deactivation processes in **DCS**-compounds are pictured successfully by combining experiments with quantum chemical calculations, in particular for the prediction for conical intersection (CI), which plays, as will see, a central role in the deactivation processes.

Some points regarding the quantification and qualification for these processes need to be instructed individually before detailing the analysis and conclusion. Firstly, before performing the above analysis, the scope for the processes working on the deactivation needs to be determined; e.g. **DSB** is free of isomerization but not **DCS**. Secondly, the deactivation processes (i.e. photoreaction, PL, IC, ISC) are at different time scales and the dynamics (valued by the rate constants k) can be extracted by calculation based on pure experimental results (e.g. $k_{r,SB}$, k_r, k_{nr}; see eq. 4.2 and eq. 4.3a) or pure computation results (e.g. $k_{r,QC}$, see eq. 4.3b) or combing both (e.g. k_{IC}, k_{ISC}, see eq.4.4) using proper equations. Thirdly, the effectiveness of certain pathways can be identified only qualitatively by the proportion of rate constants or of the yields; e.g. how effective the radiative pathway can be suggested by quantum yield $\Phi_F = k_r/(k_r+k_{nr})$, while those for IC and ISC are identified by a relative efficiency φ(IC/ISC) obtained through the PAC experiments, see the details of PAC data analysis further down. Finally, the effectiveness of IC vs. ISC is closely correlated with the specific features of the CI; the pathway towards the CI is predicted based on a simple TD-DFT scheme, while the different accessibility to CI in **DCS**-compounds is deduced by applying Hammond's postulate. The electronic features of the CI which cannot be properly caught by (TD)DFT is obtained by a multi-reference method (CASSCF), see the details of method in Chapter 3.

*The Scenario for **DSB** Deactivation.* The **DSB** photophyics are well understood as reviewed in [Gie13a]. **DSB** in $CHCl_3$ solution shows strong fluorescence of Φ_F = 0.87 and relatively long lifetime of τ_F = 1.16 ns, pointing to a rather simple scenario for excited state deactivation. The

dynamics of the radiative and radiationless channels are quantified via eq. 4.2, giving k_r = 0.75 ns^{-1} and k_{nr} = 0.11 ns^{-1} (Table 4.11), proving the prevalence of the emitting pathway.

Table 4.11: Photophysical data of the **DSB** and the **DCS-**compounds in solution (sol.; $CHCl_3$) and single crystal (SC): PL quantum yield (Φ_F), PL lifetime (τ_F), radiative rate constant (k_r; from eq. 4.2), the ratio of radiative rates $R_r = k_r(SC)/k_r(sol)$ (eq. 4.8), radiative rates $k_{r,SB}$ according to eq. 4.3a (Strickler-Berg; SB) from the experimental spectrum, and from quantum chemistry ($k_{r,QC}$; eq. 4.3b), nonradiative rate constant in total (k_{nr}; from eq. 4.2) and the contribution from internal conversion part (φ_{IC}) and intersystem crossing part (φ_{ISC}) according to the PAC analysis (see Table 4.13).

	Class		Φ_F [a]	τ_F / ns	k_r / ns^{-1}	R_r	H/J [b]	$k_{r,SB}$ / ns^{-1}	$k_{r,QC}$ / ns^{-1}	k_{nr} / ns^{-1}	φ_{IC}	φ_{ISC}
DSB	C	sol.	0.87	1.16	0.75			0.67	0.59	0.11		
		SC	0.78 [c]	3.6 [c]	0.22	0.29	H_m			0.06		
α-DCS	A	sol.	$2\cdot10^{-3}$	$5.7\cdot10^{-3}$ [h]	0.35			0.51	0.34	175	0.63	0.37
		SC	0.90 [d]	2.1 [d]	0.43	1.23	H_w			0.05		
α-DBDCS	A	sol.	$2\cdot10^{-3}$	$4.0\cdot10^{-3}$ [h]	0.50			0.59	0.39	250	0.57	0.43
		SC	0.70	13.7	0.05	0.10	H_s			0.02		
α-MODCS	B	sol.	0.02	0.18	0.11			0.07	0.09	5.4	0.61	0.39
		SC	0.66 [e]	3.5 [e]	0.19	1.72	J_w			0.10		
α-MODBDCS	B	sol.	$3\cdot10^{-3}$	$13\cdot10^{-3}$ [h]	0.23			0.21	0.15	77	0.46	0.54
		SC	0.42 [e]	4.8 [e]	0.09	0.39	H_m			0.12		
β-DCS	B	sol.	0.01	$22\cdot10^{-3}$ [h]	0.45			0.35	0.36	45	0.62	0.38
		SC	0.69 [f]	9.5 [f]	0.07	0.15	H_s			0.03		
β-DBDCS	C	sol.	0.54	1.19 [i]	0.45			0.42	0.33	0.39	0.85	0.15
		SC	0.84 [g]	5.9 [g]	0.14	0.31	H_m			0.03		
β-MODCS	C	sol.	0.20	1.33	0.15			0.17	0.18	0.60	0.37	0.63
		SC	0.73 [e]	17.8 [e]	0.04	0.26	H_m			0.02		
β-MODBDCS	C	sol.	0.31	1.38 [i]	0.22			0.28	0.25	0.50	0.50	0.50
		SC	0.46 [e]	24.2 [e]	0.02	0.09	H_s			0.02		

[a] Φ_F was measured by the relative method for solution and by the absolute method for SCs. [b] w = weak, m = medium, s = strong. [c] Ref. [Var13]. [d] Ref. [Yoo11a]. [e] Ref. [Yoo13]. [f] Ref. [Shi17]. [g] Ref. [Var14]. [h] From ultrafast TA experiments (in dioxane); for details see Table 4.14. [i] Intensity-averaged, from bi-exponential fits of transient PL experiments; see Table 4.12 for details.

Table 4.12: Amplitude (A) and lifetime (τ) of multi-components and intensity averaged lifetime (τ_F) in different time-resolved measurements in solution ($CHCl_3$), PMMA and single crystals (SC).

	Class		A_1	τ_1	A_2	τ_2	A_3	τ_3	τ_F / ns
DSB	C	$CHCl_3$	1	1.16					1.16
		PMMA	1	1.29					1.29
α-DCS	A	$CHCl_3$ [a]							
		PMMA	0.30	1.18	0.70	0.38			0.84
α-DBDCS	A	$CHCl_3$ [a]							
		PMMA	0.14	0.62	0.86	0.14	25.18	2.95	0.58
		SC	1	13.67					13.67
α-MODCS	B	$CHCl_3$	0.63	0.021	0.10	0.33	0.27	0.106	0.18
		PMMA	0.47	2.41	0.53	1.02			1.95
α-MODBDCS	B	$CHCl_3$ [a]							
		PMMA	0.06	1.73	0.11	0.62	0.83	0.15	0.83
β-DCS	B	$CHCl_3$ [a]							
		PMMA	0.67	1.48	0.33	0.86			1.35
		SC	0.34	12.29	0.66	6.35			9.50
β-DBDCS	C	$CHCl_3$	0.94	1.02	0.06	2.33			1.19
		PMMA	1	1.43					1.43
β-MODCS	C	$CHCl_3$	1	1.33					1.33
		PMMA	0.62	2.48	0.38	1.28			2.19
β-MODBDCS	C	$CHCl_3$	0.87	1.41	0.13	0.23			1.38
		PMMA	0.84	1.85	0.16	1.17			1.77

[a] Lifetimes below the time-limit of the setup; derived by ultra-fast pump-probe measurement.

For comparison, k_r can also be calculated through the SB relationship ($k_{r,SB}$) according to eq. 4.3a, via integration over the first intense band of the absorption spectrum (A_1; see Figure 4.1). The thus determined $k_{r,SB}$ exhibits a very similar value to the measured k_r, indicating that the generated emission indeed originates from the bright A_1 (S_1) state. In terms of nonradiative deactivation processes, transient absorption (TA) spectroscopy caught a fast component of ca.10 ps (Table 4.14, see the details of TA data analysis in Appendix 3), which agrees well with the previous findings[Bho05, Gin08, Hsu05] and has been ascribed to the conformational relaxation of

S_1 from the initially excited Franck-Condon (FC) region.[Bho05, Gin08] Then S_1 continuously decays from the lowest vibrational energy level, mainly via internal conversion IC_{1-0} to the ground state; on the other hand, ISC to the triplet manifold[Gin05, Mar03] and *trans-cis* isomerization[San90] are very minor pathways.

$$\Phi_F = k_r \tau_F = k_r /(k_r + k_{nr}) \quad (4.2)$$

$$k_{r,SB} = 0.667\left[cm^2 s^{-1}\right]\left\langle \tilde{\nu}_F^{-3} \right\rangle^{-1} n^2 \cdot \tilde{\nu}_A^{-1} f \quad (4.3a)$$

$$k_{r,SB} = 0.667\left[cm^2 s^{-1}\right]\frac{\tilde{\nu}_{F,vert}^3}{\tilde{\nu}_{A,vert}} n^2 f \quad (4.3b)$$

*Classification of **DCS** Photophysics.* As already mentioned, the photophysical behavior of the **DCS**-compounds in fluid solution depends largely on the position of cyano-substitution (α, β), as well as on the presence (and position) of the alkoxy-substituents; in solid solution, enhanced Φ_F are obtained against liquid solution, i.e. a general SLE effect is observed, while the magnitudes of this effect change dramatically for the different compounds; see Figure 4.2 and Table 4.11. Thus, the photophysics of **DCS**-compounds exhibit a very large diversity, i.e. either by varying substitution (position, pattern) or by changing the environment, which complicates the analysis. In order to approach this problem systematically, we categorized all compounds under investigation into three classes according to the difference in photophysical behavior, via reasonably setting the limit for 'emissive' materials at about $\Phi_F \approx 0.1$ and 'highly emissive' at about $\Phi_F \approx 0.3$.

Class A: low emissive in fluid and solid solution; i.e. **α-DCS ≈ α-DBDCS**

Class B: low emissive in fluid solution, (highly) emissive in solid solution; i.e. **α-MODBDCS < α-MODCS < β-DCS**

Class C: (highly) emissive; i.e. **β-MODCS < β-MODBDCS < β-DBDCS**

The role of dark States. As done for **DSB**, the radiative and non-radiative rates k_r, k_{nr} for **DCS**-compounds are obtained from Φ_F and τ_F via eq. 4.2. This allows to elucidate whether the radiative or the nonradiative decay channel is mainly responsible for the low Φ_F in class A & B compounds. As seen in Table 4.11, both rates differ widely among the A & B compounds, i.e. k_{nr} = 5-250 ns^{-1} and k_r = 0.11-0.50 ns^{-1}. At a first glance, the latter variation might surprise for structurally similar compounds, and could indeed suggest participation of dark states in the

emission process (i.e. state switching for the different compounds). However, calculating the radiative rates through the SB relationships from the experimental spectra (eq. 4.3a) as well as from quantum chemistry (eq. 4.3b), the obtained values both match well with the ones extracted from Φ_F and τ_F above. This agreement clearly indicates that for all compounds the emission actually occurs from the bright state (1^1A_u) that is the one responsible for the strong absorption features, regardless of high or low Φ_F. This analysis is further supported by the observation of moderate Stokes shift, as well as the TD-DFT calculations which predict that the first dark state (2^1A_g) is well above 1^1A_u (see Figure 4.13).

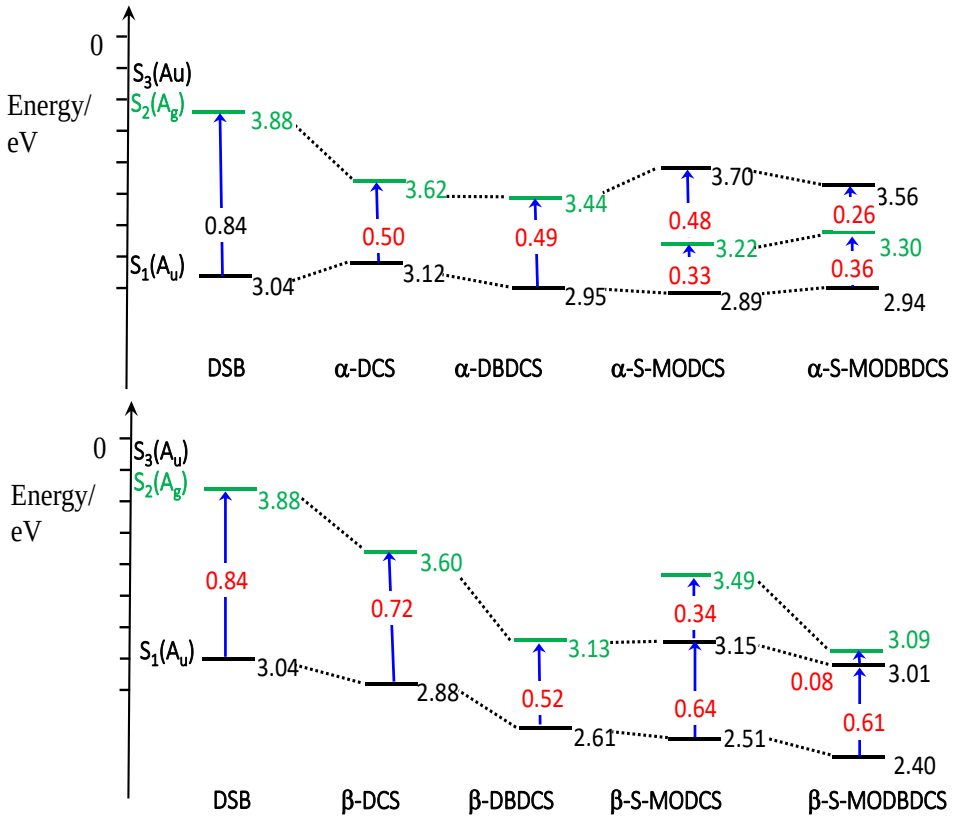

Figure 4.13: TD-DFT calculated vertical transition energies of **α/β-DCS** compounds under C_i geometry in $CHCl_3$. State switching of S_2 (A_u) and S_3(A_g) is observed for MeO-compounds in **β-DCS** series. **DSB** (C_{2h}) is given for comparison.

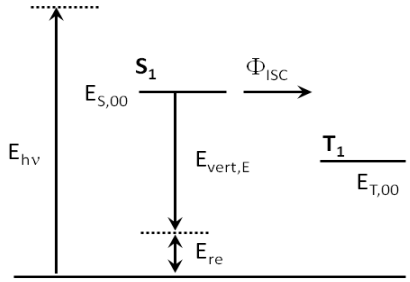

Scheme 4.4: Energy conservation for the detection of non-radiative processes.

The PAC data analysis is based on the energy conservation of all non-radiative processes, see Scheme 4.4. The respective equations for this process are

$$\Phi_{NR} \cdot E_{h\nu} = (E_{h\nu} - E_{S,00}) + (E_{S,00} - E_{T,00}) \cdot \Phi_{ISC} + E_{S,00} \cdot \Phi_{IC} + E_{re,S_0} \cdot \Phi_F \quad (4.4a)$$

and

$$1 = \Phi_F + \Phi_{IC} + \Phi_{ISC} \quad (4.4b)$$

so that

$$\Phi_{ISC} = \frac{(1 - \Phi_{NR}) \cdot E_{h\nu} - E_{vert,1-0} \cdot \Phi_F}{E_{T,00}} \quad (4.4c)$$

The values of all variables in eq. 4.4c and the results obtained are listed in detail in Table 4.13.

Table 4.13: Determination of k_{IC} and k_{ISC} from PAC exp. (E_{hv}, Φ_{NR}) via eqs. (4.4a-c); ΔE_{ST} was obtained from TD-DFT.

	E_{hv} / eV	Φ_{NR}	$E_{00}(S_1)$ / eV	$E_{v,em}$ / eV	Φ_F	τ_F /ns	k_r /ns^{-1}	k_{nr} /ns^{-1}	ΔE_{ST} / eV	$E_{00}(T_1)$ / eV	Φ_{IC}	Φ_{ISC}	k_{IC} /ns^{-1}	k_{ISC} /ns^{-1}
α-DCS	3.49	0.78	3.24	2.87	$2\cdot10^{-3}$	$5.7\cdot10^{-3}$	0.35	175	1.17	2.07	0.62	0.37	110	66
α-DBDCS	3.49	0.76	2.99	2.68	$2\cdot10^{-3}$	$4.0\cdot10^{-3}$	0.50	250	1.07	1.92	0.57	0.43	142	108
α-MODCS	3.49	0.75	2.96	2.51	0.02	0.18	0.11	5.4	0.77	2.19	0.60	0.38	3.3	2.1
α-MODBDCS	3.49	0.67	2.97	2.55	$3\cdot10^{-3}$	$13\cdot10^{-3}$	0.23	77	0.84	2.13	0.45	0.54	35	42
β-DCS	3.49	0.80	3.05	2.74	0.01	$22\cdot10^{-3}$	0.45	45	1.22	1.83	0.62	0.37	28	17
β-DBDCS	3.49	0.57	2.84	2.51	0.54	1.19	0.45	0.39	1.06	1.78	0.39	0.07	0.33	0.06
β-MODCS	3.49	0.64	2.62	2.28	0.20	1.33	0.15	0.60	1.04	1.58	0.29	0.51	0.22	0.38
β-MODBDCS	3.49	0.64	2.57	2.33	0.31	1.38	0.22	0.50	1.01	1.56	0.34	0.35	0.25	0.25

The Role of the Environment. For all **DC**S-compounds, Φ_F and τ_F increase when going from liquid to solid solution, i.e. PMMA (see Figure 4.2 and Table 4.12), which is a sign for a strong reduction of k_{nr}. In any case, the enhancement of Φ_F induced by the solid environment of PMMA is not as high as one might expect, which is evidenced by the moderate emission of B-type compounds (**α-MODCS**, **α-MODBDCS**) with Φ_F below 30%, and particularly by the low emission of A-type compounds (**α-DCS**, **α-DBDCS**) with Φ_F below 4%. These relatively weak enhancement effects suggest that PMMA doesn't effectively prevent the non-radiative decay as expected for a strictly solid environment; an effect which is assigned to the free volume

found in PMMA. The latter in fact provides cavity diameters of about 5.4 Å,[Wäs97] which doesn't allow for large amplitude motions of the molecules such as a complete cis-trans isomerization, while motions which are more restricted in space, e.g. restricted torsions around the vinyl-phenyl single bonds or the vinyl double bond should be still operative. Based on this argument, also considering that the structural difference between B- vs. A-type compounds is the presence of the methoxy-group at the central ring, the particular difference in the behavior of A- and B-type components is a clear hint that partial rotational motion of the central ring is involved in the nonradiative deactivation process; the latter will be proved further down. Compared to the A-type compounds, the rotational motion of the sterically more demanding central rings carrying the methoxy group in the B type compounds is better inhibited by the PMMA matrix, thus providing a relatively stronger SLE effect.

Nonradiative Processes in Stilbenoid Compounds. The case of *trans*-stilbene (TS), as one the most intensively studied systems in photochemistry, may shine some light to the nonradiative deactivation of **DCS**-compounds.[Lev07] Recalling the deactivation processes in TS, after reaching the bright S_1 state via photoexcitation, the primary step is a incent from the FC point along the torsional coordinate around the double bond ϕ_{DB}[Fus04] with a time constant of a few *ps*,[Bas96] which diabatically intersects with a doubly excited state. The latter descents with ϕ_{DB},[Han02] forming the main coordinate towards the 'phantom state',[Kov10] i.e. a kink-type conical intersection (CI), which might further involve a torsion around the singlet bond via a 'hula-twist' mechanism,[Fus04] to finally return to the *trans* or *cis* ground state. Thus, the intersection of the electronic states which is happening along specific torsional coordinates, effectively opens the nonradiative pathway towards the CI towards the ground state with significant configurational changes.

***DCS** Deactivation - an Initial Ultrafast Process.* As mentioned above, a short component was found in the excited state kinetics for **DSB** in solution with a time constant of 10 ps which was ascribed to torsional relaxation around the vinyl-phenyl bonds.[Bho05, Gin08, Hsu05, Gie13a] Differently, a significantly shorter process of time ca.1 ps was observed earlier in the excited state kinetics for **β-DCS**,[Cha12] which indicates that this process has more similarity to **TS** than to **DSB**, indeed suggesting that a CI might be involved in the deactivation process. For the **DCS**-compounds examined here by our *fs* TA experiments, a very short time constant of 0.4-0.9 ps was found for all **DCS**-compounds (Table 4.14), besides the main component which widely varies among the compounds to give diverse PL quantum yields as shown in Table 4.11. The similar sub-*ps* time constant among different **DCS**-compounds indicates that the initial step of deactivation is

essentially the same in the whole **DCS** family, independently on the consecutive step. Presumably, this primary step is a twist around the ϕ_{DB} in close analogy to TS. Furthermore, this analysis is supported by TD-DFT calculations which demonstrate that the double bond length for the **DCS**-compounds in S_1 is quite labile and of similar length with $r_{DB} \approx 1.40$ Å (Table 4.4); this bond is longer than the one in **DSB** ($r_{DB} = 1.38$ Å) due to the presence of the cyano-group, while in **TS** $r_{DB} = 1.42$ Å.

Table 4.14: Excited state lifetimes obtained from *fs* transient absorption studies via global fit analysis at sub 15 ps times (τ_1) and sub 400 ps times (τ_2).

	τ_1 / ps	τ_2 / ps
α-DCS	0.43	5.7
α-DBDCS	0.41	4.0
α-MODCS	0.91	190
α-MODBDCS	0.59	13
β-DCS	0.37	22
β-MODCS	0.92	> 400 ps
β-MODBDCS	0.57	> 400 ps

To test the initial steps of such scenario for the current case, we performed a torsional scan for ϕ_{DB} in S_1 (1^1A_u) around one of the two double bonds under full geometrical relaxation at the TD-DFT level, and calculated vertical emission energies to S_0 (1^1A_g) and to T_1 (1^3B_u) for each data point. In this context, it should be reminded that (TD)DFT anyway does not allow for a detailed description of the CI because of the multi-configurational nature of the CI; however, trends might be correctly reproduced as in fact shown for **TS**;[Han02] thus, a comparison between structurally similar systems like the compounds in **DCS** family should be possible and reasonable. Based on this argument, we investigated the path towards the CI using (TD)DFT for the two positional **DB**-isomers, where one is non-emissive (i.e. **α-DBDCS**), whereas the other one is emissive (i.e. **β-DBDCS**). Starting from the Franck-Condon region, i.e. with $\phi_{DB}(S_1) = 180^o$, a substantial energy barrier is seen when following the torsional scan in S_1, which thereafter descends towards a CI with the ground state potential S_0 at a torsional angle about 90^o (Figure 4.14). It is worth to point out that the ϕ_{DB} torsional motion requires substantial reorganization of the phenyl rings. For this reason, large differences in photophysical behavior between the MeO-substituted compounds vs. their non-substituted counterparts in solid PMMA

are seen, due to larger sterical requirements of the **MO**-compounds, as we discussed in the last subpoint.

***DCS** Photophysics - Access to the CI.* Comparing the torsional potentials along $\phi_{DB}(S_1)$ for **α-DBDCS** and **β-DBDCS**, the CI turned out to be essentially at the same position with respect both to the energy and twist angle. To further understand why the CI is so similar for the positional isomers, we explored the electronic nature of the CI. As (TD)DFT is not capable of providing a proper description of the CI due to its multi-reference character, CASSCF was used instead. Indeed, the frontier MOs (HOMO and LUMO) show a fundamental difference to the FC state (i.e. the *trans*-conformation); while in the latter the MOs are delocalized and of $\pi(\pi*)$ type character, the LCAO coefficients at the CI region are largely localized in the vinylene unit; furthermore, the localization is very different for the HOMO and the LUMO, giving the HOMO→LUMO excitation a strong charge-transfer (CT) character; see Figure 4.14. Due to the localized nature, the energy of the CI is essentially the same for all **DCS**-compounds. The access to the CI is controlled by the barrier height between the FC region and the CI. As seen in Figure 4.14, the barrier is considerably higher for **β-DBDCS** compared

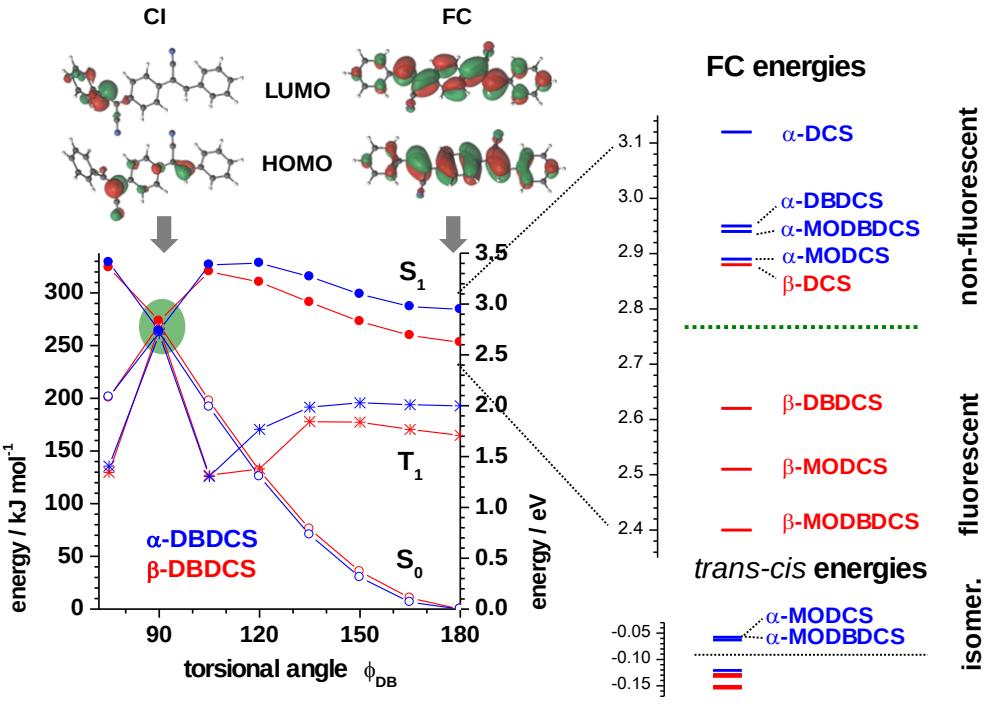

Figure 4.14: *Left*: TD-DFT rigid torsional scans of one double bond ϕ_{DB} for **α-DBDCS** and **β-DBDCS** using the optimized S_0 state in $CHCl_3$; S_0, S_1, and T_1 energies were computed for each data point. CASSCF calculated frontier HOMO- and LUMO-like orbitals which characterize the electronic structure for the CI and FC regions. *Right*: TD-DFT calculated FC energies ($E_{vert, abs}$) in $CHCl_3$, and DFT calculated ground state energies of *trans-trans* vs. *cis-trans*-isomers.

to α-**DBDCS**; therefore, the access to the CI is much easier for α-**DBDCS**, which rationalizes its faster non-radiative decay compared to β-**DBDCS**.

The differences in the barriers can be qualitatively understood from Hammond's postulate. This postulate is a hypothesis originally from physical organic chemistry, and used to predict the geometric structure of an intermediate formed in an organic chemical reaction. The idea is that smaller differences in energy between reactant/product and an intermediate implies the similarity in geometrical structure among them, and the interconversion reaction process between them will consecutively happen only involving a small structural reorganization. More specifically, if the CI is the same for all compounds, the thermodynamic stability of the primarily formed FC state ($E_{FC} = E_{vert,abs}$) will determine the barrier height of the reaction towards the CI and thus the rate. Recalling the discussion in Section 4.4.1, E_{FC} is essentially controlled by ERS, which lowers E_{FC} for the β-series compared to α-isomers. As shown in Figure 4.14, for all compounds in the α-series $E_{FC} \geq E_{CI}$ is found; this suggests poor thermodynamic stability of the FC point, and thus easier accessibility towards the CI and thus a faster nonradiative rate. This gives rise to low-emissive character in the α-series; on the other hand, the high-emissive compounds of the β-series (β-**MODCS**, β-**MODBDCS**, β-**DBDCS**) exhibit low energy with $E_{FC} \ll E_{CI}$, which explains the difference in quantum yields between two **CN**-series. A notable exception is β-**DCS**, where the stabilization of E_{FC} by ERS is insufficient due to missing further stabilizing substituents; thus, $E_{FC} \geq E_{CI}$ is still found, which makes β-**DCS** the sole low-emissive compound within the β-series. Accordingly, the SLE effect in PMMA matrix arising from the suppression of k_{nr} is ascribed to the restricted access to the CI due to the confined movements of double bond and phenyl rings in rigid PMMA, as described earlier for other related systems.[Pen16, Lon17]

The differences between α vs. β-series with respect to the occurrence/effectiveness of photoisomerization can also be rationalized by approximately applying Hammond's postulate. In analogue to TS case, the excited state of the **DCS**-compounds will relax via the CI towards the ground states exhibiting either *cis*- or *trans*- forms. We applied Hammond's postulate once again while in this case the energetic stability of the final product (i.e. *cis-trans, ct; trans-trans, tt* isomers) is the one that determine the barrier height of the reaction from the CI, as the CI is energetically fixed (see above). Thus, a comparison of the relative stability of the different isomers can explain the effectiveness of photoisomerization as a nonradiative channel (Figure 4.14). As seen in Table 4.10, the *tt*-isomer in the β-series is strongly stabilized against *ct* by ≥

0.13 eV; this inhibits isomerization and favors the *tt*-form. Differently, the stabilization in **α-MODCS** and **α-MODBDCS** is much less with a value of only 0.06 eV, which opens the channel for isomerization between *tt* and *ct*. This agrees with our (earlier discussed) signatures of *trans-cis* isomerization in the absorption spectra of **α-MODCS** and **α-MODBDCS**; see Section 4.4.1 (b) and Figure 4.1. Admittedly, some ambiguity is observed for **α-DCS** and **α-DBDCS**, which exhibit strong relative stabilization (0.12 **α-DCS** vs. 0.13 eV **α-DBDCS**) but anyway show effective isomerization; this indicates that these compounds may present borderline candidates, and additional kinetic factors have to be taken into account for these cases.

Finally, our investigation on the CI was also able to explain the results on high inter-system crossing efficiencies $\varphi_{ISC} = k_{ISC}/(k_{IC}+k_{ISC})$ which gave equal contributions for IC and ISC from the PAC experiments; see Table 4.11. In fact, investigating the T_1 energy along the ϕ_{DB} coordinate, the T_1 state intersects with the CI of S_0 and S_1. This is due to the strong CT character of the CI as a result of the strongly localized MOs (as mentioned above), because this reduces the exchange energy and thus the singlet-triplet splitting. This nicely rationalizes equally important IC and ISC deactivation pathways, despite missing heay-atom or n- π^* transitions.

In summary, in this section we discussed the excited state deactivation processes happening in **DCS**-type compounds in solution. The experimental results on diverse nonradiative deactivation effectiveness, i.e., emissive vs. non-emissive compounds, the occurrence of *trans-cis* isomerization, and IC_{1-0} vs. ISC process, were rationalized based on a simple TD-DFT scheme, applying Hammond's postulate. The decisive factor for the processes was figured out to be ERS. The latter controls both the emission color (due to the fact that ERS lowers the optical energy gap) and the photophysics (due to fact that ERS inhibits the accessibility towards CI and thus suppresses k_{nr}) of the entire **DCS** family. Similar to former studies on stilbene-like compounds, a CI was found, also here occurring along the torsional change around the double bond; this is mainly driven by the lability of the vinylene double bond in the excited state, which is not observed in the case of the parent **DSB** compound. A perspective regarding the CI description with respect to methodology and quality should be remarked. In fact, the precise theoretical description of the CI can only be achieved by a local, multi-reference representation; the latter is out of reach at the moment for large molecules as **DCS**-compounds, but will be subject of further investigations in the future. It should be further stressed in this context that simple 2-state normal mode representations based on harmonic oscillators, which were frequently done in the past, are apparently incapable to capture these ultrafast processes.

Furthermore, simple qualitative considerations as RIR are not able to explain the differences between the α- and β-series because they don't touch the core of the problem, i.e. the occurrence of the CI.

4.5 Elucidation of the Single Crystals' Properties

4.5.1 Spectral Properties

As described in Section 4.2.3, when switching the environment from the solution to the crystalline phase, significant changes in the emission spectral positions are found for all compounds. In general red-shifts are observed, however the amount of the shifts are distinctively different for the various compounds. Thus, while in solution, the fluorescence colors extend from blue to green, they extend down to the orange region in the crystals, giving a series of solid emission colors covering the whole visible range, see Figure 4.15. As especially stressed all through this thesis, the dramatic changes in the solid state emission are originated from the interplay of *intra*molecular and *inter*molecular contributions. However, a specification of the effective contributors and a quantification of these contributions are barely done, although this is crucial for an understanding of solid state emission. In this section, a full list of working factors is conceptually sorted out, and means for disentangling the contributions of different origins are designed. This is done by combining spectral analysis with TD-DFT calculations, where two contributions are separated and quantitatively identified, and the significance of both origins in solid emission color are qualitatively revealed.

*Identification of the Origins and Contributions of Spectral Shifts and Bandshapes in Solid Fluorescence Spectra. Intra*molecular and *inter*molecular factors concurrently impact the fluorescence in the solid state with respect to spectral positions as well as to bandshapes. Here we discuss four possible factors arising from *intra*- and *inter*molecular origins, and their contributions especially on the optical bandgap which manifests in the shift of the spectral positions. The first contributor of *intra*molecular origin, is the geometry of the compound, in particular twists of dihedral angles. Such twists distort the conjugation system and thus lead to hypsochromically (blue) shifts of the electronic transition by up to several hundred meV;[Mil16] on the other hand, these twists may additionally broaden the spectrum due to the active thermal population of a shallow torsional potential,[Mil16] which counteractely induces a bathochromic (red) shift of the emission maximum. Furthermore, for *inter*molecular origin, the three factors are identified, involving excitonic coupling, (anisotropic) polarizability effects as well as *inter*molecular vibronic coupling (excimeric effects). The excitonic coupling can be quantified

in the frame of a quantum chemically modified Kuhn model;[Gie13b, Gie16] the polarizability normally increases along with the refractive index found in the crystals compared to that in solution, and leads to stabilization of optical bandgap, i.e. a red shift in emission maxima; the vibronic coupling increases with the amount of π-π-overlap and leads to a general broadening and bathochromic (red) shift of the emission.[Gie04a]

The Geometrical (i.e. intramolecular) Contribution to the Spectral Shift. In solution, the emission colors of the **DCS**-compounds exhibit large variation among different **DCS**-compounds (i.e. upon the position of CN as well as the presence, number and position of alkoxy group), due to their significant impact on intramolecular structures with respect to the geometrical and electronic nature. Upon crystallization, significant bathochromic shifts are observed (Figure 4.15) and the emission colors are extended into the orange region (Figure 4.16), covering the whole visible spectrum. To quantify the crystal shift, we use the vertical energies of emission, $E_{vert,em}$, extracted from experimental PL spectra to express the emission color and thus the red shift from solution to the crystal (ΔE_{cryst}) :

$$\Delta E_{cryst} = E_{vert,em}(\text{crystal}) - E_{vert,em}(\text{solution}) \quad (4.5a)$$

As shown in Figure 4.15, the shifts (ΔE_{cryst}) vary to distinctive extent among the different **DCS**-compounds; for instance, it is negligibly small in **α-MODCS**, while it amounts up to 0.35 eV in **α-DBDCS** or **β-MODBDCS**. To explain these differences, the origin of the red shift needs to be analyzed.

As indicated in the case of **β-DCS**'s polymorphism (Section 4.3.3), possible planarization of the molecular backbone in the crystal as enabled through 'twist-elasticity' is partly contributing to the crystal shift. From the experiment side, this geometrical contribution cannot be isolated. Therefore, to quantify this intramolecular effect, we conducted TD-DFT calculations; the vertical transition energies of two calculated geometries of single molecules need to be compared. For this, TD-DFT excited state energy calculations were performed on the molecular geometry found in the X-ray crystal structure (represented by E_{vert}(monomer, crystal)), and then on the fully relaxed geometry (E_{vert}(monomer, relaxed)); for more details about computational procedure see Chapter 3 (Materials and Methods). In doing so, the energy difference resulting from the molecular geometry (ΔE_{geo}) can be extracted

$$\Delta E_{geo} = E_{vert}(\text{monomer, crystal}) - E_{vert}(\text{monomer, relaxed}) \quad (4.6)$$

In this definition, the sign of ΔE_{geo} reflects planarization ($\Delta E_{geo}<0$) or distortion ($\Delta E_{geo}>0$) of the molecular geometry when going from the isolated molecule to the crystal phase. As seen in Figure 4.15, negative ΔE_{geo} is observed for most of the compounds (**α-DBDCS**, **α-MODCS**, **α-MODBDCS**, **β-DCS**, **β-MODBDCS**) in the **DCS** family, which reflects (partial) planarization upon crystallization. This can be directly seen in the solid state arrangements extracted from the X-ray analyses (Figure 4.16) in relative to the fully optimized molecules. On the contrary, positive ΔE_{geo} is observed for **α-DCS**, **α-MODCS** and **β-DBDCS** due to stronger twists in the crystal compared to the free molecules. For comparison, **DSB** exhibits planar equilibrium structures in solution and in the crystal, thus $\Delta E_{geo} = 0$. Obviously, this calculated geometrical effect via eq. 4.6 can only partially explain the experimentally observed ΔE_{cryst} defined by eq. 4.5a, proving the concurrent importance of *inter*molecular effects for crystal spectral shift.

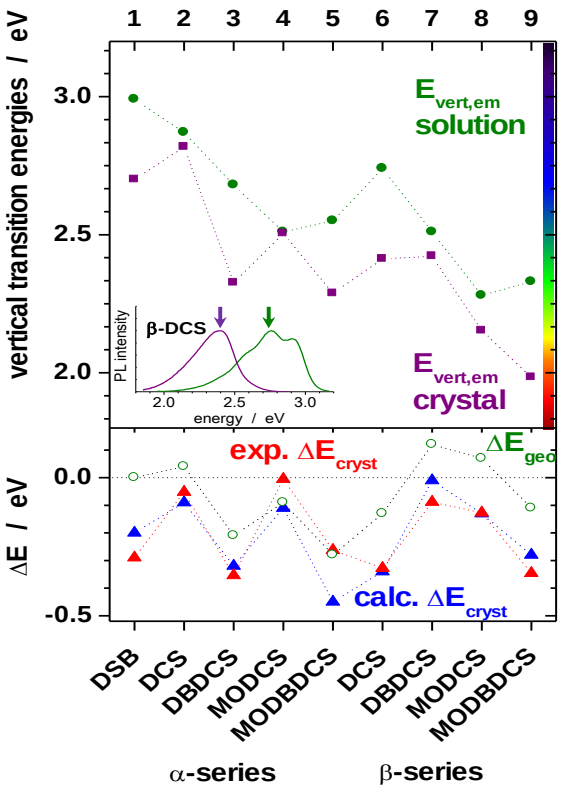

Figure 4.15: Crystal shifts of the **DCS**-compounds. Top: vertical emission energies E_{vert} in $CHCl_3$ (green circles) and in the single crystals (violet squares); references for compounds are 1: Ref. [Var13], 2: Ref. [Yoo11a], 3: Ref. [Yoo10], 4,5, 8, 9: Ref. [Yoo13], 6: this thesis, 7: Ref. [Var14]. Inset: emission spectra of **β-DCS** in $CHCl_3$ (green) and in single crystal (violet). Bottom: experimental (red) and calculated (blue) crystal shifts ΔE_{cryst}, and of the geometrical shift ΔE_{geo}; see eqs. (4.5, 6). The calculated values were obtained from monomer and dimer arrangements in the crystal vs. the fully optimized monomer; for details see Chapter 3, for the data set, see Table 4.15).

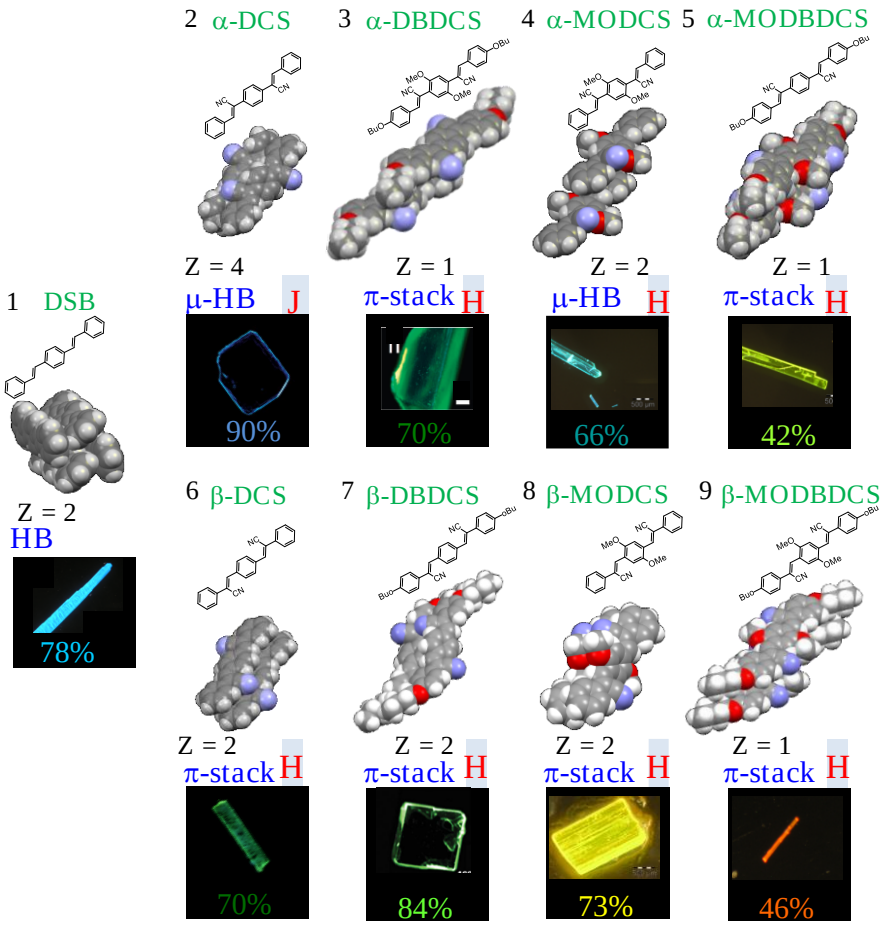

Figure 4.16: Overview on luminescent single crystals: nearest neighbor arrangements with molecules per unit cell (Z) from X-ray analysis, i.e. 1: Ref. [Var13], 2: Ref. [Yoo11a], 3: Ref. [Yoo10], 4,5, 8, 9: Ref. [Yoo13], 6: this thesis, 7: Ref. [Var14], type of arrangement (π-stacking, micro-/herringbone; μ-/HB), H vs. J-type coupling, fluorescence microscope images and quantum yields Φ_F (%).

The Electronic (i.e. intermolecular) Contribution to the Crystal Shift. As outlined in the beginning of this section, various intermolecular effects are operative in molecular solids, generally comprising excitonic,[Gie13a] polarizability,[Ege02, Hua11] and vibronic effects.[Gie04, Gie05] However, for the sake of computational simplicity, we concentrate here only on the excitonic effect, which we treat at a TD-DFT level in a simple nearest-neighbor approach, i.e. neglecting the effect of non-nearest neighbors.[3] To investigate this excitonic effect, again we calculated the vertical transition energies respectively for dimers in the arrangement taken from the X-ray

[3] As we have explained in Section 2.1.6, the excimeric effect originates from *inter*molecular contributions to vibronic coupling,[Gie04] and occurs for strongly -stacked systems which induce considerable charge-transfer contributions;[Gie05] this can be treated in an atomistic way through QMMM calculations as recently shown.[Wyk15a,Wyk15b] At the moment, however, this approach is costly, and thus beyond the goal of the current investigation.

analysis ($E_{vert}(S_1$, dimer)) and for the respective monomer using the fully relaxed geometry in vacuum ($E_{vert}(S_1$, monomer)); thus the energy differences (ΔE_{cryst}) induced by dimer formation are defined:

$$\Delta E_{cryst} = E_{vert}(S_1, \text{dimer}) - E_{vert}(S_1, \text{monomer}) \quad (4.5b)$$

It has to be stressed that the energy difference obtained in this way contains both the intramolecular geometrical effect as well as the intermolecular excitonic effect. The results based on quantum calculations via eq. (4.5b) reproduce well the experimental trends obtained according to eq. (4.5a) among the different compounds, as well as for available polymorphs of **α-DCS** and **β-DCS** (Figure 4.17), recommending this simple method for a fast screening of crystal shifts. It should be recalled in this context, that the experimental crystal shift ΔE_{cryst} contains the polarizability effect and non-nearest neighbor excitonic contributions, in addition to the geometrical and nearest dimer excitonic effects, which are however not considered in the TD-DFT calculations. Thus, a deviation in absolute position between the results from experiment and quantum calculation is expected, while a reasonable agreement between them is observed in Figure 4.15. This indicates that the (surely present) non-nearest neighbor effects are partly compensated by the polarizability changes when going from solution to the crystalline phase. In any case, it should be remarked that the polarizability effect can be estimated to not more than ~0.1 eV,[Ege02] i.e. relatively small against the calculated ΔE_{cryst} in most cases.

The electronic effect (ΔE_{ele}) can be separated from ΔE_{geo} in calculated ΔE_{cryst} by applying eq. (4.7a) $\Delta E_{cryst} - \Delta E_{geo}$, which is particular large for **β-DCS** and **β-MODCS** (Figure 4.15). This can be directly correlated with the magnitude of exciton coupling ΔE_{EC} in the dimer arrangement. In H-aggregates, ΔE_{EC} corresponds to half of the energy splitting between the lowest excited state S_1 and the S_f state which carries the most oscillator strength (Table 4.15), defined in forms of eq. 4.7b.

$$\Delta E_{EC} = \{E(S_f) - E(S_1)\}/2 \quad (4.7b)$$

As discussed in Section 4.3.1, for all **DCS**-compounds the transition which carries the oscillator strength is oriented along the long (x) axis of the molecule (Figure 4.4). Thus, if the shift of neighboring molecules along the x-axis is small (Scheme 4.2), ΔE_{EC} is expected to be large. It should be already noted here, that the results on the compounds with large ΔE_{EC} can partly support the kinetic analysis on H-aggregate formation leading to a decrease of radiative rate constant (see next Section); anyway, ΔE_{EC} is not the only decisive factor for the resulting

radiative rate constant as more factors such as trapping and aggregated-type Herzberg-Teller (AHT) coupling need to be take into account as well, as we will see there in next section.

Table 4.15: TD-DFT calculations on the fully relaxed monomer, on the monomer in the crystal geometry, and on nearest neighbor dimer arrangements: vertical transition energies and oscillator strengths (*f*) for monomers (lowest transition $E(S_1)$) and dimers (lowest transition $E(S_1)$, most intense transition $E(S_{max})$); the exciton coupling was calculated from $\Delta E_{EC} = E(S_{max}) - E(S_1)$, the crystal shift was calculated via eq. 4.5b.

		monomer, fully relaxed	**monomer, crystal**		**dimer, crystal**				
		$E(S_1)$ / eV	**$E(S_1)$ / eV**	**ΔE_{geo} / eV**	**$E(S_1)$ / eV**	**f_1**	**$E(S_{max})$ / eV**	**ΔE_{EC} / eV**	**ΔE_{cryst} / eV**
DSB		3.56	3.56	0	3.36	0.004	3.63	0.14	-0.20
α-DCS	PM1	3.69	3.73	0.04	3.60	0.02	3.79	0.09	-0.09
	PM2		3.48	-0.21	3.33	0.012	3.53	0.10	-0.36
α-DBDCS		3.53	3.32	-0.21	3.21	0.000	3.3	0.04	-0.32
α-MODCS		3.67	3.58	-0.09	3.56	2.00	3.62	0.03	-0.11
α-MODBDCS		3.65	3.37	-0.28	3.20	0.000	3.43	0.11	-0.45
β-DCS	PM1	3.42	3.46	0.04	3.43	0.001	3.60	0.09	0.01
	PM2		3.34	-0.08	3.12	0.012	3.37	0.13	-0.3
	PM3		3.29	-0.13	3.08	0.015	3.38	0.15	-0.34
β-DBDCS		3.24	3.36	0.12	3.23	0.017	3.45	0.11	-0.01
β-MODCS		3.03	3.10	0.07	2.90	0.000	3.18	0.14	-0.13
β-MODBDCS		2.94	2.83	-0.11	2.66	0.000	2.89	0.11	-0.28

Color Variation in Crystal Polymorphs (β-DCS, PM1 vs. PM2 vs. PM3). As discussed in Section 4.3.2 (b), three different polymorphs PM1-3 were observed of **β-DCS**. These polymorphs exhibit very different emission colors as shown in Figure 4.3; crystal shifts according to eq. 4.5a are plotted in Figure 4.17. In the following the analysis used for the **DCS**-compounds is applied to these polymorphs, investigating the different *intra*- and *inter*molecular contributions.

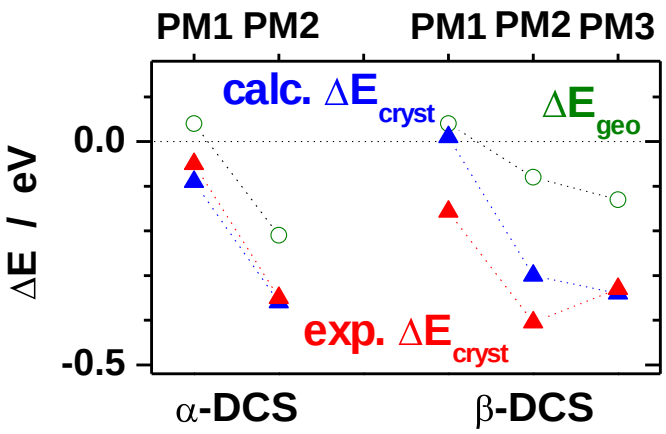

Figure 4.17: Experimental (red) and calculated (blue) crystal shifts ΔE_{cryst}, and geometrical shifts ΔE_{geo}; see eqs. (4.5, 6). The calculated values were obtained from monomer and dimer arrangements in the crystal vs. the fully optimized monomer; for details see Chapter 3). References for crystal values are **α-DCS**, PM1: Ref. [Yoo11a], PM2: [Xu16a,Xu16b]. **β-DCS**, PM1: Ref. [Xu12], PM2: [Cha12], PM3: this thesis.

Similar to the analysis of crystal shift for the entire **DCS** family, the effects here acting on the different polymorphs can be conveniently disentangled by calculating the lowest excited state S_1 of **β-DCS** in the monomer with different torsional conformations and in clusters in the different intermolecular crystal arrangements, as seen in Table 4.16. The calculated ΔE_{cryst} between different polymorphs are composed by the geometrical effect ΔE_{geo} and excitonic effect which can be quantified by ΔE_{EC} to some extent. The geometrical contributions ΔE_{geo} based on the monomer calculations obtained via eq. 4.6 is in fact large, leading to a significant bathochromic shift from PM1 (exhibiting strong twists) via PM2 to PM3 (practically planar) due to the reduction of the torsional angles (see Table 4.16). As seen in Figures 4.17, the calculated shifts are considerably larger to what was found in experiment, which indicates that this *intra*molecular effect is partially compensated in the solid state through excitonic effects, giving relatively similar positions for PM2 and PM3 while still blue shifted PM1 as discussed in Section 4.2.3. Recalling the discussion above (Section 4.3.2 (b)), in PM2 and PM3, a packing motif in a side-by-side arrangement of nearest neighbors with a small x-slip is found, suggesting H-type aggregation within the framework of the molecular exciton model;[Gie13b] In PM1, the x-slip is only 36 %, suggesting a weak coupling close to the inversion point of H-/J-aggregate.[4] The excitonic effect can be again qualitatively estimated from TD-DFT based

[4] As explained already in Section 2.1.6, it has to be once again stressed that the simple point-dipole approximation (PDA), as formulated in the classic molecular exciton model by Kasha largely fails for solid state samples, and

dimer calculations, which also here qualitatively reproduce the trends in ΔE_{cryst} as shown in Figure 4.17. Anyway, differences are observed in detail, so that we decided to include non-nearest neighbor interactions,[Gie09] i.e. extending the TD-DFT calculations to a clusters of 4 molecules (tetramers) prepared according to the X-ray structure analysis as described above in Section 4.3.2 (b). As seen in Table 4.16, the S_1 state of the calculated cluster is of similar energy for PM2 and PM3, while PM1 is hypsochromically shifted by 0.2 eV. This agrees qualitatively well with the experimental observation on the spectral positions of fluorescence (Figure 4.3 and Table 4.2), proving partial compensation of intra- and intermolecular factors (again stressing the interplay of intramolecular and intermolecular contributions on fluorescence behavior). Although the effect of polarizability change is not considered in this type of calculation, it's however not expected to be distinctively different among different polymorphs, as parallel packing of neighboring molecules is observed in all three polymorphs (Figure 4.5); therefore, rather similar anisotropic polarizabilities should be expected. Furthermore, the spectral broadening observed for PM2 and PM3 against PM1 is also ascribed to intermolecular interactions, exhibiting very substantial π-π overlap, similar to other **DCS**-based systems.[Gie13b, Var16]

Table 4.16: TD-DFT calculations on the different monomers and clusters (tetramers): vertical transition energies and oscillator strengths (*f*) for monomers (lowest transition $E(S_1)$) and clusters (tetramers; lowest transition $E(S_1)$, most intense transition $E(S_{max})$); the exciton coupling was calculated from $\Delta E_{EC} = E(S_{max}) - E(S_1)$.

	monomer		tetramer					
	$E(S_1)$ / eV	f_1	$E(S_1)$ / eV	f_1	$E(S_{max})$ / eV	f_{max}	ΔE_{EC}	ass. [a]
PM1	3.46	1.60	3.29	0.001	3.47	5.44	0.08	wH
PM2 [b]	3.34	1.68	3.11	0.003	3.50	3.03	0.20	H
PM3	3.29	1.70	3.03	0.015	3.41	3.31	0.19	H

[a] assignment: J-aggregate, (weak) H-aggregate. [b] *anti*-conformer.

In this Section, two cases, i.e., the crystallization caused spectral shift in **DCS** family as well as the polymorphism-induced spectral shift in compound **β-DCS** were both elucidated, revealing

arguments on the H/J-inversion by the so-called magic angle value (54.7°) derived from the PDA model are inappropriate in such systems.

four concurrent factors working together on the solid state emission spectra. For the flexible **DCS**-type compounds, the main *intra*molecular contribution is driven from the geometrical torsion enabled by twist elasticity, resulting in red- or blue-shifts due to planarization or twisting vs. the free molecules. For the *inter*molecular part, the excitonic effect was quantified at the TD-DFT level of theory considering nearest-neighbor interactions. The results from this type of calculations also comprise the geometrical effect, but subtracting the geometrical contributions done before the excitonic part can be extracted. Polarizability effects were neglected, justified by their rather minor contribution and their partial compensation by non-nearest neighbor interactions. Doing investigations in such way, the trends of emission maxima observed in experiments are reasonable well reproduced by quantum calculations, recommending the latter as a qualitatively good screening method for spectral shift analysis. The concurrence and equal importance of intra- and intermolecular contributions were stressed by our investigations.

4.5.2 Photophysics

Similar to the significant changes in the emission colors (i.e. $E_{vert,em}$), the emission efficiency Φ_F also vary largely when going from solution to single crystalline phase (see Section 4.2). In particular, stronger SLE effects are seen compared to the case in PMMA, in all giving a series of highly emissive crystal materials with Φ_F = 42-90% (see Figure 4.2). Different from the SLE in PMMA, SLE in these crystal has two concurrent origins like the crystal shifts discussed in the last section, i.e., *intra*- and *inter*molecular contributions; here, the SLE is dictated by two factors, the possible increase of k_r and/or the decrease of k_{nr}, as Φ_F contains both contributions (see eq. 4.2). Generally, the *intra*molecular factors such as suppressed molecular motions and defined geometries by external restrictions can generate a large reduction of k_{nr} and sometimes a small increase of k_r, being an important source of SLE; on the other hand, the *inter*molecular interactions, which may give rise to J-type aggregates, can significantly increase k_r, bearing an important contribution for SLE. It should be once more reminded, that due to the complexity of SLE, the use of the popularly anticipated RIR picture cannot reveal the actual driving force for SLE due to it's simple qualitative considerations. In contrast, in this section, we develop a quantitative analysis of the two rate constants derived from Φ_F and τ_F to reveal the origin of SLE in the different compounds. For the *inter*molecular part, a qualitative criterion for the assignment of H-/J-type aggregation in single crystal is proposed, which relies on the experimental radiative rate constants evolution from solution to the single crystals. Making use of this new measure, the aggregation type as well as the degree are qualitatively determined for

all compounds under investigation including the different polymorphs of **β-DCS**; this is further examined by (TD)DFT calculations based on a dimer assemble scheme focusing on excitonic effects.

Intramolecular Contributions to SLE in the Single Crystals. As detailed in Section 4.4.2 on the photophysics of the **DCS** family in solid solution (PMMA), solid environments commonly enhance the fluorescence via suppressing the nonradiation decay (i.e. via the IC and/or ISC channels) by restriction of large amplitude motions through the surrounding environment. In PMMA, this effect was not exceedingly pronounced due to the free volume in the PMMA matrix. Therefore, a further enhancement of luminescence is expected in more densely packed environments. This is particularly true in the poly- or single crystalline phase with usually dense packing of the molecules due to enthalpic arguments. In addition to favoring strong emission via reducing k_{nr} through restricting IC/ISC, dense packing might at the same time lead to increase of k_r, due to the planarization enabled by 'twist elasticity' as discussed in Section 4.3.3; this effect is a generally rather small but might lead to SLE constituted by concurrent radiative and nonradiative *intra*molecular contributions.

However, the dense environment is not a sufficient condition for giving an increase of Φ_F, because two factors might counteract the decrease of k_{nr} though restricted IC/ISC and the increase of k_r via planarization. One factor is H-aggregation which reduced k_r; this will be discussed in detail further down. The other factor is possible exciton trapping ($k_q \cdot c_{trap}$; with k_q as the quenching rate and c_q as the quencher concentration), which increases the overall k_{nr}, as detailed in a recent perspective paper.[Gie13a] According to this previous work, quenching is in particular effective at surfaces or grain boundaries (i.e. interfaces) of crystalline domains; thus, this factor might becomes especially pronounced in polycrystalline samples such as (spin-coated or vapor deposited) films and nanoparticles. In films, crystalline domains are typically small with < 100 nm, while in the nanoparticle sizes are typically below 100 nm; therefore, high surface:volume ratios leads to high trap concentrations $c_{trap,}$ while the small domain sizes shorten the average distances to reach the surface and/or interface.[Gie13a] Thus, PL quenching in polycrystalline samples can easily mask the SLE effect. Because of this, only monolithic (single) crystals were chosen in the current study; in fact, exciton trapping is largely reduced in such samples due to high purity, small surface:volume ratios and large distances to the surfaces. Thus, the determined nonradiative rates, $k_{nr} = (1-\Phi_F)/\tau_F$ are entirely due to the reduction of IC/ISC, which should be lower compared to solution as outlined above. Indeed, the observed non-radiative rates k_{nr} in the single crystals are in the range of just 0.02 - 0.10 ns^{-1} (see Table

4.11 and Figure 4.2), underlining the further suppression of IC/ISC in the densely packed environment in the crystalline for the entire **DCS** family.

Intermolecular Contributions to the Radiative Rate in the Crystalline State. As mentioned above, the other factor which might counteract the inhibition of IC/ISC in the crystalline state and thus might lead to a lowering of Φ_F is of i*nter*molecular origin; i.e. H-aggregation which leads to a possible decrease of k_r.[Kasha, Gie13b, Gie16] Due to frequent misconceptions in literature, it should be reminded that according to Kasha's original exciton model (as discussed in Section 2.1.6 in Chapter 2), an ideal H-aggregate, which would give $k_r = 0$ only exist under two conditions, i.e. (i) perfectly side-by-side oriented molecules (i.e., with small x-slip, and with only translationally equivalent molecules in the unit cell; Z = 1) and (ii) purely electronic transitions (i.e. negligible vibronic contributions). In reality, non-zero k_r are in any case observed even in strongly coupled H-aggregates,[Gie13b] which are accordingly caused by two possible factors. One are (even small) inclinations between the transition dipole moments in crystal arrangements with more than one molecule per unit cell (Z > 1); the other is aggregate-type Herzberg-Teller (AHT) coupling, which usually happens in the forbidden electronic transitions.[Wyk15a, Spa10] Consequently, small radiative rates caused by strong H-aggregation requires the inhibition of these factors.

Relating this concepts to our systems, large exciton coupling ΔE_{EC} (as discussed in Section 4.5.1), are particularly observed for **β-DCS** and **β-MODCS**; For smaller ΔE_{EC}, effective AHT coupling is expected to be operative, which enhances the oscillator strength of the lowest emissive state, giving somewhat emissive H-aggregation in contrast to the simple classical Kasha's model.[Wyk15a] Perfect parallel alignment of the transition dipole moments $\vec{\mu}_{01}$ in the molecular arrangement, i.e. with no other molecules within the one unit cell, are realized for crystals with one molecule per unit cell (Z = 1); among the current compounds, Z = 1 is only observed for 3 compounds out of 8, i.e. **α-DBDCS**, **α-MODCS** and **β-MODBDCS** (Figure 4.16).

Proper Assignment of H-/J-aggregation. The blue/red shift of absorption spectra when going from solution to the aggregated state is broadly used to identify the type (i.e. H vs. J) of molecular aggregation. However, such assignment can be done only in cases where the optical density is small, i.e. such as thin films or nanoparticle suspensions.[Gie13a] In contrast, in samples with a high optical density, in particular powders or crystals, a proper assignment is generally difficult to obtain by spectral measures since considerable saturation (shadowing) effects are

observed in the absorption spectra as described by Mie theory; also PLE spectra cannot be used as an alternative because inner filter effects are operative. These effects, all arising from the high optical density, in all mask the intrinsic absorption properties, preventing the assignment by absorption or PLE shifts.[Gie13a] To solve this problem, i.e. to provide a proper measure for H-/J-aggregation type assignment, a photophysical method is prefered, which relies directly on the radiative rate analysis; here, the change (decrease/increase) of the radiative rate k_r when going from solution to the single crystalline state indicates H/J-aggregation. Based on this consideration, we defined a new parameter R_r decided by the ratio of k_r in crystal and solution (eq. 4.8) as a new measure for the interacting excitonic effect.

$$R_r = k_r(\text{crystal})/k_r(\text{solution}) \qquad (4.8)$$

It should be noted in this context, that in addition to the formation of aggregates, also the polarizability (and thus the refractive index n) will also change when going from one environment to another; this will give an additional effect on k_r. As seen in eq. 4.3, k_r is a function of the polarizability, and in a first approximation it scales with n^2. Since the effective n is higher in the crystal compared to solution,[Ege02] a general increase of k_r by up to ~50% (R_r = 1.5) is expected, which is just due to the polarizability effect; this should be separated when evaluating the value of R_r. For the assignment of H-aggregation with decreased k_r thus $R_r < 1$, the polarizability induced increase is not interfering. One the other hand, a clear assignment of J-aggregation should only be done if $R_r > 1.5$; i.e., if the increase of k_r is for safely above 50%,[Var12] while values of $1 < R_r < 1.5$ would typically fall in the weak coupling regime without clear H-/J-assignment.

H-/J- Assignment for the Current Library. Analyzing the change of the radiative rate constant k_r when going from solution to the crystalline state (see Table 4.11), among eight compounds in total, six members exhibit a decrease of k_r in the monolithic crystals against fluid solution. Calculating the R_r according to eq. 4.8, $R_r < 0.2$ is obtained for **α-DBDCS**, **β-DCS**, and **β-MODBDCS**, suggesting strong H-aggregation (H_s); while $1 > R_r > 0.2$ is obtained for **α-MODBDCS**, **β-DBDCS** and **β-MODCS** as well as **DSB**, indicating medium H-coupling (H_m); weak (tentatively H_w) coupling with $1.5 > R_r > 1$ is seen for **α-DBDCS**. Thus, the majority of compounds in this family employs H-type arrangement, giving once more evidence that H-type coupling is more frequently found in molecular crystals. Different from the other compounds, **α-MODCS** is the only compound which shows (weak) J-coupling with $R_r > 1.5$, being the only candidate for real AIEE-active material; i.e., showing a synergetic *intra*molecular reduction of

k_{IC} and *inter*molecular enhancement of k_r. The statements based on the ratio analysis of k_r can be in fact confirmed by TD-DFT calculations, based on nearest-neighbor dimer calculations (based on the X-ray results); these predict J-aggregate formation only for **α-MODCS** showing a strongly allowed S_1 state with a high oscillator strength, while H-aggregates are seen for all the rest compounds, see Table 4.15.[5]

SLE Origin Analysis for H-aggregates. As discussed above, the realization of strong H-aggregation along with low k_r requires the occurrence of large ΔE_{EC} or small ATH coupling if ΔE_{EC} is small; the other factor is a parallel alignment of the transition dipole moments, and thus ideally Z = 1. Therefore, the degree of H-aggregation differs largely for the seven H-type compounds. Especially large exciton couplings ΔE_{EC} are observed for **β-DCS** and **β-MODCS**; Z = 1 is found for **α-DBDCS**, **α-MODBDCS**, and **β-MODBDCS**; in all, a strong lowering of the radiative rate (and thus low R_r) is in particular observed for **α-DBDCS**, **β-DCS** and **β-MODBDCS**.

Although largely varying degrees of H-aggregation are observed for these compounds, they all show high luminescence in the single crystalline phase against fluid or solid solution, exhibiting pronounced SLE. This gives further evidence that H-aggregation does not necessarily quench the emission, since excitonic coupling impacts the change in radiative rate, while quantum yield is influenced by both radiative and nonradiative rates. In fact, for H-type compounds with lowing k_r, there's still a possible remedy to generate SLE; for example in the current case, the SLE for the H-type **DCS**-compounds is promoted by the reduction of k_{nr} in the crystalline phase, a contribution of *intra*molecular origin as discussed above.

*H-/J- Assignment for Polymorphs of **β-DCS***. Particular interesting systems for H/J-aggregation are polymorphs as the molecular structure is identical, as obtained for **β-DCS**. As discussed above (Section 4.3.2 (b)), analyzing the relative shift along the long molecular axis (which coincides with the direction of the transition dipole moment) for the dimer packing in the X-ray structure, the three polymorphs of **β-DCS** exhibit distinctively different packing motifs. PM2 and PM3 show a side-by-side arrangement of nearest neighbors with very small x-slip, suggesting H-type aggregation. The large x-slip of 36 % in PM1 suggests weak coupling, close to the inversion point of H-/J-aggregates. Performing the TD-DFT nearest-neighbor S_1 state

[5] As stressed in the Section 2.1.6, H-/J-aggregation in molecular crystals cannot be decided solely on X-ray data by comparing the pitch angle with the magic angle $\theta_i = 54.7^o$ as frequently done in literature,[Zha17] as the latter is derived from the point dipole approximation, which is inapplicable for molecular crystals.[Gie13b, Gie16]

calculations, low oscillator strength (which is proportional to the radiative rate constant) is observed for all the polymorphs, suggesting H-aggregation, in agreement with the x-slip analysis. The oscillator strengths for all polymorphs are small, indicating different degrees of H-aggregation. For PM3, the radiative rate constant k_r obtained from this calculated oscillator strength via eq. 4.3b agrees with the one extracted from the measured PL life time τ_F and quantum yield Φ_F by $k_F = \Phi_F/\tau_F = 0.07\ ns^{-1}$ (Table 4.2). This is significantly lower than in solution ($k_F = 0.33\ ns^{-1}$), what is expected for H-aggregates.[Gie13b] Furthermore, a strong blue shift of the absorption spectrum in PM3 is observed against nanoparticle suspensions and thin films, being one more argument for the statement of H-aggregation. Once again, all three polymorphs are highly emissive, providing further examples of the realized highly luminescent H-aggregated materials, as discussed earlier.[Gie13a, Gie13b]

It is important to note that the bright emission in the solid state is not a sufficient condition for light amplification; in fact, out of the three polymorphs only PM1 shows amplified spontaneous emission (ASE; Table 4.2).[Xu12] An investigation of such polymorph-dependent ASE derived from a related material has been reviewed earlier;[Var16] there it was shown that large π-π overlap is the factor inhibiting ASE, due to low radiative rates resulting from H-aggregation in combination with spectral broadening caused by effective *inter*molecular vibronic coupling. In our current results, inhibited ASE is in fact observed for the strongly π-stacked polymorphs PM2 and PM3, while for PM1 with only slight π-overlap, ASE is active, thus confirming the previous analysis.

In this section, largely varied photophysics when going from fluid/solid solution to single crystalline have been elucidated for different **DCS**-compounds as well as for different polymorphs, by the analysis of different radiative and nonradiative rates. For analyzing the changes in the radiative rates, a new measure involving the plarizability effect is proposed to assign H- vs. J-type aggregation in single crystals where spectral shift analysis are inhibited by interference of the high optical densities. The H-/J-aggregates statement obtained by conducting this measure agrees with the lowing/enhancing oscillator strength values from the TD-DFT calculations obtained from a simple dimer picture. Since trapping is largely avoided in single crystals, the strong reduction of k_{nr} is mainly a consequence of dense packing in the single crystalline state. In all, the different origins of the emission enhancement in **DCS**-compounds is identified; thus, the SLE of the one J-aggregated compound in the library is driven by synergy of *intra*molecular and *inter*molecular contributions, while the SLE in the remaining seven H-aggregated compounds is driven by *intra*molecular contribution.

Part B Photoexcitation Dynamics of Solution-Processed ASM-OSC

The second part of the thesis is dedicated to a combined spectroscopic, morphological and computational study on a prototypical solution-processed bulk-heterojunction (BHJ) all-small-molecule organic solar cell (ASM-OSC) utilizing p-DTS(FBTTh$_2$)$_2$ as donor[Pol12] and NIDCS-MO as acceptor (see Scheme 4.5).

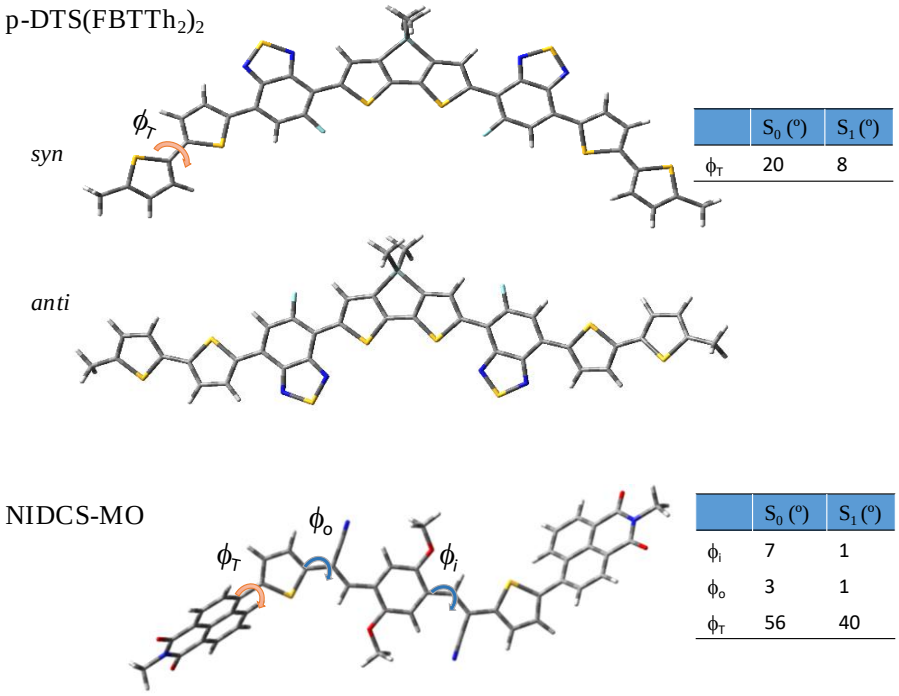

	S_0 (°)	S_1 (°)
ϕ_T	20	8

	S_0 (°)	S_1 (°)
ϕ_i	7	1
ϕ_o	3	1
ϕ_T	56	40

Scheme 4.5: Chemical structures of donor p-DTS(FBTTh$_2$)$_2$ (*syn*- and *anti*-rotamers) and acceptor NIDCS-MO. Relevant torsional angles q in the ground and first excited state (S_0, S_1) are indicated, calculated by (TD)DFT.

The study aims to explain the efficient charge extraction due to phase separation upon thermal treatment in this new class of materials combination, which give a power conversion efficiency (PCE) of 5.4% as reported by Kwon et al.[Kwo15]. For this, the dynamics (rates and yields) of the elementary processes (including exciton dissociation and diffusion, as well as dominant loss channels) will be quantified, the particular features inherent in current materials will be revealed, thus offering more general design strategies for this novel type of cells, i.e. ASM-OSC. First, in Section 4.6, the basic optical and photophysical properties will be investigated in the solution phase and in thin film samples, in order to understand the properties and dynamics of neutral excited states. Then, in Section 4.7, the annealing effect on the morphology of the blend sample will be visualized by using SNOM to PL map the domains. In Section 4.8, global and target analysis on the transient absorption (TA) data (for the procedures see

Appendix 3) will provide access to the properties and dynamics of charged excited states, yielding a series of rates and yields (from the delocalization lengths of singlet excited states and charged states, to the rates of charge transfer and parasitic exciton quenching at defects). Finally in Section 4.9, based on all the results obtained above, a comprehensive discussion on the probable mechanism acting in this photovoltaic system will be done, which will illustrate the particular features and the benefits possessed in this small-molecule-based cell (against polymer-based ones).

4.6 Investigation of the Optical and Photophysical Properties

4.6.1 Solution Spectra

Electronic Structure: Frontier MO Topologies and Energies. For ease of presentation, we use **D** and **A** to denote the p-DTS(FBTTh$_2$)$_2$ electron donor and the NIDCS-MO acceptor material, respectively, as introduced earlier by Kwon et al;[Kwo15] there, LUMO energies were estimated from the cyclic voltammogram (CV) experiment. For the current work, we calculated molecular geometries and frontier MOs of the two compounds at DFT level; the MO topologies with corresponding energies are displayed in Figure 4.18, suggesting that the MO energies from our calculation agree well with the experimental results from the original report[KWO15]. In both cases, an appealingly small offset of the LUMO energies is observed in this material mixture, which is considered as a possible reason of the high open circuit voltages eventually reached in this photovoltaic cell.

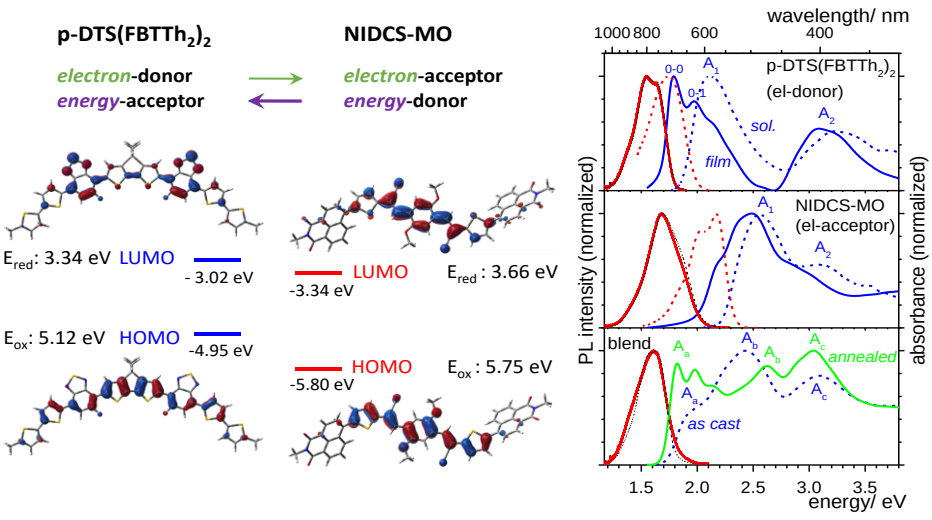

Figure 4.18: (a) DFT-optimized structures of p-DTS(FBTTh$_2$)$_2$ and NIDCS-MO with frontier MO topologies. (b) Absorption (blue) and PL (red) spectra of the samples. Top: p-DTS(FBTTh$_2$)$_2$ in solution (chloroform; dashed lines) and as spin-coated film (solid lines). Middle: NIDCS-MO. Bottom: blended film (as cast = dashed lines, annealed = solid lines).

Table 4.17: Spectroscopic data of p-DTS(FBTTh$_2$)$_2$ and NIDCS-MO in chloroform solution and (blended) films (as-cast and annealed). Absorption maxima E_{abs} (A_i; see Figure 4.18), PL maxima E_{PL}. PL quantum yields (Φ_F) and lifetimes (τ_F).

		E_{abs} / eV	**E_{PL} / eV**	**Φ_F**	**τ_F / ns**
p-DTS(FBTTh$_2$)$_2$	solution	A_1: 2.14	1.77	0.12	1.4
		A_2: 3.23			
	film [a]	A_1: 1.79	1.55	0.01 / 0.01	—
		A_2: 3.08			
NIDCS-MO	solution	A_1: 2.56	2.18	0.37	1.2
		A_2: 3.09			
	film [a]	A_1: 2.49	1.70	0.04 / 0.04	1.3 /1.5
		A_2: 2.90			
blend	as-cast	A_1: 1.96	1.64	< 0.01	—
		A_2: 2.43			
		A_3: 3.08			
	annealed	A_1: 1.82	1.64	< 0.01	—
		A_2: 2.63			
		A_3: 3.04			

[a] as-cast / annealed.

Table 4.18: (TD)DFT calculated excited states of donor (*syn* and *anti* conformers) and acceptor in vacuum (C_2 symmetry): vertical transition energy (E_{vert}), configuration interaction description (CI, values above 5% are listed; H = HOMO, L = LUMO) and corresponding oscillator strength *f*.

molecule	**rotamer**	**E_{vert} (eV)**	**CI (>5%)**	***f***
p-DTS(FBTTh$_2$)$_2$	*syn*	S_1(B): 1.67	H→L (97.9)	1.57
		S_2(B): 1.90	H→L+1 (97.5)	0.06
		S_3(A): 2.26	H-1→L (94.6)	0.16
		S_6(B): 2.74	H→L+2 (92.4)	0.95
	anti	S_1(B): 1.64	H→L (98.2)	1.77
		S_2(A): 1.89	H→L+1 (97.0)	0.02
		S_6(B): 2.78	H→L+2 (94.4)	1.12

NIDCS-MO	S_1(A): 2.20	H→L (96.6)	1.71
	S_4(A): 2.82	H-2→L (95.0)	0.33
	S_6(A): 3.23	H-3→L (81.5)	0.13
		H-1→L+1 (10.0)	
	S_8(A): 3.35	H-3→L (11.3)	0.15
		H-2→L+2 (5.7)	
		H-1→L+1 (78.4)	

Spectral Analysis of the Donor. We measured the absorption and PL spectra of **D** and **A** in dilute solutions of chloroform; the spectra are plotted in Figure 4.18 (dash lines) and the corresponding spectroscopic data are listed in Table 4.17. We assign the bands observed in these experimental spectra to the electronic transitions according to TD-DFT calculations (Table 4.18). For the absorption spectrum of **D** in solution (blue dashed line), two distinctive absorbance bands are observed in the visible region, respectively locating at 3.23 eV (384 nm; A_2) and at 2.14 eV (580 nm; A_1). For the PL spectrum (red dashed line), a peak maximum at 1.77 eV (699 nm) is found. Relying on TD-DFT analysis, A_1 originates from the electronic transition from the ground state (S_0) to the first excited singlet state (S_1), which is exclusively described by an electron promoted from the HOMO to the LUMO, without noticeable configuration interaction; A_2 is due to electronic transition from S_0 to a much higher excited state, i.e. $S_0 \rightarrow S_6$, which is mainly described by HOMO→LUMO+2, see Table 4.18. On the other hand, both absorption and PL spectra are unstructured in chloroform. This cannot be explained by the spectral broadening effect arising from strongly geometrical twists (as in the case of the **DCS** family and discussed in Refs. [Gie02] and [Mil11] for other systems) since here DFT optimization of S_0 suggests a mainly planar molecular backbone exhibiting only twists within the bithiophene moiety (see Scheme 4.5) in agreement with former studies by A. Köhler and coworkers.[Rei16] This study therefore made a solvent effect responsible for this vibronic structure loss. On the other hand, our DFT calculations give indication for the unresolved vibronic features: in fact, DFT optimization gives a clear indication for the coexistence of two different rotamers (*syn* and *anti*; see Scheme 4.5) based on a only very minor energy difference of 0.02 eV between them. The corresponding absorption spectra however exhibit a red-shift of 0.03 eV (13 nm) for the *anti*-rotamer against *syn*, which is indeed supported by the experimental data, i.e., the emission maximum is shifting depending on the excitation wavelength (Figure 4.19). Finally, with respect to the photophysical properties, we

observed that the donor molecule is moderately emissive in solution, exhibiting a PL quantum yield of $\Phi_F = 0.12$, and a lifetime of $\tau_F = 1.4$ ns (Table 4.17).

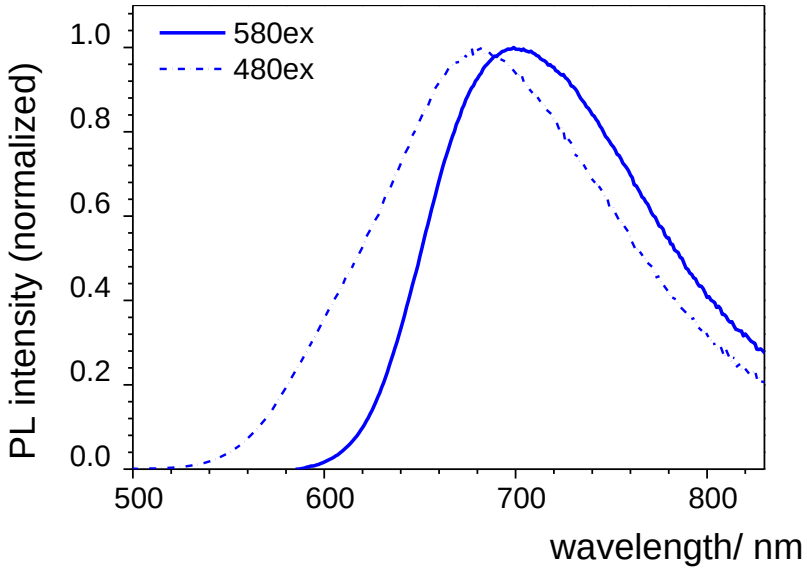

Figure 4.19: PL spectra of p-DTS(FBTTh$_2$)$_2$ in solution (chloroform); λ_{ex}: 480 nm (dashed line); 580 nm (solid line).

Spectral Analysis of the Acceptor. Similar to the donor, the acceptor in solution also shows two main absorption bands in the visible and near UV spectral region. According to the TD-DFT analysis, the peak at A_1 = 2.56 eV (485 nm) is assigned to the $S_0 \rightarrow S_1$ transition, dominated by the HOMO→LUMO excitation (see Table 4.18); the shoulder visible at A_2 = 3.09 eV (401 nm) is partial of vibronic nature, but also contains a higher transition, i.e. $S_0 \rightarrow S_4$ (Table 4.18). The PL spectrum shows a band maximum at 2.18 eV (570 nm) with some vibronic structure, while the absorption is completely unstructured. As discussed on **DCS**-compounds in part A, as well as on other related compounds in earlier publications[Gie02], the differences of the vibronic features between absorption and emission spectra are actually pointing to the different steepness of torsional potentials in the S_1 and S_0 states; i.e., considerable steepened torsional potentials around the single bonds in S_1 compared to S_0, which result from the shortening of the single bonds in S_1 compared to S_0. For the same reason, the planarization of molecule geometry in S_1 is expected, which is supported by the calculated torsional angel data (Scheme 4.5); the dihedral angels in the S_1 state around the vinyl-phenyl bond is : $\phi_i = 1°$ compared 7° in S_0; that around the vinyl-thiophene bond is $S_{0,1}$: $\phi_o = 3º, 1º$, indicating anyway a slight planarization on these motifs upon photoexcitation. However, substantial twists between the thiophene and naphthalene rings are observed both in S_0 (ϕ_T =

56°) and S_1 (40°); nevertheless, reflecting the MO typologies in Figure 4.18, the naphthalene moieties barely contribute to the frontier MOs, and thus are not involved in the transition of $S_0 \rightarrow S_1$ (mainly HOMO→LUMO, see Table 4.18. On the other hand, according to the MO topology picture in Figure 4.20, the naphthalene moieties exhibit certain contributions in HOMO-2, so that the transition $S_0 \rightarrow S_4$ (mainly HOMO-2→LUMO, see Table 4.18) shows significant charge-transfer character. With respect to the photophysics, the acceptor molecule is highly emissive in solution with $\Phi_F = 0.37$ and $\tau_F = 1.2$ ns (Table 4.17).

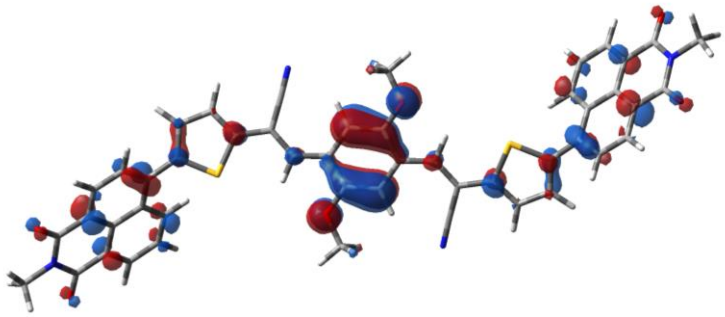

Figure 4.20: HOMO-2 of NICDCS-MO.

Comparing the absorption and emission of both compounds, we notice that the electron acceptor NIDCS-MO absorbs (and emits) at significantly higher energies compared to the electron donor DTS(FBTTh$_2$)$_2$. This has important implications for possible energy transfer, which may be operative in the blended film as the excitation energy transfer in opposite to the electron transfer; i.e., the electron acceptor (donor) acts as energy donor (acceptor), as shown in Figure 4.18. The presence of this energy transfer will be further confirmed by experimental observation, see next subsection.

4.6.2 Thin Film Samples of Pure Donor and Acceptor

Spectral Changes of Donor: Film vs. Solution, As-cast vs. Annealed. Absorption and PL spectra of **D** and **A** in spin-coated as-cast films are given as solid blue and red lines, respectively, in Figure 4.18. For the as-cast film of **D** (p-DTS(FBTTh$_2$)$_2$), both absorption and emission spectra show strong red-shifts against solution by 0.35 eV and 0.22 eV, respectively (Table 4.17); well-resolved vibronic sidebands are observed in particular in the absorption spectrum, indicated in Figure 4.18 as apparent vibronics 0-0, 0-1.[Rei16] The occurrence of vibronic structure in the film sample is considered as a clear sign for the more rigid, well-ordered environment in the film as compared to fluid solution, which steepens the torsional potentials and thus makes S_0 and S_1 potentials more similar to each other.[Sri09] In fact, single crystal X-ray analysis exhibits densely

packed, planar, π-stacked molecules which are largely slipped along their long molecular axis.[Lov13] TD-DFT calculations on a dimer cluster of nearest neighbors in the arrangement taken from X-ray analysis (Figure 4.21) consequently reveal weak H-aggregates with the lowest excited state S_1 carrying very small oscillator strength (see Table 4.19), while the exciton splitting is only 0.12 eV. Since the excitonic effect is not very active here, the observed significant spectral red-shift of the film spectra against solution is thus mainly driven by another *inter*molecular factor, i.e. a significant anisotropic polarizability effects in the well-ordered solid.[Ege02] On the other hand, *intra*molecular geometrical (planarization) effects are not expected to be important considering the essential planar molecular backbone in the equilibrium geometry of the free monomer (see Scheme 4.5). This is in particular true for the emission, which originates from a considerably planarized S_1 state also in solution (vide supra and Scheme 4.5). Thermal treatment of the film at 110ºC transforms the arrangement from an amorphous to a (poly)crystalline phase which is clearly demonstrated in X-ray diffraction (XRD) characterization,[Kwo15] while this effect is barely manifested in the optical absorption spectrum; i.e., the absorption characteristics hardly change upon this phase conversion. As the absorption probes mainly short-range interactions, the equivalent absorption spectra between the macroscopically very differently ordered two phases demonstrates that the initial step in the self-organization process of p-DTS(FBTTh$_2$)$_2$ is the formation of well ordered nuclei. This is taking place at a short range; whereas the crystallization process upon annealing is taking place at the long range; thus, the already existed order in nuclei cannot be affected and no alternation is observed in the absorption features.

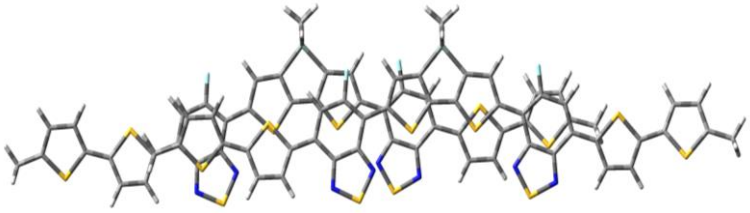

Figure 4.21: Dimer configuration of p-DTS(FBTTh$_2$)$_2$ used for the TD-DFT calculations. The structure of the single molecule was optimized by DFT and the arrangement of two neighboring molecules was adapted according to the reported single crystal X-ray structure (π-stacking distance 3.5 Å).[Lov13]

For the photophysics, as compared to solution, the emission in the films of p-DTS(FBTTh$_2$)$_2$ is strongly quenched, exhibiting Φ_F = 1% (Table 4.17). This is attributed to effective exciton trapping typically found in polycrystalline films due to small domain sizes and high surface:volume ratio,[Gie13a] which lowers the emission yield via increasing the overall nonradiative rate, as we discussed for the **DCS** family in Part A. As observed in absorption,

annealing of the film as well barely alters the spectral features of emission, despite the morphology changes.

Table 4.19: TD-DFT (CAM-B3LYP) calculation on the nearest neighbor dimer arrangement of p-DTS(FBTTh$_2$)$_2$ as shown in Figure 4.21. Vertical transition energies E_{vert}, configuration interaction description (CI, values above 5% are listed; H = HOMO, L = LUMO) and corresponding oscillator strength *f*. are listed here.

Dimer	**E_{vert} (eV)**	**composition (>5%)**	***f***
p-DTS(FBTTh$_2$)$_2$	S_1(A): 1.97	H→L (62.2)	0.03
		H-1→L+1 (13.3)	
	S_2(A): 2.09	H→L+1 (54.8)	3.15
		H-1→L(22.7)	

Spectral Changes of Acceptor: Film vs. Solution, As-cast vs. Annealed. For the as-cast film of NIDCS-MO, the absorption spectra shows only a moderate red-shift by 0.07 eV against solution (Figure 4.18 and Table 4.17), with a pre-band emerging at 2.22 eV (558 nm), giving the spectrum characters of weak H-aggregates;[Gie13b] here, the red-shift resulting from the polarizability effect overcompensates the blue shift caused by the excitonic effect.[Gie13a] According to the XRD analysis in the original report, the as-cast film is amorphous and no phase transformation happens upon annealing treatment at 110ºC,[Kwo15] keeping the absorption features constant in this temperature range; a different phase is formed at higher annealing temperatures (150ºC),[Kwo15] which exhibits blue-shifted absorption band compared to the as-cast film, being an indication of stronger H-aggregate formation in this phase. Compared to solution, the PL efficiency of the as-cast and annealed film (110ºC) both are sharply reduced (Φ_F = 4%); on the other hand, the spectra profiles of them become unstructured by blurring all vibronic features visible in solution, which all indicates that the role played by *inter*molecular vibronic contributions is non-negligible in this case.[Gie04a, Gie05, Wyk15b]

4.6.3 Blended Films

Annealing-dependent Device Performance and the Origin Analysis. As demonstrated in the original report,[Kwo15] annealing of the blended film of p-DTS(FBTTh$_2$)$_2$:NIDCS-MO (1:1) at 110°C had a significant positive impact on the corresponding device performance. This thermal-dependent performance was correlated with a significant change in the absorption spectra as shown in Figure 4.18. Comparing the blended films with the pure films in the as-cast and annealed status respectively, we realized that (unlike what might be expected for a BHJ

composition), the absorption spectra of the blended samples are never a simple superposition of the two single component spectra of pure films; instead they rather exhibit a one-component dominance in the absorption features: for the as-cast film, the spectral features seem to originate from the pure acceptor (**A**), while that for the annealed film they seem to be dominated by the pure donor (**D**).

For elucidating the origin of this annealing effect, we performed a quantitative analysis by decomposing the components in the blend, via simply subtracting the pure dominant spectrum from the blended absorption spectrum. In the first step, we subtracted the **A**-spectrum from the as-cast blended film (Figure 4.22); there the resulting spectrum indeed exhibits a **D**-like profile, while differing from the original pure **D** film in details; i.e. showing less vibronic features and blue-shifted absorption bands of A_1 and A_2. These differences indicate a less rigid and less ordered arrangement of **D**-domains before annealing. This analysis is concomitantly supported by the XRD observations of a completely amorphous structure in the as-cast blended sample while a (poly)crystalline **D**-phase occurred in the annealed blended sample.[Kwo15] For the annealed film, the same strategy was applied, but now the pure **D**-spectrum is the dominant component to be subtracted (Figure 4.22). The resulting **A**-spectrum again exhibits a blue-shift against the pure **A** film, quite similar to the new formed high-temperature phase of **A** (i.e. annealing at 150ºC)[Kwo15] which was mentioned above; this suggests a better ordered arrangement of **A**-domains after annealing. XRD experiments indeed confirmed the crystallization of **D**-phase upon annealing treatment, while the **A**-phase always shows amorphous nature.[Kwo15] The high charge mobilities observed in this photovoltaic device in principle requires a synergetic increase of order in both **A**- and **D**-phase. The original report demonstrated the **D**-phase crystallization upon annealing in the XRD results; the drastic increase of hole mobility in **D**-domains has been rationalized by the formation of fibrils favored by this order increase.[Kwo15] Our work here proves the annealing-induced order increase of the **A**-phase through a simple spectral analysis, therefore the concurrent increase of electron mobility in the **A**-phase is rationalized as well by achieving a more ordered structure.

We further recorded the emission spectra of the blended film. For the as-cast film, the main emission features look more similar to the pure donor emission, indicating the occurrence of energy transfer from the electron acceptor NIDCS-MO to the electron donor p-DTS(FBTTh$_2$)$_2$, in agreement with our analysis based on the calculated MO levels. Differently from the dramatic shape change of absorption as described above, annealing barely affects the PL spectral shapes. In both as-cast and annealed blends, PL quantum yields are below our detection limit (Φ_F <

1%), suggesting photoluminescence being a minor pathway for excited energies loss, which is expected for donor-acceptor blends with good solar cell performance.

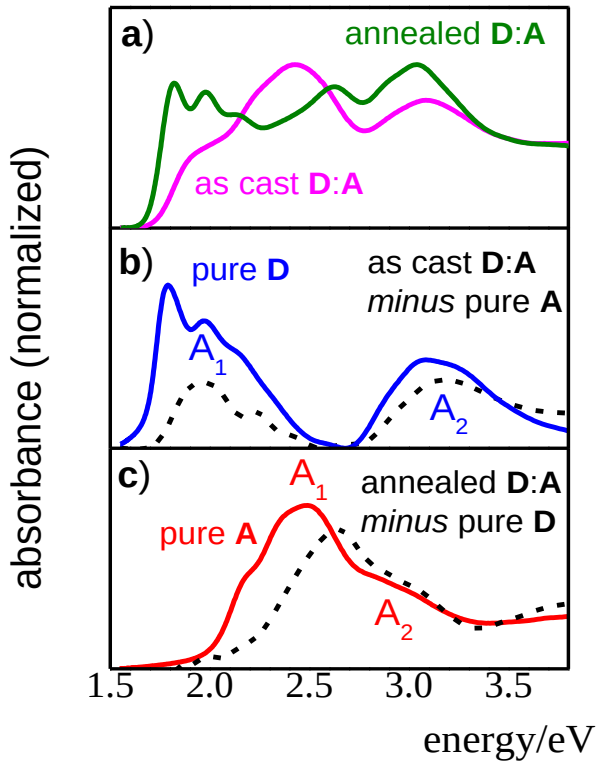

Figure 4.22: (a) Absorption spectra of a 1:1 blended film of p-DTS(FBTTh$_2$)$_2$ (**D**) and NIDCS-MO (**A**) before (magenta) and after annealing (green). (b) Absorption of the as-cast **D**:**A** film, where the spectrum of the pure **A**-film was subtracted (black, dashed line); the pure **D** film is shown for comparison (blue solid line). (c) Absorption of the annealed **D**:**A** film, where the spectrum of the pure **D**-film was subtracted (black, dashed line); the pure **A** film is shown for comparison (red solid line).

4.7 The Microscopic Visualization on BHJ Morphology

Domain Mapping by PL Imaging of the Annealed Blended Film. The local structural distributions of donor and acceptor components in the BHJ morphology can be probed by observing the variations in Raman and PL spectral features (shapes and intensity). As conventional optical microscopy is not able to resolve local distributions due to diffraction limit (ca. 200-400 nm), we used scanning near-field optical microscopy (SNOM), which can break the diffraction limit, by using sharp gold tip in the optical focus gives rise to confine the far-field to a sub-wavelength volume, allowing to probe domain distributions in polymer blends with a resolution down to ca. 10 nm.[Wan10] In the current case, Raman signals are obscured by the stronger PL features; the latter were shown to be weak in the blend (vide supra), but sufficiently strong to be used for domain mapping.

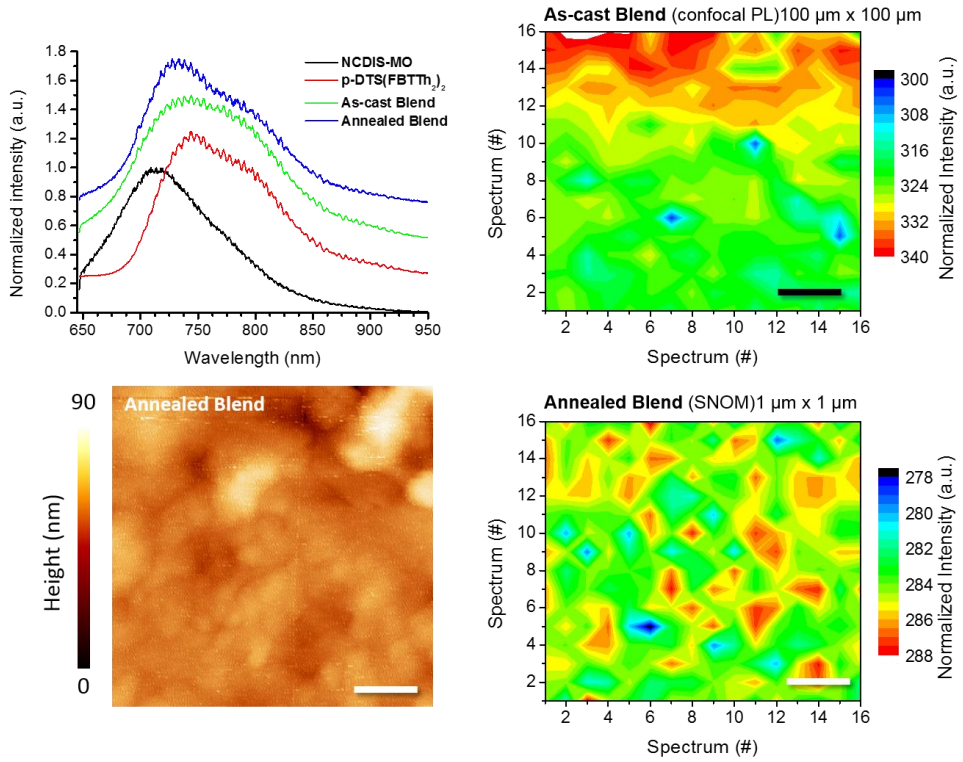

Figure 4.23: (a) PL spectra from pristine, as-cast blend and annealed blend films. (b) Confocal hyper-spectral PL image of the as-cast blend with the black scale bar indicating 20 µm. (c, d) Topography (1µm x 1µm) and the corresponding SNOM PL hyperspectral image (16 x 16 spectra) of an annealed blend films.

Confocal PL spectra of **D** and **A** in the as-cast film as well as in the annealed blend are displayed in Figure 4.23, showing a good agreement with the far-field PL (Figure 4.18); it should be especially noted that the PL spectra of the blends are more similar to the pure donor emission, and annealing barely affects the PL spectral shapes, indicating **A→D** energy transfer.

First, confocal microscopy was used to identify an area of 100 µm x 100 µm in the as-cast blended film, which exhibits the PL spectra with very similar spectral profile showing homogeneity with PL intensity variation of ca.15 % (Figure 4.23b). PL microscopy images demonstrate lateral homogeneity of the PL spectral shapes on a 100 nm to 100 µm scale, thus excluding any regions of **D** or **A** access which would lead to electrical performance loss. This demonstrates the good processability of these blends from solution.

After annealing, we employed SNOM to map the PL as well as scan the topology for a much smaller area of 1 µm x 1µm, where relatively smooth topographic features (Figure 4.23c) and less than 5 % PL intensity variations (Figure 4.23d) are observed. All these observations confirm the homogeneous **D**/**A** distributions in any status of blended films; on the other hand, better homogeneity upon annealing is proved, which provides more evidence for the

annealing-induced high charge mobility, indeed evidencing morphological reasons to the good PCE in this cell.

4.8 The Analysis of Time-resolved Transient Absorption Spectra

TA spectra of pure **D** (Figure 4.24a) and **A** (Figure 4.24b) films are measured with excitation energies within their respective $S_0 \rightarrow S_1$ transitions (Figure 4.18); i.e. at 2.0 and 2.43 eV respectively. Under these conditions, none of the TA spectra show spectral evolution, see the represented symbols in Figure 4.24a,b, revealing no changes in energy coordinate as time evolves. This is confirmed by perfect global fits using a model that only considered a single state undergoing two parallel reactions, the results are expressed by the lines in Figure 4.24a,b (the details of global and target analysis and the model depiction will be discussed further down).

Band Assignment in the Donor TA Spectrum. Since no spectral evolution occurring, the strong and narrow photoinduced absorption band (PA) of **D** at 1.03 eV (Figure 4.24a) can be safely assigned to an excited state transition of the singlet exciton in the **D**-phase, denoted by PA_{SD}. The other PA band with weaker absorption at 1.4 eV is tentatively assigned due to a transition of the singlet exciton to a higher lying, weaker coupled state. Bands of formally negative TA position at 1.8, 2.0, and 2.2 eV are all assigned to transient photobleach (PB_D), because these positions coincide with the vibronically resolved ground state absorption spectrum (GSA), see the dashed curve in Figure 4.24a.

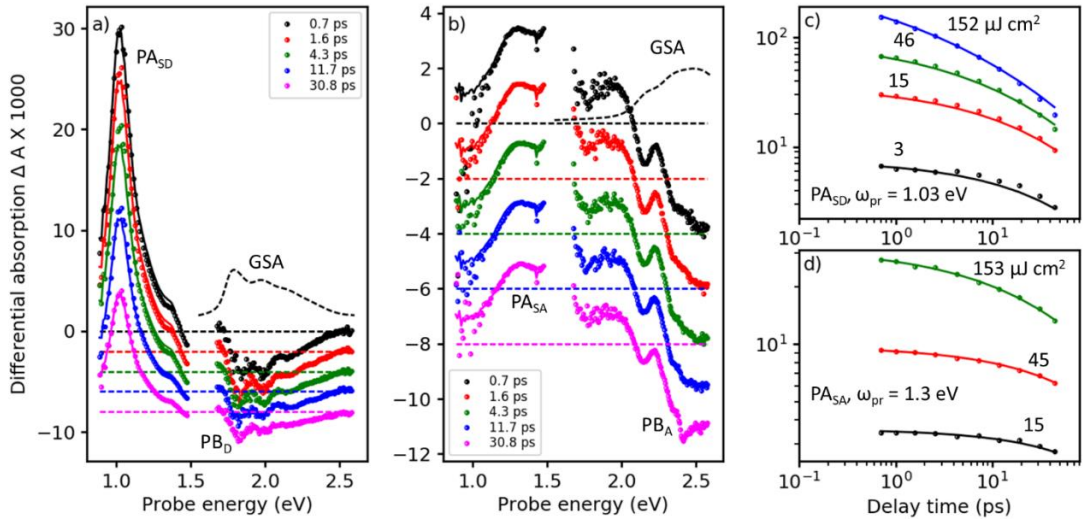

Figure 4.24: Femtosecond TA spectroscopy of a) pure donor (D) film, pumped at 620 nm, and b) pure acceptor (A) film pumped at 510 nm (symbols), at pump-probe delays as shown in the inset. Lines are fits from a target analysis (for details see Appendix 3). c) TA dynamics at a probe energy of ω_{pr} = 1.03 eV in D film at pump energies given next to the curves (symbols) and fits (lines) by the same target

analysis as in panel a. d) same for the acceptor films probed at 1.3 eV, with the target analysis from panel b.

Band Assignment in the Acceptor TA spectrum. For the **A**-film (Figure 4.24b), a similar picture emerges. The broad PA band at 1.3 eV is assigned to the excited state transition of the singlet exciton (PA_{SA}). This transition is possibly followed by a second transition in the spectral range around 1.6 eV which is not accessible to our TA setup. The weaker PA band at 1.9 eV is indicating a third transition of the singlet exciton to a higher lying state. Bands of formally negative TA at 2.1 and 2.5 eV coincide with the vibronic structure of the GSA spectrum (given as dashed curve) and thus are assigned to PB bands. Compared to the GSA spectrum, the vibronic feature in the TA spectra is better visible. This is probably due to a hole burning effect resulted by the relatively narrow-band pump pulse. It has also be noted in this context, that electroabsorption[Mar10] might contribute at early time delays, and dispersive motion[Sir01] might contribute at long time delays.

Quantification of Excited State Delocalization (L_{exc}). The method to quantify the amplitude of excited state delocalization (L_{exc}) applied in current case is comparing a single molecule with respect to the absorption cross-section in its ground state (σ_{mol}) to an excited state (σ_{exc}); this method is feasible due to the good match between the lowest energetic GSA band and the PB bands for all the pure films (**D** and **A**) across the whole spectral region. For ease of presentation, the calculated results are displayed here, while details regarding the procedure are found in Appendix 3. The calculation for the donor phase (**D**-phase) gives $L^D_{exc} = \sigma_{exc}/\sigma_{mol} \approx 0.7$, which is close to unity; however, significant uncertainties involved in the evaluation of the cross-sections should be taken into account. For the acceptor phase (**A**-phase), we find $L^A_{exc} = 0.4$. As seen in Figure 4.24b, a PA band around 2.2 eV significantly superposes the PB_A band; this fact leads to our prediction that the apparent value of PB_{exc} is actually decreased and thus L_{exc} must be increased. Due to all these values, we conclude that singlet excited states in both the **D**- and **A**-phases are localized on single molecules. This finding is in fcat confirmed by TD-DFT calculations of the excitonic interaction in the donor phase based on a dimer scheme (Figure 4.21), showing a weak *inter*molecular coupling with an excitonic splitting of only 0.12 eV (Table 4.19).

Occurrence of Singlet-singlet Annihilation (SSA) and Picosecond Exciton Quenching Process. TA dynamics are presented in Figure 4.24c,d, which were measured in the maxima of the singlet PA bands in the **D** and **A** film, respectively. Comparing the decay traces after pumping at three different pump intensities, a significant contribution of intensity-dependent singlet-singlet

annihilation (SSA) to the overall decay is found. Since SSA occurs only at high exciton densities, it is not relevant under normal operational conditions of OSCs; here, however, we use it as a probe for exciton mobility.[Mik12, Sha10] The comparison of Figure 4.24c and d demonstrates that SSA in **D** is stronger than that in the **A** film under the same pumping conditions. It should also be noted here that in both **D** and **A** films the TA dynamics at the lowest intensity is very similar to that at the second lowest one, which suggests the presence of an exciton quenching channel active on the picosecond time scale; this agrees with the observation that Φ_F of pure films are highly reduced relative to the solutions (Table 4.17).

Table 4.20: Fitting parameters for the global fits applied to the TA spectra in Figure 4.24 and Figure 4.25. An asterisk (*) indicates that the value has been fixed

Sample	**R_a / nm**	**D_{exc} / $cm^2\ s^{-1}$**	**c_Q / $10^{18}\ cm^{-3}$**	**$\Phi_{F,calc}$**	**IQE_{calc}**	**k_{ct} / s^{-1}**
D	1*	$9.1\cdot10^{-2}$	6.3	0.8%	0%	0
A	2.91	$4.9\cdot10^{-5}$	2.4	14%	0%	0
D:A as cast	1*	$9.1\cdot10^{-2}$*	2.16		48%	$4\cdot10^{10}$
D:A annealed	1*	0.33	3.5		35%	$1\cdot10^{10}$

Singlet Exciton Dynamics Modeling. With the above qualitative analysis at hand, the singlet exciton dynamics can be modeled. For this, it is assumed that (i) the diffusion-controlled exciton quenching at indestructible quenching sites at a concentration c_Q is homogeneous, and (ii) diffusion-enhanced exciton annihilation is operated by a Förster resonance energy transfer mechanism with typical annihilation distance R_a. Meanwhile, as a cross-check, the resulting concentration-time dependence of singlet states (S(t)), is used to predict the PL quantum yield in the solid state in the limit for negligible annihilation (for details see Appendix 3). For the **D** film, a very good match between measured and calculated Φ_F for predominantly one-dimensional exciton diffusion is found, see Table 4.20. This agrees with the quasi-one dimensional align,emt of the molecules in the X-ray crystal structure,[Lov13] and further justifies our assumption that diffusion is dominant in the annihilation process. Therefore, the fitted diffusion constant of 0.09 cm^2/s, and the resulting quencher molar fraction in the lower ‰ range are considered as reliable. For the **A** film, the best fits of the TA dynamics overestimate Φ_F, yielding 14% (20%) for 3D (1D) diffusion instead of 4% in experiment, see Table 4.20. It should be noted that although the fits at low intensity (Figure 4.24d, black curve) are perfect, the actual dynamics are however very small, which implies a substantial error in the evaluation..

Singlet Dissociation in the As-cast Blend. Figure 4.25a shows the TA spectra of the as-cast blend, after pumping at 2.0 eV. Referring to the absorption spectra in Figure 4.22, it suggests that under these conditions virtually only singlet excitons in the **D**-phase are able to be excited but not the ones in the **A**-phase. This is indeed confirmed by the observation of the PA_{SD} band at 1.03 eV in the early TA spectra for times < 2 ps (obtained by comparing black and red symbols in Figure 4.25a to the red spectrum in Figure 4.24a). However, even at a short delay time of only 700 fs, we already observe a band around 1.2-1.3 eV. Since exciton transfer from **D** to **A** is prohibited due to energetic reasons (*vide supra*), we conclude that a large portion of the excited singlet states primarily generated in the **D**-phase have already dissociated into charge separated states within a short time (less than 700 fs). This point of view is further corroborated by finding the PB features from both **D** and **A** already on the femtosecond time scale, i.e. compare the visible range in Figure 4.25a and Figure 4.24b.

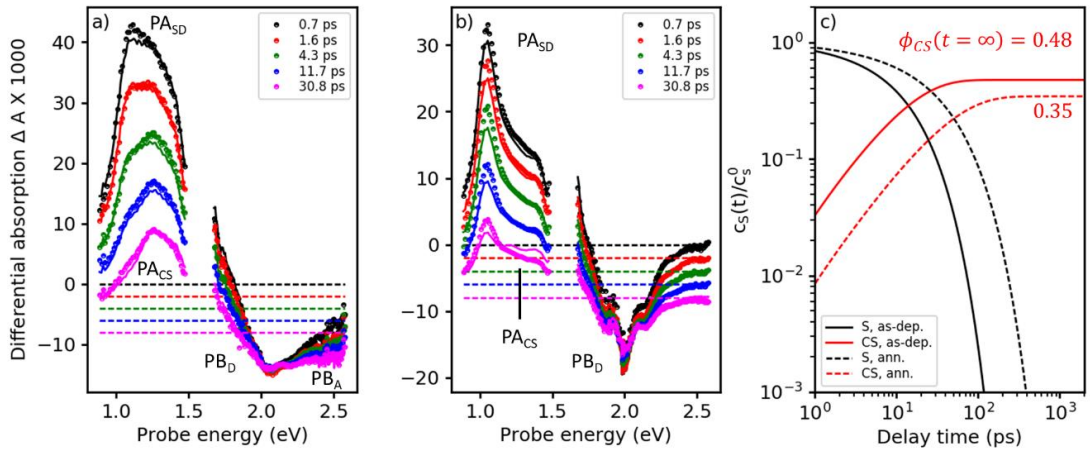

Figure 4.25: Femtosecond TA spectra for the as-cast and the annealed blend (panel a and b, respectively). Symbols: experimental data, lines: global fits from a target analysis with k_{ct} as the only free kinetic parameter (for details see Appendix 3). c) Dynamics of singlet states and charge separated states (black and red curves, respectively) at solar intensities for the as-cast and the annealed blend (solid and dashed curves, respectively), as obtained from a target analysis globally fitting TA spectra at 3 different pump intensities and extrapolating to solar conditions. The asymptotic value for the charge carrier yield φ_{CS} after long times, disregarding geminate recombination.

Singlet Decay and Charge Transfer in the As-cast Blend. Figure 4.25a exhibits active singlet decay in the as-cast blend in the lower picosecond regime. This is quite similar to what was observed in as-cast blends of classic polymer OSC materials (i.e. P3HT:PCBM)[Laq10, Guo09], and suggests the absence of phase separation. In fact, homogeneous distribution of **D** and **A** was already demonstrated by the TEM micrographs in the original report of Kwon et al.[Kwon15] and was confirmed here in the multi-component analysis of the absorption spectrum in the as-cast

blend (see the dashed line in Figure 4.22b). In this scenario, i.e. in the absence of phase separation, a large portion of charge transfer (CT) states can be formed by resonantly excited singlet excitons in the **D**-phase with nearest neighboring **A** molecules through certain wavefunction overlap. Thus CT state formation can be achieved without prior exciton diffusion, which therefore occurs with (sub) *p*s dynamics.[Fal14] Such a situation is indeed confirmed at different excitation wavelengths where the primary excitation is the **A**-singlet exciton, see Appendix 3.

Charge Transfer in the Annealed Blend. The situation in the annealed blend is drastically changed, as seen in Figure 4.25b. Here, the singlet exciton remains the dominant photoexcitation for at least 50 ps. By assuming a 2-states target model, see eq. 4.9, but setting the interfacial charge transfer constant $k_{CT} \neq 0$, the TA spectra in both annealed and as-cast blends are successfully reproduced, see solid lines in Figure 4.25a and b. It should be stressed, that the target analysis conducted here goes beyond a simple global fitting procedure (see details in Appendix 3). Besides a good fit of model to experiment, a good target analysis additionally requires the resulting characteristic spectra to be those of pure states and thus allows to obtain branching ratios and yields of photophysical pathways; this is (a priori) not possible with a global fit procedure. The analysis in Figure 4.25a,b shows that both the region of PA and of PB are fitted nearly perfectly over the whole time, probe energy, and pump intensity range (only one intensity is displayed here, for the other two see Appendix 3). This good fit, combined with the pure characteristic spectra of singlet and charged states (see Appendix 3), justifies the fitted parameters in Table 4.20.

For the as-cast film, a charge transfer time of around 25 ps is found, and the diffusion constant for excitons in the **D**-phase does not show any significant change upon blending. In the annealed blend, the situation is very different; here, the diffusion constant exhibits a clear increase, which is correlated to the formation of larger domains, which reduces the amount of grain boundaries, and reduces the quencher concentration. As a consequence, for the annealed blend, the charge transfer time increases to around 100 ps.

Prediction of Yields. The original report of Kwon et al gave a value for the internal quantum efficiency (IQE) of 45%.[Kwo15] In our work, as a cross-check, we predict the yield of charge separated states under solar conditions, applying eq. 4.9, to make a comparison with experiment (see Figure 4.25c). For the as-cast blend, a charge carrier yield of 48% is found, which has to be enhanced by the number of ultrafast carrier generation. A very high IQE is obtained via summarizing these channels, which strongly contrasts with the published low PCE.[Kwo15] This

finding is however in agreement with investigations in the prototype polymer-based solar cell, P3HT:PCBM, where the discrepancy between ultrafast charge carrier generation and low current output has been shown to be a result of geminate recombination.[Laq10] By the parameters in Table 4.20, we predict an IQE of 35%, not far from the published value of 45% at 620 nm. The discrepancy may be due to the different sample statistics. Nonetheless, considering the fact that the calculated value refers only to charge generation while the measured one also takes into account geminate recombination, seems to suggest that the experimental IQE value in the annealed blend is limited by defect quenching while geminate recombination plays only a minor role.

4.9 Unraveling the Operating Mechanism

For achieving high PCE values, good charge generation and extraction yields as well as high V_{OC} values are required at the same time. In the previous report of the current system,[Kwo15] the BHJ blend has shown high V_{OC} values (up to 1.0 V), ascribed to the higher reduction potential (i.e. in a simple one-electron picture following Koopmans' theorem the LUMO level) of the acceptor against the standard acceptor PCBM; this means that a larger fraction of the initial photon energy is conserved in the charge separated states. The driving force for exciton dissociation however gets decreased, when increasing the reduction potential, which thus might reduce the exciton dissociation yield. Thus, a balance has to be found between a high driving force and high V_{OC} values. As shown in the previous Section, parasitic quenching processes are slow in the current device due to the high purity of the blend materials, which is capable to accommodate exciton dissociation times as long as 100 ps. This exciton dissociation time found in the current blend is longer than the numbers found in any high-efficiency polymer-based BHJ blend, which gives ASM-OSCs a great potential for efficient charge transfer even at low driving forces, and the latter can further allow higher V_{OC} values without sacrificing exciton dissociation yields.

A further aspect, which is of critical concern for OSCs, is the formation of free carriers from the primary bound interfacial CT states. In order to compete successfully with geminate recombination, the Coulomb binding energy of the interfacial CT state should not exceed the thermal energy. For polymer OSCs, it was shown that both wavefunction delocalization,[Few15] and/or strong coupling (either by a hot or coherent mechanism) [Gra13, Fal14, Vel16] can minimize binding energies. As discussed above, the evaluation of the relative photobleach in Figure 4.24 indicates that in the blend films, both neutral and charged excited states are essentially confined on single molecules. Therefore, strong coupling by wavefunction delocalization is not

operative, and cannot effectively reduce the Coulomb binding energies. Consequently, thermal activation for charge separation is expected, and will be (very) slow; thus charge recombination has to be even slower to generate efficient IQE.

Such a requirement, i.e. slow charge recombination to allow for activated charge separation in the relatively strongly bound CT state, can be actually fulfilled in the limit of weak electronic coupling **D**-**A** systems as found in the current ASM-OSC; for this, we define the free carrier yield by eq. 4.9, where

$$\phi_{fc} = \phi_{CT} \cdot (1 - \phi_{CR}) = \frac{k_{CT}}{k_{CT}+k_q} \cdot \left(1 - \frac{k_{CR}}{k_{CR}+k_{sep}}\right) \qquad (4.9)$$

ϕ_{CT} and ϕ_{CR} are the yields for charge transfer by exciton dissociation and charge recombination, respectively. The rate of exciton quenching by defects, k_q is taken from the global fit to Figure 4.25b, while the charge separation rate is given by $k_{sep} = k_{hop} \cdot e^{-\frac{\Delta E_{sep}}{k_B T}}$, where the hopping rate k_{hop} is obtained from the charge mobility given in Ref [Kwo15] assuming Langevin and Einstein relations, and the exponential term gives the probability for an attempt to hop to be successful, where ΔE_{sep} is the coulomb binding energy of the interfacial CT complex (for details see Appendix 3). The rates k_{CT} and k_{CR} are the Marcus rates for charge transfer and recombination, respectively, which obtained in the following way in the typical notation:[Car12]

$$k_{CT;CR} = \sqrt{\frac{\pi}{\hbar^2 \lambda_s k_B T}} |V|^2 \sum_{\upsilon}^{\infty} \frac{e^{-S} S^{\upsilon}}{\upsilon!} exp\left[\frac{-\left(\upsilon E_{\upsilon} + \lambda_s + \Delta G^0_{CT;CR}\right)^2}{4\lambda_s k_B T}\right], \qquad (4.10)$$

where the Huang-Rhys factor is given by $S = \lambda_{\upsilon}/E_{\upsilon}$, λ_v being the internal reorganization energy and E_v the vibrational energy of an effective mode. The external reorganization energy (see Appendix 3) is given by λ_s, υ is the vibrational quantum number, V is the coupling between **D** and **A**, k_B is Boltzmann's constant, and $\Delta G^0_{CT;CR}$ is the Gibbs free energy change for charge transfer and charge recombination, respectively, given by [Ree17]

$$\Delta G^0_{CT} = \left[e\left(E^0_{D,ox} - E^0_{A,red}\right) - E_{opt}\right] - E_c \;;\; \Delta G^0_{CR} = E_{opt} - \Delta G^0_{CT}, \qquad (4.11)$$

where e is the elementary charge, $E^0_{D,ox}$ is the formation energy of a fully (electronically and geometrically) relaxed donor cation, $E^0_{A,red}$ is the formation energy of a fully relaxed acceptor anion, both readily available from cyclovoltammetry (CV). The effect of the different dielectric constants of the solvent for CV measurements and the blend, respectively, on the external

reorganization energies, is taken into account by applying a correction energy E_c [Ree17] (for details see Appendix 3). The optical band gap is given by E_{opt}.

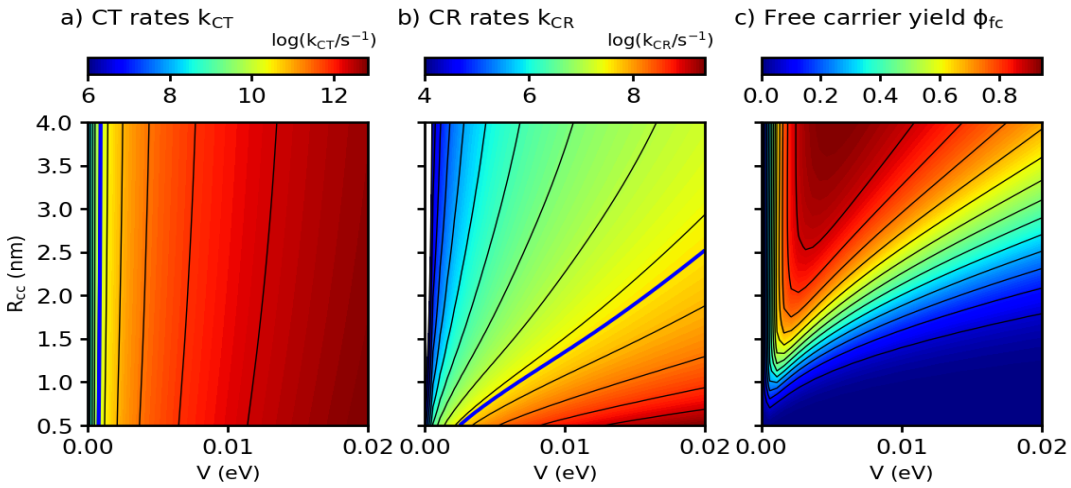

Figure 4.26: Charge transfer (CT) rates, charge recombination (CR) rates, and free carrier yields ϕ_{CT}, calculated using eq. 4.10 and 11, as function of the center-to center distance R_{cc} between donor D and acceptor A and the D-A coupling V (panel a, b, and c, respectively). Parameters: E_{opt} = 1.77 eV, λ_v = 0.1 eV, $\mu_e = \mu_h = 10^{-4} cm^2/Vs$, $k_q = 10^{10}$ s^{-1}, T = 298 K. For details of the calculation see Appendix 3.

Both λ_s and ΔE_{sep} depend on the center-to center distance of **D** and **A** charge density, R_{cc}, so that the **D**-**A** coupling V and R_{cc} are the only free parameters. In Figure 4.26, the predicted rates for charge transfer and recombination as function of R_{cc} and V are shown (panel a and b, respectively). Figure 4.26a indicated that k_{CT} depends strongly on V but very weakly on R_{cc}. As R_{cc} is expected to change the contribution of the Coulomb attraction to the reorganization energy, this observation implies that the crossing point between the respective potential energy parabola for initial and final states in the Marcus picture is very close to the minimum of the initial state (see also Appendix 3). The breaking of the exciton therefore takes place with an activation energy close to zero, which shows that the frontier energy levels of **D** and **A** are well chosen in the current system. The bold blue line close to the left corner in Figure 4.26a indicates the position where $k_{CT} = k_q$ and thus $\phi_{CT} = 0.5$: thus, improving ϕ_{CT} means to move towards the right of the blue line. In contrast, the charge recombination rates k_{CR} in Figure 4.26b depend on both R_{cc} and V. For CR, k_{CR} increases (and thus the activation energy for CR decreases) for decreasing R_{cc}, i.e., the crossing point occurs in the Marcus inverted region; this is a favorable situation for photovoltaics. The blue line in Figure 4.26b indicates where k_{CR} = k_{sep} and thus $\phi_{CR} = 0.5$; thus, minimizing ϕ_{CR} means moving to the left of the blue line. From this, it becomes clear that there is an optimum range of R_{cc}/V combinations for the free charge

carrier yield, as depicted in Figure 4.26c. Taking the parameters from the proceeding work,[Kwo15] it is shown that ϕ_{fc} increases for decreasing D-A coupling V; this fully agrees with the qualitative prediction made above. Thus, a general design rule for ASM-OSCs can be formulated: (i) charge recombination should be (very) slow to allow for activated separation of the CT complex; (ii) on the other hand, the high structural definition of small molecules allows extended exciton lifetimes and low driving forces for exciton dissociation. Thus, by weak **D**-**A** coupling these requirements can in fact be satisfied, being an important perspective for extending this small-molecule strategy towards lower optical bandgaps to enhance light absorption.

Chapter 5

Conclusions

5.1 SLE in the DCS Family of Compounds

Solid state luminescence enhancement (SLE) has evolved to a key research area in the field of conjugated organic materials due to the significant implications for real-world applications. Despite the fact that diverse SLE-active materials have been created under the now popular term "aggregation induced emission" (AIE), the mechanistic aspects are still unclear. While the AIE community as well realized in the meantime that aggregation (*inter*molecular contributions) might not be the only factor for SLE, also the conceptual understanding of *intra*molecular factors - expressed in the physically ambiguous "restriction of intramoleuclar rotation" (RIR) term - is little developed. Therefore, careful studies are needed, to resolve the complex interplay of different radiative and nonradiative deactivation processes, geometrical vs. electronic factors. and *intra*- and *inter*molecular contributions. To understand SLE better especially in its mechanistic details, we have performed a combined photophysical and computational investigation on a library of eight different compounds. The latter is derived from a prototype example of SLE materials, i.e. distyrylbenzenes with cyano-substituents in the vinylene unit (**DCS**-compounds), via varying bi-cyano-substitution in the inner (α) or outer (β) position, and adding bi-alkoxy-substituents in the central (methoxy, **MO**) and/or terminal (butoxy, **DB**) phenyl-rings. This systematical variation of chemical substitution gives rise to sharply different photoresponses in different environments (fluid solution, solid solution, monolithic crystals) in particular for different positional isomers. These rich phenomenological signs may be driven differently from all possible SLE-controlling parameters, thus offering a unique chance to draw a holistic SLE picture with all contributions disentangled and quantified. For doing this, a variety of spectroscopic techniques (quantitative steady-state and *ps* time-resolved PL, *fs* transient absorption (TA), photoacoustic calorimetry (PAC), combined with appropriate quantum-chemical methods (TD-DFT, CASSCF) and available structural (X-ray) data are utilized to allow for a qualitative and quantitative assessment of all SLE factors.

In fluid solution, the (absorption and emission) spectral positions exhibit a dependence on substitution's position and presence; i.e. red-shifted spectral maxima are observed for the the β- vs. the α-series. This shift is shown to be mainly driven by electronic factors, which we coined "enhanced resonance stabilization" (ERS). Furthermore, upon alkoxy-substitution in the central ring, a characteristic 'camel hump' shape of the absorption spectrum is observed, where the intensity ratio of the 'humps' differs upon **CN** position, **MO** orientation, as well as

additional **DB** substitution in the terminal rings; the current studies revealed equal importance of electronic and geometrical contributions to this effect. Different absorption and PL band shapes were observed among the library of compounds, mainly driven by geometrical factors.

The emission efficiencies in fluid solution depend dramatically on the specific substitution pattern. The entire α-series is very low-emissive ($\Phi_F \leq 2\%$), whereas in the β-series only **β-DCS** is low emissive ($\Phi_F = 1\%$), while the other compounds are (highly) emissive ($\Phi_F = 20$-54%). Analyzing the time-resolved PL data, it was shown that these variations are driven by different nonradiative rates k_{nr}, which cannot be explained in a simple RIR picture since the local environment of the single bonds is the same for all compounds. Our TA studies revealed a similar initial deactivation scenario for all compounds: initially, an ultra-fast (0.4-0.9 ps) process around the vinyl double bond is observed due to the bond's lability compared to the parent **DSB**, leading to a conical intersection (CI) from where internal conversion (IC) and inter-system crossing (ISC) are followed with similar contributions demonstrated by PAC analysis. Thus, the accessibility to the CI is decisive for the emission efficiency; as the CI is of localized electronic character, it's very similar in energy for all compounds. For this reason the energy of the initially created Franck-Condon (FC) state decides on the activation barrier height which controls the access to the CI. This is effectively prevented in the β-series by ERS, making β-series emissive compared to the α-analogues; only for **β-DCS** the ERS is insufficient due to missing further stabilizing alkoxy groups, making **β-DCS** the only low-emissive compound within the β-series.

In the crystalline phase, distinctively different emission colors from that in fluid solution were observed, giving a library of colorful crystals covering the whole visible range. The origin of these dramatic crystal shifts were elucidated through a combined spectroscopic and quantum-chemical analysis, demonstrating that *intra*molecular contributions arising from geometrical non-/twisted structures are of similar importance as *inter*molecular contributions due to excitonic coupling in the solid state. The occurrence of non-/twisted structures was even observed for one and the same molecule under different crystal growth conditions, leading to polymorphism. The ability of the **DCS** molecules to react so sensitively to external constraints, the so called "twist elasticity" was fully rationalized in the current work by a detailed quantum-chemical analysis.

Independent on the substitution, all compounds give enhanced emission when switching the environment from fluid solution to monolithic crystals as well as to solid solutions (PMMA)

of the materials, thus showing SLE however to different degrees, proving that "aggregation" (AIE) is not a necessary condition for SLE. In PMMA, the SLE effect is relatively small which can be traced back to the remaining free volume in PMMA which can only partly suppress the nonradiative process. Differently, in the single crystals, the densely packed environment effectively inhibits IC/ISC (k_{nr} = 0.02- 0.12 ns^{-1}) and leads to highly luminescent crystals with Φ_F varying in a range of 46-90%. The variations are mainly driven by differences in the radiative rates k_r as induced by H- vs. J-aggregation. Seven out of the eight compounds here are H-aggregated as revealed in the frame of the quantum-chemically improved molecular exciton model. Importantly, even for strong H-aggregates high Φ_F were observed, further evidencing that "aggregation-caused quenching" (ACQ) is nonoperative under these low-trap and low surface:volume conditions in single crystals; whereas effective trapping were observed in polycrystalline samples like films and nanoparticle suspensions.[Gie13a] In the H-aggregates SLE in mainly driven by *intra*molecular contributions; i.e., a large reduction of $k_{nr.}$ In the only one J-aggregated compound (**α-DCS**), a synergetic effect of suppression of k_{nr} and increase of k_r induced by J-aggregation was found, identified as a real synergetic AIEE effect.

In all, the current in-depth combined photophysical and computational study of a library of structurally similar compounds allowed for a detailed understanding of the origin of color variation and SLE phenomenon is revealed, via disentangling geometrical vs. electronic effects, radiative and nonradiative channels as well as *intra*- and *inter*molecular contributions, being an important step towards the urgently required rational materials design.

5.2 Photoexcitation Dynamics of Solution-Processed All-small-molecule Organic Solar Cells

Emerging as an alternative route for traditional polymer:fullerene composed bulk heterojunction (BHJ) organic solar cells (OSCs), the integration of solution-processed small molecule in fullerene-free OSCs has made great progress, reaching power conversion efficiencies (PCE) comparable to classic OSCs during a short time. Strong attempts have been seen in the last few years to entirely replace polymers, creating solution-processed all-small-molecule organic solar cells (ASM-OSCs). Obviously the distinctive features of small molecules relative to polymers such as high purity and, possibly, well ordered structure are supposed to be decisive factors, however a in-depth photophysical analysis of ASM-OSCs was missing by now. For this, we present here a combined experimental, computational and

morphological study of the photoexcitation dynamics on a prototypical solution-processed BHJ ASM-OSC with p-DTS(FBTTh$_2$)$_2$ as donor (**D**) and NIDCS-MO as acceptor (**A**); this cell was reported earlier to show a PCE of 5.4% after annealing at 110ºC due to a significant morphology change.[Kwo15]

In the present work, insight into the morphology change upon annealing was gained by a detailed analysis of the ground state absorption spectra. In the as-cast blend, the analysis revealed the features of both amorphous **D**- and **A**-phases in agreement with the earlier X-ray analysis. In the annealed blend, the **A**-phase is amorphous, however different from that in the as-cast blend as stronger H-type interactions were observed, while the **D**-phase resembles that of the pure crystalline **D**-film. The PL in the as-cast and annealed blends is largely quenched; the remaining PL originates from effective **A**→**D** energy transfer. Lateral homogeneity was demonstrated by confocal and scanning near-field microscopy, thus excluding any regions of **D** or **A** access which would lead to electrical performance loss.

The central part of the study is a global and target analysis based on femtosecond transient absorption (TA) spectra, to quantify the photovoltaic elementary processes. The analysis revealed that both neutral and charged excited states are localized on single **D** and **A** molecules due to small excitonic coupling, so that wavefunction delocalization doesn't play a role in this kind of cell; this was fully confirmed by quantum chemical calculations. Target analysis of the time-resolved TA spectra allowed the extraction of quencher concentrations and and charge-transfer rates. In the annealed blends, the exciton dissociation rate is only 0.01 ps^{-1}, i.e. much slower than in polymer-based OSCs. Thus, it is the superior high structural definition of the small molecule systems, which can tolerate slow transfer rates without loosing efficiency. Semi-classical Marcus theory analysis of the electron transfer reaction permitted to demonstrate that actually the weak electronic coupling between **D** and **A** is the key point to achieve efficient charge separation in the small molecule systems without effective delocalization of the wavefunctions. This new insight into the operating mechanism should enable highly efficient solution-processed ASM-OSCs, when tuning the absorption properties towards lower optical bandgaps.

In a broader sense, the current work has been dedicated to the elucidation of structure-property relationships in highly defined conjugated materials for applications in optoelectronics, utilizing small molecules all based on the cyano-vinyl synthon. To achieve such understanding, combined spectroscopic, computational and structural characterization was required. This was done by using the integrative approach of the host core group,

complemented by advanced structural, spectroscopic, microscopic and computational techniques, conducted during research stays in partner groups at IMDEA and abroad. This gave the present work a truly interdisciplinary and international ambience, necessary to fully resolve the complex mechanistic aspects of organic solid state photophysics.

Conclusiones (ES)

5.1 SLE en la Familia de Compuestos DCS

El aumento de luminiscencia en el estado sólido (SLE) ha evolucionado hasta convertirse en un área de investigación clave en el campo de los materiales orgánicos conjugados, debido a la relevancia de las implicaciones que tiene en aplicaciones del mundo real. A pesar del hecho de que diversos materiales SLE-activos han sido creados bajo el término popularizado como "emisión inducida por agregación" (AIE), los aspectos relativos al mecanismo por el que ésta tiene lugar todavía se desconocen. Mientras la comunidad AIE entretanto se ha dado cuenta también de que la agregación (contribuciones *inter*moleculares) podría no ser el único factor para observar SLE, la comprensión conceptual de los factores *intra*moleculares – expresados de manera físicamente ambigua con el término "restricción de la rotación intramolecular" (RIR) – se encuentra poco desarrollada. Por ello, son necesarios estudios minuciosos que resuelvan la compleja combinación de procesos de desactivación radiativa y no-radiativa, de factores geométricos y electrónicos, así como de las contribuciones *intra*- e *inter*moleculares. Para comprender mejor la SLE, especialmente en lo relativo a los detalles del mecanismo, se ha llevado a cabo una investigación en la que se combinan técnicas fotofísicas y computacionales que se han aplicado sobre una librería de ocho compuestos diferentes. Dicha librería deriva de un ejemplo-prototipo de materiales SLE, a saber, distirilbencenos con sustituyentes ciano en la unidad vinílica (compuestos DCS), en los que se varía la posición de sustitución de los grupos ciano entre interna (α) o externa (β), y a los que se añade sustituyentes bi-alcoxi en el anillo central (metoxi, **MO**) y/o terminal (butoxi, **DB**). Esta variación sistemática de la sustitución química da lugar a foto-respuestas pronunciadamente distintas en los diferentes entornos (disolución fluida, disolución sólida, cristales monolíticos), en particular, para los diferentes isómeros de posición. Todas estas ricas señales fenomenológicas puede que estén promovidas por distintos parámetros de entre todos aquellos que controlan la SLE, ofreciendo así una oportunidad única de trazar una imagen holística de todas las contribuciones esclarecidas y cuantificadas. Para ello, se han utilizado diversas técnicas espectroscópicas [PL cuantitativa de estado estacionario y resuelta en el tiempo (*ps*), absorción transitoria en escala de *fs* (TA), calorimetría fotoacústica (PAC)], combinadas con métodos químico-cuánticos apropiados (TD-DFT, CASSCF) y los datos estructurales (rayos X) disponibles, con el fin de permitir una evaluación cualitativa y cuantitativa de todos los factores responsables de la SLE.

En disolución fluida, las posiciones espectrales (absorción y emisión) muestran una dependencia de la presencia y la posición de sustitución; esto es, se observa un

desplazamiento hacia el rojo de los máximos del espectro en la serie-β respecto a la -α. Este desplazamiento se muestra que está principalmente promovido por factores electrónicos, que nosotros acuñamos "estabilización por resonancia acentuada" (ERS). Además, tras la sustitución alcoxi del anillo central, se observa una forma característica de tipo 'joroba de camello' en el espectro de absorción, en la que la relación de intensidad entre las 'jorobas' difiere según la posición de los **CN**, la orientación **MO**, así como la sustitución **DB** adicional en los anillos terminales; nuestros estudios revelaron que las contribuciones electrónicas y geométricas presentan una importancia equitativa sobre este efecto. Las diferentes formas de las bandas PL y de absorción observadas en los diferentes compuestos de la librería responden principalmente a factores geométricos.

Las eficiencias de emisión en disolución sólida dependen de manera radical del patrón de sustitución específico. La serie-α es, en su totalidad, muy poco emisora ($\Phi_F \leq 2\%$), mientras que en la serie-β, únicamente **β-DCS** es poco emisor ($\Phi_F = 1\%$), siendo el resto de compuestos (muy) emisores ($\Phi_F = 20\text{-}54\%$). El análisis de los datos PL con resolución temporal mostró que dichas variaciones responden a diferentes constantes no-radiativas k_{nr}, que no pueden ser explicadas con un modelo RIR simple ya que el entorno local de los enlaces simples es el mismo en todos los compuestos. Nuestros estudios TA revelaron un escenario de desactivación inicial para todos los compuestos: inicialmente, se observa un proceso ultra-rápido (0.4-0.9 ps) en torno al doble enlace vinílico debido a la labilidad de dicho enlace en comparación al de la molécula de referencia **DSB**, que conduce a una intersección cónica (CI) desde la que prosiguen procesos de conversión interna (IC) y de cruce entre sistemas (ISC) con contribuciones similares, tal y como demostraron los análisis PAC. Por ello, la accesibilidad a la CI es decisiva para la eficiencia de emisión; como la CI es de naturaleza electrónica localizada, resulta ser muy similar en energía en todos los compuestos. Por esta razón, la energía del estado Franck-Condon (FC) creado inicialmente decide la altura de la barrera de activación que controla el acceso a la CI. Ésta es evitada de manera eficaz en la serie-β por ERS, haciendo que la serie-β sea emisora en comparación con los análogos-α; únicamente en el caso de **β-DCS** la ERS es insuficiente debido a la falta de los también estabilizadores grupos alkoxi, haciendo de **β-DCS** el único compuesto de baja emisión de la serie-β.

En la fase cristalina, se observaron colores de emisión claramente diferentes a los de la disolución fluida, dando lugar a una colección de coloridos cristales en todo el rango del espectro visible. El origen de estos acusados desplazamientos en los cristales se elucidó

mediante un análisis espectroscópico y químico-cuántico combinado, demostrando que las contribuciones *intra*moleculares procedentes de estructuras geométricamente giradas/no-giradas tienen una importancia similar a las contribuciones *inter*moleculares debidas a acoplamientos excitónicos en estado sólido. La ocurrencia de estructuras giradas/no-giradas se observó incluso en la misma molécula en función de las condiciones de crecimiento del cristal, dando lugar a polimorfismo. La habilidad de las moléculas de **DCS** de reaccionar de manera tan sensible a los condicionantes externos, la llamada "twist elasticity", ha sido totalmente racionalizada en el presente trabajo mediante un detallado análisis químico-cuántico.

Independientemente de la sustitución, todos los compuestos dan lugar a un incremento de la emisión cuando se cambia el entorno de disolución fluida a cristales monolíticos así como a disoluciones sólidas (PMMA) de los materiales, mostrando así SLE, aunque en diferentes grados, probando que la "agregación" (AIE) no es una condición necesaria para la SLE. En PMMA, el efecto SLE es relativamente pequeño, algo que puede ser adscrito al volumen libre remanente en PMMA el cual, únicamente puede suprimir en parte el proceso no-radiativo. De forma diferente, en los monocristales, la elevada densidad del entorno inhibe de manera efectiva los procesos IC/ICS (k_{nr} = 0.02- 0.12 ns^{-1}) conduciendo a cristales con luminiscencia muy elevada, con Φ_F que varían en el rango de 46-90%. Las variaciones están principalmente provocadas por las diferencias en las velocidades radiativas k_r inducidas por la agregación de tipo H frente a agregación de tipo J. Siete de los ocho compuestos en este caso son agregados de tipo H, tal y como se reveló en el marco del modelo excitónico molecular mejorado químico-cuánticamente. Cabe destacar que, incluso en agregados de tipo H fuertes se observaron Φ_F elevados, poniendo de nuevo en evidencia que la "desactivación causada por la agregación" (ACQ) no es operativa en monocristales bajo estas condiciones de relación superficie:volumen pequeña y baja concentración de defectos, mientras que en muestras policristalinas, como películas y suspensiones de nanopartículas, se observó "trapping" efectivo.[Gie13a] En los agregados de tipo H, SLE está determinado principalmente por contribuciones *intra*moleculares, como una gran reducción de k_{nr}. En el único compuesto agregado de tipo J (**α-DCS**), se encontró un efecto sinérgico de supresión de k_{nr} e incremento de k_r inducido por la agregación de tipo J, y se identificó como un efecto AIEE sinérgico real.

En resumen, el riguroso estudio combinado fotofísico y computacional de una librería de compuestos estructuralmente parecidos ha permitido una racionalización detallada del origen de la variación de color y ha revelado el fenómeno SLE, mediante la separación de efectos

geométricos y electrónicos, de canales radiativos y no-radiativos así como de contribuciones *intra*- e *inter*moleculares, constituyendo un importante paso hacia el urgentemente requerido diseño racional de materiales.

5.2 Dinámica de Fotoexcitación de Células Solares Orgánicas de Moléculas Pequeñas Procesadas en Disolución

La integración de moléculas pequeñas procesadas en disolución en células solares orgánicas (OSCs) libres de fullereno, que apareció como alternativa a las OSCs tradicionales de tipo heterounión distribuida o "bulk heterojunction" (BHJ) compuestas por polímero:fullereno, ha experimentado un gran avance, alcanzando eficiencias de conversión energética (PCE) en tiempos cortos comparables a las de las OSCs clásicas. Durante los últimos años, se han visto grandes intentos de reemplazar por completo los polímeros, creando células solares orgánicas de moléculas pequeñas (ASM-OSCs) procesadas en disolución. Resulta obvio que las características que distinguen a las moléculas pequeñas de los polímeros, tales como una elevada pureza y, posiblemente, una estructura bien ordenada, se consideren factores decisivos, sin embargo, hasta el momento, no existía un análisis fotofísico en profundidad de las ASM-OSCs. Es por ello que aquí presentamos un estudio combinado experimental, computacional y morfológico de la dinámica de fotoexcitación de un prototipo de ASM-OSC de tipo BHJ procesada en disolución con p-DTS(FBTTh$_2$)$_2$ como dador (**D**) y NIDCS-MO como aceptor (**A**); anteriormente, se describió una PCE de 5.4% tras cristalización por "annealing" a 110 ºC debido a un significativo cambio morfológico.[Kwo15]

En el presente trabajo, se ha ganado entendimiento sobre el cambio morfológico tras el "annealing" a través de un análisis detallado de los espectros de absorción del estado fundamental. En la mezcla "as-cast", el análisis reveló las características de ambas fases amorfas **A** y **D**, de acuerdo con análisis previos de rayos X. En la mezcla "annealed", la fase **A** es amorfa, aunque diferente de la de la mezcla "as-cast" ya que se observaron interacciones de tipo H más fuertes, mientras que la fase **D** se parece a la del film **D** puro cristalino. La fotoluminiscencia en las mezclas "as-cast" y "annealed" se encuentra muy desactivada; el origen de la fotoluminiscencia remanente se encuentra en una transferencia efectiva de energía **A**→**D**. Se demostró la existencia de homogeneidad lateral mediante microscopia confocal y de escaneo de campo cercano, excluyendo así cualquier región de acceso de **D** o **A** que pudiera conducir a pérdidas de rendimiento eléctrico.

La parte central del estudio es un análisis global y enfocado basado en absorción de “transient” (TA) de femtosegundo, para cuantificar los procesos fotovoltaicos elementales. El análisis desveló que ambos estados excitados, neutro y cargado, están localizados sobre moléculas individuales de **D** y **A** debido a un acoplamiento excitónico pequeño, de manera que la deslocalización de la función de onda no juega ningún papel en este tipo de célula; esto quedó totalmente confirmado por cálculos químico-cuánticos.

Un análisis enfocado de los espectros TA resueltos en el tiempo permitió la extracción de concentraciones de desactivadores y velocidades de transferencia de carga. En las mezclas cristalizadas por "annealing", la velocidad de disociación del excitón es sólo de 0.01 ps^{-1}, mucho más baja que en las OSCs basadas en polímeros. De ahí que la superior definición estructural de los sistemas de moléculas pequeñas pueda tolerar velocidades bajas de transferencia sin pérdida de eficiencia.

El análisis de la reacción de transferencia de electrones según la teoría semi-clásica de Marcus permitió demostrar que el débil acoplamiento electrónico entre **D** y **A** constituye la clave para lograr una separación de carga eficiente en los sistemas de moléculas pequeñas sin deslocalización efectiva de las funciones de onda. Esta nueva percepción del mecanismo de operación debería permitir la obtención de ASM-OSCs procesadas en disolución muy eficientes al modular las propiedades de absorción hacia separaciones ópticas de banda menores.

En un sentido más amplio, el presente trabajo se ha dedicado a la elucidación de relaciones estructura-propiedad en materiales conjugados muy definidos con aplicaciones en optoelectrónica, utilizando moléculas pequeñas basadas en el sintón ciano-vinilo. Para lograr dicha comprensión, se requirió la combinación de distintas técnicas de caracterización espectroscópica, computacional y estructural. Esto pudo llevarse a cabo gracias al enfoque integrador del grupo anfitrión, complementado por técnicas estructurales, espectroscópicas, microscópicas y computacionales avanzadas, llevadas a cabo durante diversas estancias de investigación en grupos colaboradores en el propio IMDEA y en el extranjero. Ello proporcionó al presente trabajo el verdadero ambiente interdisciplinar e internacional necesario para resolver completamente los complejos aspectos del mecanismo de la fotofísica en estado sólido de sistemas orgánicos.

References

[Ale07] J. V. Alemán, A. V. Chadwick, J. He, M. Hess, K. Horie, R. G. Jones, P. Kratochví l, I. Meisel, I. Mita, G. Moad, S. Penczek, R. F. T. Stepto, Definitions of terms relating to the structure and processing of sols, gels, networks, and inorganic-organic hybrid materials (IUPAC Recommendations 2007), *Pure Appl. Chem.*, 2007, **79**, 1801-1829.

[An02] B.-K. An, S.-K. Kwon, S.-D. Jung, S. Y. Park, *J. Am. Chem. Soc.*, 2002, **124**, 14410-14415.

[An12] B.-K. An, J. Gierschner, S. Y. Park, *Acc. Chem. Res.*, 2012, **45**, 544-554.

[And90] (a) K. Andersson, P.-Å. Malmqvist, B.O. Roos, A.J. Sadlej, K. Wolinski, *J. Phys. Chem.*, 1990, **94**, 5483-5488; (b) K. Andersson, P.-Å. Malmqvist, B.O. Roos, *J. Chem. Phys.*, 1992, **96**, 1218-1226; (c) K. Andersson, Tesis Doctoral, Universidad de Lund, Suecia, 1992.

[Ant06] Anthony, J. E. *Chem. Rev.*, 2006, **106**, 5028-5048.

[Arn92] L. G. Arnaut, R. A. Caldwell, J. E. Elbert, L. A. Melton, *ReV. Sci. Instrum.*, 1992, **63**, 5381-5389.

[Atk11] P. W. Atkins, R. S. Friedman, *Molecular Quantum Mechanics*; Fifth Edit.; Oxford University Press: Oxford, 2011.

[Avo12] Avogadro: an open-source molecular builder and visualization tool. Version 1.2. http://avogadro.cc/.

[Bar00] G. P. Bartholomew, G. C. Bazan, X. H. Bu and R. J. Lachicotte, *Chem. Mater.*, 2000, **5**, 1422-1430.

[Bar81] P. F. Barbara, S. D. Rand, P. M. Rentzepis, *J. Am. Chem. Soc.*, 1981, **103**, 2156-2162.

[Bas96] J. S. Baskin, L. Bañares, S. Pedersen, A. H. Zewail, *J. Phys. Chem.*, 1996, **100**, 11920-11933.

[Bau96] R. Bauernschmitt, R. Ahlrichs, *Chem. Phys. Lett.*, 1996, **256**, 454-464.

[Bel09] D. Beljonne, C. Curutchet, G. D. Scholes and R. J. Silbey, *J. Phys. Chem.B*, 2009, **113**, 6583-6599.

[Ben92] P. J. Benning, D. M. Poirier, T. R. Ohno, Y. Chen, M. B. Jost, F. Stepniak, G. H.

Kroll, J. H. Weaver, J. Fure, R. E. Smalley, *Physical Review B*, 1992, **45**, 6899-6913.

[Ber02] J. Bernstein, *Polymorphism in Molecular Crystals*, Oxford University Press, New York, 2002.

[Ber03] L. Bernasconi, M. Sprik, J. Hutter, *J. Chem. Phys.*, 2003, **119**, 12417-12431.

[Ber16] G. J. O. Beran, *Chem. Rev.*, 2016, **116**, 5567-5613.

[Bho05] C. J. Bhongale, C.-W. Chang, C.-S. Lee, E. W.-G. Diau, C.-S. Hsu, *J. Phys. Chem. B*, 2005, **109**, 13472-13482.

[Bin16] (a) S. Chen, Y. Liu, L. Zhang, P. C. Y. Chow, Z. Wang, G. Zhang, W. Ma, H. Yan, *J. Am. Chem. Soc.*, 2017, **139**, 6298-6301; (b) X Li, X. Liu, W. Zhang, H.-Q. Wang, J. Fang, *Chem. Mater.*, 2017, **29**, 4176-4180; (c) F. Zhao, S. Dai, Y. Wu, Q. Zhang, J. Wang, L. Jiang, Q. Ling, Z. Wei, W. Ma, W. You, C. Wang, X. Zhan, *Adv. Mater.*, 2017, 1700144; (d) H. Bin, L. Gao, Z.-G. Zhang, Y. Yang, Y. Zhang, C. Zhang, S. Chen, L. Xue, C. Yang, M. Xiao, Y. Li, *Nat. Commun.*, 2016, **7**, 13651; (e) Z. Li, K. Jiang, G. Yang, J. Y. L. Lai, T. Ma, J. Zhao, W. Ma, H. Yan, *Nat. Commun.*, 2016, **7**, 13094; (f) R. Yu, S. Zhang, H. Yao, B. Guo, S. Li, H. Zhang, M. Zhang, J. Hou, *Adv. Mater.*, 2017, in print. DOI: 10.1002/adma.201700437; (g) D. Baran, R. Shahid Ashraf, D. A. Hanifi, M. Abdelsamie, N. Gasparini, J. A. Röhr, S. Holliday, A. Wadsworth, S. Lockett, M. Neophytou, C. J. M. Emmott, J. Nelson, C. J. Brabec, A. Amassian, A. Salleo, T. Kirchartz, J. R. Durrant, I. McCulloch, *Nat. Mater.*, 2017, **16**, 363-370; (h) G. Zhang, G. Yang, H. Yan, J.-H. Kim, H. Ade, W. Wu, X. Xu, Y. Duan, Q. Peng, *Adv. Mater.*, 2017, **29**, 1606054; (i) B. Fan, K. Zhang, X.-F. Jiang, L. Ying, F. Huang, Y. Cao, *Adv. Mater.*, 2017, in print, DOI: 10.1002/adma.201606396; (j) W. Wang, C. Yan, T-K Lau, J. Wang, K. Liu, Y. Fan, X. Lu, X. Zhan, *Adv. Mater.*, DOI*:* 10.1002/adma.201701308.

[Bro11] A. M. Brouwer, *Pure Appl. Chem.*, 2011, **83**, 2213-2228.

[Bue74] R.J. Buenker, S.D. Peyerimhoff, *Theor. Chim. Acta*, 1974, **35**, 33.

[Cal97] Jr. W. D. Callister, *Materials science and engineering, an introduction.* 4th edn. New York: John Wiley and Sons, Inc., 1997.

[Car12] D. Caruso, A. Troisi, *Proc. Natl. Acad. Sci.*, 2012, **109**, 13498-13502.

[Cas09] M.E. Casida, *Journal of Molecular Structure: THEOCHEM*, 2009, **914**, 3-18.

[Cas95] M.E. Casida, en *Recent Advances in Density Functional Methods*, vol. 1, (D.P. Chong, ed.), World Scientific, 1995.

[Cas98] M.E. Casida, C. Jamorski, K.C. Casida, D.R. Salahub, *J. Chem. Phys*., 1998, **108**, 4439-4449.

[Cha12] C.-W. Chang, C. J. Bhongale, C.-S. Lee, W.-K. Huang, C.-S. Hsu, E. W.-G- Diau, *J. Phys. Chem. C*, 2012, **116**, 15146-15154.

[Che17] W. Chen, Q. Zhang, *J. Mater. Chem. C*, 2017, **5**, 1275-1302.

[Chi10] G. Chidichimo and L. Filippelli, *International Journal of Photoenergy*, Volume 2010 (2010), 123534.

[Chi12] Z. Chi, X. Zhang, B. Xu, X. Zhou, C. Ma, Y. Zhang, S. Liu, J. Xu, *Chem. Soc. Rev.*, 2012, **41**, 3878-3896.

[Chu13] J. W. Chung, S.-J. Yoon, B.-K. An, S. Y. Park, *J. Phys. Chem. C*, 2013, **117**, 11285-11291.

[Ciz66] (a) J. Čížek, *J. Chem. Phys.*, 1966, **45**, 4256; (b) J. Čížek, *Adv. Chem. Phys.*, 1969, **14**, 35; c) J. Čížek, J. Paldus, *Int. J. Quantum Chem.*, 1971, **5**, 359.

[Cor01] J. Cornil, D. Beljonne, J.-P. Calbert, J.-L. Bredas, *Adv. Mater.*, 2001, **13**, 1053-1067.

[DiP07] R. E. Di Paolo, J. Seixas de Melo, J. Pina, H. D. Burrows, J. Morgado, A. L. Maçanita, *ChemPhysChem*, 2007, **8**, 2657-2664.

[Dob16] A.L. Dobryakov, M. Quick, D. Lenoir, H. Detert, N.P. Ernsting, S.A. Kovalenko, *Chem. Phys. Lett.*, 2016, **652**, 225-229.

[Dot97] S. E. Dottinger, M. Hohloch, D. Hohnholz, J. L. Segura, E. Steinhuber, M. Hanack, *Synthetic Metals*, 1997, **84**, 267-268.

[Döt98] S. E. Döttinger, M. Hohloch, J. L. Segura, E. Steinhuher, M. Hanack, A. Tompert, D. Oelkrug, *Adv. Mater.*, 1997, **9**, 233-236.

[Dou13] L. Dou, J. You, Z. Hong, Z. Xu, G. Li, R. A. Street, Y. Yang, *Adv. Mater.*, 2013, **25**, 6642-6671.

[Dre01] A. Drechsler, M. A. Lieb, C. Debus, A. J. Meixner, G. Tarrach, *Opt. Express*, 2001, **9**, 637-644.

[Dre03] A. Dreuw, J.L. Weisman, M. Head-Gordon, *J. Chem. Phys.*, 2003, **119**, 2943.

[Dua15] P. Duan, N. Yanai, Y. Kurashige, N. Kimizuka, *Angew. Chem. Int. Ed.*, 2015, **54**, 7544-7549.

[Dyk09] T. E. Dykstra, E. Hennebicq, D. Beljonne, J. Gierschner, G. Claudio, E. R. Bittner, J. Knoester and G. D. Scholes, *J. Phys. Chem. B*, 2009, **113**, 656-667.

[Eft14] A. F. Eftaiha, J.-P. Sun, I. G. Hill, G. C. Welch, *J. Mater. Chem. A*, 2014, **2**, 1201-1213.

[Ege02] (a) H.-J. Egelhaaf, J. Gierschner, D. Oelkrug, *Synth. Met.*, 2002, **127**, 221-227. (b) Y.-S. Huang, J. Gierschner, J. P. Schmidtke, R. H. Friend, D. Beljonne, *Phys. Rev. B.*, 2011, **84**, 205311.

[ElB68] M. A. El-Bayoumi and F. M. Abdel-Halim, *J. Chem. Phys.*, 1968, **48**, 2536-2541.

[Eom15] I. Eom, S. J. Lim, S. Y. Park, T. Joo, *Rapid Commun. Photosc.*, 2015, **1**, 1-3.

[Etx15] (a) I. Etxebarria, J. Ajuria, R. Pacios, *Org. Electr.* 2015, **19**, 34-60; (b) R. Volpi, M. Linares, *Chem. Modell.* 2017, **13**, 1-26; (c) J. Yu, Y. Zheng, J. Huang, *Polymers*, 2014, **6**, 2473-2509; (d) L. Lu, T. Zheng, Q. Wu, A. M. Schneider, D. Zhao, L. Yu, *Chem. Rev.*, 2015, **115**, 12666-12731.

[Fac13] A. Facchetti, *Materials Today*, 2013, **16**, 123-132.

[Fal14] S. M. Falke, C. A. Rozzi, D. Brida, M. Maiuri, M. Amato, E. Sommer, A. De Sio, A. Rubio, G. Cerullo, E. Molinari, C. Lienau, *Science*, 2014, **344**, 1001-1005.

[Fer16] F. Fernández-Lázaro, N. Zink-Lorre, Á. Sastre-Santos, *J. Mater. Chem. A*, 2016, **4**, 9336–9346.

[Few15] S. Few, J. M. Frost, J. Nelson, *Phys. Chem. Chem. Phys.*, 2015, **17**, 2311-2325.

[Fis75] G. Fischer, G. Seger, K. A. Muszkat, E. Fischer, *J. Chem. SOC., Perkin Trans.*, 1975, **2**, 1569-1576.

[Foc30] V.A. Fock, *Z. Phys.*, 1930, **15**, 126.

[Fus04] W. Fuß, C. Kosmidis, W. E. Schmid, S. A. Trushin, *Angew. Chem. Int. Ed.*, 2004, **43**, 4178-4182.

[Gau09] M. J. Frisch, G. W. Trucks, H. B. Schlegel, G. E. Scuseria, M. A. Robb, J. R. Cheeseman, G. Scalmani, V. Barone, B. Mennucci, G. A. Petersson, H. Nakatsuji, M. Caricato, X. Li, H. P. Hratchian, A. F. Izmaylov, J. Bloino, G. Zheng, J. L. Sonnenberg, M. Hada, M. Ehara, K. Toyota, R. Fukuda, J. Hasegawa, M. Ishida, T. Nakajima, Y. Honda, O. Kitao, H. Nakai, T. Vreven, J. A. Montgomery, Jr., J. E. Peralta, F. Ogliaro, M. Bearpark, J. J. Heyd, E. Brothers, K. N. Kudin, V. N. Staroverov, R. Kobayashi, J. Normand, K. Raghavachari, A. Rendell, J. C. Burant, S. S. Iyengar, J. Tomasi, M. Cossi, N. Rega, J. M. Millam, M. Klene, J. E. Knox, J. B. Cross, V. Bakken, C. Adamo, J. Jaramillo, R. Gomperts, R. E. Stratmann, O. Yazyev, A. J. Austin, R. Cammi, C. Pomelli, J. W. Ochterski, R. L. Martin, K. Morokuma, V. G. Zakrzewski, G. A. Voth, P. Salvador, J. J. Dannenberg, S. Dapprich, A. D. Daniels, Ö. Farkas, J. B. Foresman, J. V. Ortiz, J. Cioslowski, D. J. Fox, Gaussian 09, Revision D.01, Gaussian, Inc, Wallingford 2009.

[Gie02] J. Gierschner, H.-G. Mack, L. Lüer, D. Oelkrug, *J. Chem. Phys.*, 2002, **116**, 8596-8609.

[Gie03] J. Gierschner, H.-G. Mack, H.-J. Egelhaaf, S. Schweizer, B. Doser, D. Oelkrug, *Synth. Met.*, 2003, **138**, 311-315.

[Gie04] J. Gierschner, D. Oelkrug, in H. Nalwa (Ed.): *Encyclopedia of Nanoscience and Nanotechnology*, American Scientific Publishers, 2004, **8**, 219-238.

[Gie04a] J. Gierschner, H.-G. Mack, D. Oelkrug, I. Waldner, H. Rau, *J. Phys. Chem. A*, 2004, **108**, 257-263.

[Gie05] J. Gierschner, M. Ehni, H.-J. Egelhaaf, B. Milián Medina, D. Beljonne, H. Benmansour, G. C. Bazan, *J. Chem. Phys.*, 2005, **123**, 144914.

[Gie07] J. Gierschner, J. Cornil, H.-J. Egelhaaf, *Adv. Mater.*, 2007, **19**, 173-191.

[Gie09] J. Gierschner, Y.-S. Huang, B. Van Averbeke, J. Cornil, R. H. Friend, D. Beljonne, *J. Chem. Phys.*, 2009, **130**, 044105.

[Gie13a] J. Gierschner, L. Lüer, B. Milián-Medina, D. Oelkrug, H.-J. Egelhaaf, *J. Phys. Chem.*

Lett., 2013, **4**, 2686-2697.

[Gie13b] J. Gierschner, S. Y. Park, *J. Mater. Chem. C*, 2013, **1**, 5818-5832.

[Gie16] J. Gierschner, S. Varghese, S. Y. Park, *Adv. Opt. Mater.*, 2016, **4**, 348-364.

[Gin08] G. Ginocchietti, E. Cecchetto, L. De Cola, U. Mazzucato, A. Spalletti, *Chem. Phys.*, 2008, **352**, 28-34.

[Glo96] Glossary of basic terms in polymer science (IUPAC Recommendations 1996), PAC, 1996, **68**, 2289.

[Goe84] U. M. Goesele, *Prog. Reaction Kinetics*, 1984, **13**, 63-161.

[Gor87] P. F. Gordon, P. Gregory, *Organic Chemistry in Colour*, Springer 1987.

[Gra13] G. Grancini, M. Maiuri, D. Fazzi, A. Petrozza, H.-J. Egelhaaf, D. Brida,G. Cerullo, G. Lanzani, *Nature Mat.*, 2013, **12**, 29-33.

[Gri04] S. Grimme, J. Comput. Chem., **25**, 1463-1473, 2004.

[Gro90] E.K.U. Gross, W. Kohn, *Adv. Quantum Chem.*, 1990, **21**, 255-291.

[Gul08] A. Gulino, F. Lupo, G. G. Condorelli, M. E. Fragala, M. E. Amato, G. Scarlata, *J. Mater. Chem.*, 2008, **18**, 5011-5018.

[Guo09] J. Guo, H. Ohkita, H. Benten, S. Ito, *J. Am. Chem. Soc.*, 2010, **132**, 6154-6164.

[Han02] W.-G. Han, T. Lovell, T. Liu,L. Noodleman, *ChemPhysChem*, 2002, **3**, 167-178,

[Han12] M. D Hanwell, D. E Curtis, D. C Lonie, T. Vandermeersch, E. Zurek, G. R Hutchison; *J. Cheminformatics*, 2012, 4-17.

[Har28] D.R. Hartree, *Proc. Cambridge Philos. Soc.*, 1928, **24**, 328-342.

[He11] Y. He, Y. Li, *Physical Chemistry Chemical Physics*, 2011, **13**, 1970-1983.

[Hei05] G. Heimel, M. Daghofer, J. Gierschner, E. J. W. List, A. C. Grimsdale, K. Müllen, D. Beljonne, J. L. Brédas, E. Zojer, *J. Chem. Phys.*, 2005, **122**, 054501.

[Hes17] N. J. Hestand, F. C. Spano, *Acc. Chem. Res.*, 2017, **50**, 341-350.

[Hn02] M. Hanack, B. Behnisch, H. Häckl, P. Martinez-Ruiz, K.-H. Schweikart, *Thin Solid Films*, 2002, **417**, 26-31.

[Hoh64] P. Hohenberg and W. Kohn. *Phys. Rev.* B, 1964, **136**, 864-871.

[Hoh98] M. Hohloch, C. Maichle-Mössmer, M. Hanack, *Chem. Mater.,* 1998, **10**, 1327-1332.

[Hor15] A. Horneber, K. Braun, J. Rogalski, P. Leiderer, A. J. Meixner, D. Zhang, *Phys.Chem.Chem.Phys.*, 2015, **17**, 21288-21293.

[Hot93] S. Hotta, K. Waragai, *Adv. Mater.*, 1993, **5**, 896-908.

[Hsu05] F.-C. Hsu, S. H. Lin, J.-K. Wang, *Chem. Phys. Lett.*, 2005, **411**, 103-107.

[Hua11] Y.-S. Huang, J. Gierschner, J. P. Schmidtke, R. H. Friend, D. Beljonne, *Phys. Rev. B*, 2011, **84**, 205311.

[Hur73] B. Huron, P. Rancurel, J.P. Malrieu, *J. Chem. Phys.*, 1973, **58**, 5745.

[Kas65] M. Kasha, H. R. Rawls, M. Ashraf El-Bayoumi, *Pure Appl. Chem.,* 1965, **11**, 371-392.

[Kle95] M. Klessinger, J. Michl, *Excited States and Photochemistry of Organic Molecules*, VCH, Weinheim, 1995.

[Ko17] E. Y. Ko, G. E. Park, J. H. Lee, H. J. Kim, D. H. Lee, H. Ahn, M. A. Uddin, H. Y. Woo, M. J. Cho, D. H. Choi, *ACS Appl. Mater. Interfaces*, 2017, **9**, 8838-8847.

[Koh65] W. Kohn and L.J. Sham, *Phys. Rev.*, 1965, **140**, A1133-1138.

[Koh98] B. E. Kohler, T. Itoh, *J. Phys. Chem.*, 1988, **92**, 5120-5122.

[Kov10] S. A. Kovalenko, A. L. Dobryakov, I. Ioffe, N. P. Ernsting, *Chem. Phys. Lett.,* 2010, **493**, 255-258.

[Kru98] B. P. Krueger, G. D. Scholes, and G. R. Fleming, *J. Phys. Chem. B*, 1998, **102**, 5378-5386.

[Kwo15] O K. Kwon, J.-H. Park, D. W. Kim, S. K. Park, S. Y. Park, *Adv. Mater.*, 2015, **27**, 1951-1956.

[Kwo15b] O. K. Kwon, J.-H. Park, S. K. Park, S. Y. Park, *Adv. Energy Mater.*, 2015, **5**, 1400929.

[Kwo16] (a) O. K. Kwon, J.-H. Park, S. Y. Park, *Org. Electron.*, 2016, **30**, 105-111; (b) G. Feng, Y. Xu, J. Zhang, Z. Wang, Y. Zhou, Y. Li, Z. Wei, C. Li, W. Li, *J. Mater. Chem.*

A, 2016, **4**, 6056-6063; (c) J. Min, O. Kyu Kwon, C. Cui, J.-H. Park, Y. Wu, S. Y. Park, Y. Li, C. J. Brabec, *J. Mater. Chem. A*, 2016, **4**, 14234-14240; (d) R. Xin, J. Feng, C. Zeng, W. Jiang, L. Zhang, D. Meng, Z. Ren, Z. Wang, S. Yan, *ACS Appl. Mater. Interfaces*, 2017, **9**, 2739-2746.

[Kya13] (a) A. K. K. Kyaw, D. H. Wang, D. Wynands, J. Zhang, T.-Q. Nguyen, G. C. Bazan, A. J. Heeger, *Nano Lett.*, 2013, **13**, 3796-3801; (b) V. Gupta, A. K. K. Kyaw, D. H. Wang, S. Chand, G. C. Bazan, A. J. Heeger, *Sci. Rep.*, 2013, **3**, 1965.

[Lan01] F. J. Lange, M. Leuze, M. Hanack, *J. Phys. Org. Chem.*, 2001, **14**, 474-480.

[Lan99] F. Lange, D. Hohnholz, M. Leuze, H. Ryu, M. Hohloch, R. Freudenmann, M Hanack, *Synth. Met.*, 1999, **101**, 652-653.

[Laq10] I. A. Howard, R. Mauer, M. Meister, F. Laquai, *J. Am. Chem. Soc.*, 2010, **132**, 14866-14876.

[Leu02] M. Leuze, M. Hohloch, M. Hanack, *Chem. Mater.*, 2002, **14**, 3339-3342.

[Lev07] B. G. Levine, T. J. Martínez, *Annu. Rev. Phys. Chem.*, 2007, **58**, 613-634.

[Li12] X. Li, Y. Xu, F. Li, Y. Ma, *Org. El.*, 2012, **13**, 762-766.

[Li14] K. Li, B. Liu, Chem. *Soc. Rev.*, 2014, **43**, 6570-6597.

[Li16] S. Li, L. Ye, W. Zhao, S. Zhang, S. Mukherjee, H. Ade, J. Hou, *Adv. Mater.*, 2016, **28**, 9423-9429.

[Lia17] N. Liang, W. Jiang, J. Hou, Z. Wang, *Mater. Chem. Front.*, 2017 in print.

[Lin12] Y. Lin, Y. Li, X. Zhan, *Chem. Soc. Rev.*, 2012, **41**, 4245-4272.

[Lin14] Y. Lin, X. Zhan, *Mater. Horiz.*, 2014, **1**, 470-488.

[Liu13] (a) Y. Liu, C.-C. Chen, Z. Hong, J. Gao, Y. Yang, H. Zhou, L. Dou, G. Li, Y. Yang, *Sci. Rep.*, 2013, **3**, 3356-3364; (b) B. Kan, Q. Zhang, M. Li, X. Wan, W. Ni, G. Long, Y. Wang, X. Yang, H. Feng, Y. Chen, *J. Am.Chem. Soc.*, 2014, **136**, 15529-15532.

[Lon17] M. G. S. Londesborough, .J. Dolanský, L. Cerdán, K. Lang, T. Jelínek, J. M. Oliva, D. Hnyk, D. Roca-Sanjuán, A. Francés-Monerris,J. Martinčík, M. Nikl, J. D. Kennedy, *Adv. Opt. Mater.*, 2017, **5**, 1600694.

[Lov13] J. A. Love, C. M. Proctor, J. Liu, C. J. Takacs, A. Sharenko, T. S. van der Poll, A. J. Heeger, G. C. Bazan, T.-Q. Nguyen, *Adv. Funct. Mater.*, 2013, **23**, 5019-5026.

[Löw02] (a) C. Löwe, C. Weder, *Adv. Mater.*, 2002, **14**, 1625-1629; (b) B. R. Crenshaw, C. Weder, *Chem. Mater.*, 2003, **15**, 4717-4724; (c) B. R. Crenshaw, C. Weder, *Adv. Mater.*, 2005, **17**, 1471-1476; (d) J. Kunzelman, M. Kinami, B. R. Crenshaw, J. D. Protasiewicz, C. Weder, Adv. Mater., 2008, **20**, 119-122. (e) B. R. Crenshaw, M. Burnworth, D. Khariwala, A. Hiltner, P. T. Mather, R. Simha, C. Weder, *Macromol.*, 2007, **40**, 2400-2408; (f) J. Kunzelman, B. R. Crenshaw, C. Weder, *J. Mater. Chem.*, 2007, **17**, 2989-2991; (g) B. T. Makowski, J. Lott, B. Valle, K. D. Singer, C. Weder, *J. Mater. Chem.*, 2012, **22**, 5190-5196

[Luo01] J. Luo, Z. Xie, J. W. Lam, L. Cheng, H. Chen, C. Qiu, H. S. Kwok, X. Zhan, Y. Liu, D. Zhu, B. Z. Tang, *Chem. Commun.*, 2001, 1740-1741.

[Mac09] G. Macchi, B. Milián Medina, M. Zambianchi, R. Tubino, J. Cornil, G. Barbarella, J. Gierschner, F. Meinardi, *Phys.Chem.Chem.Phys.*, 2009, **11**, 984-990.

[Mag12] L. Maggini and D. Bonifazi, *Chem. Soc. Rev.*, 2012, **41**, 211-241.

[Mar03] E. Marri, D. Pannacci, G. Galiazzo, U. Mazzucato, A. Spalletti, *J. Phys. Chem. A*, 2003, **107**, 11231-11238.

[Mar10] A. Marsh, J. M. Hodgkiss, S. Albert-Seifried, R. H. Friend, *Nano. Letters*, 2010, **10**, 923-930, DOI: 10.1021/nl9038289.

[Mar16] M. Martínez-Abadía, S. Varghese, R. Giménez, M. B. Ros, *J. Mater. Chem. C*, 2016, **4**, 2886-2893.

[Mec53] A. Meckler, *J. Chem. Phys.*, 1953, **21**, 1750.

[Mei03] F. Meinardi, M. Cerminara, A. Sassella, R. Bonifacio, R. Tubino, *Phys. Rev. Lett.*, 2003, **91**, 247401.

[Mer08] Mercury, C. F. Macrae, I. J. Bruno, J. A. Chisholm, P. R. Edgington, P. McCabe, E. Pidcock, L. Rodriguez-Monge, R. Taylor, J. van de Streek and P. A. Wood, *J. Appl. Cryst.*, 2008, **41**, 466-470.

[Mik12] O. V. Mikhnenko, H. Azimi, M. Scharber, M. Morana, P. W. M. Blom, M. A. Loi, *Energy Environ. Sci.*, 2012, **5**, 6960-6965.

[Mil04] B. Milián-Medina, Tesis Doctoral, Universidad de Valèncía, Spain, 2004.

[Mil08] B. Milián-Medina, J. E. Anthony, J. Gierschner, *ChemPhysChem.*, 2008, **9**, 1519-1523.

[Mil11] B. Milián-Medina, S. Varghese, R. Ragni, H. Boerner, E. Ortí, G. M. Farinola, and J. Gierschner, *J. Chem. Phys.*, 2011, **135**, 124509.

[Mil16] R. Milad, J. Shi, A. Aguirre, A. Cardone, B. Milián-Medina, G. M. Farinola, M. Abderrabba, J. Gierschner, *J. Mater. Chem. C*, 2016, **4**, 6900-6906.

[Mil17] B. Milián-Medina, J. Gierschner, *J. Phys. Chem. Lett.*, 2017, **8**, 91-101.

[Mis12] A. Mishra, P. Bäuerle, *Angew. Chem. Int. Ed.*, 2012, **51**, 2020-2067.

[Mol34] C. Møller, M.S. Plesset, *Phys. Rev.*, 1934, **46**, 618.

[Mol16] Molcas 8.0: F. Aquilante, J. Autschbach, R. K. Carlson, L. F. Chibotaru, M. G. Delcey, L. De Vico, I. Fdez. Galván, N. Ferré, L. M. Frutos, L. Gagliardi, M. Garavelli, A. Giussani, C. E. Hoyer, G. Li Manni, H. Lischka, D. Ma, P. Å. Malmqvist, T. Müller, A. Nenov, M. Olivucci, T. B. Pedersen, D. Peng, F. Plasser, B. Pritchard, M. Reiher, I. Rivalta, I. Schapiro, J. Segarra-Martí, M. Stenrup, D. G. Truhlar, L. Ungur, A. Valentini, S. Vancoillie, V. Veryazov, V. P. Vysotskiy, O. Weingart, F. Zapata, R. Lindh, *J. Comp. Chem.*, 2016, **37**, 506-541.

[Nat75] National Research Council. *Materials and Man's Needs: Materials Science and Engineering -- Volume I, The History, Scope, and Nature of Materials Science and Engineering*, 1975, Washington, DC: The National Academies Press. https://doi.org/10.17226/10436.

[Nat95] National Research Council. *Computational and Theoretical Techniques for Materials Science*, 1995, Washington, DC: The National Academies Press. https://doi.org/10.17226/9025.

[Ng15] K. K. Ng, G. Zheng, *Chem. Rev.*, 2015, **115**, 11012-11042.

[Niu10] Y. Niu, Q. Peng, C. Deng, X. Gao, Z. Shuai, *J. Phys. Chem. A*, 2010, **114**, 7817-7831.

[NREL] https://www.nrel.gov/pv/assets/images/efficiency-chart.png

[Oel01] D. Oelkrug, J. Gierschner, H.-J. Egelhaaf, L. Lüer, A. Tompert, K. Müllen, U. Stalmach, H. Meier, *Synth. Met.*, 2001, **121**, 1693-1694.

[Oel96] D. Oelkrug, A. Tompert, H.-J. Egelhaaf, M. Hanack, E. Steinhuber, M. Hohloch, H. Meier and U. Stalmach, *Synth. Met.*, 1996, **83**, 231-237.

[Oel98] D. Oelkrug, A. Tompert, J. Gierschner, H.-J. Egelhaaf, M. Hanack, M. Hohloch, E. Steinhuber, *J. Phys. Chem. B*, 1998, **102**, 1902-1097.

[Oli17] E. F. Oliveira, J. Shi, F. C. Lavarda, L. Lüer, B. Milián-Medina, J. Gierschner, J. Chem. Phys., 2017, **147**, 034903.

[Ost16] O. Ostroverkhova, *Chem. Rev.*, 2016, **116**, 13279-13412.

[Pen16] X.-L. Peng, S. Ruiz-Barragan, Z.-S. Li, Q.-S. Li, L. Blancafort, *J. Mater. Chem. C*, 2016, **4**, 2802-2810.

[Pev11] R. Peverati and D. G. Truhlar, *J. Chem. Phys.*, 2011, **135**, 191102.

[Pie95] K. Pierloot, B. Dumez, P.-O. Widmark, B. O. Roos, *Theor. Chim. Acta*, 1995, **90**, 87-144.

[Pol12] T. S. van der Poll, J. A. Love, T.-Q. Nguyen, G. C. Bazan, *Adv. Mater.*, 2012, **24**, 3646-3649.

[Prl16] A. Prlj, N. Doslic, C. Corminboeuf, *Phys. Chem. Chem. Phys.*, 2016, **18**, 11606-11609.

[Ral76] K. Ralls, T. H. Courtney, and J. Wulff, *Introduction to Materials Science and Engineering*. John Wiley & Sons, 1976.

[Ran07] B. P. Rand, J. Genoe, P. Heremans, J. Poortmans, *Progress in Photovoltaics*, 2007, **15**, 659-676.

[Ree17] T. A. Reekie, M. Sekita, L. M. Urner, S. Bauroth, L. Ruhlmann, J.-P. Gisselbrecht, C. Boudon, N. Trapp, T. Clark, D. M. Guldi, F. Diederich, *Chem. Eur.J.*, 2017, **23**, 6357-6369.

[Rei16] M. Reichenberger, J. A. Love, A. Rudnick, S. Bagnich, F. Panzer, A. Stradomska, G. C. Bazan, T.-Q. Nguyen, A. Köhler, *J. Chem. Phys.*, 2016, **144**, 074904.

[Rob77] J. D. Roberts, and M. C. Caserio, *Basic Principles of Organic Chemistry*, 1977, second edition W. A. Benjamin, Inc., Menlo Park, CA. ISBN 0-8053-8329-8.

[Roc12] D. Roca-Sanjuán, F. Aquilante, R. Lindh, *WIREs Comp. Mol. Sci.*, 2012, **2**, 585-603.

[Rog16] J. Rogalski, K. Braun, A. Horneber, M. van den Berg, J. Uihlein, H. Peisert, T. Chassé, A. J. Meixner, D. Zhang, *Vibr. Spectroscop.*, 2017, **91**, 128-135.

[Ron14] J. Roncali, P. Leriche, P. Blanchard, *Adv. Mater.*, 2014, **26**, 3821-3828.

[Roo51] Roothaan, *C. Rev. Mod. Phys.*, 1951, **23**, 69-89.

[Roo80] (a) B.O. Roos, P.R. Taylor, P.E.M. Siegbahn, *Chem. Phys.*, 1980, **48**, 157; (b) B.O. Roos, *Int. J. Quantum Chem. Symp.*, 1980, **14**, 175-189; (c) B.O. Roos, en *Advances in Chemical Physics; Ab Initio Methods in Quantum Chemistry-II*, (K.P. Lawley, ed.), John Wiley & Sons Ltd., 1987, 399.

[Roy79] R. Roy, *Interdisciplinarity and Higher Education*, J.J. Kockelmans (Ed.), Pennsylvania State University Press, 1979, 96-161.

[Sad02] Sheldrick, G. M. SADABS: Program for Performing Absorption Corrections to Single-Crystal X-ray Diffraction Patterns; University of Göttingen, Göttingen, Germany, 2002.

[Sai00] SAINT, Bruker AXS Inc., Madison, WI, 2000.

[Sal03] J. Saltiel, Y. P. Sun, in *Photochromism* (Ed.: H. D. Bouas-Laurent), Elsevier Science, Amsterdam, 2003, 64-164.

[Sal68] J. Saltiel, 0. C. Zafirious, E. D. Megarity, A. A. Lamola, *J. Am. Chem. Soc.*, 1968, **90**, 4759-4760.

[San90] (a) K. Sandros, M. Sundahl, O. Wennerström, U. Norinder, *J. Am. Chem. Soc.*, 1990, **112**, 3082-3086; (b) M. Sundahl, O. Wennerström, K. Sandros, T. Arai, K. Tokumaru, *J. Phys. Chem.*, 1990, **94**, 6731-6734.

[Sau15] G. Sauvé, R. Fernando, *J. Phys. Chem. Lett.*, 2015, **6**, 3770-3780.

[Sch01] K.-H. Schweikhart, M. Hohloch, E. Steinhuber, M. Hanack, L. Lüer, J. Gierschner, H.-J. Egelhaaf, D. Oelkrug, *Synth. Met.*, 2001, **121**, 1641-1642.

[Sch10] F.A. Schaberle, R.M.D. Nunes, M. Barroso, C. Serpa, L.G. Arnaut, *Photochem. Photobiol. Sci.*, 2010, **9**, 812-822

[Sei99] S. Seixas de Melo, L. M. Silva, L. G. Arnaut, R. S. J. Becker, *J. Chem. Phys.*, 1999, **111**, 5427-5433.

[Seo14] J. Seo , J. W. Chung , J. E. Kwon, S. Y. Park, *Chem. Sci.*, 2014, **5**, 4845-4850.

[Ser00] C. Serpa, L.G.Arnaut, *J. Phys. Chem. A*, 2000, **104**, 11075-11086.

[Sha10] P. E. Shaw, A. Ruseckas, J. Peet, G. C. Bazan, I. D. W. Samuel, *Adv. Funct. Mater.*, 2010, **20**, 155-161.

[She01] Sheldrick, G. M. SHELXTL: Suite of Programs for Crystal Structure Analysis, Incorporating Structure Solution (XS), Least- Squares Refinement (XL), and Graphics (XP); University of Göttingen, Göttingen, Germany, 2001.

[Shi10] M. Shimizu, T. Hiyama, *Chem. Asian J.*, 2010, **5**, 1516-1531.

[Sir01] P. J. Brown, H. Sirringhaus, M. Harrison, M. Shkunov, R.H. Friend, *Phys. Rev. B*, 2001, **63**, 125204.

[Spa03] F. C. Spano, *Chem. Phys. Lett.*, 2000, **331**, 7-13.

[Spa10] F. C. Spano, *Acc. Chem. Res.*, 2010, **43**, 429-439.

[Sri09] G. Srinivasan, J. A. Villanueva-Garibay, K. Müller, D. Oelkrug, B. Milián Medina, D. Beljonne, J. Cornil, M. Wykes, L. Viani, J. Gierschner, R. Martinez Alvarez, M. Jazdzyk, M. Hanack, H.-J. Egelhaaf, *Phys.Chem.Chem.Phys.*, 2009, **11**, 4996-5009.

[Ste07] R. F. Stephen, and E. T. Mark, *Chem. Rev.*, 2007, **107**, 923-925.

[Str62] S. J. Strickler, R. A. Berg, *J. Chem. Phys.*, 1962, **37**, 814-821;

[Tan08] Y. Tanaka, N. Sasaki, and A. Ohmiya, *The Plant Journal*, 2008, **54**, 733-749.

[Tan13] B. Z. Tang, A. Qin (Eds.), *Aggregation-Induced Emission: Applications*, Wiley 2013.

[Toz98] D.J. Tozer, N.C. Handy, *J. Chem. Phys.*, 1998, **109**, 10180-10189.

[Toz99] D.J. Tozer, R.D. Amos, N.C. Handy, B.O. Roos, L. Serrano- Andres, *Mol. Phys.*, 1999, **97**, 859-868.

[Van02] C. M. L. Vande Velde, F. Blockhuys, C. Van Alsenoy, A. T. H. Lenstra, H. J. Geise, *J. Chem. Soc., Perkin Trans.* 2002, **2**, 1345-1351.

[Var11] Varghese, S. Das, S. *J. Phys. Chem. Lett.*, 2011, **2**, 863-873.

[Var12] S. Varghese, S.-J. Yoon, E. M. Calzado, S. Casado, P. G. Boj, M. A. Díaz-García, R. Resel, R. Fischer, B. Milián-Medina, R. Wannemacher, S. Y. Park, J. Gierschner, *Adv. Mater.*, 2012, **24**, 6473-6478.

[Var13] S. Varghese, S. K. Park, S. Casado, R. Fischer, R. Resel, B. Milián-Medina, R. Wannemacher, S. Y. Park, J. Gierschner, *J. Phys. Chem. Lett.*, 2013, **4**, 1597-1602.

[Var14] S. Varghese, S-J. Yoon, S. Casado, R. Fischer, R. Wannemacher, S. Y. Park, J. Gierschner, *Adv. Opt. Mater.*, 2014, **2**, 542-548.

[Var16] S. Varghese, S. K. Park, S. Casado, R. Resel, R. Wannemacher, L. Lüer, S. Y. Park, J. Gierschner, *Adv. Funct. Mater.*, 2016, **26**, 2349-2356.

[Vel16] E. Vella, H. Li, P. Grégoire, S. M. Tuladhar, M. S. Vezie, S. Few, C. M. Bazán, J. Nelson, C. Silva-Acuña, and E. R. Bittner, *Scientific Reports*, 2016, **6**, 29437.

[Vik74] J. P. Vikesland, S. J. Strickler, *J. Chem. Phys.*, 1974, **60**, 660-663.

[Wan10] X. Wang, D. Zhang, K. Braun, H.-J. Egelhaaf, C. J. Brabec, A. J. Meixner, *Adv. Funct. Mater.*, 2010, **20**, 492-499.

[Wan11] X. Wang, H. Azimi, H.-G. Mack, M. Morana, H.-J. Egelhaaf, A. J. Meixner, D. Zhang, *Small*, 2011, **7**, 2793-2800.

[Wan14] X. Wang, H.-J. Egelhaaf, H.-G. Mack, H. Azimi, C. J. Brabec, A. J. Meixner, D. Zhang, *Adv. Energy Mater*., 2014, 1400497.

[Wäs97] C. Wästlund, F. H. J. Maurer, *Macromol.*, 1997, **30**, 5870-5876.

[Won98] K. S. Wong, H. Wang, G. Lanzani, *Chem. Phys. Lett.*, 1998, **288**, 59-64.

[Wu03] C. C.Wu, M. C. DeLong, Z. V. Vardeny, J. P. Ferraris, J. J. Gutierrez, *Synth. Met.*, 2003, **137**, 939-941.

[Wu05] C. C. Wu, E. Ehrenfreund, J. J. Gutierrez, J. P. Ferraris, Z. V. Vardeny, *Phys. Rev. B*, 2005, **71**, 081201.

[Wür11] F. Würthner, T. E. Kaiser, C. R. Saha-Möller, *Angew. Chem. Int. Ed.*, 2011, **50**, 3376-3410.

[Wür16] F. Würthner, C. R. Saha-Möller, B. Fimmel, S. Ogi, P. Leowanawat, D. Schmidt, *Chem. Rev.*, 2016, **116**, 962-1052.

[Wyk15a] M. Wykes, R. Parambil Mangattu, D. Beljonne, J. Gierschner, *J. Chem. Phys.*, 2015, **143**, 114116.

[Wyk15b] M. Wykes, S. K. Park, S. Bhattacharyya, S. Varghese, J. E. Kwon, D. R. Whang, I. Cho, R. Wannemacher, L. Lüer, S. Y. Park, J. Gierschner, *J. Phys. Chem. Lett.*, 2015, **6**, 3682-3687.

[Xu12] Y. Xu, H. Zhang, F. Li, F. Shen, H. Wang, X. Li, Y. Yu, Y. Ma, *J. Mater. Chem.*, 2012, **22**, 1592-1597.

[Xu16a] Y. Xu, K. Wang, Y. Zhang, Z. Xie, B. Zou, Y. Ma, *J. Mater. Chem. C*, 2016, **4**, 1257-1262.

[Xu16b] Y. Xu, Z. Xie, H. Zhang, F. Shen, Y. Ma, *CrystEngComm*, 2016, **18**, 6824-6829.

[Yan11] Z.-Q. Yan, Z.-Y. Yang, H. Wang, A.-W. Li, L.-P. Wang, H. Yang, B.-R. Gao, *Spectrochim. Acta A*, 2011, **78**, 1640-1645.

[Yan17] (a) L. Yang, S. Zhang, C. He, J. Zhang, H. Yao, Y. Yang, Y. Zhang, W. Zhao, J. Hou, *J. Am. Chem. Soc.*, 2017, **139**, 1958-1966; (b) H. Bin, Y. Yang, Z.-G. Zhang, L. Ye, M. Ghasemi, S. Chen, Y. Zhang, C. Zhang, C. Sun, L. Xue, C. Yang, H. Ade, Y. Li, *J. Am. Chem. Soc.*, 2017, **139**, 5085-5094.

[Yeh04] H.-C. Yeh, W.-C. Wu, Y.-S. Wen, D.-C. Dai, J.-K. Wang, C.-T. Chen, *J. Org. Chem.*, 2004, **69**, 6455-6462.

[Yoo10] S.-J. Yoon, J. W. Chung, J. Gierschner, K. S. Kim, M.-G. Choi, D. Kim, S. Y. Park, *J. Am. Chem. Soc.*, 2010, **132**, 13675-13683.

[Yoo11a] S.-J. Yoon and S. Y. Park, *J. Mater. Chem.*, 2011, **21**, 8338-8346.

[Yoo11b] S.-J. Yoon, J. H. Kim, J. W. Chung and S. Y. Park, *J. Mater. Chem.*, 2011, **21**, 18971-18973.

[Yoo13] S.-J. Yoon, S. Varghese, S. K. Park, R. Wannemacher, J. Gierschner, S. Y. Park, *Adv.*

Opt. Mater., 2013, **1**, 232-237.

[Zha16] W. Zhang, J. Yao, Y. S. Zhao, *Acc. Chem. Res.*, 2016, **49**, 1691-1700.

[Zha17] J. Zhang, S. Ma, H. Fang, B. Xu, H. Sun, I. Chan, W. Tian, *Mater. Chem. Front.*, 2017, **1**, 1422-1429.

[Zhu13] L. Zhu and Y. Zhao, *J. Mater. Chem. C*, 2013, **1**, 1059-1065.

[Zol03] H. Zollinger, *Color Chemistry*, 3rd rev. Verlag Helvetica Chimica Acta; Wiley-VCH, Weinheim, 2003, 1201-1213. DOI: 10.1039/c6qm00247a.

Appendix 1

X-ray Result

Table A1.1 Summary of crystallographic data for PM3 of **β-DCS**.

Parameters	**β-DCS** (PM3)	
Empirical formula	$C_{24}H_{16}N_2$	
Formula weight	332.39	
T, K	296.(2)	
λ, Å	0.71073 Å	
Crystal system	monoclinic	
Space group	*P-1 21/n 1*	
a, Å	5.8602(15)	
b, Å	3.9118(10)	
c, Å	36.866(9)	
α, deg	90	
β, deg	94.433(14)	
γ, deg	90	
V, Å^3	842.6(4)	
Z	2	
d_{calc}, Mg/m^3	1.310	
F(000)	348	
μ ($Mo_{K\alpha}$), mm^{-1}	0.077	
Theta range for data collection, °	3.33 to 28.26	
Limiting indices	$-6 \leq h \leq 6$,	$-4 \leq k \leq 4$, $-43 \leq l \leq 43$
Goodness-of-fit on F^2	1.095	

Appendix 2

TCSPC Data Analysis

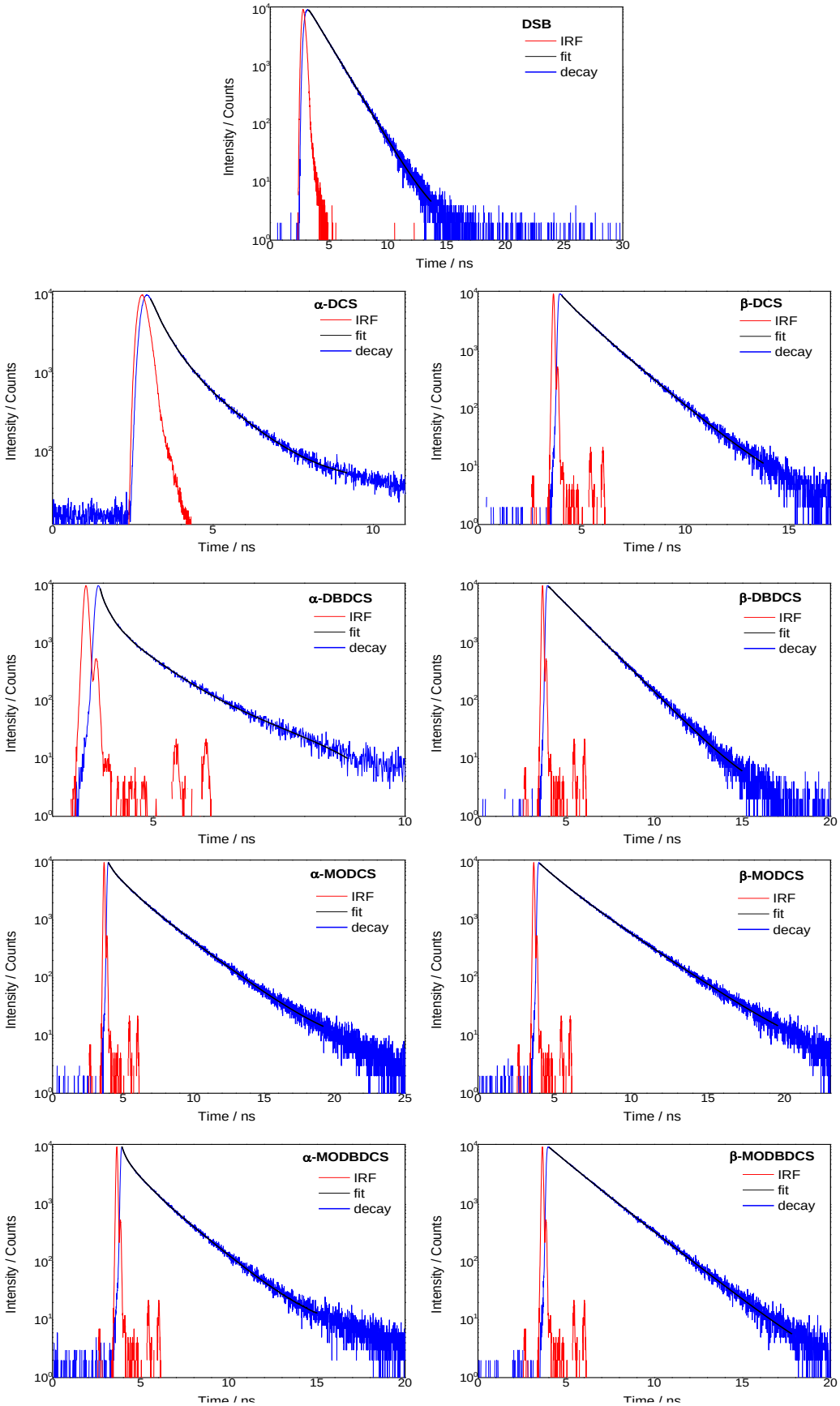

Figure A1.1a:TCSPC time traces (blue), instrumental response function (red) and exponential fit (black) of **DSB** and the **DCS**-compounds in $CHCl_3$.

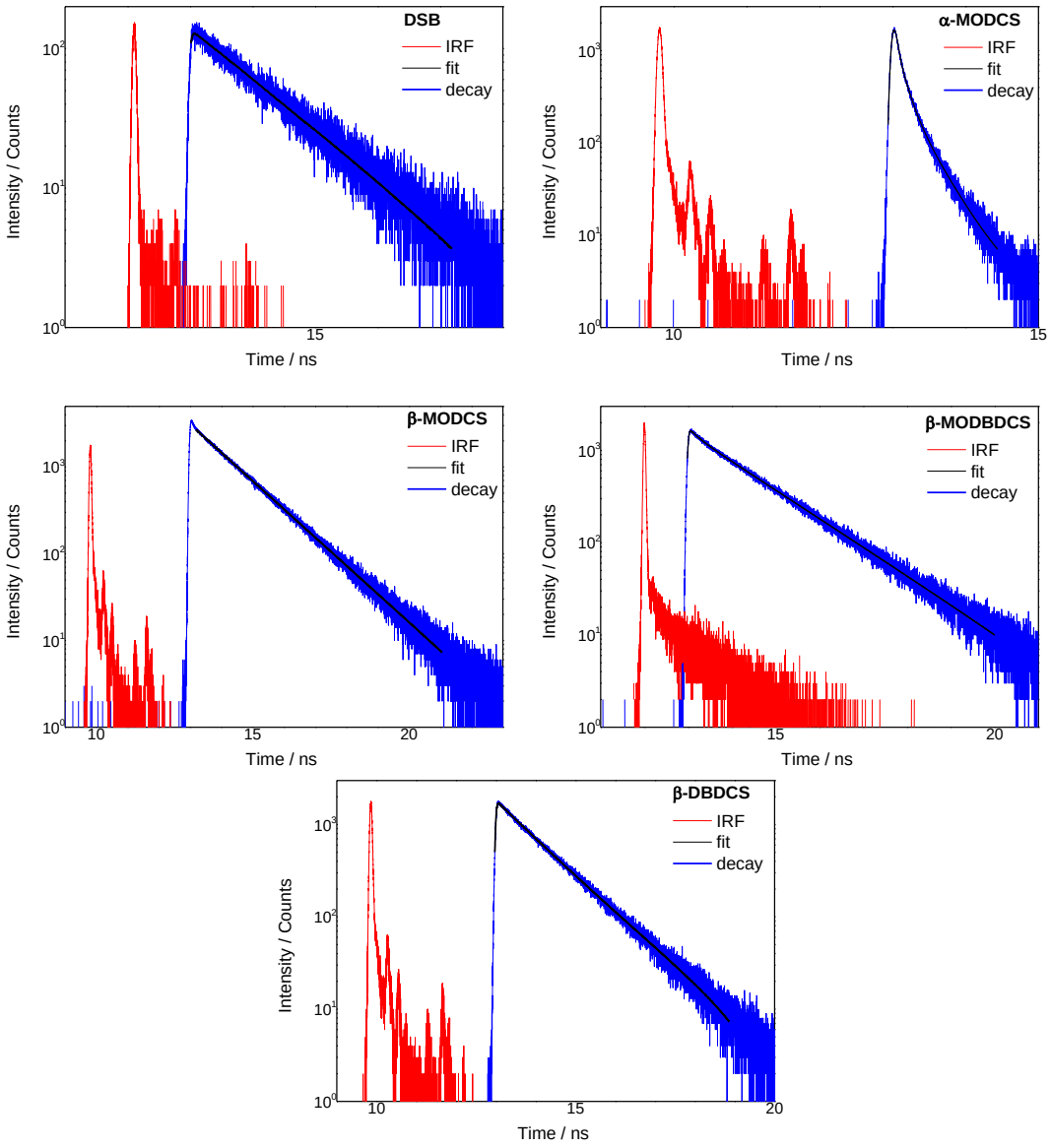

Figure A1.1b:TCSPC time traces (blue), instrumental response function (red) and exponential fit (black) of **DSB** and the **DCS**-compounds in PMMA.

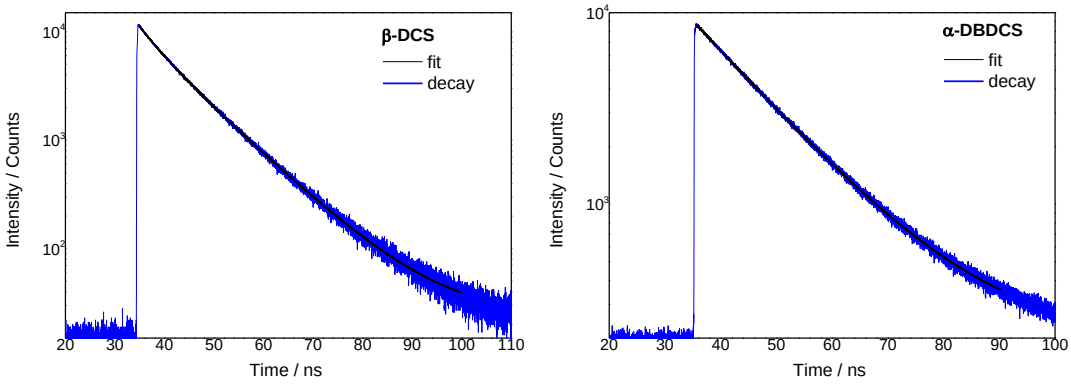

Figure A1.1c:TCSPC time traces (blue), exponential fit (black) of **DSB** and the **DCS**-compounds in single crystals.

Appendix 3

TA Data Analysis

CONTENTS

Appendix 3.1 TA Data Analysis in the DCS-compounds

We performed *f*s TA measurements on the 1,4-Dioxane solutions of the **DCS**-compounds (Scheme 4.1), in order to catch the ultrafast (*f*s-*p*s) processes during the excited state deactivation. The description of the setup see Section 3.2.1, the obtained rate constants see Table A3.1/4.14, and the details/procedures of the data analysis see below.

It is known for some of the investigated compounds that after excitation of the lowest energetic transition, solvent reorganization a/o planarization dynamics occur on a femtosecond to early picosecond time scale.[Won98] These phenomena are observable in transient absorption (TA) spectra as spectral evolutions of the photoinduced absorption (PA) and stimulated emission bands. In order to characterize these phenomena, we performed a global fitting highlighting the first 10 ps after careful removal of the chirp of the probe pulse and the coherent artifact of the solvent. Figure A3.1 shows an example of the procedure. Then a global fitting procedure is performed on the right panel of Figure A3.1, assuming a two-state sequential model. This simple model is of course not justified to describe solvent reorganization and planarization dynamics, both being processes involving a multitude of energy levels and associated rate constants. However, it is not the scope of this subject to model early exciton relaxation dynamics; for such scope a different quantum mechanical approach would be needed. Therefore, the resulting first order time constants should be seen

as characteristic time constants for the underlying complex kinetics, and the resulting characteristic spectra should be seen as evolution-associated differential spectra.[Sto04]

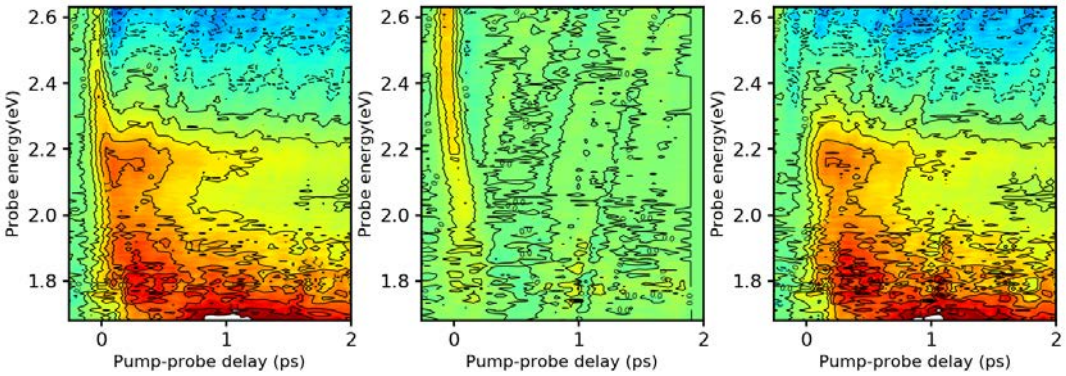

Figure A3.1: Transient absorption (TA) spectroscopy in **α-DBDCS** in Dioxane. Left: as-measured & chirp removed; middle: coherent artifact of Dioxane measured at the same pump intensity; right: TA spectrum with coherent artifact of solvent removed.

Global fitting is resolving the well-known Beer-Lambert Law by stating it as a matrix equation,

$$A(\lambda, t) = \sigma(\lambda, i) \cdot n(i, t) \tag{A3.1}$$

A(λ,t) being the time and probe-wavelength-resolved transient absorption, σ(λ,i) the cross-section spectrum for component i, and n(i,t) the area density of component i, where $n(i,t) = \sum_{x=0}^{d} c(i,x,t)$, c(i,x,t) being the depth (x) resolved concentration of compound i at time t. We minimize the squared error between the measured A(λ,t) and the one calculated in eq. A3.1 by two nested nonlinear optimizations: the inner one solves eq. A3.1 for σ(λ,i) by Gaussian elimination for a given n(i,t), which in turn is optimized by the outer one varying the two first order rate constants for a unidirectional two-states model $0 \xrightarrow{g} A \xrightarrow{k_1} B \xrightarrow{k_2} 0$. The instrumental time resolution is modeled by a Gaussian generation function. Table A3.1/4.14 shows the obtained rate constants.

Table A3.1/4.14: Excited state lifetimes obtained from *fs* transient absorption studies via global fit analysis at sub 15 ps times (τ_1) and sub 400 ps times (τ_2).

	τ_1 / ps	τ_2 / ps
α-DCS	0.43	5.7
α-DBDCS	0.41	4.0
α-MODCS	0.91	190

α-MODBDCS	0.59	13
β-DCS	0.37	22
β-MODCS	0.92	> 400 ps
β-MODBDCS	0.57	> 400 ps

Appendix 3.2 TA Data Analysis in the Photovoltaic D-A Blend

A3.2.1 TA Spectroscopy Analysis

a) Absorption cross-sections

Lambert-Beer's Law relates the optical density OD to the concentration of an absorber or molecule or monomer, C_m, given in M=moles/liter:

$$OD = -log_{10}T = \varepsilon_m \cdot C_m \cdot d \tag{A3.2}$$

Herein, $T = I_{tr}/I_0$ is the transmission, given by the ratio of transmitted to incident light (I_{tr} and I_0, respectively), d is the film thickness, and ε_m is the molar extinction coefficient, given in units of cm^{-1} M^{-1}. This definition is handy for analytical chemistry. Physicists define Lambert-Beer's law by the natural absorbance A_n:

$$A_n = -\ln T = \sigma_m \cdot c_m \cdot d \tag{A3.3}$$

Herein, the film thickness d is given in cm, the concentration c_m is given in cm^{-3} so that the absorption cross-section σ_m attains the unit cm^2. By using the definition of the base of a logarithm,

$$\log_{10} T = \ln T / \ln 10 \tag{A3.4}$$

we can insert A3.2 and A3.3 into A3.4 and obtain

$$\varepsilon_m \cdot C_m \cdot d = \sigma_m \cdot c_m \cdot d / \ln 10 \tag{A3.5}$$

Expressing C_m in units of c_m, that is

$$C_m = c_m \cdot r_{conv}/N_A \tag{A3.6}$$

N_A=6.022e23 mol^{-1} being Avogadro's constant and r_{conv} = 1000 cm^3/dm^3 the conversion factor between cubic centimeters and liters, we obtain

$$\sigma_m = \varepsilon_m \cdot r_{conv} \cdot \ln 10 / N_A \quad \text{(A3.7)}$$

showing that it is simple to go from σ_m to ε_m and back. Both depend on the irradiated wavelength λ in the same way. The definition of an absorber can be freely chosen; the choice will define the unit for the exciton size in section B. In conjugated polymers, it is convenient to choose a repetition unit as the monomer, while in small molecules, the monomer is obviously the molecule itself. Once a monomer is chosen, its concentration is calculated by

$$c_m = \rho / m_m \quad \text{(A3.8)}$$

where ρ is the specific density of the film (in g cm^{-3}), and m_m is the mass of a monomer in g. Using molecular masses of 1219.89 and 1019.28 g/mol for the donor and acceptor molecule, and a typical density of 1.3 g/cm^3, a film thickness of 95 nm gives the ground state absorption cross-sections as shown in Figure A3.2.

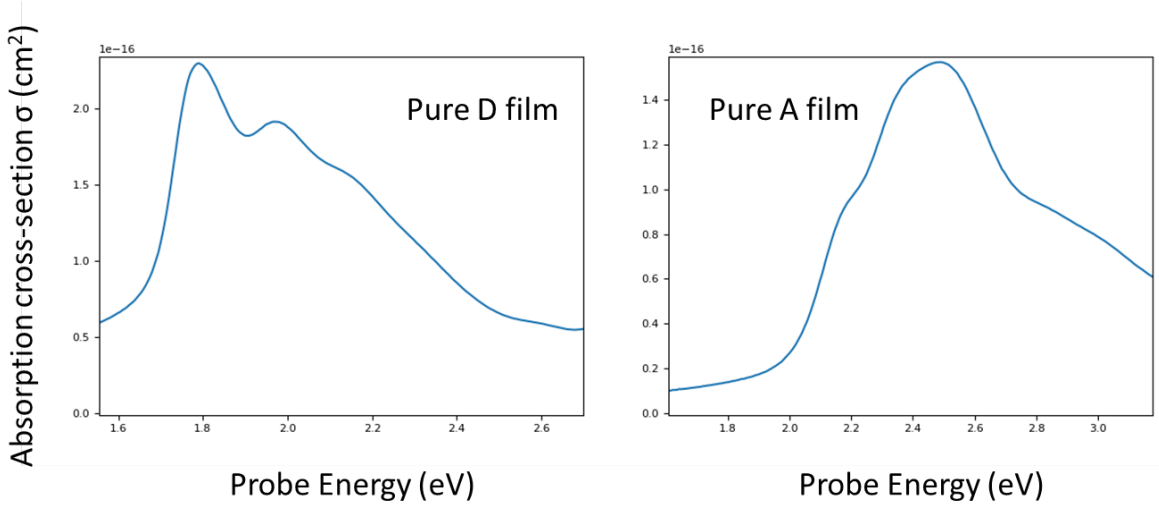

Figure A3.2: Absolute absorption cross sections of pure donor and acceptor films (left and right panel, respectively).

b) Calculation of Excited State Delocalization

Quantitative theory of transient photobleach. The theory of transient excitonic optical nonlinearities has been elaborated for two-dimensional excitons[Sch85] and later applied also

to quasi one-dimensional excitons in carbon nanotubes.[Lue09] The theory relies on the phase space filling model (PSF) requiring that an exciton state cannot be excited twice, because the Pauli exclusion principle must hold. Therefore, the presence of excited states causes a reduction of the ability of the electronic system to absorb further photons at the same wavelength. In transient absorption (TA) spectra, this reduction of the total oscillator strength due to the presence of excited states becomes visible as a transient photobleach (PB). According to the PSF, the relative change of the total oscillator strength f of an absorption band is equal to the relative occupation of available excitations:

$$\frac{\delta f}{f} = -N/N_s \tag{A3.9}$$

where N is the density of excited states and N_s is the saturation density. The relative change of the total oscillator strength is experimentally accessible by measuring the relative photobleach:

$$\frac{\partial f}{f} = -PB_{rel} = \frac{\Delta A}{A_n} \tag{A3.10}$$

The differential absorption ΔA is given by

$$\Delta A = A_p - A_{np} = \ln(T_{np}) - \ln(T_p) = -ln\left(\frac{T_p}{T_{np}}\right) = -ln\left(\frac{T_p - T_{np}}{T_{np}} + 1\right) = -ln\left(\frac{\Delta T}{T} + 1\right) \tag{A3.11}$$

where A_n is the natural absorbance defined in A3.3, and the suffices “p” and “np” signify “pump pulse on” and “pump pulse off”, respectively. The differential transmission ΔT/T in the right most term in eq. A3.11 is the quantity usually measured in TA spectroscopy.

Lambert-Beer’s law for the differential absorption is given by

$$\Delta A = \sigma_{exc} \cdot c_{exc} \cdot d = \sigma_{exc} \cdot N_{exc} \tag{A3.12}$$

where σ_{exc} is the cross-section in cm^2 of the ground state bleach caused by one excited state, N_{exc} is the area density of excited states, and c_{exc} is the concentration of excited states, which can be calculated by

$$c_{exc} = N_p \cdot (1 - T)/d \tag{A3.13}$$

with N_p as the surface density of pump pulse photons (in cm^{-2}) and T is the transmission at the pump wavelength, ignoring reflection and scattering losses. Inserting A3.12 and A3.3 into A3.10, we obtain:

$$\frac{\sigma_{exc}}{\sigma_m} \cdot \frac{c_{exc}}{c_m} = \frac{N}{N_s} \tag{A3.14}$$

According to the definition, $N = c_{exc}$. The saturation density N_s finally, is related to the size of the excited state L_{exc}, i.e the electron hole correlation length, i.e., the distance at which the probability to find both electron and hole at the same time is 1/e or $1/e^2$ of the maximum value for one-dimensional or two-dimensional excited states, respectively. Thus, $N_s = c_m/L_{exc}$ and therefore

$$L_{exc} = \sigma_{exc}/\sigma_m \tag{A3.15}$$

In the absence of disorder, the result for L_{exc} in A3.13 should be independent of the chosen detection wavelength as long it is the same for σ_{exc} and σ_m. However, in the presence of disorder, energy relaxation by energy transfer and transient hole burning effects generally cause the spectral shape of the PB band to be markedly different from that of the ground state absorption (A) band. Assuming that disorder acts on the transition energies but not on the transition cross-sections, we can integrate over the respective bands to get a better approximation for L_{exc} for disordered systems:

$$L_{exc}^{disorder} = \frac{\int_{\omega_{min}}^{\omega_{max}} \sigma_{exc}(\omega)}{\int_{\omega_{min}}^{\omega_{max}} \sigma_m(\omega)} = \frac{f_{exc}}{f_m} \tag{A3.16}$$

where the integration limits are chosen such as to minimize overlap with adjacent bands. The total oscillator strengths for the monomer and the excited states (f_m and f_{exc}, respectively), if defined this way, will have a unit of [cm^2 eV].

The biggest sources of error are:

- Uncertainty of pump pulse intensity (20%)
- Uncertainty of density and local thickness (20%)
- Superposition of PB band with PA so that PB is underestimated (20%)

- Superposition with stimulated emission (SE) so that PB is overestimated (< 5% in conjugated polymers but up to 50% in rigid systems like phthalocyanines and carbon nanotubes)

The first two contributions dominate if L_{exc} values from different samples must be compared, while excited state localization due to exciton dissociation in a single experiment can be traced with higher precision.

c) Global and Target Analysis

Analysis of the pure D (donor) and A (acceptor). Femtosecond transient absorption (TA) spectroscopy is used to trace photophysics that occur on a time scale of femto to picoseconds. However, the spectral signatures of photoexcited states in TA spectra generally overlap, so matrix decomposition techniques need to be used to obtain the time-resolved populations of the various photoexcited states separately. The mathematics of the proceduce has been described by van Stokkum *et al.*[Sto04] Here, we generalize to arbitrary photoexcitation dynamics.

We apply Beer-Lambert's Law,

$$A_c(t,\omega) = \sum_i c_i(t)\sigma_i(\omega) \qquad \text{(A3.17)}$$

to find the calculated transient absorption $A_c(t,\omega)$ reproducing the measured transient absorption spectrum $A(t,\omega)$, which depends on time t and probe energy ω, by a superposition of states i with characteristic time-resolved concentration $c_i(t)$ and energy-dependent absorption cross-section $\sigma_i(\omega)$. Eq. A3.2 can be written in matrix form:

$$A_c = c \times \sigma \qquad \text{(A3.18)}$$

In eq. A3.18, each column of the c matrix represents one complete concentration-time dependence of a state i, while each row of the σ matrix represents the full (time-invariant) spectrum of that state i. Of course, any linear combination σ' of the spectra in the σ matrix

$$\sigma' = s \times \sigma \qquad \text{(A3.19)}$$

s being the spectral weight matrix, can also solve eq. A3.18, as can be seen by introducing A3.19 into A3.18:

$$A_c = c \times s^{-1} \times \sigma' \tag{A3.20}$$

and substituting $c \times s^{-1} \equiv c'$:

$$A_c = c' \times \sigma' \tag{A3.21}$$

Comparing A3.21 and A3.18 highlights the crux in global spectral modeling: There is an infinite number of combinations of c' and σ' that all reproduce the measured TA spectra perfectly. Our goal is to find the photophysical dynamics c and the photophysical spectra σ, not some linear combinations c' and σ'. Multiplying A3.18 by the inverse matrix of the spectra, σ^{-1}, we get

$$A_c \sigma^{-1} = c \tag{A3.22}$$

The interpretation of A3.22 is as follows: as there is only one inverse of the spectra, there is one and only one matrix c solving A3.22. Consequently, if the spectra of the photoexcited states are known, we are guaranteed to find the photophysical concentrations. Vice versa, if the concentrations are known, we are guaranteed to find the photophysical cross-sections.

In the present work, we find the spectra of the singlet excitons by performing TA spectroscopy on the pure donor (**D**) and acceptor (**A**) molecules. In Figure A3.3, we excited the pure **D** at 620 nm. The TA spectra in the near infrared spectral region are dominated by a single band at 1.03 eV. There is a shoulder at 1.2 eV which could be caused by additional states like triplets or charge states. If this were the case then these states should have different relaxation kinetics and therefore should cause a spectral evolution with the pump-probe delay time t. We can safely reject this scenario by perfect reproduction of the TA spectra at all probe wavelengths, delay times, and pump intensities with one set of parameters (namely k_a and k_{tr}) in a target model assuming only a single state (see Figure A3.4). The parameters k_a and k_{tr} are interpreted in the main manuscript as rate constants for exciton annihilation and trapping, allowing us to find the exciton diffusion constant and the density of traps.

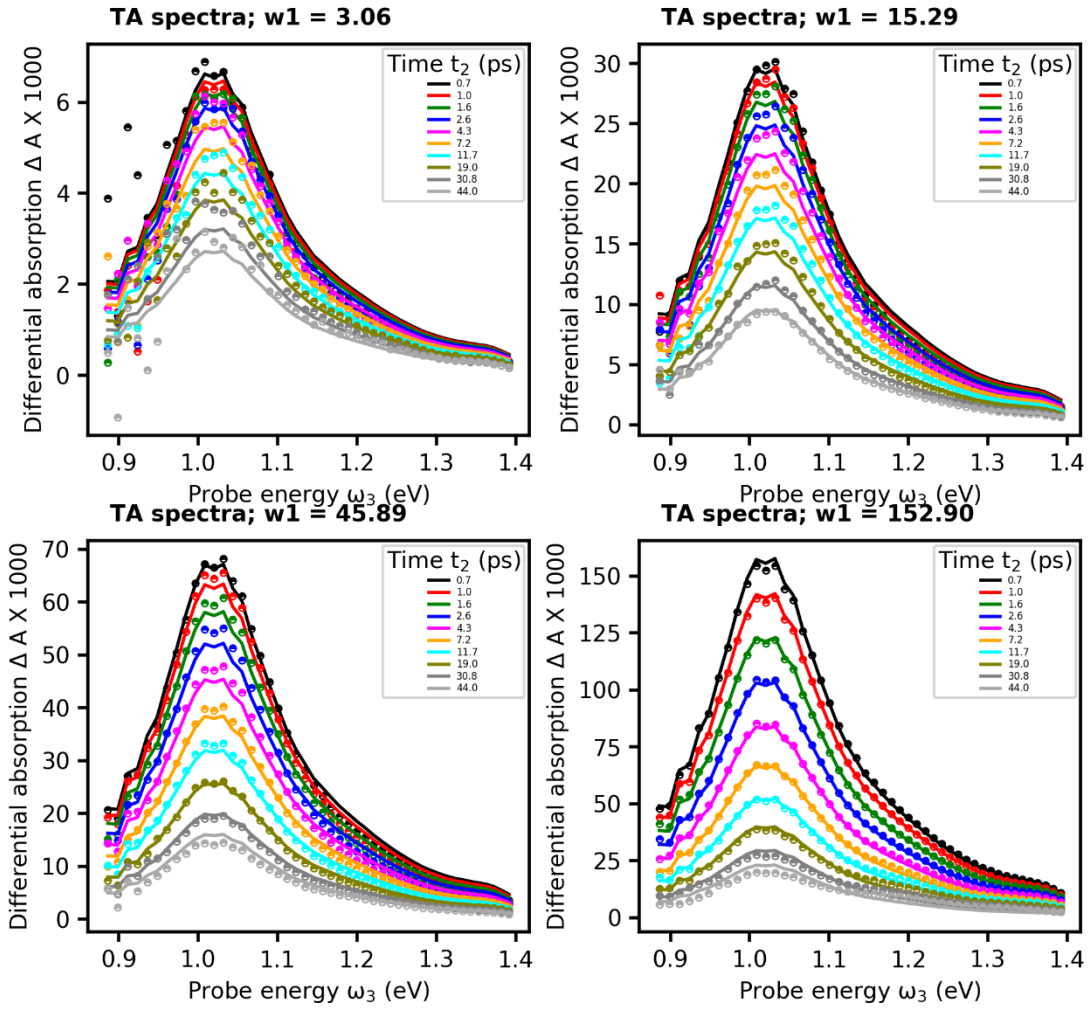

Figure A3.3: TA spectra of the donor pumped at 620 nm with four different pump energies, given as "w1" in μJ cm^{-2}. Symbols are experimental data points, lines of same color are global fits according to the target model depicted in Figure A3.4.

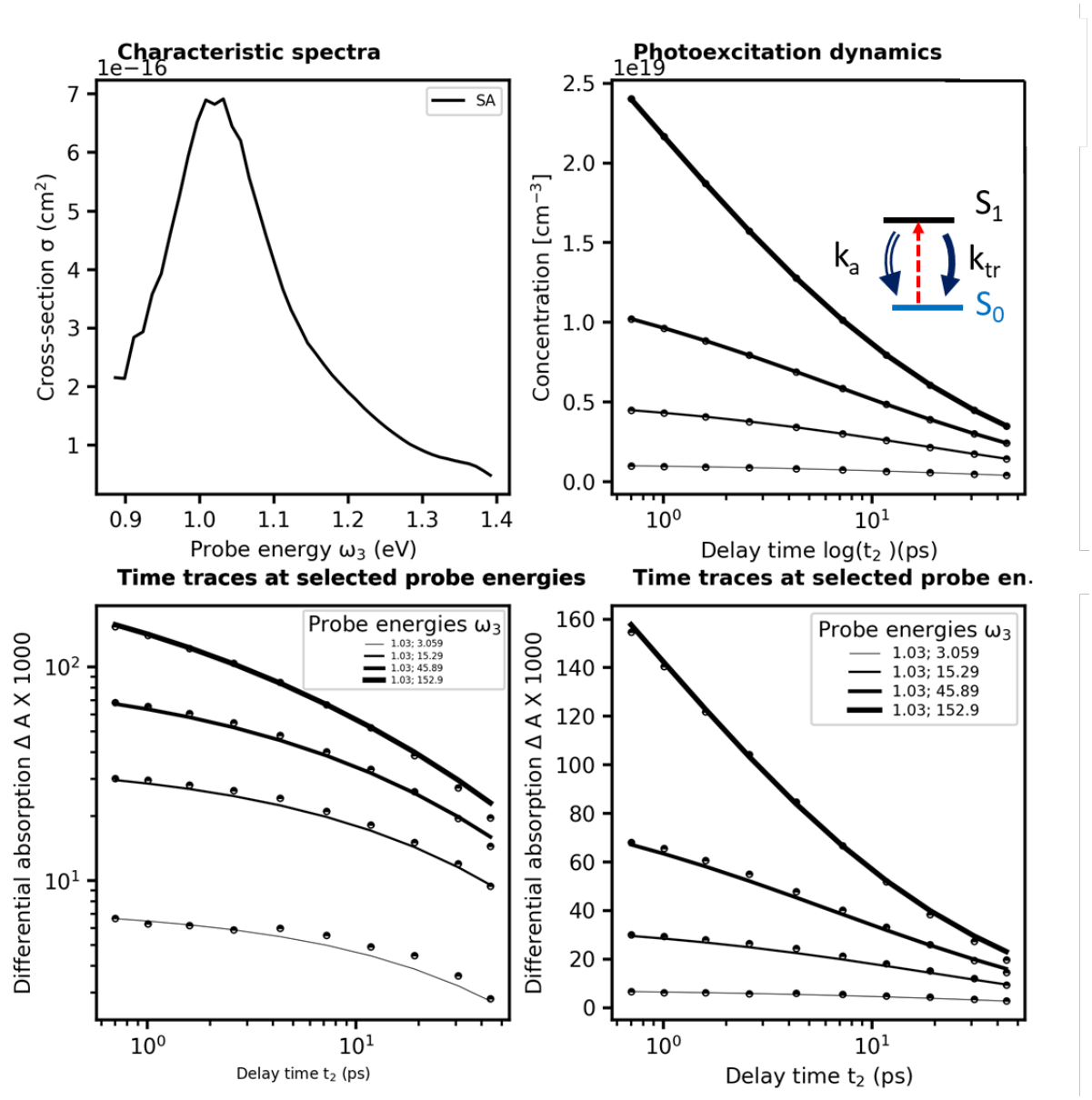

Figure A3.4: Result of target analysis of intensity dependent TA spectra in Figure A3.3. The target model is given in the right upper panel. An upward arrow indicates the excitation process, downward arrows indicate first order and second order relaxation processes (one-line and double-line arrows, respectively), here caused by diffusion-controlled exciton trapping and annihilation (rate constants k_{tr} and ka, respectively). The cross-sections and concentrations in the upper row correspond to σ and c in eq. A3.18.

In the same way, we obtain the characteristic spectrum and the relaxation constants from the pure **A** film excited at 510 nm, see Figure A3.5 and 6.

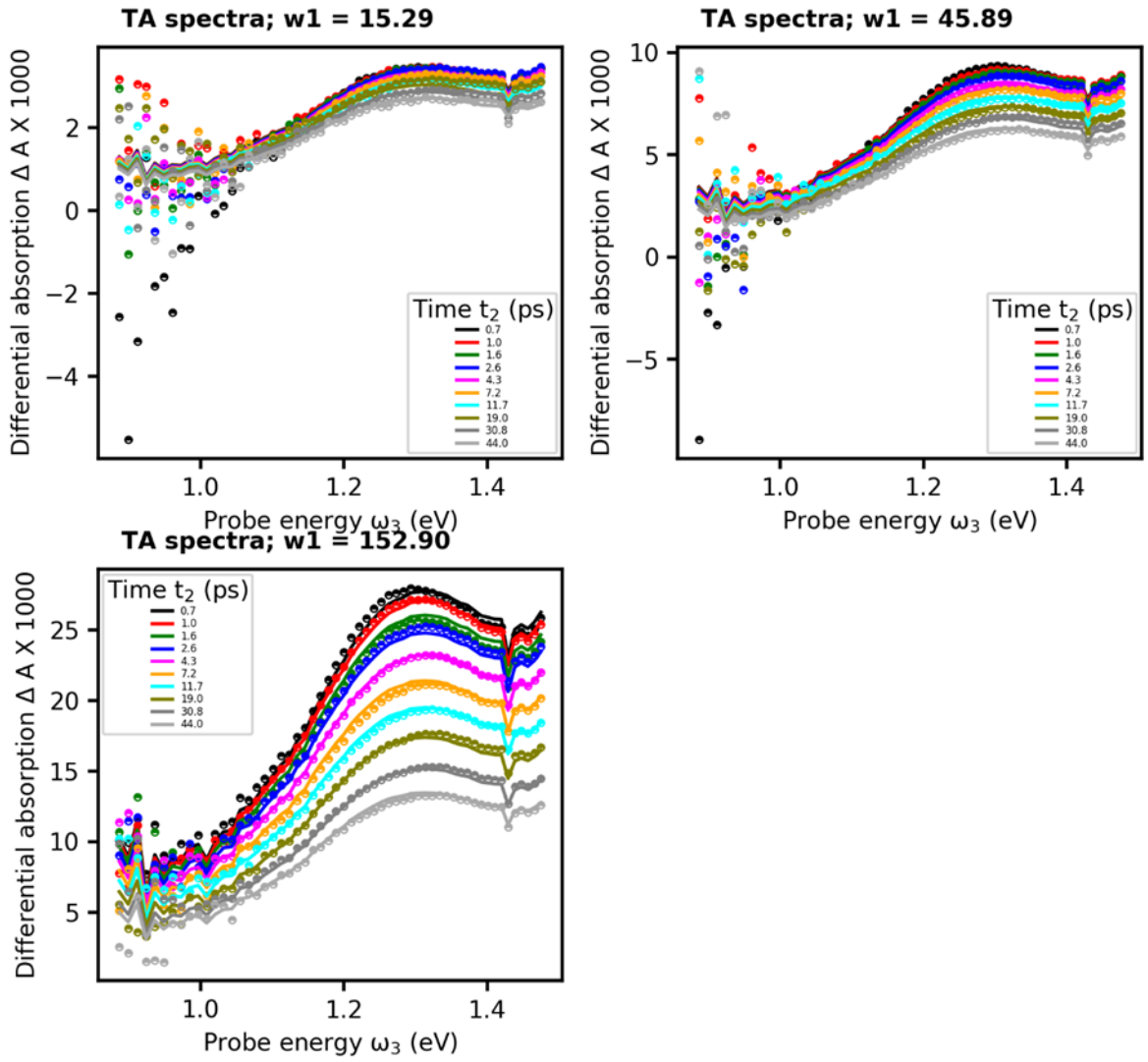

Figure A3.5: TA spectra of the acceptor pumped at 510 nm with three different pump energies, given as "w1" in μJ cm^{-2}. Symbols are experimental data points, lines of same color are global fits according to the target model depicted in Figure A3.6.

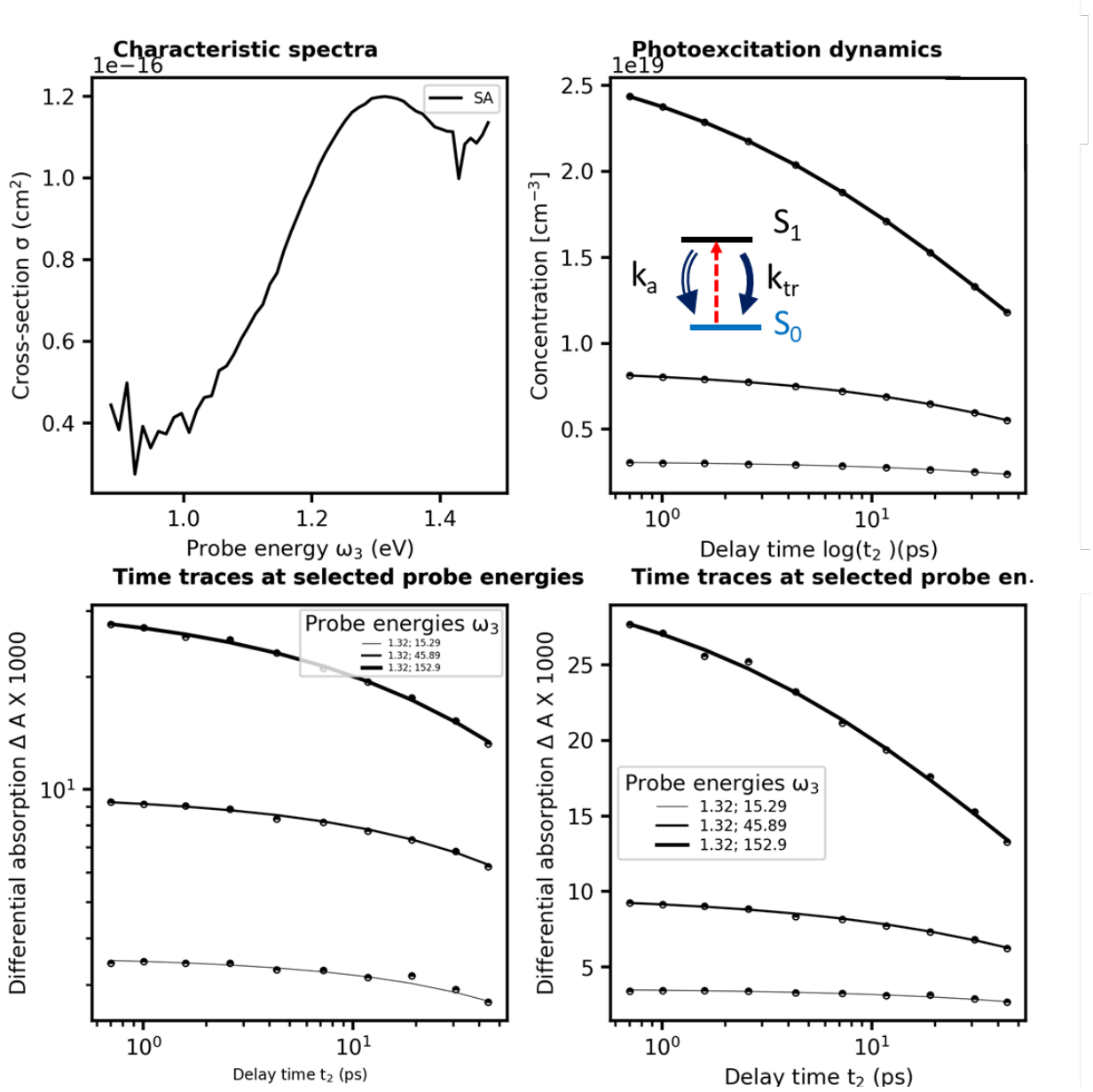

Figure A3.6: Result of target analysis of intensity dependent TA spectra in Figure A3.5. The target model is given in the right upper panel. An upward arrow indicates the excitation process, downward arrows indicate first order and second order relaxation processes (one-line and double-line arrows, respectively), here caused by diffusion-controlled exciton trapping and annihilation (rate constants k_{tr} and ka, respectively). The cross-sections and concentrations in the upper row correspond to σ and c in eq. A3.18.

Analysis of the blend sample. The information obtained in Figures. A3.3-6 is essential for the quantification of the elementary decay paths in the photovoltaic blends. We now have sufficient knowledge about the excited state absorption cross-sections of singlet states such that we can solve the rather complex target model for the blends, see upper right panels in Figures A3.8 and 10. As only two states are active in the overall relaxation process, precise knowledge of the spectral shape of the charge separated state is not necessary. Nonetheless, we verified that the excited state spectra we predict for the charge separated state coincide with nanosecond transient absorption spectra of the blends, thus assuring the long-lived nature of the species assigned to charge separated states.

In Figure A3.7, we show TA spectra of the as-deposited blend excited at 620 nm. We deploy the target model shown in Figure A3.8 and it fits perfectly. This confirms the overall layout of the target model, but not the value of the involved rate constants. To get these, we must exploit the information we got about the excited state spectra of the donor exciton. According to eq. A3.21, we must adjust the matrix c' such that c'=c. Then according to eq. A3.22, σ'=σ. We accomplish this by tuning the rate constants of the target model until we find a satisfactory reproduction of the known σ of the singlet state. In our software realization (written in Python and based on open source packages such as numpy, scipy, matplotlib), this is done semi-automatically, by manually varying the charge transfer constant and optimizing the other parameters by nonlinear optimization. We find that only for a charge transfer rate of 1/25 ps, the resulting excited state spectra are acceptable. This notion is based on the following criteria:

- The absolute value of the cross-section of the singlet state is about 6e-16 cm^2, similar to the value obtained for the pure donor.
- The spectral shape of the donor singlet does not re-appear in the spectral shape of the charge separated state. If this were the case, it would demonstrate the presence of off-diagonal terms of the spectral weight matrix s in eq. A3.19. The obtained cross-sectiond would therefore be mixed states, not pure ones. According to eq. A3.22, if the cross-sections are mixed, the concentrations will also be mixed, and therefore wrong.
- The contribution of the *donor* photobleach (PB) region for both singlet and charge separated states is the same and agrees quantitatively with the cross-section for ground state absorption, compare with Figure A3.2. We have very little excitonic coupling, so we exclude exciton localization. Therefore, we know that our excited state,

irrespective whether neutral or charged, occupy a single molecule. We can therefore require to find the value of $\sigma_{GSA} \approx 2 \cdot 10^{-16} cm^2$ that we obtain from Figure A3.2, for both singlets and charged states. This is exactly the case.

- The contribution of the *acceptor* PB increases due to the charge separation process because we resonantly pump the donor excitons.

In the same way, we analyze the TA spectra of the annealed blend, see Figures A3.9 and 10. The fits are perfect, so the layout of the target model is good. Only for a charge transfer rate of 1/100 ps, we are able to minimize the presence of the sharp and easily visible donor singlet state in the cross-section spectrum for the charge separate state. At 1.03 eV, the maximum of the **D** singlet state, we find only an oscillatory behavior, which might point to a first derivative component in the deactivation of the **D** singlet state, e.g. by spectral relaxation.

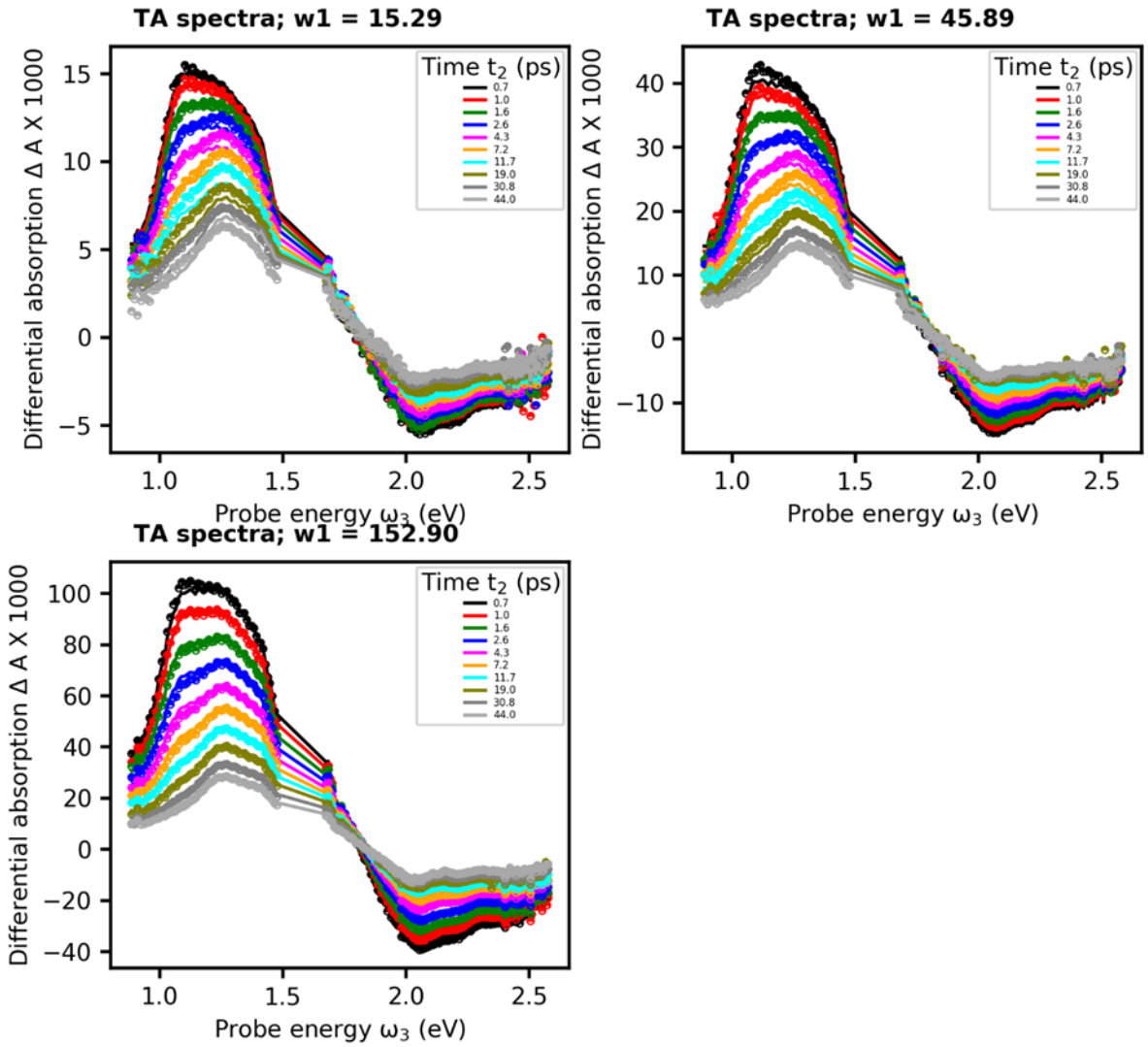

Figure A3.7: TA spectra of the as-deposited blend pumped at 620 nm with three different pump energies, given as "w1" in μJ cm^{-2}. Symbols are experimental data points, lines of same color are global fits according to the target model depicted in Figure A3.8.

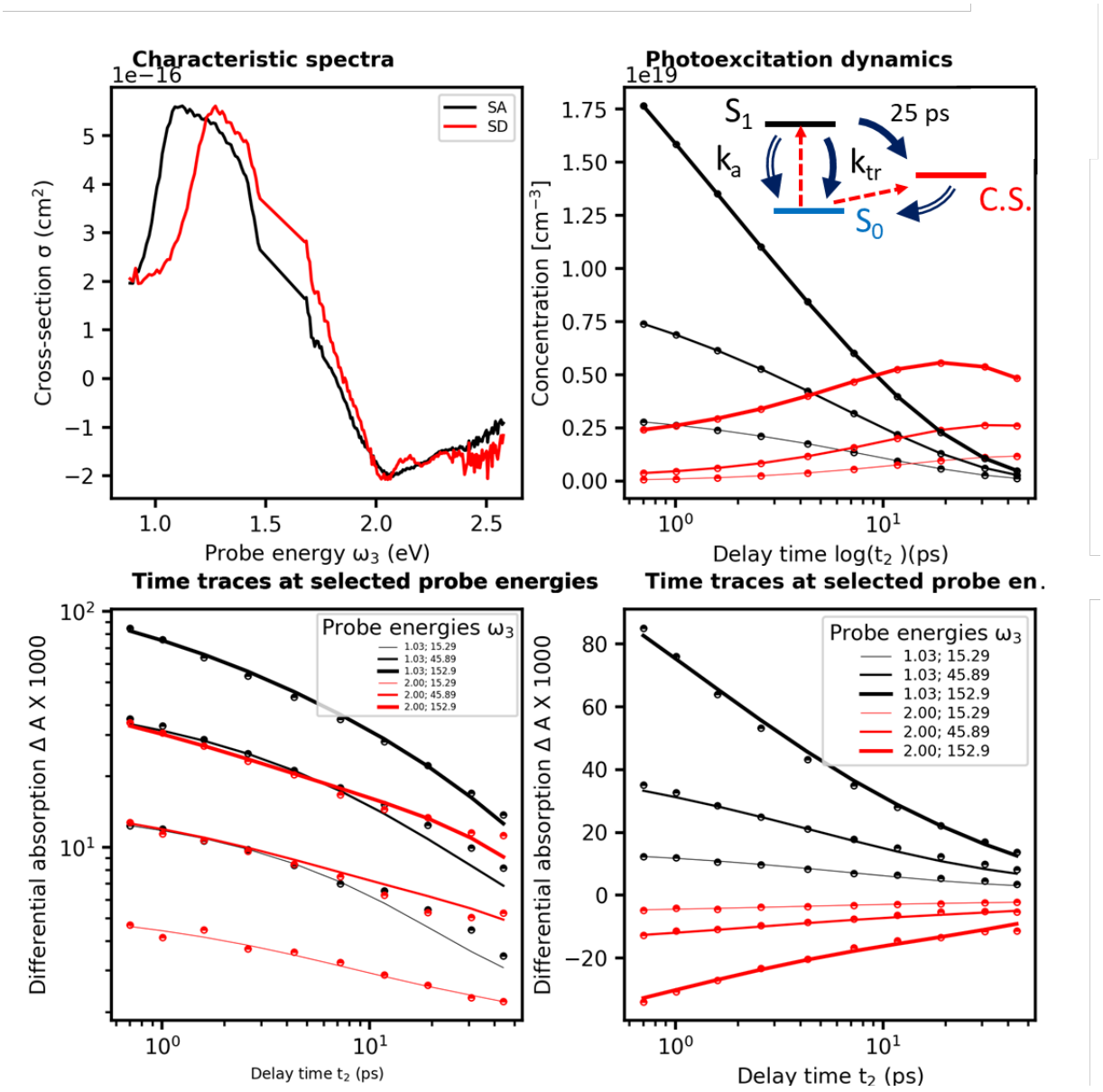

Figure A3.8: Result of target analysis of intensity dependent TA spectra in Figure A3.7. The target model is given in the right upper panel. Photoexcited states appear in same color as the corresponding cross-sections and concentrations in the upper row of the figure. Upward arrows indicate the excitation process, downward arrows indicate first order and second order relaxation processes (one-line and double-line arrows, respectively).

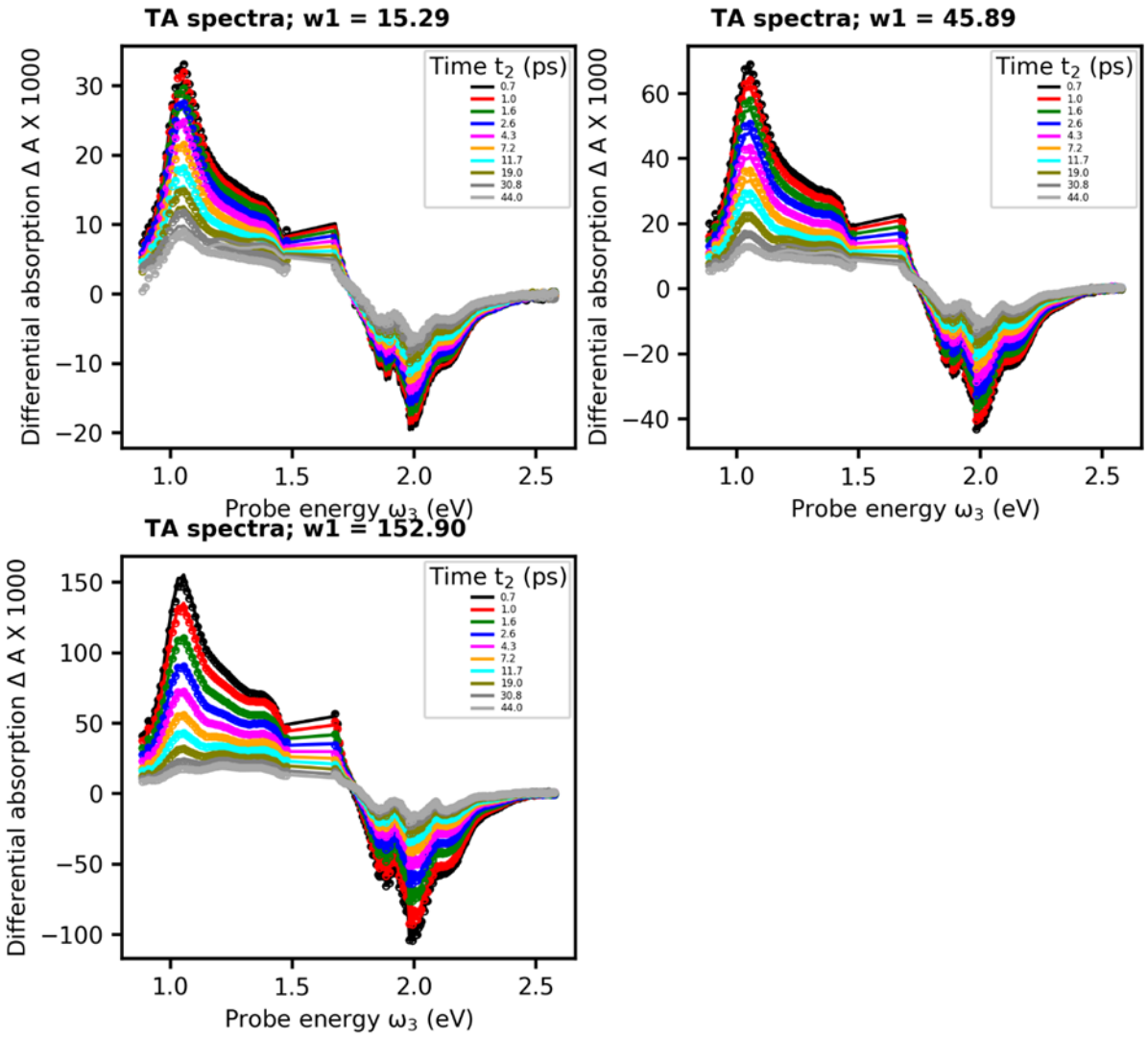

Figure A3.9: TA spectra of the annealed blend pumped at 620 nm with three different pump energies, given as "w1" in μJ cm^{-2}. Symbols are experimental data points, lines of same color are global fits according to the target model depicted in Figure A3.10.

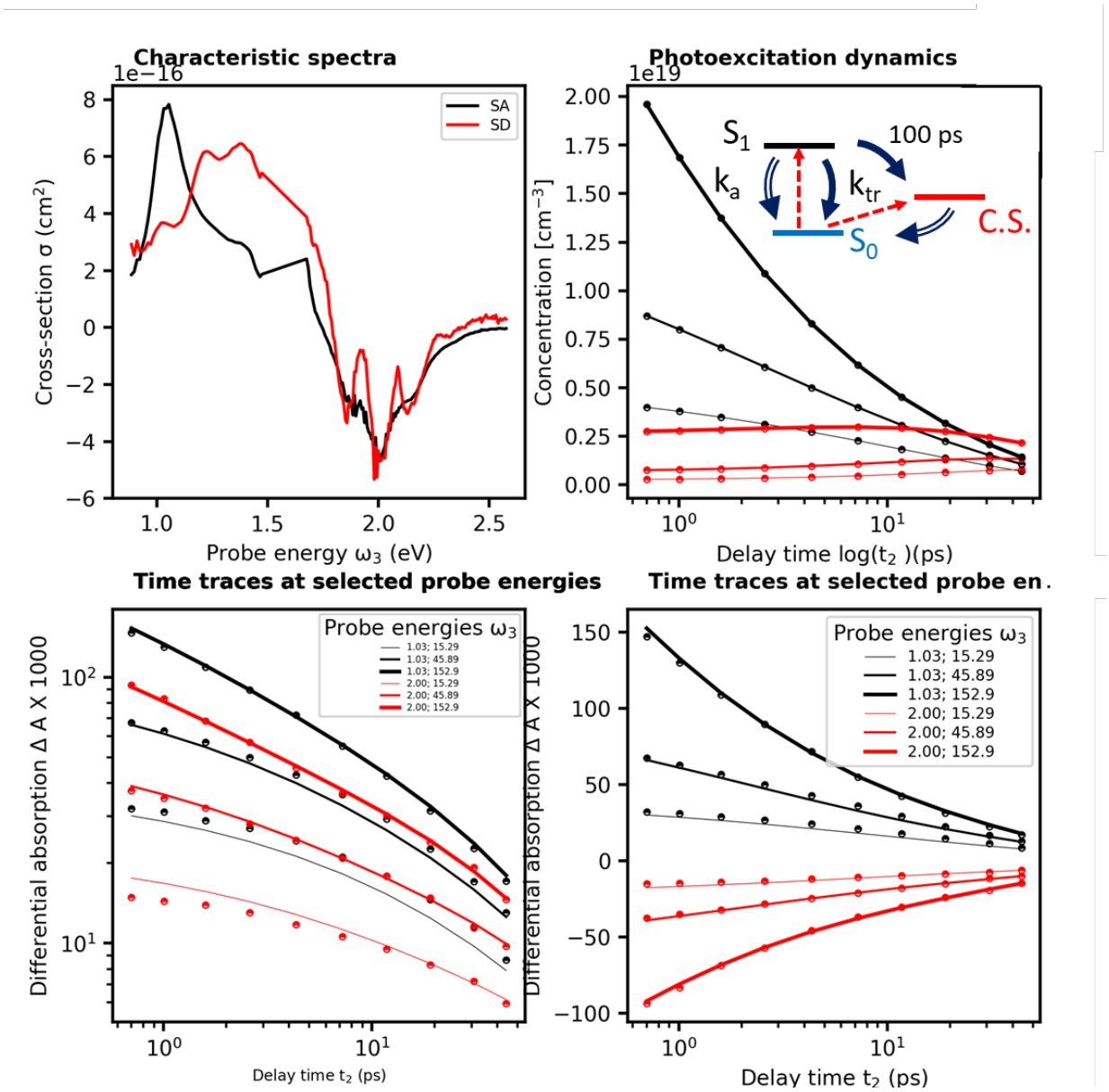

Figure A3.10: Result of target analysis of intensity dependent TA spectra in Figure A3.9. The target model is given in the right upper panel. Photoexcited states appear in same color as the corresponding cross-sections and concentrations in the upper row of the figure. Upward arrows indicate the excitation process, downward arrows indicate first order and second order relaxation processes (one-line and double-line arrows, respectively).

A3.2.2 Exciton Diffusion

We have modeled singlet exciton dynamics by assuming diffusion-controlled exciton quenching at indestructible quenching sites at a concentration c_Q, assumed homogeneous, in

parallel with diffusion-enhanced exciton annihilation by a Foerster resonance energy transfer mechanism with typical annihilation distance R_a.

For both processes, we assume the same exciton diffusion constant D_{exc} so that the rate equation becomes:[Goe84]

$$\frac{dS}{dt} = -k_q^0(t) \cdot S - \left(k_q^\infty + k_F + k_{nr} + k_{ct}\right) \cdot S - (k_a^0(t) + k_a^\infty) \cdot S^2. \qquad \text{(A3.23)}$$

Herein, in the case of three-dimensional diffusion, $k_q^0(t) = 4\pi \cdot R_q^2 \cdot D_{exc} \cdot c_Q / \sqrt{2\pi D_{exc} t}$, $k_q^\infty = 4\pi \cdot R_q \cdot D_{exc} \cdot c_Q$, $k_a^0(t) = \frac{2}{3}\pi^{3/2} R_a^3 \tau_F^{-1/2}$, and $k_a^\infty = 4\pi \cdot 0.676 \cdot {D_{exc}}^{3/4} \cdot R_0^{3/2} \cdot \tau_F^{-1/4}$, while in the case of predominantly one-dimensional diffusion, $\left(k_q^\infty = k_a^\infty\right) \approx 0$, $k_q^0(t) = 4\pi \cdot D_{exc} \cdot R_q^2 \cdot c_Q / \sqrt{\pi D_{exc} t}$ and $k_a^0(t) = 2\pi \cdot R_q^2 \cdot D_{exc} \cdot c_Q / \sqrt{\pi D_{exc} t}$. The parameter k_{ct} is the exciton dissociation (charge transfer) constant at the D-A interface which we set zero for the pure **A** and **D** films. Assuming electron transfer as the quenching mechanism, we can set the reaction radius to the nearest neighbor distance of R_q=1 nm.[ALin14]

A3.2.3 Calculation of the Free Carrier Yield

The overall chain of photovoltaic elementary processes is summarized in Scheme A3.1.

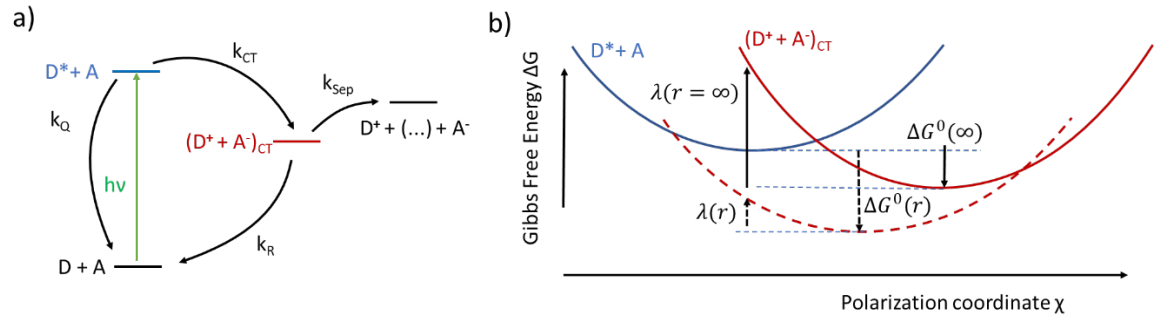

Scheme A3.1: a) Elementary processes for free carrier generation in a bulk heterojunction solar cell, b) Gibbs free energy (ΔG) surfaces as function of the polarization coordinate χ, showing the dependence of the driving force ΔG^0 and the reorganization energy λ on the center-to center distance r of the donor (**D**) and acceptor (**A**) excess charge densities, for the electronic states involved in the calculation of k_{CT}. Similar representations can be given for the calculation of k_R and k_{Sep}.

According to Scheme A3.1a, the yield of free carriers is given by

$$\phi_{fc} = \phi_{CT} \cdot \phi_{Sep} = \frac{k_{CT}}{(k_{CT}+k_Q)} \cdot \frac{k_{Sep}}{(k_{sep}+k_R)}, \quad \text{(A3.24)}$$

where ϕ_{CT} and ϕ_{sep} are the yields for charge transfer and charge separation, respectively, and k_{CT}, k_Q, k_{Sep}, and k_R are the rates for charge transfer, exciton quenching, charge separation and charge recombination, respectively. By a target analysis, we have found an experimental value for k_Q and a lower limit for k_{CT} (since in the annealed sample, charge transfer is diffusion controlled). The three relevant charge transfer processes $Y \epsilon \{CT, Sep, R\}$ can be described by semiclassical Marcus theory:

$$k_Y = \sqrt{\frac{\pi}{\hbar^2 \lambda_s(r) k_B T}} |V(r,p)|^2 \sum_v^{\infty} \frac{e^{-S} S^v}{v!} exp\left[\frac{-\left(v E_v + \lambda_s(r) + \triangle G_Y^0(r)\right)^2}{4\lambda_s(r) k_B T}\right] \quad \text{(A3.25)}$$

where the Huang-Rhys factor is given by $S = \lambda_v / E_v$, λ_v being the internal reorganization energy and E_v the vibrational energy of an effective mode. The external reorganization energy is given by $\lambda_s(r)$, where r is the center-to center distance of the oxidized donor (**D**) and reduced acceptor (**A**) excess charge densities, υ is the vibrational quantum number, V is the coupling between **D** and **A**, k_B is Boltzmann's constant, and $\Delta G_Y^0(r)$ is the Gibbs free energy change ("driving force") for charge transfer process Y. Ignoring entropy contributions to the driving force, we can express ΔG_Y^0 as the difference of the minima of the potential energy surfaces of the final and initial states for process Y, $E_f(\chi)$ and $E_i(\chi)$, respectively, both depending on the polarization coordinate χ (see Scheme A3.1b):

$$\Delta G_0^Y = \min\left(E_f^Y(\chi)\right) - min\left(E_i^Y(\chi)\right) \quad \text{(A3.26)}$$

Since the quantities on the right side of eq. A3.26 are not directly accessible, we need to introduce a series of intermediate steps that are accessible either experimentally or by quantum chemical calculations. Weller has derived a simple formula for the energy of the final state, starting from cyclovoltammetric measurements of the donor first oxidation and acceptor first reduction potentials and considering the dependence of the solvation enthalpies of the final state in solvents of different dielectric constant.[Wel82] However, in their derivation, they did not consider the solvation enthalpy of the neutral initial state. By writing down reversible pathways for solvation of ground, excited and charged states, optical

excitation and charge transfer, one can show that Weller's equation remains valid if one assumed that the solvation enthalpy of ground states does not depend on the dielectric constant. The correct equation for the driving force for charge transfer, explicitly considering solvation of neutral species, is given by:

$$\Delta G_0^{CT} = -E_{opt} + E_{ox}^D - E_{red}^A + k\left(-\frac{1}{2\varepsilon_{ref} r_d} - \frac{1}{2\varepsilon_{ref} r_a} + \frac{1}{2\varepsilon_{inf}^{ref} r_d} + \frac{1}{2\varepsilon_{inf}^{ref} r_a} - \frac{1}{2\varepsilon_{inf} r_d} - \frac{1}{2\varepsilon_{inf} r_a} + \frac{1}{2\varepsilon_r r_d} + \frac{1}{2\varepsilon_r r_d} + E_c\right) \quad \text{(A3.27)}$$

with $k = q^2/(4\pi\varepsilon_0)$, E_{opt} = 1.77 eV as the optical bandgap of the donor, $E_{ox}^D = qP_{ox}^D = 5.12\ eV$ and $E_{red}^A = qP_{red}^A = 3.66\ eV$ are the first oxidation and first reduction potentials, respectively, of the donor and acceptor, respectively, times the unit charge q to obtain energy units and measured by cyclovoltammetry in dichloromethane, r_d and r_a are the radii of the cavities (assumed spherical) occupied by the donor and acceptor, respectively, obtained by calculating the volume occupied by the molecules from their molecular mass and assuming a density of $\rho_{film} = 1.3\ g/cm^3$, $\varepsilon_r = 3.6$ is the relative dielectric constant, assumed isotropic, of the **D-A** blend, $\varepsilon_{ref} = 8.93$ is the relative dielectric constant of dichloromethane, $\varepsilon_{inf} = \varepsilon_{inf}^{ref} = 3.0$ is the optical relative dielectric constant of both dichloromethane and the **D-A** blend. The coulomb energy E_c is given by

$$\Delta E_C = \sum_{d\in D^+, a\in A^-} \frac{q_d q_a}{4\pi\varepsilon_0\varepsilon_r r} \quad \text{(A3.28)}$$

where the overall excess charge density of **D+** and **A-** is represented as partial point charges q_a and q_d on acceptor and donor atoms, respectively, as can be obtained by a Mulliken population analysis. Using these values, we can draw the potential energy parabola for the ground state, the excited state and the charge separated state. It is clearly displayed that for the parameters chosen, charge transfer proceeds virtually without activation energy thus justifying the relative independence of the charge transfer rate k_{ct} of the **D-A** distance r (see Figure 4.26 in Section 4.9 of the main body), defined as the distance between the centers of gravity of the donor and acceptor excess charge distributions. It is further displayed that charge recombination proceeds far in the Marcus inverted region, thus justifying the increase of k_{CR} with decreasing distance, see Figure 4.26 in Section 4.9. Further parameters for the calculation of Figure 4.26 in Section 4.9 were: $\lambda_v = 0.12\ eV$, a_0 = 1 nm (hopping distance)

to calculate a hopping rate $k_{hop} = \frac{1}{t_{hop}} = D/a_0^2$, being the inverse of the hopping time, where the diffusion constant is calculated via the Einstein relation $D = \mu k_B T$, where $\mu = 10^{-4} cm^2/Vs$ is the effective charge mobility taken from Reference [Kwo15], $k_B = 8.617 \cdot 10^{-5} eV/K$ is Boltzmann's constant, and T = 293 K is the temperature.

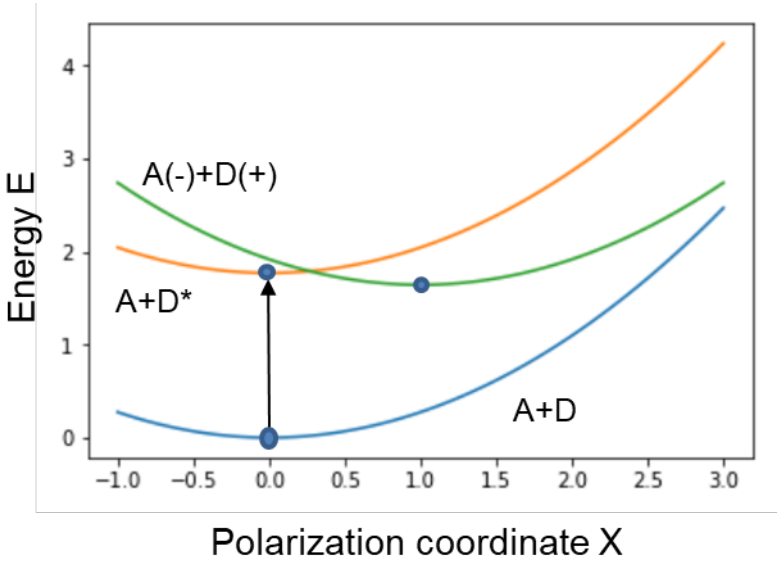

Figure A3.11: Potential energy parabola, as function of the polarization coordinate X, for the ground state, the donor singlet excited state, and the charge separated state (blue, orange, green parabola, respectively). Dots indicate the energy minima.

References

[Won98] K. S. Wong, H. Wang, G. Lanzani, *Chem. Phys. Lett.*, 1998, **288**, 59−64.

[Sto04] I. H.M. van Stokkum, D. S. Larsen, R. van Grondelle, *Biochim. Biophys.Acta*, 2004, **1657**, 82-104.

[Sch85] S. Schmitt-Rink, D. S. Chemla, D. A. B. Miller, *Phys. Rev. B.*, 1985, **32**, 6601-6609.

[Lue09] L. Lüer, S. Hoseinkhani, D. Polli, J. Crochet, T. Hertel, G. Lanzani, *Nature Phys.*,2009, **5**, 54-58.

[Sto04] I. H. M. Van Stokkum, D. S. Larsen, R. van Grondelle, *Biochimica et Biophysica Acta*, 2004, **1658**, 82-104.

[Goe84] U. M. Goesele, *Prog. Reaction Kinetics*, 1984, **13**, 63-161.

[ALin14] J. D. A. Lin, O. V. Mikhnenko, J. Chen, Z. Masri, A. Ruseckas, A. Mikhailovsky, R. P. Raab, J. Liu,. P. W. M. Blom, M. A. Loi, C. J. Garcia-Cervera, I. D. Samuel, T-Q. Nguyen, *Mater. Horiz.*, 2014, **1**, 280-285.

[Wel82] A. Weller, *J. Phys. Chem.*, 1982, **133**, 93-98.

[Kwo15] O. K. Kwon, J.-H. Park, S. K. Park, S. Y. Park, *Adv. Energy Mater.*, 2015, **5**, 1400929.

Appendix 4

List of

Equations/Schemes/Figures/Tables

List of Equations

List of Schemes

List of Figures

List of Tables

Appendix 5

Abbreviations and Symbols

Abbreviations and Symbols

SPR	Structure-property Relationship
MP	Material Paradigm
OLED	Organic Light-emitting Diode
OFET	Organic Field-effect Transistor
OSC	Organic Solar Cell
AIE	Aggregation-induced Emission
ACQ	Aggregation-induced Quenching
RIR	Restricted Intramolecular Rotation
AIEE	Aggregation-induced Enhanced Emission
SLE	Solid State Luminescence Enhancement
TE	Twist Elasticity
DSB	Distyrylbenzene
DCS	Di-CN-styrylbenzene
TPE	Tetraphenylsilole
PMMA	Poly-methyl Methacrylate
SC	Single Crystal
NP	Nanoparticle
PM	Polymorph
BHJ	Bulk Heterojunction
ASM-OSC	All-small-molecule OSC
PCBM	[6,6]-phenyl-C_{61}-butyric acid methyl ester
D	(electron) Donor
A	(electron) Acceptor
H/HOMO	Highest Occupied Molecular Orbital
L/LUMO	Lowest Unoccupied Molecular Orbital

IC	Internal Conversion
ISC	Intersystem Crossing
TR	Thermal Relaxation
PES	Potential Energy Surface
CI	Conical Intersections
DFT	Density Functional Theory
TD-DFT	Time-dependent Density Functional Theory
CASSCF	Complete-active-space Self-consistent Field
CASPT2	Complete-active-space Second-order Perturbation
Abs	UV-Vis Absorption
PL	Photoluminescence
TA	Transient Absorption
PAC	Photoacoustic Calorimetry
SNOM	Scanning Near-field Optical Microscopy
QC	Quantum-chemical
HMO	Huckel Molecular Orbital Method
MO	Molecular Orbital
AO	Atomic Orbital
LCAO	Linear Combination of Atomic Orbital
CI	Configuration Interaction
GSA	Ground State Absorption Spectrum
ESA	Excited State Absorption Spectrum
TDM	Transition Dipole Moment
AHT	Aggregated Herzberg-Teller
CT	Charge Transfer
PCM	Polarizable Continuum Model

I	Inductive Effect
M	Mesomeric Effect
EN	Electronegativity
BO	Born-Oppenheimer Approximation
FC	Franck-Condon principle
SB	Stickler-Berg
PLE	Excitation Spectrum
TCSPC	Time-correlated Single Photon Counting
IRF	Instrument Reaction Function
DSC	Differential Scanning Calorimetry
ESP	Electrostatic Potential
SEM	Scanning Electron Microscope
PVT	Physical Vapor Transport
ASE	Amplified Spontaneous Emission
ERS	Enhanced Resonance Stabilization
TS	*Trans*-stilbene
PA	Photoinduced Absorption
PB	Photobleach
SSA	Singlet-singlet Annihilation
CV	Cyclovoltammetry
CR	Charge Recombination

k_r / k_{nr}	radiative/nonradiative rate
Φ_F/τ_F	PL quantum yield/lifetime
S_0	ground State
S_1/T_1	first excited single/triplet State
n	refractive index
E_{vert}/E_{00}	vertical/adiabatic transition energy
E_{EC}	excitonic coupling
E_{Stok}	Stokes shift
ΔE_{eq}	equilibration/organization energy
$\vec{\mu}$	transition dipole moment
f	oscillator strength
θ_i	magic angle
α	bond angle
ϕ	torsional angle
φ	probabilities/effectiveness
fs	femtosecond
ps	picosecond
V_{OC}	open circuit voltage
V_{SC}	short circuit voltage
L_{exc}	excited state delocalization
σ	absorption cross-section
k_{CT}	charge transfer rate